UNIVERSITÄT LEIPZIG

REPORT
Institute für Physik
The Physics Institutes
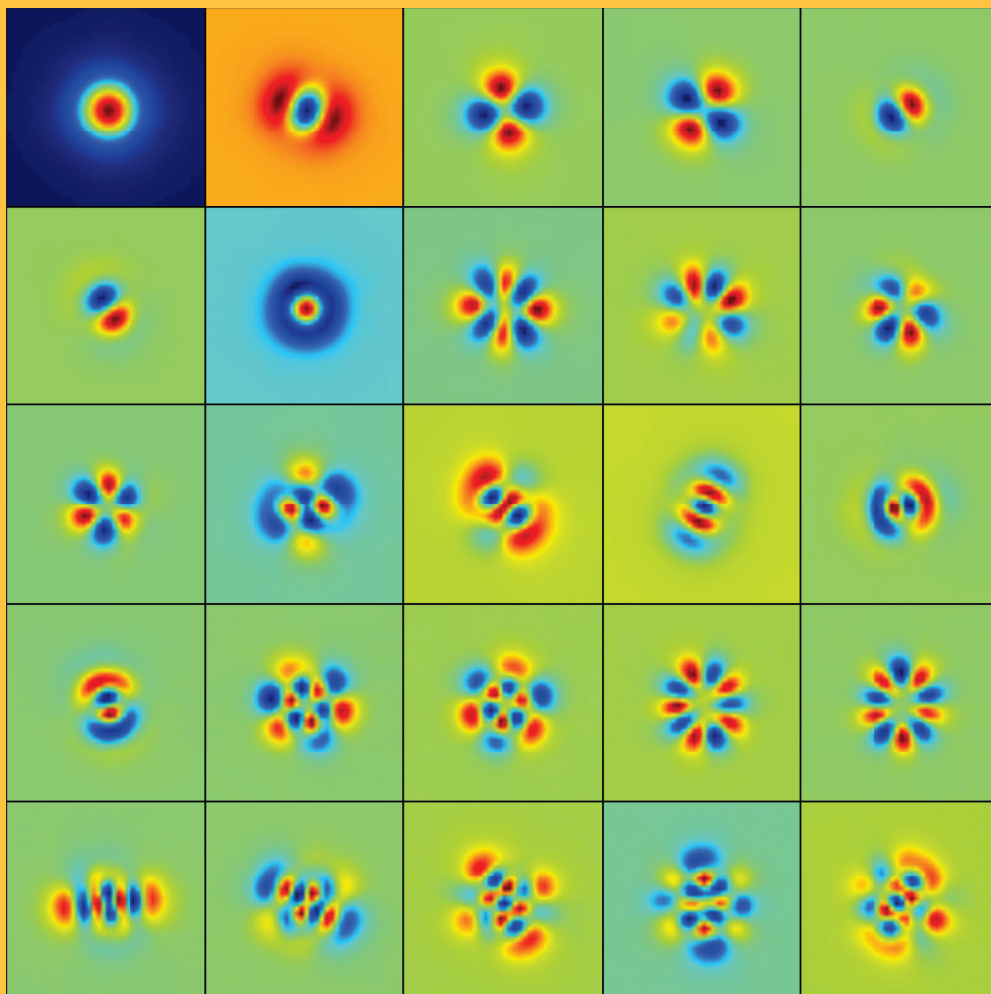
2016

Front cover
The images show the first 25 eigenmodes of conformational fluctuations for a freely diffusing DNA molecule in the center-of-mass frame obtained via principal-components analysis. Strong positive excursions in conformational fluctuations are mapped here to a red color, whereas strong negative excursions are represented in blue. Zero fluctuations at the edges of every mode are in a different color for every panel.

Back cover
TCO2017

Institut für Experimentelle Physik I
Institut für Experimentelle Physik II
Institut für Theoretische Physik

Fakultät für
Physik und Geowissenschaften

Universität Leipzig

Institute for Experimental Physics I
Institute for Experimental Physics II
Institute for Theoretical Physics

Faculty of Physics and Earth Sciences

Universität Leipzig

Report 2016

Addresses

Institute for Experimental Physics I

Linnéstraße 5
D-04103 Leipzig, Germany
Phone: +49 341 97-32654
Fax: +49 341 97-32598
WWW: https://www.physgeo.uni-leipzig.de/fakultaet/institutebereiche/peter-debye-institut/
Mailing
address: Postfach 100 920, D-04009 Leipzig, Germany

Institute for Experimental Physics II

Linnéstraße 5
D-04103 Leipzig, Germany
Phone: +49 341 97-32650
Fax: +49 341 97-32668
WWW: https://www.physgeo.uni-leipzig.de/fakultaet/institutebereiche/felix-bloch-institut/
Mailing
address: Postfach 100 920, D-04009 Leipzig, Germany

Institute for Theoretical Physics

Brüderstraße 16
D-04103 Leipzig, Germany
Phone: +49 341 97-32420
Fax: +49 341 97-32548
WWW: https://www.physgeo.uni-leipzig.de/fakultaet/institutebereiche/theoretische-physik/
Mailing
address: Postfach 100 920, D-04009 Leipzig, Germany

Preface

The 2016 Report of the Physics Institutes of the Universität Leipzig presents a hopefully interesting overview of our research activities in the past year. It is also testimony of our scientific interaction with colleagues and partners worldwide. We are grateful to our guests for enriching our academic year with their contributions in the colloquium and within our work groups. We mention especially Dr. Martin Weigel from Coventry University, UK, who has spent in 2016 his sabbatical in the group of Prof. Janke.

We announce that since early 2017 the Institutes for Experimental Physics I and II have been renamed into *Peter Debye Institute for Soft Matter Physics* and *Felix Bloch Institute for Solid State Physics*. Our history is a source of pride and motivation alike.

The top-level research at the Peter Debye Institute for Soft Matter Physics is reflected by the recent funding of two principle investigators by the European Research Council (ERC). The work of Ralf Seidel on the gene editing technique CRISPR is supported with an ERC Consolidator Grant and the research of Josef Käs on the role of physical processes in cancer progression has been awarded with an ERC Advanced Grant.

One of the special events at the Peter Debye Institute for Soft Matter Physics in 2016 was the first Soft Matter Day. In a one day event, all the departments of the institute presented their current research in talks and posters. The group leaders gave insight into their vision for the future research at the Peter Debye Institute. About one hundred scientists and students took part in this event. Also, members of other institutes and faculties enjoyed the scientific discussions until the late evening and a closing BBQ.

At the Felix Bloch Institute for Solid State Physics a new division for "Applied Magnetic Resonance", headed by Prof. Dr. Nikolaus Weiskopf, member of our institute and director at Max Planck Institute for Human Cognitive and Brain Sciences (MPI-CBS) in Leipzig, has been established. A 9 tesla physical properties measurement system (PPMS) was installed end of 2016; the LIPSION accelerator is in the process of being upgraded with an ECR ion source. Both measures are funded through the scheme "Großgeräte nach Art. 91b GG".

The BuildMoNa Minisymposium on "Metamaterials" end of September was organized by Marius Grundmann and Frank Cichos with nine invited speakers from Germany, France and USA. At the end of November the 17th International Workshop on Recent Developments in Computational Physics "CompPhys16" organized by Wolfhard Janke took place in Leipzig. Around 60 scientists from over 10 different countries exchanged ideas and discussed recent progress in several fields of computational physics.

Scientific work has successfully continued in the Centers of Excellence (Sonderforschungsbereiche) SFB 762 "Functionality of Oxide Interfaces" and SFB TRR 102 "Polymers under Multiple Constraints: Restricted and Controlled Molecular Order

and Mobility". SFB 762 has started 2016 into its third (and last) funding period (2016–2019). Work also continues in DFG Forschergruppe 1616 on photonic nanowires. New challenges are pursued in H2020 project "LOMID", the DFG/ANR Project "Ulysses", the EU IRSES Network DIONICOS "Dynamics of and in Complex Systems" and in the newly established DFG Schwerpunktprogramm SPP 1796 "FFlexCom" as well as in the second funding period of the DFG SPP 1726 "Microswimmers – From Single Particle Motion to Collective Behavior". The International Graduate College "Statistical Physics of Complex Systems" of the Deutsch-Französische Hochschule run by the computational physics group in cooperation with the partners Université de Lorraine, Nancy, Coventry University and the National Academy of Sciences of Ukraine in Lviv, Ukraine, has been prolonged in 2016 and started in January 2017 its 4th funding period from 2017–2020. A joint project with Leibniz-Institute for Surface Modification (IOM) is going on for "Sensors based on single atoms".

Our activities and success is only possible with the generous support from various funding agencies for which we are very grateful and which is individually acknowledged in the brief reports.

Leipzig,
August 2017

F. Cichos
M. Grundmann
W. Janke
Directors

Contents

III   Institute for Theoretical Physics   209

10 Computational Quantum Field Theory   211

1

Structure and Staff of the Institutes

1.1 Institute for Experimental Physics I

1.1.1 Office of the Director

Prof. Dr. Frank Cichos (Director)

1.1.2 Molecular Nano-Photonics, Molekulare Nanophotonik [MON]

Prof. Dr. Frank Cichos

Technical staff

Dipl.-Phys. Andrea Kramer
Dipl.-Phys. Uwe Weber

PhD candidates

Dipl.-Phys. Marco Braun
Dipl.-Phys. Andreas Bregulla
Martin Fränzl, M.Sc.
André Heber, M.Sc.
Santiago Muiños Landin, M.Sc.
Dipl.-Phys. Romy Schachoff
Tobias Thalheim, M.Sc.

Students

Alice Abend
Jennifer Arndt
Alexander Fischer
Sergio Ortega
Choongeun Park

Ricardo Rose
Falko Schmidt

1.1.3   Molecular Physics, Molekülphysik [MOP]

Prof. Dr. F. Kremer

Secretary

Kerstin Lohse

Technical staff

Dipl.-Ing. (FH) Jörg Reinmuth
Dipl.-Phys. Wiktor Skokow

Academic staff

Dr. Wilhelm Kossack
Dr. Arthur Markus Anton (graduated Nov 2015)
Dr. Emmanuel Urandu Mapesa

PhD candidates

M. Edu. Falk Frenzel
Dipl.-Phys. Nils Neubauer

Students

cand. M. Edu. Patricia Prinz

1.1.4   Soft Matter Physics, Physik der weichen Materie [PWM]

Prof. Dr. Josef A. Käs

Secretary

Claudia Brück

Technical staff

Dr. Undine Dietrich
Dipl.-Phys. Bernd Kohlstrunk

Academic staff

Dr. Jörg Schnauß
Dr. Mareike Zink

PhD candidates

Uta Allenstein, M.Sc. (zusammen mit Prof. Mayr)
Katharina Anna Bela, M.Sc.
Martin Glaser, M.Sc.
Tom Golde, M.Sc.
Dipl.-Phys. Tina Händler
Paul Heine, M.Sc.
Kantida Juncheed, M.Sc.
Hans Kubitschke, M.Sc.
Jürgen Lippoldt, M.Sc.
Philine Hietschold M.Sc.
Erik Morawetz, M.Sc.
Dipl.-Phys. Steve Pawlizak
Saddam Moyazur Rahman, M.Sc. (BBZ, Forschergruppe M. Zink)
Dipl.-Phys. Carsten Schuldt
Dipl.-Phys. Enrico Warmt
Emilia Wisotzki, M.Sc.

Students

Carlotta Ficorella
Pablo Gottheil
Yookyung Ha
Sebastian Henn
Yonah Karkheck
Thomas Lettau
Till Möhn
Paul Mollenkopf
Markus Sommerfeld
Teresa Tschirner
Cary Tutmarc
Astrid Weidt
Joey Wittenbecher
Isabella Marie Forncon Wood

1.1.5 Biological Physics, Biologische Physik [BIP]

Prof. Dr. Claudia Mierke

Secretary

Kerstin Lohse

Technical staff

Dipl.-Ing. Kathrin Koch

PhD candidates

Stefanie Puder, M.Sc.
Dipl.-Phys. Tony Fischer
Tom Kunschmann, M.Sc.
Jeremy Perez, M.Sc.
Nils Wilharm, M.Sc.
Frank Sauer, M.Sc.

Students

Alexander Hayn
Anthony Ogbuehi
Sebastian Ronneberger

1.1.6   Molecular Biophysics, Molekulare Biophysik [MBP]

Prof. Dr. Ralf Seidel

Secretary

Kerstin Lohse

1.2   Institute for Experimental Physics II

1.2.1   Office of the Director

Prof. Dr. Marius Grundmann (director)
Prof. Dr. Pabolo Esquinazi (vice director)

1.2.2   Magnetic Resonance of Complex Quantum Solids, Magnetische Resonanz Komplexer Quantenfestkörper [MQF]

Prof. Dr. Jürgen Haase

Secretary

Sophie Kirchner
Sandy Ehlers
Sandra Meurer

Technical staff

Gert Klotzsche
Stefan Schlayer
Horst Voigt

Academic staff

PD Dr. Marko Bertmer
Prof. Dr. Dieter Freude
Dr. Michael Jurkutat
Prof. Dr. Andreas Pöppl
Dr. Richard Reznicek

PhD candidates

Nina Dvoyashkina, M.Sc.
Stefan Friedländer, M.Sc.
Nataliya Georgieva, M.Sc.
Robin Gühne, M.Sc.
Seungtaik Hwang, M.Sc.
Dipl.-Phys. Alexander Jäger
Arafat Hossain Khan, M.Sc.
Dipl.-Phys. Jonas Kohlrautz
Anastasiia Kultaeva, M.Sc.
Kathrin Lorenz, M.Sc.
Dipl.-Phys. Matthias Mendt
Steven Reichardt, M.Sc.
Daniel Schneider, M.Sc.
Marufa Zahan, M.Sc.

Students

Felix Bolling, B.Sc.
Manuel Lindel, B.Sc.
Elisabeth Vonhof, B.Sc.

1.2.3 Nuclear Solid State Physics, Nukleare Festkörperphysik [NFP]

Prof. Dr. Jan Meijer

Secretary

Birgit Wendisch

Technical staff

Dipl.-Phys. Steffen Jankuhn
Carsten Pahnke
Dipl.-Ing. Joachim Starke

Academic staff

Dr.-Ing. Michael Kieschnick (since October 2016)
Dr. Sébastien Pezzagna

PhD candidates

Sascha Becker, M.Sc.
Tobias Herzig, M.Sc. (since October 2016)
Dipl.-Math. Roger John, B.Sc.
Jan Lehnert, M.Sc. (till February 2016)
Tobias Lühmann, M.Sc. (since February 2016)
Nicole Raatz, M.Sc.
Paul Räcke, M.Sc.
Robert Staacke, M.Sc.
Ralf Wunderlich, M.Sc.

Students

Youssef Albanay, M.Sc. (till June 2016)
Camila Bräutigam (since July 2016)
Stefan Dietel, B.Sc. (since January 2016, till October 2016)
Janson Dwan, B.Sc. (till December 2016)
Jakob Helbig, B.Sc.
Alexander Kühne, B.Sc. (since November 2016)
Johannes Küpper, B.Sc.
Michael Mensing, M.Sc. (till January 2016)
Frederic Renner (since June 2016)
Marcel Rietzschke, B.Sc. (since May 2016)
Clemens Scheuner, B.Sc. (since November 2016)
Erik Wiedemann, B.Sc.
Anne-Dorette Ziems, B.Sc. (since June 2016, till December 2016)

1.2.4   Semiconductor Physics, Halbleiterphysik [HLP]

Prof. Dr. Marius Grundmann

Secretary

Anja Heck
Birgit Wendisch

Technical staff

Dipl.-Phys. Gabriele Benndorf
Monika Hahn
Dipl.-Ing. Holger Hochmuth
Dipl.-Phys. Jörg Lenzner
Dipl.-Phys. Axel Märcker
Gabriele Ramm
Roswitha Riedel

Academic staff

Dr. Heiko Frenzel
Prof. Dr. Michael Lorenz
PD Dr. Rainer Pickenhain
Prof. Dr. Bernd Rheinländer (retired)
Dr. Rüdiger Schmidt-Grund
Dr. Chris Sturm
Dr. Holger von Wenckstern
Dr. Chang Yang

PhD candidates

Sofie Bitter, M.Sc.
Stefan Hohenberger, M.Sc.
Marcus Jenderka, M.Sc.
Robert Karsthof, M.Sc.
Max Kneiß, M.Sc.
Abdurashid Mavlonov, M.Sc.
Tom Michalsky, M.Sc.
Dipl.-Phys. Stefan Müller
Anna Reinhardt, M.Sc.
Steffen Richter, M.Sc.
Peter Schlupp, M.Sc.
Alexander Shkurmanov, M.Sc.
Daniel Splith, M.Sc.
Martin Thunert, M.Sc.
Lukas Trefflich, M.Sc.
Haoming Wei, M.Sc.
Marcel Wille, M.Sc.
Zhang Zhipeng, M.Sc.
Vitaly Zviagin, M.Sc.

Students

Tobias Abel
Philipp Bischoff
Raffael Deichsel
Oliver Herrfurth
Rebecca Hölldobler
Tanja Jawinski
Florian Jung
Evgeny Krüger
Oliver Lahr
Stefan Lange
Steffen Lanzinger
Manuel Raphael Lindel
Sophie Müller
Karim Nafis Imtiaz
Ahsan Rasheed
Laurenz Thyen
Benjamin Wehr
Anna Werner

1.2.5 Solid State Optics and Acoustics, Festkörperoptik und -akustik [FKO]

vacant

1.2.6 Superconductivity and Magnetism, Supraleitung und Magnetismus [SUM]

Prof. Dr. Pablo Esquinazi

Secretary

Sandy Ehlers

Technical staff

Dr. Winfried Böhlmann
Dipl.-Krist. Annette Setzer

Academic staff

Prof. Dr. Michael Ziese
Dr. José Barzola-Quiquia
Dr. Israel Lorite Villalba
Dr. Yogesh Kumar

PhD candidates

Francis Bern, M.Sc.
Christian Eike Precker, M.Sc.
Bogdan Semenenko, M.Sc.
Markus Stiller, M.Sc.

Students

Lukas Botsch, B.Sc.
Tiago Rafael Silva Cordeiro, B.Sc.
Mahsa Zoraghi, B.Sc.
Andrea Schwetzler

1.3 Institute for Theoretical Physics

1.3.1 Office of the Director

Prof. Dr. Wolfhard Janke (director)

Secretary

Gabriele Menge
Susan Moreno
Lea Voigt

1.3.2 Computational Quantum Field Theory, Computerorientierte Quantenfeldtheorie [CQT]

Prof. Dr. Wolfhard Janke

Academic staff

Dr. Stefan Schnabel
Dr. Niklas Fricke
Dr. Jonathan Gross
Dr. Suman Majumder
Dr. Johannes Zierenberg

PhD candidates

M.Sc. Johannes Bock
M.Sc. Momchil Ivanov
M.Sc. Ravinder Kumar ("co-tutelle" with Coventry University, UK)
Dipl.-Phys. Martin Marenz
Dipl.-Phys. Marco Müller
Dipl.-Phys. Hannes Nagel

Dipl.-Phys. Andreas Nußbaumer
M.Sc. Philipp Schierz

Students

Kieran Austin
Marius Bause
Henrik Christiansen
Jan Meischner
Fabio Müller
David Oberthür
Simon Schneider
Benjamin Schott
Paul Spitzner
Ronja Stübel
Tobias Weiss Shane Carlson
Lisa Fiedler
Adrian Häußler
Philipp Hess
Michel Michalkow
Felix Neduck
Katharina Tholen
Robert Wiesen
Chris Allen

1.3.3 Quantum Field Theory and Gravity, Quantenfeldtheorie und Gravitation [QFG]

Prof. Dr. Rainer Verch (Speaker)

Prof. Dr. Gerd Rudolph (retired)

Academic staff

Prof. Dr. Rainer Verch
Priv.-Doz. Dr. Michael Bordag
Dr. Thomas-Paul Hack
Dr. Matthias Schmidt

PhD candidates

Tobias Diez, M.Sc.
Erik Fuchs, M.Sc.
Michael Gransee, M.Sc.
Mathias Hänsel, M.Sc.
Felix Kurpicz, M.Sc.

Students

Mohammed Belhassen
Sandesh Bhat
Stanislaw Kazmin
Sebastian Knappe
Richard Neidhardt
Justus Neumann
Thies-Albrecht Ohst
Marie Rodal
Maik Wessling
Johannes Zähle

Retired

Prof. em. Bodo Geyer
Prof. em. Gerd Rudolph
Prof. em. Armin Uhlmann

1.3.4 Statistical Physics, Statistische Physik [STP]

Prof. Dr. Bernd Rosenow

Academic staff

Dr. Casper Drukier
Dr. Andreas Kreisel

PhD candidates

Giovanni Frigeri, M.Sc.
Lukas Kimme, M.Sc.
Martin Treffkorn, M.Sc.
Heinrich-Gregor Zirnstein, M.Sc.
Niels John, M.Sc.

Students

Florian Knoop
Enrico Lohmann
Pit Strub
Matthias Thamm
Tobias Leckel
Sina Teichert
Thomas Suchanek

1.3.5   Theory of Condensed Matter, Theorie der kondensierten Materie [TKM]

Prof. Dr. Ulrich Behn (Speaker)
Prof. Dr. Klaus Kroy

Prof. Dr. Dieter Ihle (retired)
Prof. Dr. Adolf Kühnel (retired)

PhD candidates

Rüdiger Kürsten, M.Sc. (until 28 February 2016)
Gianmaria Falasco, M.Sc.
Stefano Steffenoni, M.Sc.
Dipl.-Phys. Sebastian Sturm
Dipl.-Phys. Jakob Bullerjahn
Dipl.-Phys. Marc Lämmel
Richard Pfaller, M.Sc.
Sven Auschra, M.Sc.

Students

Stefan Landmann, B.Sc.
Johann Müller, B.Sc.
Claudio Schöller, B.Sc.
Daniel Rose, B.Sc.
Tim Herpich, B.Sc.
Constantin Huster, B.Sc.
Benjamin Streitz, B.Sc.
Mona Guthardt, B.Sc.

1.3.6   Theory of Elementary Particles, Theorie der Elementarteilchen [TET]

Prof. Dr. Stefan Hollands

Prof. Dr. Klaus Sibold (retired)

Academic staff

PD Dr. Roland Kirchner
PD Dr. Holger Perlt
Dr. Ko Sanders
PD Dr. Arwed Schiller
Dr. Jochen Zahn

I

Institute for Experimental Physics I

2

Molecular Nano-Photonics

2.1 Introduction

Studying dynamic processes at the level of single molecules and particles in soft materials, the group has recently started to explore the release of heat from single molecules and nanoparticles. These absorbing chromophores are able to convert optical energy into heat, if their fluorescence quantum yield is low. This released heat is generating a steady state spatial temperature profile as they are embedded in a large heat bath, which is their solvent environment. This local temperature profile allows a number of new studies, which range from fundamental physical aspects of Hot Brownian Motion (HBM) to the active motion of self-propelled particles. In particular this field of research of the group addresses

- Thermally propelled particles and micromachines

- Manipulation and trapping of single nano-objects in solution

- Transmission microscopy of Rayleigh- and Mie-particles

- Manipulation of living cells by local temperature fields

- Heat conduction at the nanoscale

During the year 2016 the Molecular Nanophotonics Group has celebrated a number of achievements. Among them are:

- Prof. Dr. Cichos has spent a sabbatical at Princeton University working with Prof. Dr. Haw Yang at the Department of Chemistry.

- Marco Braun has been awarded with the 2nd BuildMoNa price for his research on single particle trapping in temperature fields.

Collaborations with the groups of Prof. Dr. Klaus Kroy (Universität Leipzig), Prof. Dr. Michael Mertig (TU Dresden), Prof. Dr. Alois Würger (University of Bordeaux) and Prof. Dr. Haw Yang (Princeton University) have been very fruitful. Collaborative measurements with the groups of Prof. Dr. Friedrich Kremer and Prof. Dr. Marius Grundmann have been carried out.

Frank Cichos

2.2   Manipulation of single molecules in a thermophoretic trap

T. Thalheim, M. Braun, F. Cichos

The confinement of micro-objects, which are governed by Brownian motion, via optical tweezers has been a major development in soft matter as well as biophysical sciences to allow for first insights into molecular interactions and reactions as well as protein aggregation processes. Since then, lots of new tools to even trap single molecules were devised as, for example, the Anti-Brownian Electrokinetic trap (ABEL trap) or plasmonic traps. Common to all these approaches is that the thermally driven fluctuations of the particle of interest are counteracted via the application of forces, which are generated by electric fields or field gradients or plasmonic near fields. In this project we recently developed a thermophoretic trap which is able to confine Brownian motion with the help of temperature gradients generated by converting optical energy of a focused laser beam into temperature [1]. Here, a plasmonic structure in form of an array of gold nanocircles (Figure 2.1) is used for this process. The physical phenomenon utilized in these experiments is termed thermophoresis or Ludwig–Soret effect. Our setup allows for controlling the number of particles or molecules in the trap using an optical feedback mechanism. This paves the way for utterly new types of bio-molecular interaction dynamics assays on single molecules.

Figure 2.2 shows a single λ-DNA molecule whose center of mass (COM) motion was thermophoretically confined. Since the temperature field approximately decays with the inverse distance from the heat source, the temperature gradients are strongly inhomogeneous in the trap. This, in turn, induces different thermophoretic drift velocities of different monomers of the extended λ-DNA molecule trapped. For the circular geometry used in our experiments the temperature gradients are stronger in the outer region of the trap than in the center. We therefore expect the DNA density to be compressed in addition to the confinement of the COM motion (Figure 2.2B). To check for this behavior, we apply a principal components analysis (PCA) as introduced by Cohen and Moerner [2]. PCA is a model-free statistical tool which decomposes the whole fluctuations of the λ-DNA molecule into eigenmodes and sorts them according to the amount of corresponding eigenvalues in a descending order (Figure 2.2C and
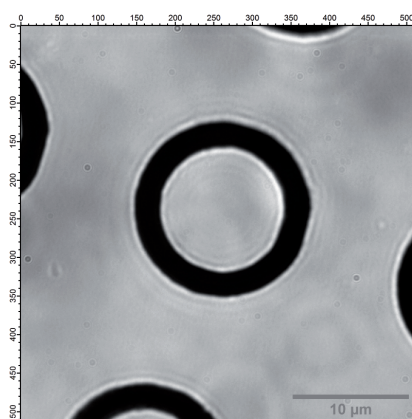
Figure 2.1: Array of thermophoretic traps. Every trap has a diameter of 10 μm.

D). Eigenmodes with high corresponding eigenvalues reconstitute a large part of the overall λ-DNA's fluctuations, whereas eigenmodes with small corresponding eigenvalues are negligible. Every recorded image can be reconstructed via a linear combination of these eigenmodes. Current results suggest a weak influence of the inhomogeneous temperature gradients on the dynamics and structure of the λ-DNA [3]. To magnify possible influences on the conformation of extended molecules due to these gradients, T4-DNA, which has a 3.5 times longer contour length than λ-DNA, is under current investigation .

The project is funded within the CRC TRR 102 "Polymers under Multiple Constraints".

[1] M. Braun, F. Cichos: ACS Nano **7**, 11200 (2013), doi:10.1021/nn404980k
[2] A. Cohen, W. Moerner: PNAS **104**, 12622 (2007), doi:10.1073/pnas.0610396104
[3] M. Braun et al.: Proc. SPIE **9922**, 99220Z (2016), doi:10.1117/12.2239481
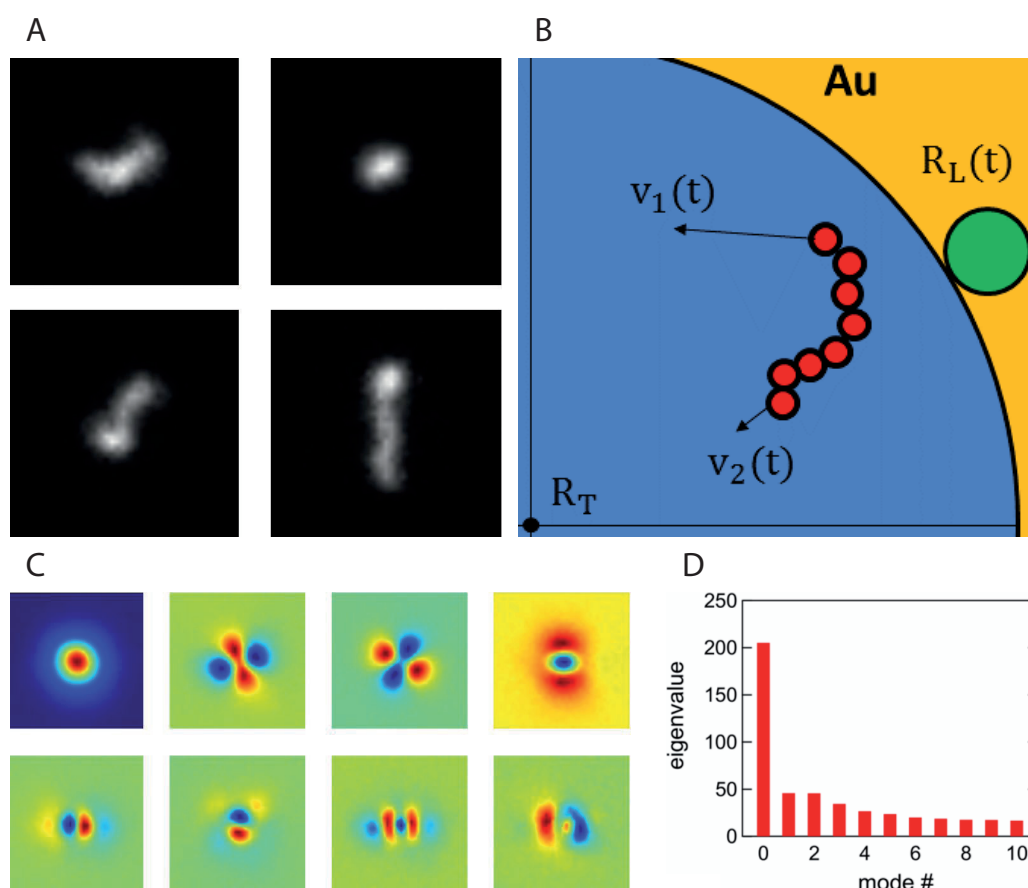
Figure 2.2: A) Snapshots of a trapped λ-DNA molecule. The size of a snapshot spans 4.6×4.6 μm^2. **B)** Scheme of the thermophoretic trap. The heating laser beam (green) can be re-positioned via an optical feedback algorithm such that the COM of the λ-DNA (red dots) is driven to the center of the trap (R_T). Different monomers of the DNA experience a different thermophoretic drift (arrows). **C)** First eight eigenmodes computed with the principal components analysis of the DNA snapshots. A red color indicates negative contributions, a blue color positive contributions. **D)** Corresponding eigenvalues of the eigenmodes from C).

2.3   Feedback driven self-organization of artificial micro-swimmers

F. Cichos, U. Khadka[*], H. Yang[*]

[*]Department of Chemistry, Princeton University, USA

Self-organization is the generation of order out of local interactions in non-equilibrium. It is deeply connected to all fields of science from physics, chemistry to biology where functional living structures self-assemble and constantly evolve all based on physical interactions. The emergence of collective animal behavior, of society, language or learning are the result of a self-organization process as well, though they involve abstract interactions arising from sensory inputs, information processing, storage and feedback resulting in collective behaviors as found in crowds of people, flocks of birds, swarms of bacteria or schools of fish.
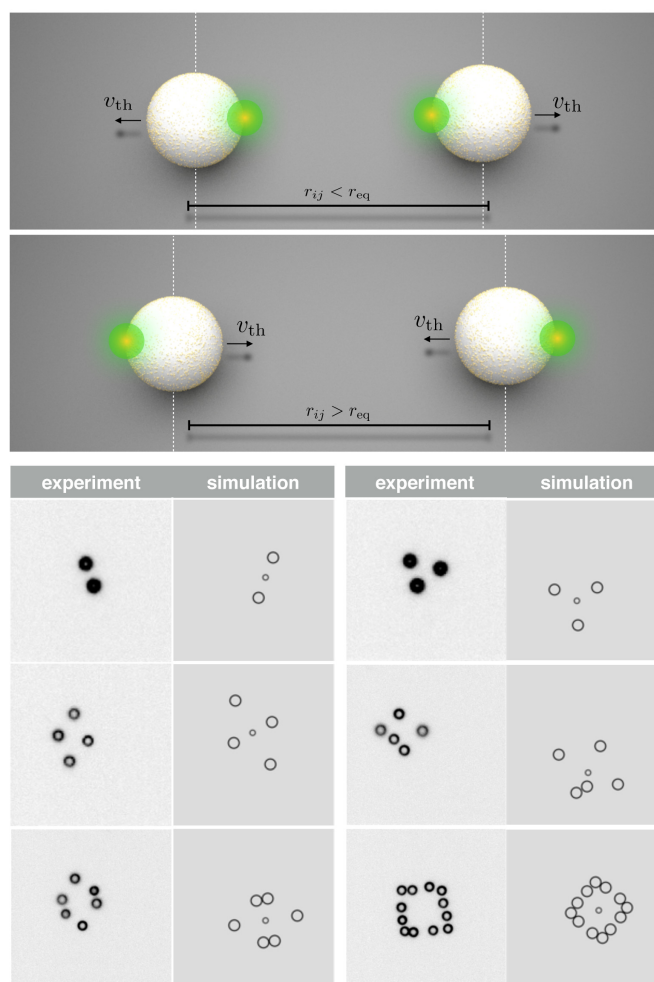
Figure 2.3: Sketch of the feedback rule applied to the swimmer motion. If the distance of two swimmers is above or below a certain value, the thermophoretic propulsion is used to push them back to the right distance. The bottom images show the self-organized structures of a different number of swimmers obtained by applying the feedback together with simulated structures.

Within this project we introduce information-based interactions to the behavior of multiple self-thermophoretic microswimmers. A real time feedback of other swimmer positions controls the swimming direction of the swimmers and results in a self-assembly into internally active structures. The emerging structures reveal unusual geometries, diffuse like passive clusters of colloids, but possess internal dynamical degrees of freedom that are determined by the feedback to the active particles.

The self-propulsion mechanism of the artificial microswimmers in the presented study relies on self-thermophoresis but involves no asymmetric structure yet an asymmetric energy release. The swimmer is constructed of a melamine resin particle which is at 30 % of its surface covered uniformly by gold nanoparticles of about 10 nm diameter. Illuminating the particle asymmetrically by a focused laser beam generates an inhomogeneous surface temperature and results in the desired self-thermophoretic motion. This design implements the required level of control over the swimming direction in two dimensions. The swimming direction is set by the laser position on the circumference of the particle rather than by the orientation of the particle itself. Therefore, the timescale of the rotational diffusion of the particle is unimportant for the steering of the swimmer. This control mechanism is employed to introduce an information exchange between individual swimmers reminiscent of the interactions in flocks of birds, schools of fish or crowds of people. The information on other swimmer positions is the sensory input to steer the motion of the actual swimmer. The swimmer responds by adjusting its propulsion direction or speed. A simple pairwise interaction rule as presented in Figure 2.3 leads to self-organized structures with their center of mass diffusing as a passive object, but with an internal dynamics that is fueled by the self-propulsion of the particles (see Figure 2.4).
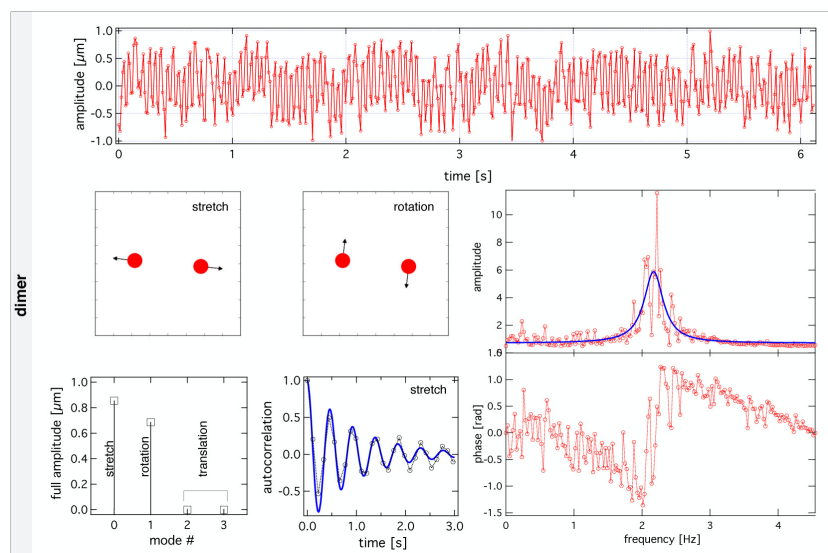
Figure 2.4: Bond length dynamics of two feedback coupled microswimmers. Top graph shows the deviation of the bond length from the adjusted value of 7.1 μm. Middle left and center graphs show the two normal modes obtained from a principal components analysis. Bottom left and middle show the eigenvalues of the normal modes and the dynamics of the stretching vibration. The bottom right graph displays the Fourier transform of the bond length dynamics in amplitude and phase.

This application of information exchange provides a wide perspective on the study of self-organization under the influence of signal exchange and noise, memory and even involving artificial intelligence to evolve the behavior of real active micro-objects into functional swarms.

2.4   Thermoelectric effects at the nanoscale

M. Fränzl, F. Cichos

Within this project we are investigating thermally generated electric fields in locally heated electrolyte solutions. The thermoelectric effect in an electrolyte is long known on a macroscopic level. The present work points at phenomena that occur at the nanoscale in the vicinity of heated metal nanostructures. In this context, the most remarkable aspect is the thermoelectric charging, that is the accumulation of a net charge in the vicinity of a heated non-ionic particle in an electrolyte solution.

In the last decades thermophoresis of charged colloids was mainly discussed in terms of thermo-osmotic pressure. In short, the temperature gradient along the particle surface deforms the electric double layer and thus induces a stationary salt-ion flow. This thermo-osmotic mechanism drives the particle to the cold, opposite to the temperature gradient. However, in recent years several experiments revealed that charged colloids may move in either direction, depending on the electrolyte composition and the temperature.

In addition to the thermo-osmotic driving [1], the thermoelectric or Seebeck effect of the electrolyte solution turns out to be of major importance. Because of their specific solvation energy, salt ions in water have the tendency to diffuse opposite to the temperature gradient towards colder regions [2]. However, in general the thermal diffusion coefficients of positive and negative ions are different, giving rise to surface charges at
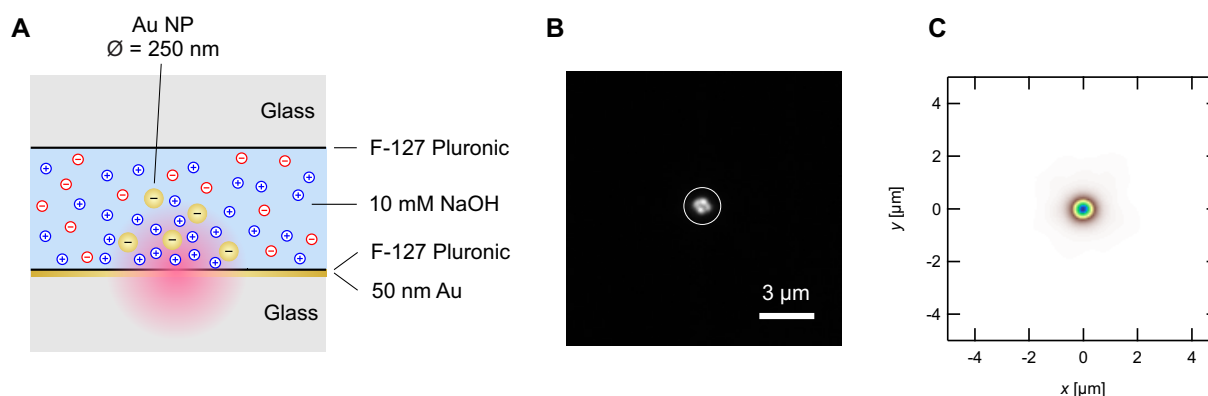
Figure 2.5: A) Principle of the experiment and sample design. The 10 mM NaOH solution is contained between two glass cover slides with a gap of about 3.5 μm. The bottom glass cover silde is coated with a 50 nm gold film and heated using a 532 nm laser with a beam waist of 500 nm from below. Citrate stabilized gold nanoparticles with a diameter of 250 nm are used as tracer particles. To prevent the nanoparticles from sticking, the surfaces where treated with pluronic. **B**) Darkfield image from gold colloids attracted to a hot spot in the center of the image. **C**) Example for the accumulated scattering intensity of a single 250 nm gold colloid trapped in a thermoelectric field with a heating laser power of 1 mW.

the hot and the cold boundary of the sample, and to a macroscopic thermoelectric field. This field, in turn, can drive charged colloids in the solution to the hot or to the cold, depending on the sign of the electrolyte Seebeck coefficient [3].

The present work addresses the thermoelectric charging of a hot spot in NaOH solution. We locally heated a 50 nm gold film using a focused 532 nm laser within a suspension of 250 nm gold colloids in 10 mM NaOH solution and investigated the resulting colloidal transport (Figure 2.5A). Since the sign of the electrolyte Seeback coefficient is negative for NaOH, the positively charged Na^+ ions accumulate at the hot spot. The citrate stabilized gold colloids are charged negatively, thus, they are attracted to the hot spot generated by the heating laser (Figure 2.5B). We report that the thermoelectric charging effect can be used for trapping single nanoparticles (Figure 2.5C). Furthermore, by steering the laser beam, the nanoparticle can be translated with the ion cloud and the hot spot, respectively.

The project is funded within the DFG-ANR project "Thermoelectric Effects at the Nano-scale".

[1] A.P. Bregulla et al.: PRL **16**, 188303 (2016), doi:10.1103/PhysRevLett.116.188303
[2] E.D. Eastman: J. Am. Chem. Soc. **50**, 283 (1928), doi:10.1021/ja01389a007
[3] A. Würger: PRL **101**, 108302 (2008), doi:10.1103/PhysRevLett.101.108302

2.5   Studying thermal transport with single particle photothermal deflection microscopy

A. Heber, M. Selmke, F. Cichos

Single non-fluorescent absorbers can be efficiently imaged using, for example, photothermal microscopy. Here, gold nanoparticles are frequently chosen as labels due to their high absorption cross section and chemical stability. Single optically controlled nano-sources of heat have been used, for example, to control biochemical reactions or the propagation of heat or grow nanostructures. In particular, for the latter application, it would be beneficial to have a nanoparticle that can also act as a catalyst and a probe for studying thermal transport at the same time.

Photothermal microscopy is based on the heat-induced change of the refractive index. A heating laser is tuned to the absorption resonance of the absorbing label. The part of the incident radiation being absorbed is released as heat into the environment, which creates a localized temperature profile. In combination with thermal expansion, a localized refractive profile around the particle is created. A second off-resonant laser beam detects the refractive index. As the refractive index change is typically in the order of 10^{-4} the transmission changes are also tiny. Therefore, the heating laser is intensity modulated at about 100 kHz. The modulation and the photothermal effect create a modulation of the detection laser which is amplified by a lock-in amplifier. The temperature profile is not instantaneously established. Therefore, the magnitude and phase delay of the transmission modulation will depend on the distance to the heat source and the modulation frequency.

Here, we focus a heating laser onto a gold nanoparticle which is either embedded in a polymer (Polydimethylsiloxane – PDMS) or a liquid crystal (4-Cyano-4'-pentylbiphenyl

– 5CB). The detection laser is scanned over the whole extent of the thermal lens and
deflections in one direction are measured using a slit detector. In Figure 2.6A and C
the phase delay between heating and detection laser is shown, which is caused by the
thermal diffusivity of the medium surrounding the nanoparticle. To extract the thermal
diffusivity from the phase delay (see Figure 2.6B) a ray optics model is developed.
The ray optics model applies Fermat's principle to a refractive index profile caused
by a thermal wave and takes the diffraction limit into account but averaging over
multiple impact parameters. For the line profiles (see Figure 2.6) a thermal diffusivity
of $(1.27 \pm 0.06)\,\mathrm{m^2\,s^{-1}}$ is extracted, which compares well with macroscopic laser flash
measurements yielding $(1.30 \pm 0.02)\,\mathrm{m^2\,s^{-1}}$.

As the whole spatial extent of the thermal lens is probed, it should be possible to
detect heterogeneities in the thermal transport. In the first step, a control experiment
is conducted to verify that photothermal deflection is capable of detection anisotropies
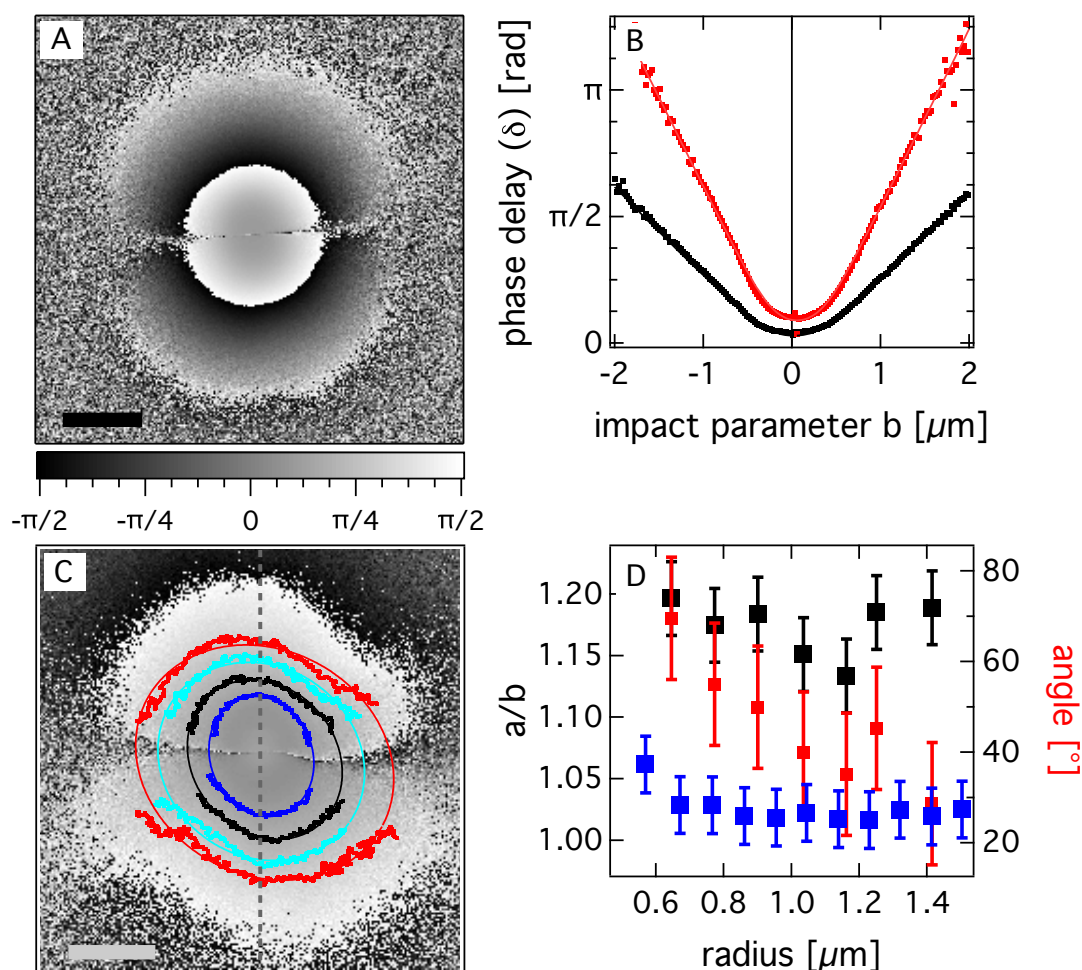
Figure 2.6: A) Phase delay of the photothermal deflection signal at a modulation frequency of
200 kHz in PDMS and **B)** the corresponding line profile at 200 kHz (red) and additionally
at 50 kHz (black). The solid lines are fits to the experimental data. **C)** Phase delay of the
photothermal deflection signal at 50 kHz in 5CB. Contour lines are overlaid where the phase is
0.4 (blue), 0.6 (black), 0.8 (light blue) and 1.0 rad (red). **D)** Orientation (5CB – red) and anisotropy
(5CB – black, PDMS – blue) of the thermal transport determined with least square ellipse fit to
different contour lines. The scale bars correspond to 1 μm.

in the thermal transport. From the phase delay image (see Figure 2.6A) contour lines at different phase delays are extracted. Using a least square ellipse fit, the lengths of semi-major a, and semi-minor axis b are determined. The anisotropy of the thermal diffusivity is then proportional to $\sqrt{b/a}$. It is close to one for PDMS indicating isotropic thermal transport. Then, the experiment is repeated in 5CB (see Figure 2.6). From the contour lines, a/b is extracted as well as the orientation of the major axis (see Figure 2.6D). The orientation of the major axis agrees well with a polarization contrast measurement. The anisotropy is lower than expected from macroscopic measurements due to the sample geometry. The gold nanoparticles are in direct contact with an isotropic glass substrate lowering the measured anisotropy.

[1] A. Heber et al.: ACS Photonics **4**, 681 (2017) doi:10.1021/acsphotonics.7b00044

2.6   Reinforcement learning of artificial self-thermophoretic microswimmers

S. Muiños-Landin, F. Cichos

Living organisms down to the scale of single bacteria have to respond and adapt to environmental signals which range from structural obstacles to chemical gradients or gravitational fields. This involves the nonequilbrium response of complex chemical networks with specialized sensors. In this project we introduce processes of learning and adaption to the behavior of single and multiple artificial microswimmers. Our microswimmers are symmetric polymer spheres with a 30 % homogeneous coverage of 10 nm gold nanoparticles (see Figure 2.7A). An asymmetric heating of the gold particles on the surfaces by a focused laser breaks the symmetry of low Reynolds number hydrodynamics and propels the particle by thermo-osmotic surface flows. The direction of swimming is controlled by the laser position on the particle circumference and thus completely independent of rotational diffusion as for all other types of microswimmers. Given this high level of control of the propulsion of the swimmers, we apply machine learning techniques to develop navigation strategies which are created, executed and improved autonomously by the system as a real decision maker. Specifically by using reinforcement learning algorithms, we develop a control system that learns from its interaction with the environment. For this purpose the possible positions of the particle represent a state of the particle in which it can execute an action out of a given set of actions. (inset Figure 2.7A and B). By sparsely supplying a reward, i.e. for achieving a certain target, the swimmer finds an optimal strategy, a policy, which is the best chain of actions to reach the target. By defining all these elements in an experiment we have developed a system that directly learns in real time from interactions, evolves autonomously and is able to solve tasks (see Figure 2.7D and E). This first demonstration paves the way for the study and application of adaptive swarm behavior to artificial micro- and nanomachines.
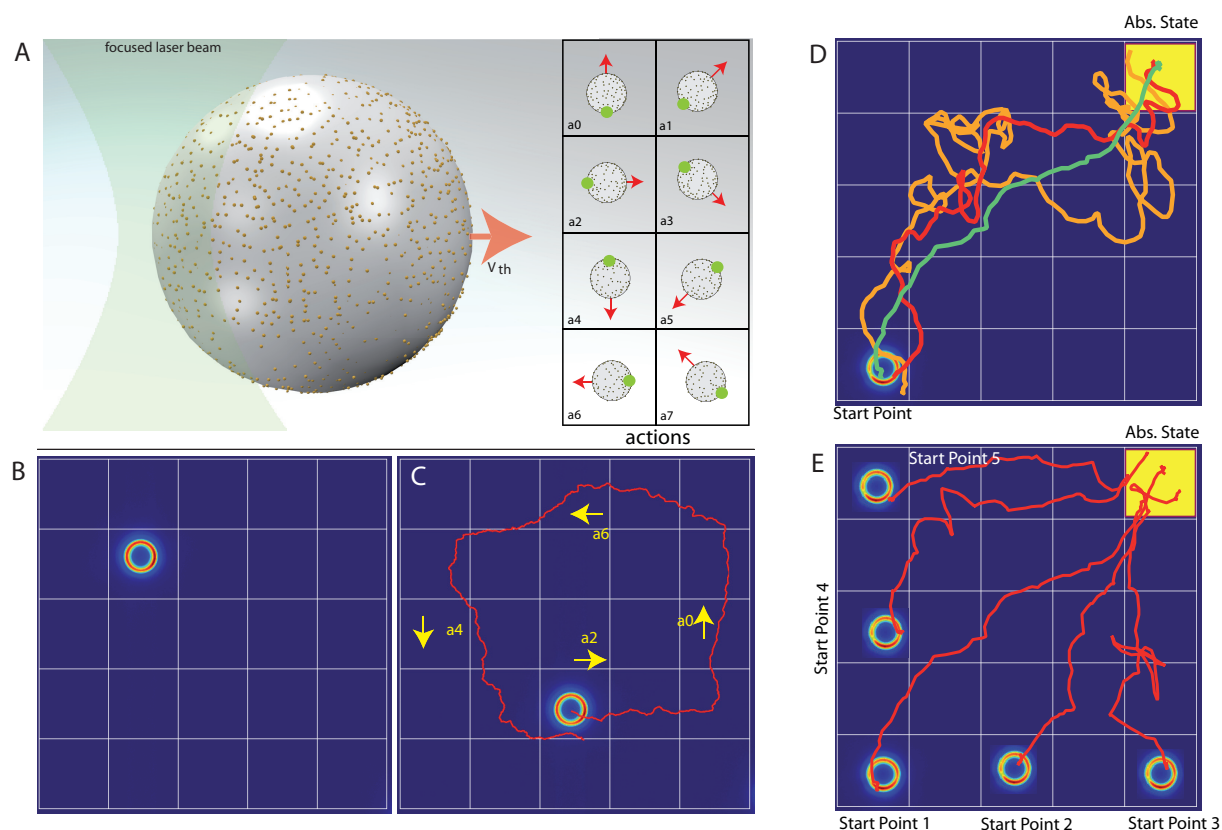
Figure 2.7: A) Using a focused laser beam, the symmetric geometry of the swimmer employed here makes it possible to obtain a well-defined heated region only in the area where the laser is focused (symmetry breaking). This makes the propulsion of the particle towards its cold side possible. Different actions can be defined as different heating points giving different propulsion directions (red arrows). **B**) Typical dark field image of the swimmer in water. The sample space is divided into a grid defining a gridworld where each cell represents a state. **C**) Example of the manual control of the swimmer by applying different actions. **D**) Autonomous behavior. The relationship between state and action is analyzed considering the reward obtained after each transition (maximum reward at the absorption state is represented by a yellow square). The figure shows the path followed by the swimmer after different amounts of iterations of the system, which means different learning times. The orange line corresponds to the minimum and the green line to the maximum learning time. **E**) After enough iterations the system finds the optimal action to perform in each state. The absorption state is reached independently of where the starting point is.

2.7 Hot nanoswimmers

R. Schachoff, F. Cichos

Hot Brownian swimmers are thermally anisotropic Brownian particles driven by optical heating. The geometric asymmetry of the swimmers establishes an asymmetric temperature profile in the surrounding solvent upon particle heating. The thermo-osmotic flow along the surface of the swimmer leads to a phoretic self-propulsion. We studied hot Brownian swimmers that are synthesized from a gold nanoparticle of variable diameter and a tail of a DNA helix bundle (6HB or 24HB). Here, the highly localized optical heating of the nanoparticles creates a steep temperature gradient over the DNA tail.

The ballistic propulsion of the swimmer is retained only for times shorter than the rotational diffusion time that scales with the radius cubed. At longer times the motion of the swimmer appears enhanced diffusive but the overall change in the diffusion coefficient for the chosen particle complex will be only in the per mille region, since rotational Brownian motion randomizes the direction of propulsion. We use our unique split focus geometry in twin-focus photothermal correlation spectroscopy (twin-PhoCS) [1] to detect small flow velocities on small length and time scales (nm/ms). We are, thus, able to show a clear swimmer characteristic of the gold nanoparticle–DNA complex in dependence on the heating power that is clearly distinguishable from pure hot Brownian motion which is performed by heated gold nanoparticles themselves. Here, the split focus is arranged perpendicular to the optical axis to circumvent measuring artifacts
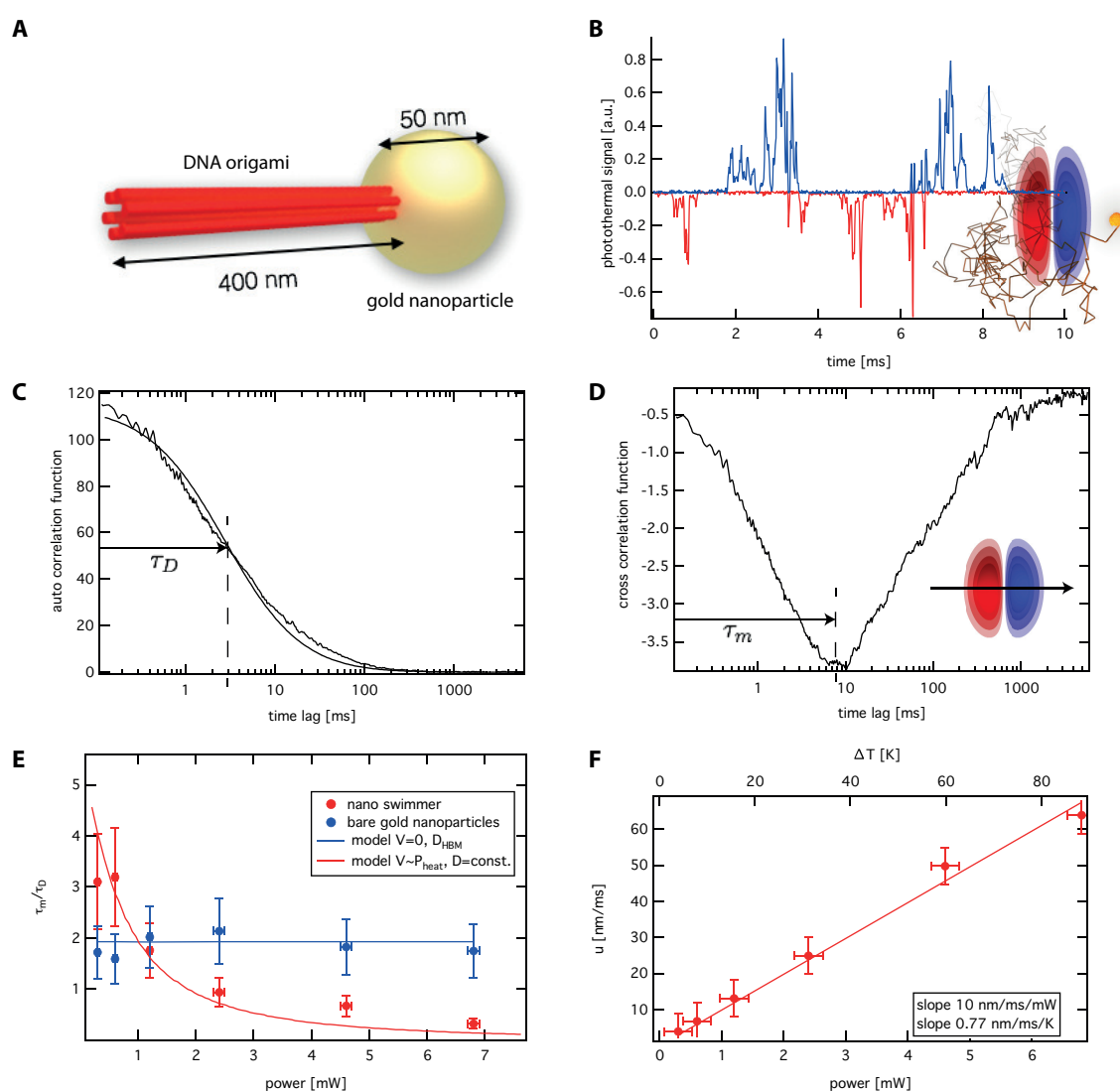
Figure 2.8: A) Scheme of the studied nanoswimmers, comprising a gold nanoparticle as heat source and a DNA origami tail generating the thermophoretic drift. **B)** Time trace of the positive and negative photothermal signal. **C)** Autocorrelation function with typical diffusion time τ_D. **D)** Cross-correlation function with position of the correlation peak τ_m. **E)** Ratio τ_m/τ_D for bare gold nanoparticles and nanoswimmers. **F)** Thermophoretic drift velocity u extracted from fits of the cross-correlation function for varying heating powers.

due to flow velocities that are exerted by radiation pressure. We took time traces with a temporal resolution of $20\,\mu$s on pure gold nanoparticles with a diameter of 50 nm as reference measurement and on 50 nm gold nanoparticles conjugated with a 400 nm long DNA origami tail (6HB) at varying heating intensities. Analyzing the autocorrelation functions provides the diffusion times τ_D. As expected, both species showed good agreement with the theory of hot Brownian motion with no indication of a swimming behavior. From the cross-correlation function the position of the minimum τ_m was used to calculate the ratio τ_m/τ_D that shows a clear signature for the swimmers for which this ratio decreases with increasing heating power. In contrast, this ratio remains constant for bare gold nanoparticles. Fitting the cross-correlation functions we obtained a linear dependence of the thermophoretic flow velocity u on the heating power, and thus, the temperature rise at the surface of the gold nanoparticles. This result is in full correspondence with theoretical predictions with a scaling factor of 0.77 nm/ms per K. The smallest measured flow velocity of 4 nm/ms is by a factor 5 smaller than the smallest flow velocity measured with twin-PhoCS in axial direction [1], since the peak to peak distance $\delta = \omega_i$, $i = \{x, y, z\}$ for the corresponding direction differs by the factor $\gamma = 5$. Thus, measuring in the x-split configuration is even more sensitive due to the γ-fold smaller distance of the detection volume peaks as compared to the z-split configuration. Here, we demonstrated a reliable measuring tool for the thermophoretic flow velocities of nanoswimmers that are not accessible with conventional widefield microscopy techniques due to their insufficient temporal and spatial resolution.

[1] M. Selmke et al.: RSC Adv. **3**, 394 (2013), doi:10.1039/C2RA22061J

2.8   Hot Brownian motion

A. Fischer, F. Cichos

We have recently in collaboration with the group of Prof. Kroy at the theory department shown, that the Brownian motion of heated spherical nanoparticles can be described be new effective parameters for the temperature and the viscosity of the surrounding medium. One of the interesting effects is that the effective temperature is now coupled to the hydrodynamic flow field created by the motion of the nanoparticle thereby dissipating its kinetic energy. Thus, different degrees of freedom such as the rotational and translational motion possess in this thermal non-equilibrium different effective temperatures. In this project we study the instantaneous velocity distribution of a heated microparticle. At very short times, when the above described flow fields have not yet been established, the particle is supposed to show a new effective temperature, which is defined by its kinetic energy or its velocity. In thermal equilibrium this corresponds to the Maxwell–Boltzmann distribution. In thermal non-equilibrium there are so far no experimental results on this effective temperature. To measure this effective temperature we use an optical tweezer setup as depicted in Figure 2.9. Particles which can be heated by a solid state laser at 532 nm are trapped by an infrared laser (1064 nm). The laser heating is supplied in counter-propagating beams to prevent a displacement of the particle due to radiation pressure. The fluctuations of the particle are imaged onto a knife-edge prism and recorded by a balanced photodiode and a fast analog to

digital converter. With the help of this setup we will be able to measure the velocity autocorrelation function of a single heated microparticle at nanosecond time resolution.
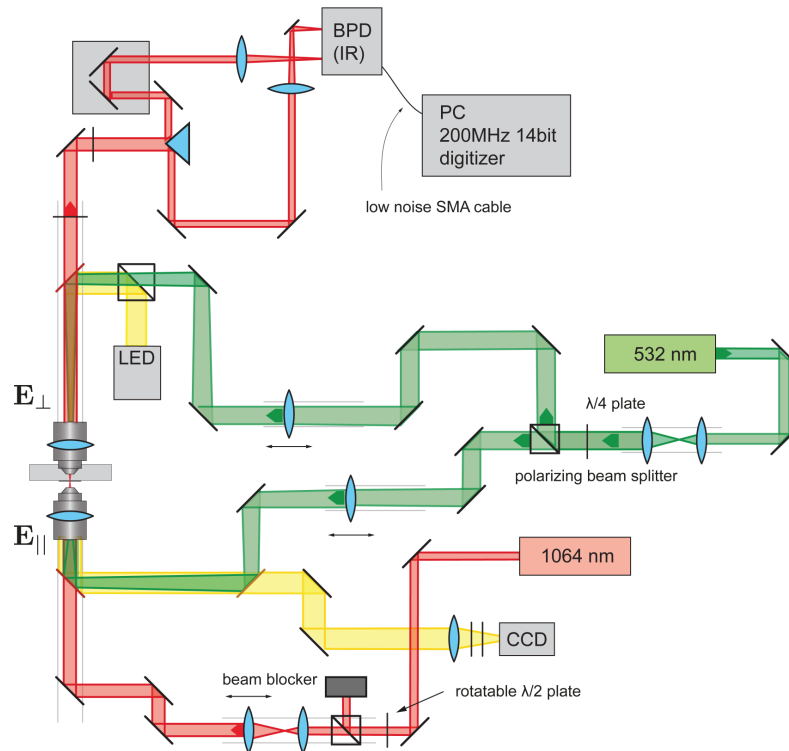
Figure 2.9: Scheme of the experimental optical tweezer setup to measure the instantaneous velocity of a heated microparticle in solution.

2.9 Funding

2.10   Organizational Duties

Frank Cichos
- Director of the Institute for Experimental Physics I
- Vice Speaker of the Collaborative Research Center Transregio 102 "Polymers under Multiple Constraints"
- Member of the Steering Committee of the Graduate School BuildMoNa
- Member of the Faculty Council
- Head of the Aptitude Commission (M.Sc. Physics)
- Vice head of the PhD Board of the Faculty
- Vice head of the Board of the Faculty for Quality Management
- Member of the Examination Board (Physics/Meteorology)
- Referee: Phys. Rev. B, Phys. Rev. Lett., Nature, Nature Photonics, Chem. Phys. Lett., Appl. Phys. Lett., ACS Petroleum Research Fund, Medical Research Council

2.11   External Cooperations

Academic

- TU Dresden
  Prof. Dr. Michael Mertig

- Unviversité de Bordeaux
  Prof. Dr. Alois Würger

- TU Chemnitz
  Prof. Dr. Christian von Borczyskowski

- Universität Mainz
  Prof. Dr. Thomas Basché

- Princeton University
  Prof. Dr. Haw Yang

- MPI Kohlenforschung Mühlheim
  Dr. Frank Marlow

- Universität Stuttgart
  Prof. Dr. Clemens Bechinger

- MPI Intelligente Systeme
  Prof. Dr. Peer Fischer

2.12   Publications

Journals

A.P. Bregulla, A. Würger, K. Günther, M. Mertig, F. Cichos: *Thermo-osmotic flow in thin films*, Phys. Rev. Lett. **116**, 188303 (2016)

K. Kroy, D. Chakraborty, F. Cichos: *Hot microswimmers*, Eur. Phys. J. Spec. Top. **225**, 2207–2225 (2016)

G. Falasco, R. Pfaller, A.P. Bregulla, F. Cichos, K. Kroy: *Exact symmetries in the velocity fluctuations of a hot Brownian swimmer*, Phys. Rev. E **94**, 030602(R) (2016)

A.P. Bregulla, F. Cichos: *Polarization of thermophoretic swimmers in external temperature fields*, Proc. SPIE **9922**, 99221L (2016)

M. Braun, T. Thalheim, K. Günther, M. Mertig, F. Cichos: *Thermophoretic trapping and manipulation of single molecules*, Proc. SPIE **9922**, 99220Z (2016)

Patents

F. Cichos, M. Braun, M. Selmke, R. Schachoff: *Twin-focus photothermal correlation spectroscopy method and device for the characterization of dynamical processes in liquids and biomaterials with the help of absorbing markers*, US Patent 9,360,416 B2 (2016)

Talks

A. Heber, M. Selmke, M. Braun, F. Cichos: *Resonances from thermal waves using photothermal deflection microscopy*, DPG Spring Meeting, Regensburg, 6–11 March 2016

S. Muiños-Landin, A.P. Bregulla, F. Cichos: *Interactions of self-thermophoretic swimmers*, DPG Spring Meeting, Regensburg, 6–11 March 2016

S. Muiños-Landin, A.P. Bregulla, F. Cichos: *Interactions of self-thermophoretic swimmers*, Soft Matter Day, Leipzig, 10 June 2016

T. Thalheim, M. Braun, A.P. Bregulla, F. Cichos: *Thermophoretic trapping of single and multiple colloids and DNA molecules*, Soft Matter Day, Leipzig, 10 June 2016

F. Cichos: *Real and artificial interactions of artificial microswimmers*, Active and Smart Matter: A New Frontier for Science and Engineering, Syracuse, USA, 20–23 June 2016

F. Cichos: *Thermophoretic trapping and manipulation of single molecules*, SPIE Optics & Photonics, San Diego, USA, 28 August – 1 September 2016

F. Cichos: *Polarization of thermophoretic swimmers in external temperature fields*, SPIE Optics & Photonics, San Diego, USA, 28 August – 1 September 2016

A. Heber, M. Selmke, F. Cichos: *Measuring thermal diffusivities with photothermal single particle microscopy*, Nanoscale and Microscale Heat Transfer V, Santorini, Greece, 25–30 September 2016

Posters

A. Abend, R. Schachoff, F. Cichos: *Photothermal detection of single gold nanoparticles in living fibroblasts*, DPG Spring Meeting, Regensburg, 6–11 March 2016

A. Fischer, F. Cichos: *Hot Brownian motion on short time scales*, DPG Spring Meeting, Regensburg, 6–11 March 2016

T. Thalheim, M. Braun, A. Bregulla, F. Cichos: *Single DNA molecules and colloids in a thermophoretic trap*, DPG Spring Meeting, Regensburg, 6–11 March 2016

A. Heber, M. Selmke, F. Cichos: *Resonances from thermal waves using photothermal deflection microscopy*, Annual BuildMoNa Conference, Leipzig, 14–15 March 2016

S. Muiños-Landin, A.P. Bregulla, F. Cichos: *Interactions of self-thermophoretic swimmers*, Microswimmers Annual Meeting, Bonn, 19–20 May 2016

A. Abend, R. Schachoff, F. Cichos: *Photothermal detection of single gold nanoparticles in living fibroblasts*, Soft Matter Day, Leipzig, 10 June 2016

A.P. Bregulla, A. Würger, K. Günther, M. Mertig, F. Cichos: *Thermo-osmotic flow in thin films*, Soft Matter Day, Leipzig, 10 June 2016

A. Fischer, M. Selmke, F. Cichos: *Hot Brownian motion at short time scales*, Soft Matter Day, Leipzig, 10 June 2016

A. Heber, M. Selmke, F. Cichos: *Resonances from thermal waves using photothermal deflection microscopy*, Soft Matter Day, Leipzig, 10 June 2016

R. Schachoff, A. Abend, F. Cichos: *Photothermal detection and correlation spectroscopy of single gold nanoparticles in living cells*, Soft Matter Day, Leipzig, 10 June 2016

S. Muiños-Landin, A.P. Bregulla, F. Cichos: *Interactions of self-thermophoretic swimmers*, BIONAV: Principles of Biological and Robotic Navigation, Dresden, 29–31 August 2016

F. Schmidt, A. Magazzù, A. Callegari, L. Biancofiore, F. Cichos, G. Volpe: *Microscopic engine powered by critical demixing*, 4th International Soft Matter Conference, Grenoble, France, 12–16 September 2016

T. Thalheim, M. Braun, J. Zierenberg, W. Janke, F. Cichos: *Manipulation of single molecules in a thermophoretic trap*, 5th Retreat SFB/TRR 102, Lohmen, 28–30 September 2016

S. Muiños-Landin, U. Khadka, A.P. Bregulla, H. Yang F. Cichos: *Steerable symmetric photo-phoretic micro-swimmers*, Microswimmers International Conference, Bonn, 4–7 October 2016

2.13 Graduations

Doctorate

- Marco Braun
  Optically controlled manipulation of single nano-objects by thermal fields
  June 2016

- Andreas Bregulla
  Role of thermo-osmotic flows at low Reynolds numbers for particle driving and collective motion
  June 2016

Master

- Falko Schmidt
  Criticality, the key to new micro- and nanomachines
  November 2016

Bachelor

- Jennifer Arndt
  Herstellung und Charakterisierung thermophoretisch getriebener magnetischer Janus-Partikel
  August 2016

- Choongeun Park
  Optimierung von Photon Nudging Strategien
  July 2016

2.14 Guests

- Julián Gargiulo, M.Sc.
  University of Buenos Aires, Argentina
  21–23 April 2016

- Prof. Haw Yang, PhD
  Princeton University, USA
  12–13 September 2016

- Prof. Giovanni Volpe, PhD
  University of Gothenburg, Sweden
  1 November 2016

3

Molecular Physics

3.1   Introduction

This is my first report as an emeritus professor; in March 2015 I have retired. But this does not mean that I have moved away from research. Instead, I focus on the fields of Broadband Dielectric and Fourier Transform Infrared Spectroscopy; in both we have profound expertise and the two have proven to be complementary and highly versatile in the physics of soft and hard condensed matter. In detail we study the dielectric properties of polymeric Ionic Liquids (PIL), a project funded by the German Science Foundation within a "Knowledge-transfer-project (Erkenntnistransferprojekt)" together with Prof. Veronika Strehmel, FH Krefeld and Merck KGaA in Darmstadt. Currently under review for the second funding period (2015 - 2019) is an application - titled "Broadband Dielectric and IR Spectroscopy to study molecular dynamics and order in nanometer domains of end-fixed polymers" - within the Collaborative Research Center (CRC) of the universities in Halle and Leipzig, "Polymers under multiple constraints: restricted and controlled molecular order and mobility". Furthermore, a common endeavor for the "Establishment of spectroscopic techniques for operational in ovo-gender determination in domestic chicken (Gallus gallus f. dom.)" (Coordinator: Prof. Dr. Maria-Elisabeth Krautwald-Junghanns, GZ: 2813IP003 (2015 - 2017) requires utmost commitment. Additionally, several book projects are progressing within the series "Advances in Dielectrics". So I can look back on a successful year 2016, and I do look forward to continue research in soft matter physics with highest engagement and ambition.

Friedrich Kremer

3.2 Molecular Order in Cold Drawn, Strain-Recrystallized Poly-(Caprolactone)

W. Kossack, A. Seidlitz[*],T. Thurn-Albrecht[*], F. Kremer

[*]Institut für Physik, Martin-Luther-Universität Halle-Wittenberg, Halle

Biaxial order in cold-drawn Poly-Caprolactone (PCL)-films is studied revealing insights into plastic deformation, fibrillation and rupture of polymeric systems. In the course of drawing, the initially spherulitc structures[1] (Fig. 3.1a,c) are deformed (Fig. 3.1a,b) and finally rearranged into fibrils.[2] This process is driven by the alignment of the polymers main chains (grey lines) with the stretching direction (horizontal); and leads to nearly perfectly order of the crystallites (Hermans orientation function, $S = 0.9 \pm 0.1$), and less ordered, amorphous regions ($S \sim 0.34 \pm 0.1$). Surprisingly, the IR-spectra (Fig. 3.1d,e) indicate a reduction in crystallinity and the existence distorted crystallites in the fibrils, which contradicts the ideas of "melting and recrystallization" or "fine slip processes".[2]
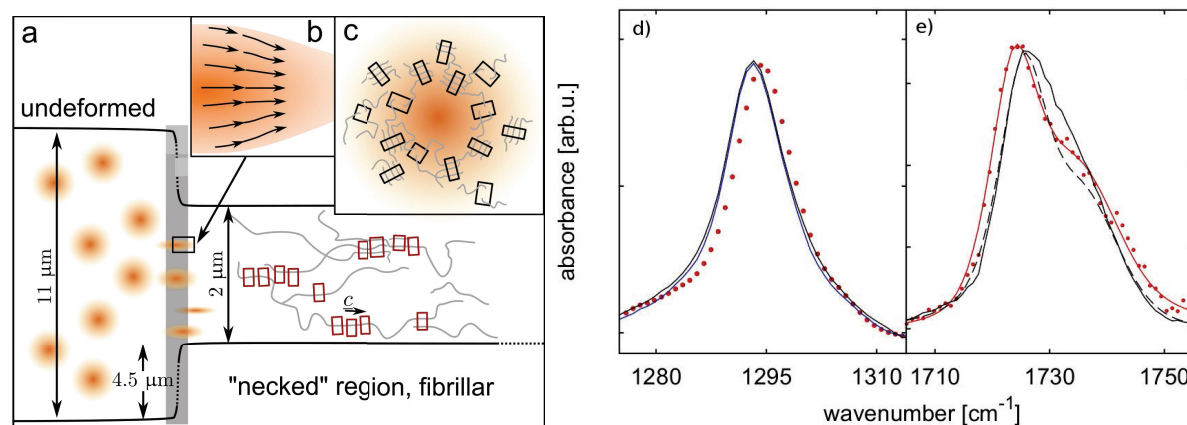
Figure 3.1: a–c) Scheme of the deformation mechanism in a PCL-thin film: a) contains the overview b) is a magnification of the flow lines (arrows) within a spherulite, whereas c shows the initial, spherulitic structure. d–e) IR spectra of PCL in the plastically deformed strained polymer before (solid black) and after release of the stress (solid blue); Red dots and lines respectively depict spectra and fits of PCL crystallized form the melt on a substrate. The black dashed line in e) corresponds to a hypothetic free standing film of same crystallinity as in the supported case.

[1] Kossack, W., Seidlitz, A., Thurn-Albrecht, T., Kremer, F., Macromolecules, 49, 3442–3451 (2016)

[2] Kossack, W., Seidlitz, A., Thurn-Albrecht, T., Kremer, F., Macromolecules, 50, 1056,1065 (2017)

3.3 Hydrogen bonding equilibria in self-healing polymers

W. Kossack, D. Döhler[*], W. Binder[*], F. Kremer

*Institute of Chemistry, Martin-Luther-Universität Halle-Wittenberg, Halle

Restoration of large volume damage together with mechanical stability of self-healing polymers requires fast and efficient reversible crosslinking processes together with the presence of a static network.[1] We investigate differently branched and end-functionalized Poly-isobutylenes (Fig. 3.2) as model compounds of self-healing polymers.[2] Using Temperature dependent IR-spectroscopy (Fig. 3.3) we determine the fractions of differently strong H-bonded amine groups, which make up the physical network of the material and therefore grant mechanical stability.[3] Above $T = 60°C$ the number of free/non-bonded (band at 3450 cm^{-1}) as well as only singly bonded NH-groups (3290 cm^{-1}) increases on expense of the more complex bonded amine groups (3200 cm^{-1}). Simultaneously, the degree of association of the carbonyl groups decreases, proving the importance of attractive interactions between the two groups.
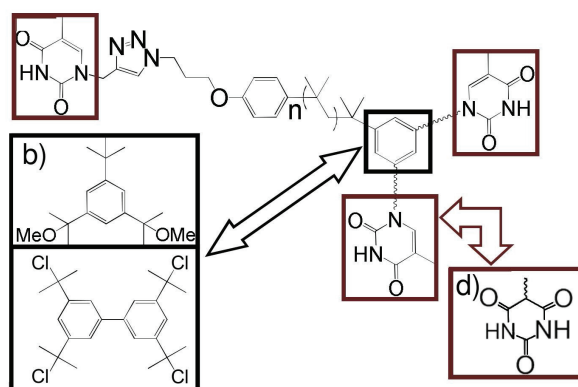
Figure 3.2: Chemical structure of the studied functionalized Poly Isobutylenes: Different linkers (black framed) allow linear, three or four-armed molecules. The chain ends are functionalized with barbiturate or thymin (framed red).
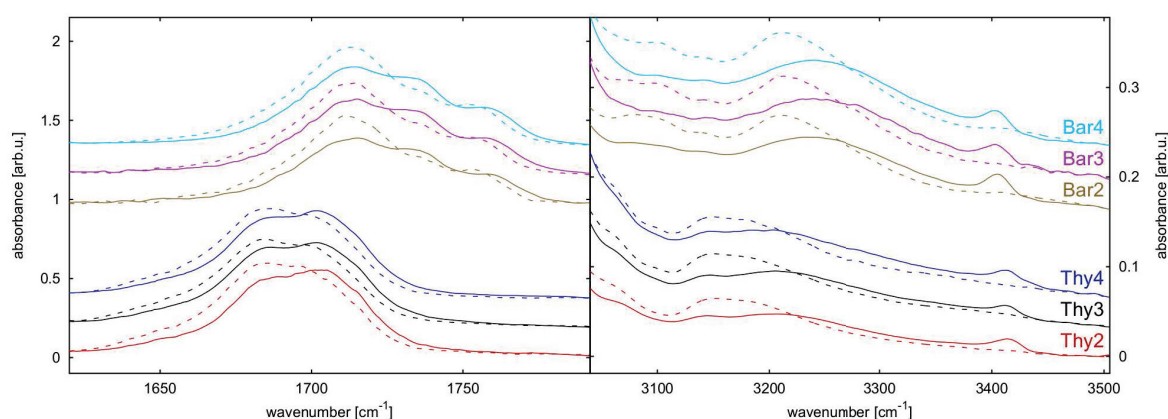
Figure 3.3: IR spectra of thymin (Thy) or barbiturate (Bar) functionalized chains with 2, 3 or 4 arms at −10°C (dashed) and 150° (solid).

[1] W.H. Binder, Ed., "Self-healing polymers: from principles to applications", Weinheim: Wiley-VCH-Verlag (2013)

[2] D. Döhler, H. Peterlik, and W. H. Binder, "A dual crosslinked self-healing system: Supramolecular and covalent network formation of four-arm star polymers" Polymer, 69, 264–273 (2015)

[3] W. K. Kipnusu et al., "The interplay between inter- and intra-molecular dynamics in a series of alkylcitrates", Soft Matter, 9, 4681–4686 (2013)

3.4 Spatial Orientation and Order of Structure-Defining Subunits in Thin Films of a High Mobility n-Type Copolymer

A.M. Anton, R. Steyrleuthner[*†], W. Kossack D. Neher[*†], F. Kremer

[*]Institut für Experimentalphysik, Freie Universität Berlin, Berlin, Germany
[†]Institut für Physik und Astronomie, Universität Potsdam, Potsdam, Germany

Orientation and order of distinct molecular subunits in solid layers of the high mobility n-type copolymer poly[N,N'-bis(2-octyldodecyl)-1,4,5,8-naphthalenediimide-2,6-diyl]-5,5'-(2,2'-bithiophene) P(NDI2OD-T2) are investigated by means of infrared transition moment orientational analysis (IR-TMOA). This novel spectroscopic technique based on concurrent absorbance measurements of structure-specific bands in dependence on inclination and polarization of the incoming light enables to determine the complete tensor of absorption independently for each transition moment. As a result, for nanometer thin films pronounced in-plane anisotropy arising from self-aggregated order is detected, which, however, is no longer discernable for micrometer-thick samples.[1] In contrast, the out of plane orientation (inclination of molecular subunits) is retained irrespective of the widely varying layer thicknesses (150×10^{-9} vs. 1.4×10^{-6}m). Thus, the conception of the sample morphology occurs as stratification of slightly misaligned layers of oriented polymers; with increasing film thickness the macroscopic in plain order diminishes, whereas the out of plain orientation is preserved.

[1] A. M. Anton, R. Steyrleuthner, W. Kossack, D. Neher, F. Kremer, Macromolecules 49, 1788–1806,(2016)
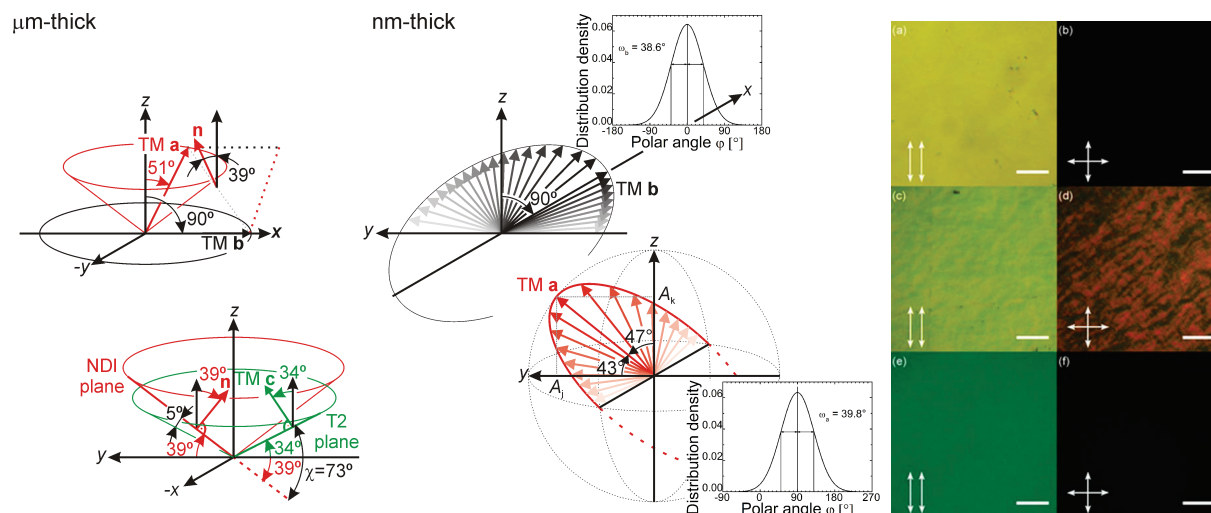
Figure 3.4: Scheme (left) For the micrometer thick sample TM a (red) is equally distributed at the lateral surface of a cone (opening angle $\Theta = 51°$); TM b (black) is found within the xy-plane ($\Theta = 90°$). Their vector cross product gives the NDI plane's normal vector **n** ($\Theta = 39°$), which is consequently rotationally symmetric distributed. The same holds true for TM c (T2 unit, green). The cutting angle results either as sum of or difference between the particular inclinations ($\Theta = 73°$ or $\Theta = 5°$) The micrographs (right) of the blank ZnSe window (top row), as well as, the micrometer thick film (bottom row) at linear-polarized light or with crossed polarizers (arrows) exhibit no birefringent properties. For the nanometric sample macroscopic anisotropy in absorption arises (middle row, domains indicating long range order): TM b is distributed only within the xy plane; TM a is symmetrically tilted ($\Theta = 47°$, only one direction is shown). Note that TMs a and c may be tilted in both directions (upward or downward). Each scale bar represents a length of 100×10^{-6} m.[1]

3.5 Biomimetic spider silk's high toughness based on the similar morphology as the natural template

A.M. Anton, A. Heidebrecht[*], N. Mahmood[†], M. Beiner[†], T. Scheibel[*], F. Kremer

[*]Lehrstul für Biomaterialien, Universität Bayreuth
[†]Experimental Polymer Physics, Martin-Luther-Universität Halle-Wittenberg, Halle

Spiders' dragline silk exhibits remarkable characteristics as exceptional biocompatibility or high tensile strength combined with great elasticity. Its mechanical properties are based on a refined architecture on the molecular scale: Proteins with highly repetitive core motifs aggregate into nanometer-sized crystals rich on alanine in β-sheet secondary structure and surrounded by an amorphous glycine-rich matrix. During spinning the amorphous parts are elongated which orients both substructures and, in addition, give rise to an inherent non-equilibrium state. Thus, external stress is directly transferred to the nanocrystals, while the tendency to contract is counterbalanced by surrounding fiber structure. However, it was not possible to recreate artificially this exceptional architecture so far.

The combination of Wet spinning and post-treatment of a biomimetic protein results in fibers with the identical nanostructure and comparable toughness than the natural

template.[1] We found that unoriented alanine-rich β-sheet nanocrystals with the same size as in natural silk are already formed during wet spinning (Fig. 3.5), while the glycine-rich motifs establish the amorphous section. Furthermore, post-spinning strain orients this composite leading to a non-equilibrium on nanoscale that is, in addition, accompanied by enhanced mechanical properties. Our results demonstrate in detail how macroscopic mechanical properties originate from the molecular organization: Pre-stressed chains apportion applied stress directly to the crystallites enabling to dissipate huge mechanical load as identical to the mechanism in natural dragline silk.[2]
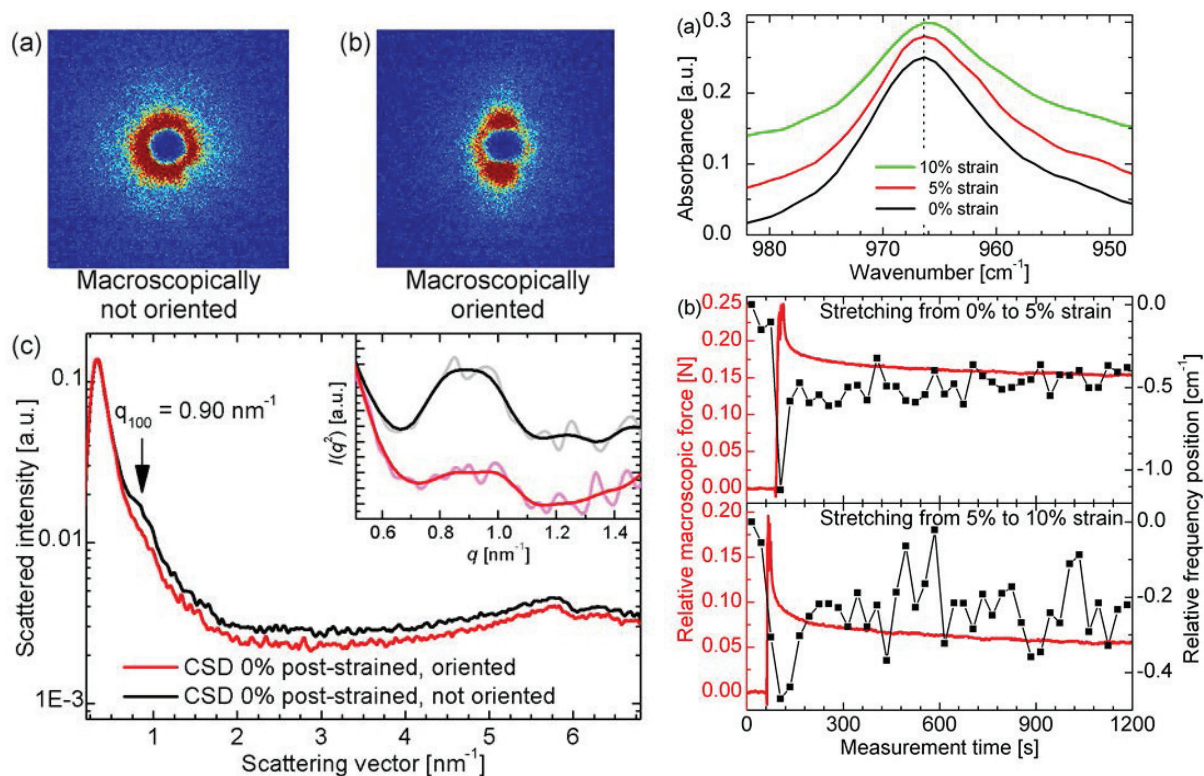
Figure 3.5: Left: SAXS pattern of biomimetic fibers macroscopically (a) not and (b) well oriented. (c) Inte-grated intensity gives the crystal size of 7.0 nm.
Right: a) The fre-quency position of the polyalanine peak is shift as a conse-quence of the applied force (b) Relative force (red) and relative frequency position (black) during the elongation of the biomimetic post-treated sample from (top) 0 to 5% and (bottom) 5 to 10% strain. The difference between the black and the red curve in panel a corresponds to the first and the last position in the top diagram of panel b; the difference between the red and the green curve reflects the first and the last position in the bottom diagram.

[1] A. Heidebrecht, L. Eisoldt, J. Diehl, A. Schmidt, M. Geffers, G. Lang, T. R. Scheibel, Adv. Mater. 27, 2189–2194 (2015)
[2] A. M. Anton, A. Heidebrecht, N. Mahmood, M. Beiner, T. Scheibel, F. Kremer, submitted

3.6   Charge transport and molecular dynamics in highly conductive Polymeric Ionic Liquids

F. Frenzel, R. Guterman[*], A.M. Anton, J. Yuan[*], F. Kremer

[*]Max Planck Institute for Colloids and Interfaces, Potsdam (Golm)

Glassy dynamics and charge transport are studied for the polymeric Ionic Liquid (PIL) poly[tris(2-(2-methoxyethoxy)ethyl)ammonium acryloxypropyl-sulfonate] (PAAPS) with varying molecular weight (9700, 44200, 51600 and 99500 g/mol) by Broadband Dielectric Spectroscopy (BDS) in a wide frequency ($10^{-2} - 10^{7}$ Hz) and temperature range (100 – 400 K), and by Differential Scanning Calorimetry (DSC) and AC-chip calorimetry.[1] The dielectric spectra are characterized by a superposition of (i) relaxation processes, (ii) charge transport and (iii) electrode polarization. The relaxation processes (i) are assigned to the dynamic glass transition and a secondary relaxation. Charge transport (ii) can be described by the random free-energy barrier model as worked out by Dyre et al.[2].; the Barton-Namikawa-Nakajima (BNN) relationship is well fulfilled over more than 8 decades. Electrode polarization (iii) follows the characteristics as analyzed by Serghei et al.[3]; with deviations on the low frequency side. The proportionality between the relaxation rate of the dynamic glass transition and the charge carrier hopping rate reflects the nature of charge transport as glass transition assisted hopping (Fig. 3.6).
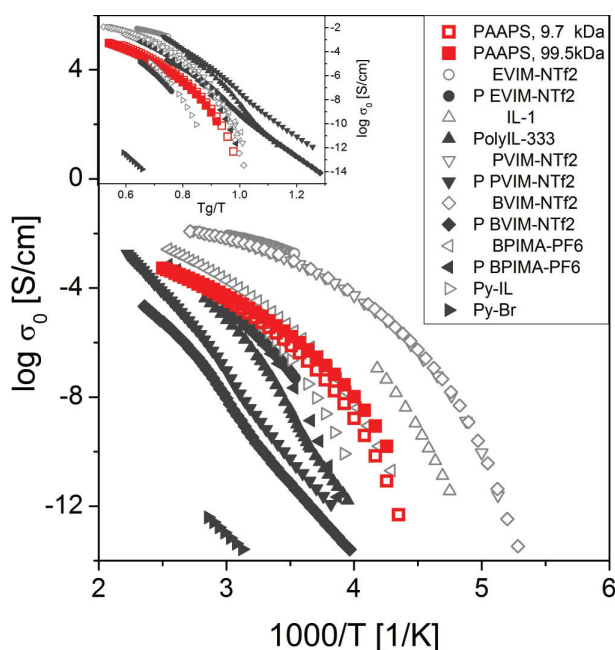
Figure 3.6: Comparative presentation of the dc-conductivity σ_0 vs. inverse temperature for the aforementioned PILs of different molecular weights (red), as well as literature data of six other PILs (gray, filled symbols) and corresponding monomeric counterparts (gray, open symbols). The inset holds the same data scaled with respect to the calorimetric glass transition temperature T_g. Error bars are smaller than the size of the symbols, unless indicated otherwise.

The PIL under study exposes the highest dc-conductivity values observed for this class of materials below 100° C, so far; and for the first time a conductivity increase by

rising degree of polymerization. The comparison of the polymeric Ionic Liquids under study with others implies conclusions on the design of novel highly conductive PILs.[1]

[1] Frenzel, F.; and Guterman, R.; Anton, A.M.; Yuan, J.; and Kremer, F. Molecular Dynamics and Charge Transport in Highly Conductive Polymeric Ionic Liquids. Macromolecules, 2017, DOI: 10.1021/acs.macromol.7b00554

[2] Dyre, J. C.; Schroder, T. B. Universality of AC Conduction in Disordered Solids, Rev. Mod. Phys. 2000, 72, 873–892.

[3] Serghei, A.; Tress, M.; Sangoro, J. R.; Kremer, F. Electrode polarization and charge transport at solid interfaces. Phys. Rev. B: Condens. Matter Mater. Phys. 2009, 80, 184301.

3.7   Funding

3.8   Organizational Duties

Friedrich Kremer
- Principal Investigator in the "Leipzig School of Natural Sciences - Building with Molecules and Nano-Objects" in the framework of a Graduate School funded by the "Federal Excellence Initiative". This supports several Ph.D. projects.

3.9   External Cooperations

Academic

- Technische Universität München
  Prof. Dr. C.M. Papadakis, J. Zhang

- Leibniz-Institut für Polymerforschung Dresden
  Dr. P. Uhlmann, R. Winkler

- Martin-Luther-Universität Halle-Wittenberg
  Prof. Dr. T. Thurn-Albrecht, A. Seidlitz

- Fraunhofer Institut für Werkstomechanik IWM, Halle
  PD Dr. M. Beiner, Dr. N. Mahmood

- Department of Chemical and Biomolecular Engineering, University of Tennessee, Knoxville
  Prof. Dr. J.R. Sangoro

- Hochschule Niederrhein, Institute of Organic Chemistry
  Prof. Dr. Strehmel

- Medizinische Fakultät Carl Gustav Carus der Technischen Universität Dresden
  Prof. Dr. Gerald Steiner

Industry

- Novocontrol, Hundsangen, Germany
- MERCK KGaA, Darmstadt, Germany
- Lohmann Tierzucht GmbH
- EVONTA-Technology GmbH

3.10 Publications

Journals & Chapters

Anton, A.M., R. Steyrleuthner, W. Kossack, D. Neher, F. Kremer, "Spatial Orientation and Order of Structure-Defining Subunits in Thin Films of a High Mobility n-Type Copolymer", Macromolecules 49, 1798-1806 (2016) DOI: 10.1021/acs.macromol.5b02420

Frenzel, F., Y.F. Makafui, M. Schulz, A.M. Anton, W.H. Binder, F. Kremer, "Molecular Dynamics and Charge Transport in Polymeric Polyisobutylene-Based Ionic Liquids", Macromolecules 49, 2868-2875 (2016) DOI: 10.1021/acs.macromol.6b00011

Kossack, W., A. Seidlitz, T. Turn-Albrecht, F. Kremer, "Interface & confinement induced order and orientation in thin films of Poly-e-caprolactone", Macromolecules, 49, 3442-3451 (2016) DOI: 10.1021/acs.macromol.6b00473

Holländer L., W. Kossack, M. Kollosche, W. Wirges, F. Kremer, R. Gerhard, "Influence of the remanent polarisation on the liquid crystal alignment in composite films of ferro-electric poly(vinylidene fluoride-trifluoroethylene) and a cyanobiphenyl-based liquid crystal", Liquid Crystals, 43, 1514-1521 (2016) DOI: 10.1080/02678292.2016.1185174

Schneider D., N. Gomopoulos, C.Y. Koh, P. Papadopoulos, F. Kremer, E.L. Thomas, G. Fytas, "Nonlinear control of high-frequency phonons in spider silk", Nature Materials 15, 1079-1083 (2016) DOI: 10.1038/NMAT4697

Neubauer N., M. Treß, R. Winkler, E.U. Mapesa, W.K. Kipnusu, P. Uhlmann, F. Kremer, "Molecular Dynamics of Swollen Poly(2-vinylpyridine) Brushes", Macromolecules, 49 (16) 6101-6105 (2016) DOI: 10.1021/acs.macromol.6b00363

Stangner T., C. Wagner,C. Gutsche, K. Stangner, D. Singer, S. Angioletti-Uberti, F. Kremer "Probing Receptor-Ligand Interactions on a Single Molecule Level Using Optical Tweezers" In: "Encyclopedia of Biocolloid and Biointerface Science", Edited by Hiroyuki Ohshima, Volume 2, First Edition, John Wiley & Sons Inc; 915-932 (2016) DOI: 10.1002/9781119075691.ch74

3.11   Graduations

Doctorate

- Dipl.-Phys. Arthur Markus Anton
  Infrarotspektroskopie zur Strukturanalyse weicher Materie

3.12   Guests

- Prof. Dr. Michael Vogel
  TU Darmstadt
  30. April 2015

- Prof. Dr. Bernd Stühn
  TU Darmstadt
  11. June 2015

4

Soft Matter Physics

4.1   Introduction

The Soft Matter Physics group focuses on a quantitative understanding of biological cell phenotype and function from a complex, emerging materials perspective encompassing all length scales from molecules to tissues, which places the group in a pioneering and leading position in the novel area Physics of Cancer.

The emphasis of the Soft Matter Physics group is on the material properties of biological cells as key determinants of their character and functions, including tumor progression. This requires an integral approach that spans the length scales from molecules to tissues. For this research we are uniquely positioned by our ability to concurrently purify cytoskeletal proteins and have access to clinical tissue samples.

Our research employs a wide variety of cutting edge experimental techniques such as super resolution microscopy, DNA-nanotechnolgy, biomimetic microenvironments, and a unique range of methods to characterize the mechanical and adhesive properties of cells and tissues. The combination of research on reconstitued cytoskeletal elements and cells as well as tissues *in statu nascendi*, i.e. *in vivo* and *in vitro* studies, allows to determine fundamental cell bio-physics and to investigate how they emerge from coalescing sub-cellular components. A main focus is to understand the epithelial to mesenchymal transition (EMT), which occurs in many pathological processes such as cancer or fibrosis, from a physics perspective using concepts from active soft matter and unjamming transitions. We work closely with international partners such as Prof Sack at the Charité and Profs Manning and Marchetti at the University of Syracuse and find the support of the National Cancer Institute (NCI) and the German Cancer Research Center. Our leading role concerning the Physics of Cancer has been documented by an international panel for the NCI and manifests itself by the annual Physic of Cancer conference hold in Leipzig.

Josef A. Käs

4.2 New results in the field of 3D spheroid motility - self-propelled Voronoi Model

S. Grosser, L. Oswald, J.A. Käs

We have cells grow into multicellular tumour spheroids in order to anaylse their rheology. We know that some of these are fluid and some have rigid properties. We take complete 3D confocal image stacks with nuclei and actin stained. We fixate the spheroids, remove lipids with Triton-X, stain with SiR-DNA (deep red)(or Hoechst) and Phalloidin-Alexa488. Spheroids are embedded in an 80% Glycerole / 20% H2O mixture to optically clear them. We automatically detect nuclei positions using adaptive thresholding and actin cortices using watershedding from the nucleus seeds to find **actual cell shapes**, which are compared to the predictions of the newly developed 3D SPV model (private communication from Prof. M. Lisa Manning and Dr. Matthias Merkel, University of Syracuse).
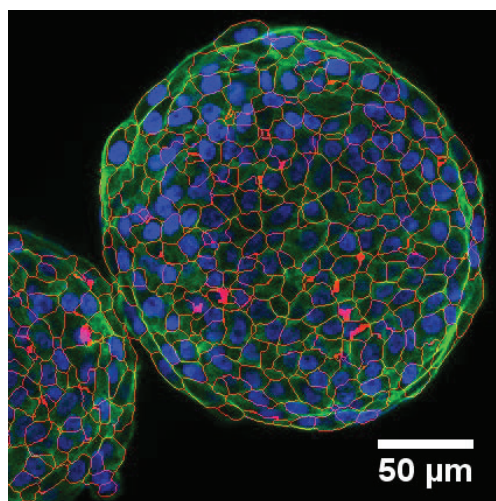
Figure 4.1: Slice through MCF-10A spheroid; confocal image showing nuclei and actin. Red: segmentation
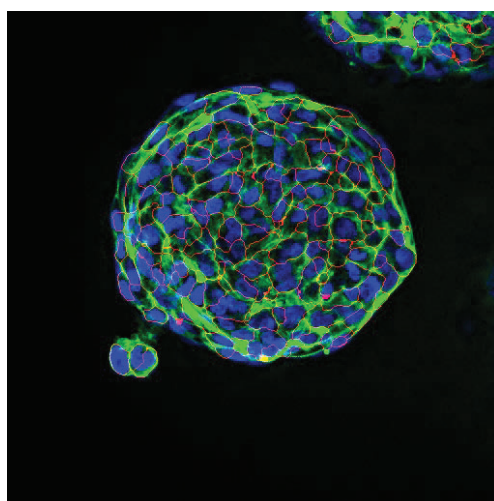
Figure 4.2: Slice through MDA-MB-436 spheroid

Results:

- We can see through virtually complete spheroids of 150 μm diameter using this method.

- We see a more regular pattern in MCF-10A spheroids and a more amorphous pattern in MDA-MB-436.

- MCF-10A have a more pronounced actin cortex signal, while MDA-MB-436 show less pronounced cortical signal, which makes them much harder to detect; the automatic segmentation seems not to be 100% correct for the MDA-MB-436, we are still working to improve that.

- **MCF-10A spheroids have low shape indices near the transition**, especially inside the spheroids. Shape indices are larger in the outer shell - this fits to our fluidity experiments (last year). These results are the first for 3D cellular jamming.

MDA-MB-436 have higher indices with a broader and spatially heterogeneous distribution.

- In both samples, shape index is higher for larger cells. We know that our MDA-MB-436 spheroids are always larger than MCF-10A spheroids of the same cell count, so naturally MDA-MB-436 cells are bigger. It is not necessary insufficient segmentation that MDA-MB-436 cells are larger and indices are higher, although the segmentation is not perfect for MDA-MB-436, as stated before.
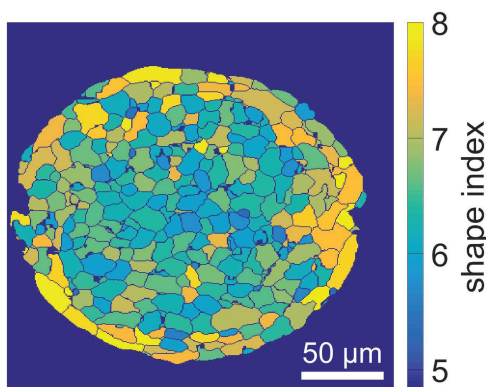
Figure 4.3: Slice through MCF-10A spheroid
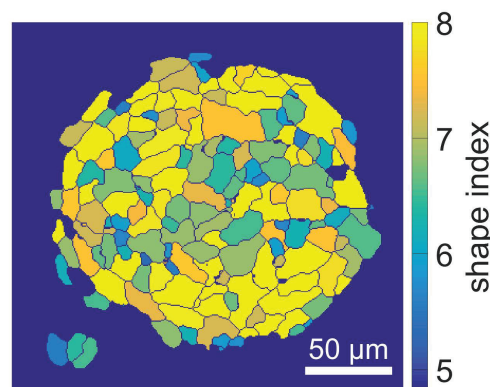
Figure 4.4: Slice through MDA-MB-436 spheroid
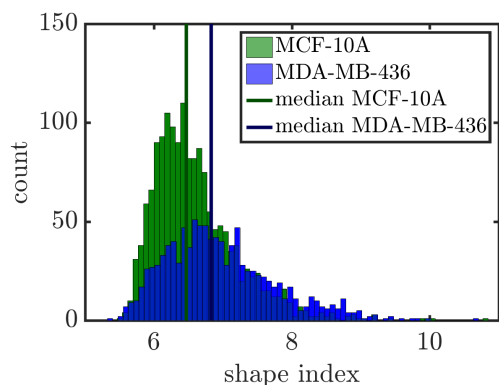
Figure 4.5: Shape index histogram for the 3D segmentation of multicellular spheroids. To our knowledge, this is the worldwide first segmentation of that kind. The mesenchymal MDA-MB-436 cells have on average higher shape indices than the MCF-10A, which form a jammed solid.
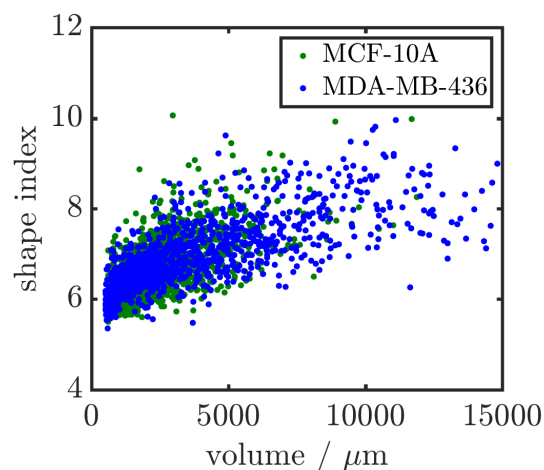
Figure 4.6: Experimentally, we observe a strong dependence of shape indices on cell volume, so far not treated by the literature. Cell shape is governed by the interplay of adhesion and cortical tension, and of course one would expect them to scale differently with cell size.

4.3   Traction force microscopy for tumour spheroids

L. Oswald, S. Grosser, J.A. Käs

We have established the experimental and analysis tools in our lab to interpret measurements of tumour spheroid traction forces. We have successfully embedded tumour spheroids, which were grown in agarose overlay culture, into collagen matrices (see figure 4.7) and have used phase contrast imaging to track displacements in the matrix gel structure via particle image velocimetry (PIV). Fluorescence imaging at the same time allows to identify the spheroid structure and to assess invading cells tracks.

These allow for the first time to make experimental observations about the dependence of traction forces involved in the tumour surroundings on matrix composition, such as collagen or matrigel, matrix stiffness, metastatic potential, or spheroid size. We show the experimentally detected scaling of matrix deformation with spheroid size in figure 4.8. So far, no serious theories on the scaling behaviour of cellular spheroids exist.
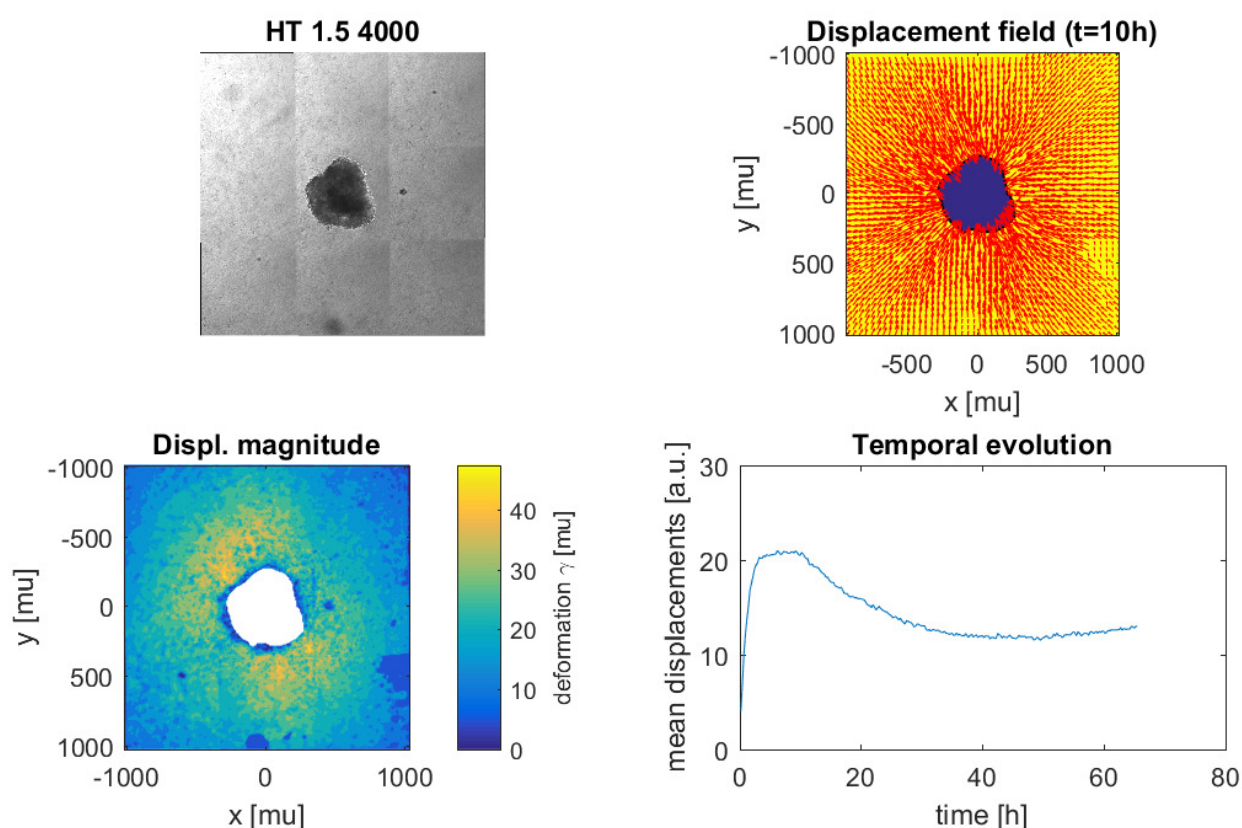
Figure 4.7: Traction force microscopy for tumour spheroids: Original images, calculated displacement fields vectors and magnitudes, and temporal development of tumour tractions.
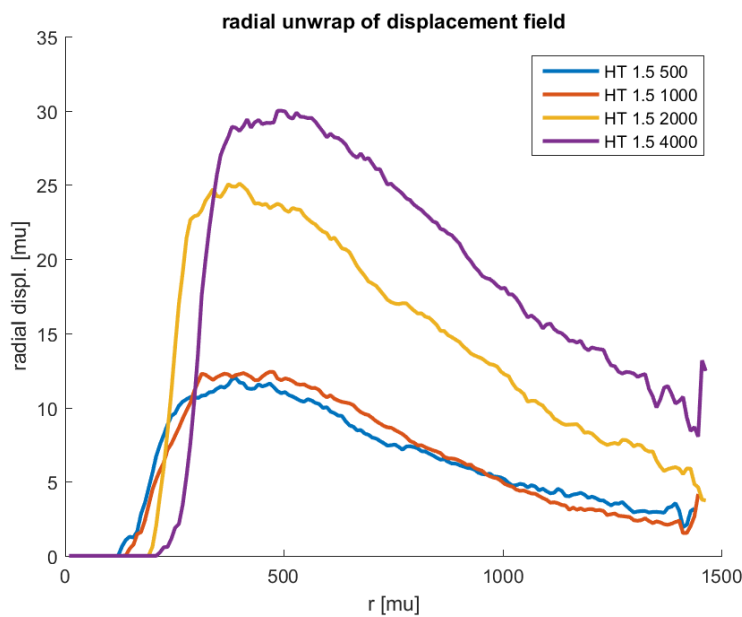
Figure 4.8: Inward displacements of extracellular matrix caused by the spheroids. Spheroids are HT1080 with 500, 1000, 2000, 4000 cells respectively. Larger spheroids cause larger displacements but no predictions have been made on the behaviour.

4.4 Transition from a linear to a harmonic potential in collective dynamics of a multifilament actin bundle

J. Schnauß[*†], T. Golde, C. Schuldt[*†], B.U.S. Schmidt, M. Glaser, D. Strehle, T. Händler, C. Heussinger[‡], J.A. Käs

[*]Institute for Exp. Physics, PWM
[†]Fraunhofer IZI, Leipzig
[‡]Institut for Theoretical Physics, Georg-August-University, Göttingen

Modeling approaches and recent experimental data have shown that depletion forces between suspended, rod-like particles display different signatures depending on the orientation of these particles. It has been shown that depletion-driven, axial attraction of two rods yields a constant contractile force of 0.1 pN, which corresponds to a linear energy potential. We extended these pairwise interactions to a multi-filament level by investigating arising dynamics within actin bundles. Without any additional proteins such as crosslinkers or molecular motors, we found contractile forces in a biologically relevant regime of up to 3 pN. Generated forces due to bundle relaxation were not constant as in a two filament case, but decayed exponentially with a mean decay time of 3.4 s (figure 4.9). These different dynamics are explained within the frame of a mathematical model (and supported by simulations) by taking pairwise interactions to a multi-filament scale [1].

[1] J. Schnauß et al.: Phys. Rev. Lett. **2016** 116, 108102
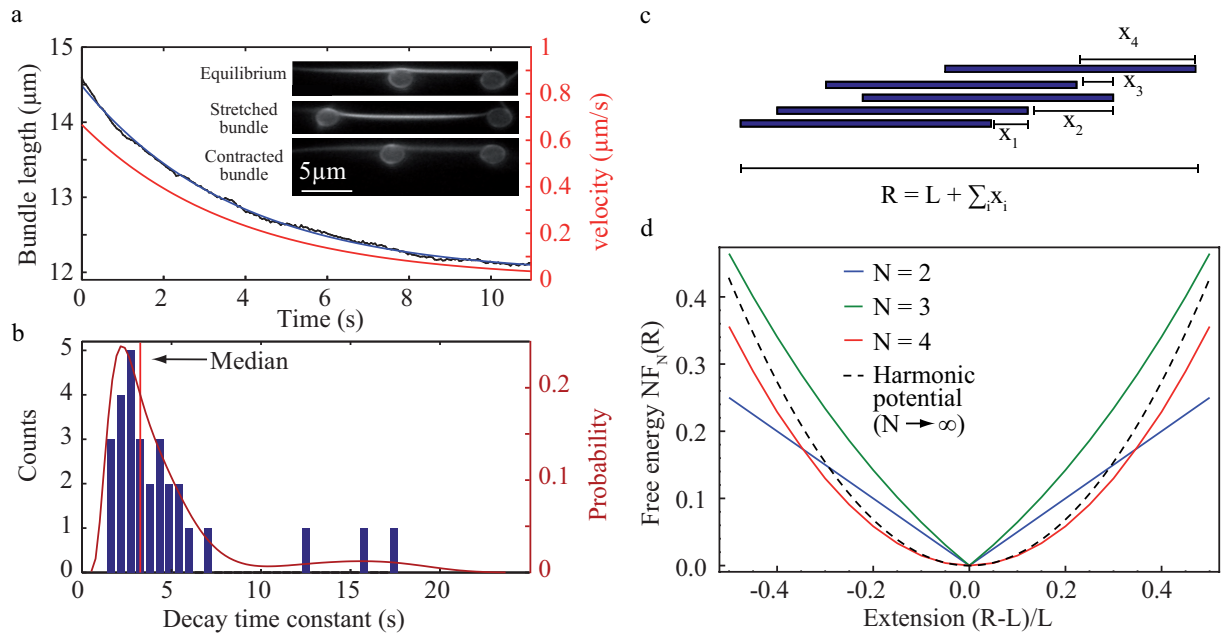
Figure 4.9: (a) Actin bundle contractions can be caused by a crowded environment inducing attractive depletion forces. Recorded bundle lengths over time during contraction processes can be well-described by an exponential decay function. This fitting function can be differentiated allowing an evaluation of the contraction velocity (red graph). (b) According decay times of various contraction events of differing bundles are consistent with a median of 3.4 s. (c) The exponentially decaying form can be described within a mathematical model in an idealized 2d-scenario, where forces are applied at the first (i = 1) and at the last filament (i = N). (d) Free energies $F_N(R)$ vs. extension R-L show a strong dependency on the filament number N. A two-filament bundle (N = 2) has a linear energy landscape, but with only a few filaments (N = 4) the asymptotic, harmonic form (dashed) is nearly reached [1].

4.5   Tuning synthetic semiflexible networks by bending stiffness

C. Schuldt[*†], T. Schnauß[*†], T. Händler, M. Glaser, J. Lorenz[†], T. Golde, J.A. Käs, D.M. Smith[†]

[*]Institute for Exp. Physics, PWM
[†]Fraunhofer IZI, Leipzig

Classical physics of flexible polymers and rigid rods is not sufficient to describe the mechanics of complex soft matter. Nontrivial mechanical responses arise from semiflexible polymers as the underlying building blocks, which for instance form the shaping scaffold of cells called the cytoskeleton. The established experimental model for these polymers, filamentous actin, is limited since its central property - the persistence length - cannot be tuned freely. We used structurally tunable DNA nanotubes to experimentally evaluate the impact of this crucial parameter on entangled networks. We were able to validate inherent characteristics of semiflexible polymers and networks such as persistence length, inextensibility, reptation, and mesh size as well as concentration scaling. However, the scaling of the elastic plateau with persistence

length ($G_0 \propto l_P$) opposes predominant theoretical predictions emphasizing the need to further develop the theoretical framework to capture experimental results [1].
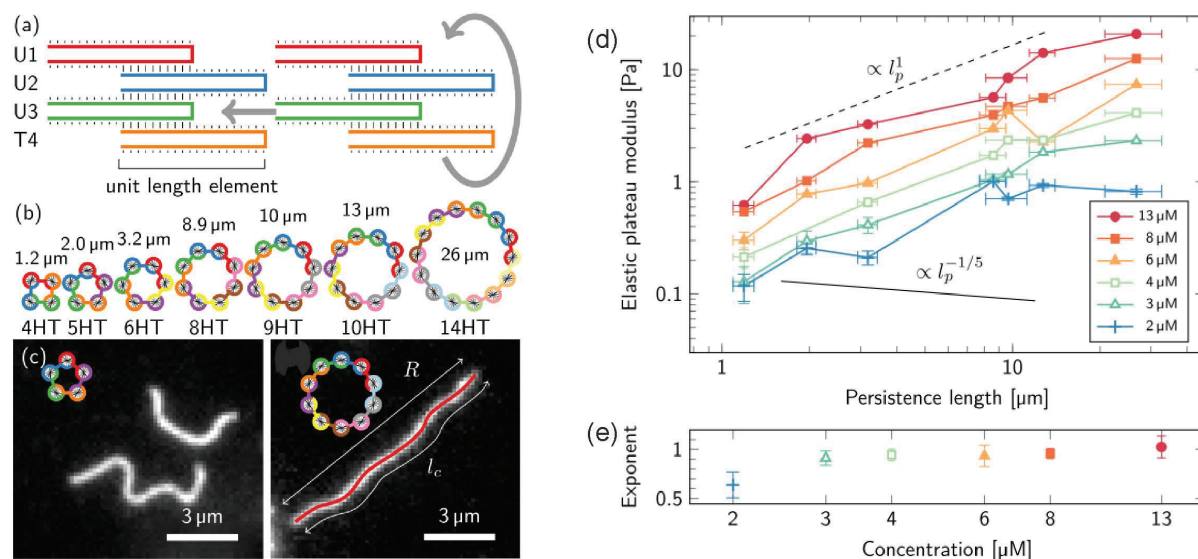
Figure 4.10: (a) Schematic of the assembly of a 4HT formed of four distinct 42-mers. (b) Cross section of seven different nHTs with according values for persistence length. (c) Epifluorescent images of labeled nHTs at the surface. The filament contour is overlaid in red. (d) Persistence length scaling for different network concentrations of the elastic plateau modulus. (e) The approximated power law exponent gives a mean value of 1. Images adapted from [1].

[1] C. Schuldt et al.: Phys. Rev. Lett. **2016** 117, 197801

4.6 Self-assembly of hierarchically ordered structures in DNA nanotube systems

M. Glaser, J. Schnauß*†, T. Tschirner, B. Schmidt, M. Moebius-Winkler†, J.A. Käs, D.M. Smith†

*Institute for Exp. Physics, PWM
†Fraunhofer IZI, Leipzig

Pattern formation is an incredibly complex process, which is observed in various disciplines and on different size and time scales. The self-assembly of molecular and macromolecular building blocks into such organized patterns has been studied over the last years in various fields. Especially in polymeric solutions the formation of aster-like structures caused by self-assembly effects is a well-known effect. Involved components show a high structural diversity ranging from cellular constructs to solutions of ferromagnetic colloids or synthetic plastics. Despite their structural diversity, they show some unifying properties although their mechanical properties are significantly different. To date the mechanical properties of the underlying components, however, cannot be controllably varied to study their influence on pattern formation. In this study we

overcome this limitation using DNA nanotubes with programmable mechanical properties. Depending on the involved strands, well-defined DNA nanotubes are formed with varying circumferences and stiffness, respectively. With this new approach, we are able to investigate pattern formations with one specific material with the ability to vary the underlying persistence length of the polymers. In our study, the self-assembly of these nanotubes is driven by depletion forces caused by the presence of polyethylene glycol (PEG). To monitor the influence within this complex parameter space we varied the concentration of the depletant as well as the concentration and stiffness of the DNA nanotubes (4.11). Our findings show a diverse outcome including networks, star-like structures and a needle-like phase, which compare to observations made in various other systems (4.11). They show a strong dependence not only on concentration and depletion strength, but also on underlying mechanical properties of the nanotubes. These results provide a broader view on the complex assembly mechanisms involved in the field of DNA nanotechnology. They emphasize the general effect inevitable attractive forces present in crowded environments have on systems of self-assembling soft matter. These underlying mechanisms should be considered for macromolecular soft matter structures when applied in crowded systems such as cells.
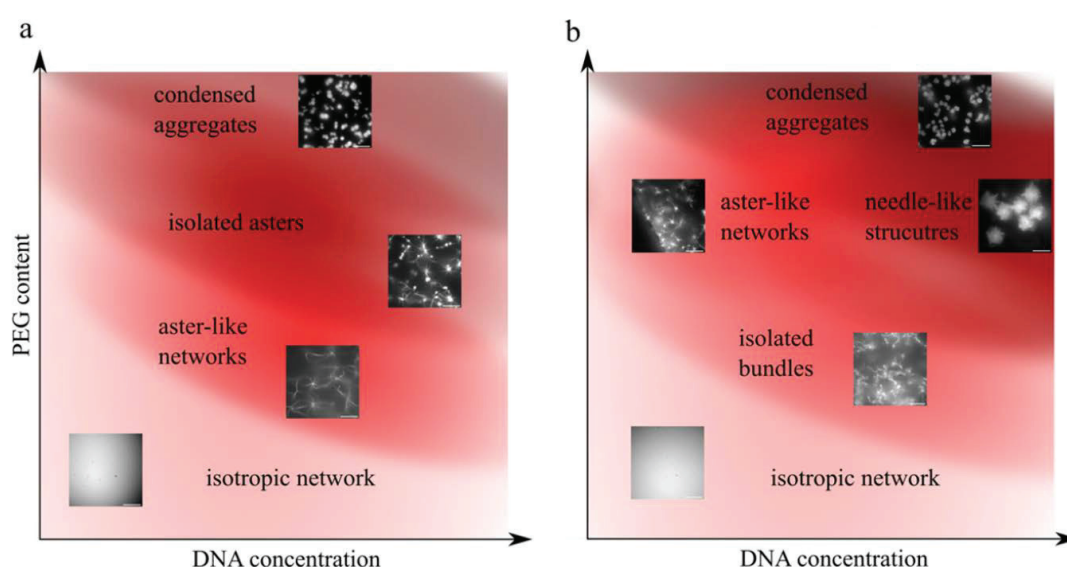
Figure 4.11: Suggested overview diagram for observed self-assembled states, as a function of the attraction strength (depletion forces) and DNA concentration. (a) Flexible nanotubes (4HT). (b) Semiflexible and stiffer nanotubes (6-10HT).

4.7 A new definition of jamming: Beyond T1 transitions and MSD

J. Lippoldt, S. Grosser, P. Heine, L. Oswald, J.A. Käs

The ability of cells to migrate in their environment is critical in many aspects of biology. Especially interesting is the apparent difference between solid-like tissues were cells stay at their place and a fluid-like structure of a developing embryo or a metastatic

cancer. The root cause for its difference in behavior is believed to be jamming transition in epithelial tissues. Theoreticians usually quantify a jamming transition by energy barriers for T1 transitions, the minimal requirement for a neighborhood change. Those are inaccessible in experiments. Current experimental approaches rely on statistical analysis of a large number of cells and time steps, making it hard to analysis heterogeneities and changing individual properties cells [1]. We introduce a new measure of jamming, which allows for a heterogeneous analysis of experiments and simulations alike. We use cells with stained nuclei to obtain cell tracks from time series. We then performed a Voronoi tessellation for each image around the middle of the cell nuclei, to investigate the neighbor relations. Even for a dense layer of epithelial cell, T1 transitions do not stop occurring. This is might be in part, because the tessellation does not depict the actual cell shape, which is hard to obtain for a movie. The other reason is that cells can wiggle in their cavities. Therefore, the occurrence of T1 transitions is not a good measure to quantify jamming. We used two different approaches. Firstly, we counted the number of new neighbors a cell obtained in a certain time limit, which did not share a neighbor with the cell at start. This quantifies the number of neighborhood exchanges near the cells and gives a good measure of how fluid the region is in that timeframe. A jammed system has nearly no neighborhood exchanges. The second approach was to look for cell that squeeze through two of their neighbors. Those events should have a high energy barrier in a jammed system and are extremely rare for them. One sees a critical slowing down of the time required for a squeezing event during the jamming transition. The data shown here is in very good agreement with the SPV model of Lisa Manning and Christina Marchetti [2]. While density is correlated to the jammed state, even the shape parameter of the Voronoi tessellation (and not the real shape, or an evolved surface) has a stronger correlation.

Figure 4.12: Nuclei of MCF-10A cells were detected with a self-written matlab algorithm. The tracks were made with the ImageJ plugin TrackMate.
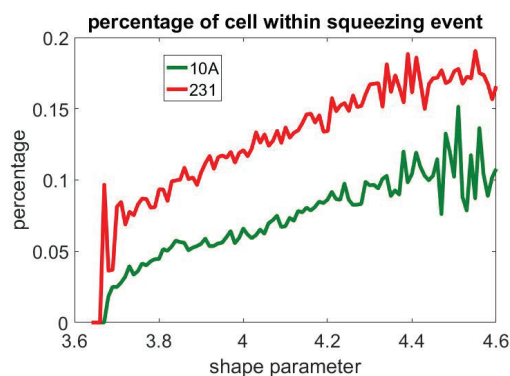
Figure 4.13: Percentage of cells that are squeezing through two neighbors, over their shape parameter. It approaches zero near the critical value of the SPV model.

[1] J. H. Kim et al.: Nature Mat. **2013** 12, 856-863
[2] D. Bi et al.: Physical Rev. X **2016** 6, 021011
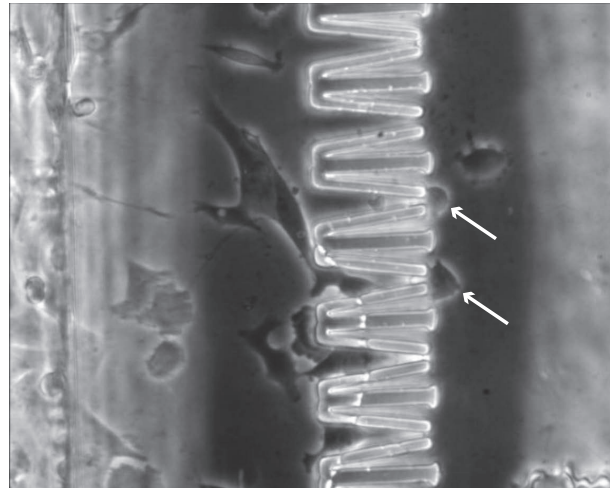
Figure 4.14: Crossing of constriction channels. Mesenchymal-like MDA-MB-231 cells sqeeze their way through narrowing SU8 constriction (2-10 μm) in a blebbing-like motion.

4.8 Invasive behavior and individual cell jamming in microconstriction channels

P. Heine, C. Ficorella, R. Martinez[*], R. Osellame[*], J.A. Käs

[*]Inst. of Photonics and Nanotechnology, CNR & Dept. of Physics, Politecnico di Milano, Italy

In cancer invasion physical constraints such as neighbor interactions and compartment penetration profoundly impact cellular motion. The imposed spatial restrictions can lead to collective motion within tissues, where the jamming transition denotes the switch from a fluid-like unjammed to a solid-like almost-frozen system state. The exact nature of this phenomenon remains poorly understood, however recent studies have revealed that cellular properties influence this transition. Single-cell properties like contractility, cortical tension, adhesion and motility can be analyzed and compared against cell layer performance in a crowded environment. This study is particularly interesting for epithelial cells which undergo a remarkable carcinogenetic transition to a mesenchymal phenotype during tumor development. This Epithelial-Mesenchymal Transition (EMT) facilitates a variety of mechanical and biochemical changes within the affected cells, which produces drastic changes in their cell polarity, cell-cell adhesion, migratory and invasive properties. In this transition epithelial cells transform from small, regularly shaped, circular cells to a large and irregular mesenchymal phenotype.

By subjecting cells to extremely confining microenvironments, created via multiphoton excitation of an SU8 negative photoresist, we plan to investigate a particular type of motion employed by invasive mesenchymal cells. This motion is characterized by transient almost-spherical protrusions of the cell membrane and is termed blebbing motion (see figure 4.14). Blebbing motion has been shown to be used as a coping mechanism by cancerous cells subjected to chemotherapy drugs which target lamellipodium formation and other migratory functions. Additionally aggressive melanoma cells which are destined to form metastases in distant tissues utilize blebbing motion to cross the endothelium. An exploration of the exact mechanisms which govern the transition into this particular motility mode might elucidate a variety of open questions arising in the physics of metastases formation.
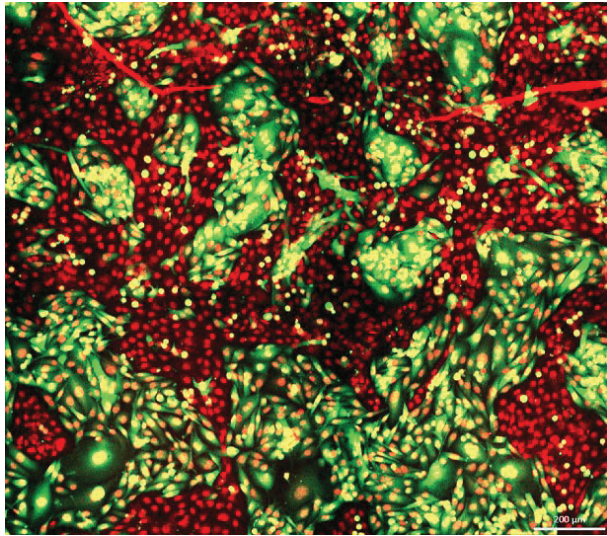
Figure 4.15: Demixing of confluent cell layers: In a 80%/20% co-culture of MCF-10A/MDA-MB-231 cells, the epithelial MCF-10A cells compose a dense sheet of caged cells, while the mesenchymal-like MDA-MB-231 cells assemble into seemingly uncaged pools within the layer at a slightly lower density.

4.9 How demixing and crowding behavior influence the invasive potential of composite tumor-like systems

P. Heine, J. Lippoldt, S. Grosser, L. Oswald, J.A. Käs

The progression of cancer invasion is regulated through microenvironmental properties and their transformation for example in compartment penetration but critically also by the tumor composition itself. The heterogeneity of this system gives rise to an interesting phenomenon termed the jamming transition, a switch from a fluid-like unjammed cell layer to an almost solid-like state. While not entirely understood, recent studies have revealed that single-cell properties like contractility, cortical tension, adhesion and motility influence this transition and have a profound impact on the cell layer behavior in a crowded environment. During the epithelial-mesenchymal transition a plethora of mechanical and biochemical changes lead to a drastic shift in cell polarity, shape, cell-cell adhesion, migratory and invasive properties. Our investigation of mixed systems of metastatic and benign cells exposed a demixing process of the two cell types and vastly different crowding performance. While epithelial cells form a dense sheet of caged cells, the mesenchymal-like cells compose seemingly uncaged pools within the layer, illustrated in figure 4.15. This makes this a particularly fascinating system to study due to its bifurcational nature, which could allow for a transition between fluid and solid cell layer and vice versa.

4.10 Optical stretching in continuous flows

E.W. Morawetz, R. Stange, T. Kießling, J.A. Käs

Microrheology of living cells is a promising approach for medical research, since the correlation between the rheologic behavior of cells and their malfunctioning becomes more pronounced with ongoing research [1–3]. The rheologic behavior is mainly determined by the cytoskeleton of a cell, which executes different functions in migration, proliferation and signaling [4]. Microrheology of living cells has therefore developed an

increasing need for high throughput measurements. The possibility to measure several hundred cells within hours, like it is possible with current Optical Stretcher devices, gives a huge statistical advantage that balances out the broad distribution of properties in biological specimen [2, 3]. It allows for the assignment of characteristic values to samples consisting of large numbers of individual cells. Short measurement times make it possible to investigate time sensitive processes and counteract temporal changes of the sample. Still, to be applicable in a prognostic manner even higher throughput rates have to be achieved. We addressed this task and developed the "in flow optical stretcher" (IFOS), a concept of non-invasive optical cytometry capable of high throughputs. It deforms whole cells in a continuous flow by optical forces, bypassing steps of cell positioning. We created a prototype with the use polydimethylsiloxane soft lithography. The IFOS is comparable to current optical stretcher devices regarding the measurement principle, but the time needed for a microrheological measurement of a single cell is significantly reduced. We were able to conduct a successful proof of premise experiment. MCF-10A cells were treated with cytochalasin D to soften their cytoskeleton and increase deformability. In the IFOS these cells were trapped and deformed while they moved through the measurement chamber in no longer than 0.5-2 s per cell. This concept of light based microrheology would allow for significantly higher throughputs than current Optical Stretcher devices can reach, while working in the same frequency and force regimes.
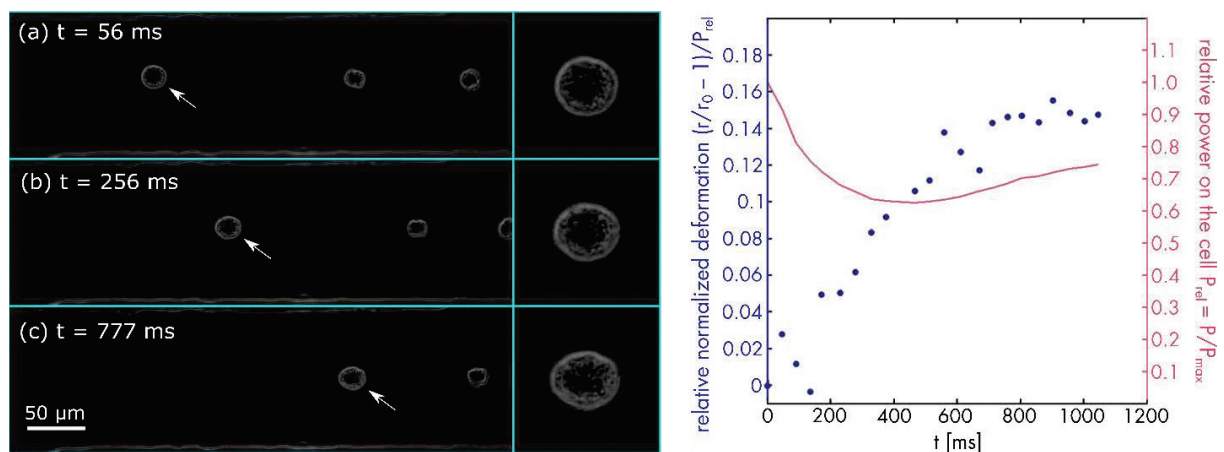
Figure 4.16: Deformation of a cell in the IFOS, represented by three time points of the process as well as the deformation graph. Laser fibers are positioned left and right outside the pictures with their beam axis along the flow path of cells. Laser power is 1200 mW each. The cell indicated by the white arrow moves from the left to the right. It gets trapped at (a), starts to show deformation at (b) and reaches the maximum deformation at (c). In (c), other cells are stably trapped between the flow and the radiation forces from the laser on the right and line up along the beam axis. The indicated cell gets deformed continuously while flowing along the chamber. The graph on the right side shows the relative deformation of the pictured cell in blue. It is normalized by the power on the cell, which is dependent on its position in the chamber and represented by the red graph. Time is set to zero at the moment the cell is fully trapped by the dual beam trap and in focus.

[1] K. A. Ward et al.: Biorheology **1991** 28, 301-313

[2] J. Guck et al.: Biophys. J. **2005** 88(5), 3689-3698

[3] A. Fritsch et al.: Nature Physics **2010** 6(10), 730-732
[4] E. Elson et al.: Ann. Rev. Biophysics Biophysical Chemistry **1988** 17, 397-430

4.11   Proteomic Details of Differential Adhesion Hypothesis

H. Kubitschke, S. Grosser, L. Oswald, S. Pawlizak, A. Fritsch, J.A. Käs

We analysed the mechanical properties of three epithelial/mesenchymal cell lines (MCF-10A, MDA-MB-231, MDA-MB-436) associated with properties from benign to metastatic tumours, to quantify the role of cell cohesion in cell sorting and compartmentalization. The analysis included quantitative mass spectroscopy SILAC, of the underlying proteome of the cell lines. We developed a unique set of methods to measure cell - cell adhesiveness, cell stiffness and cell shapes, and compare the results to predictions from cell sorting in mixtures of cell populations. We find that the final sorted state is extremely robust among all three cell lines independent of epithelial or mesenchymal state, suggesting that cell sorting may play an important role in organization and boundary formation in tumours (see figure 4.17).
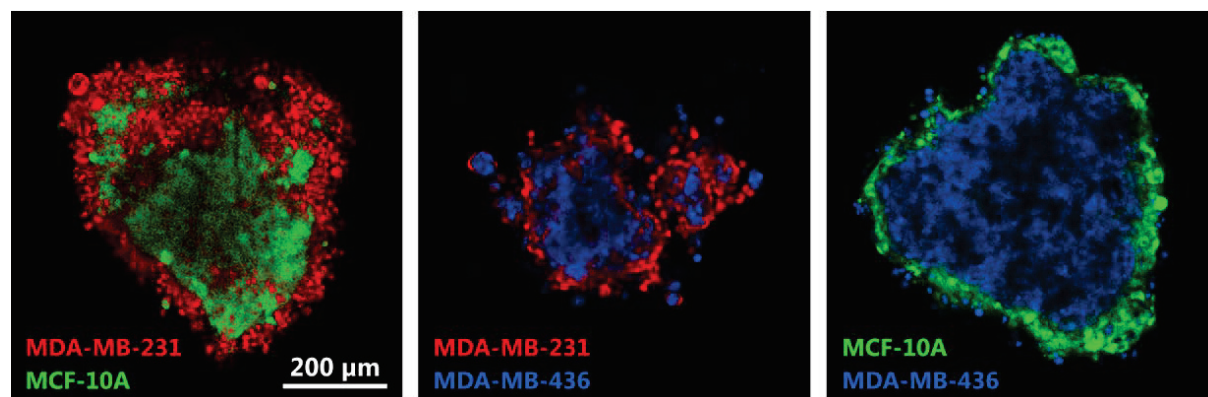
Figure 4.17: CLSM sections of 3D segregation experiments with the three mixing combinations of MCF-10A, MDA-MB-231 and MDA-MB-436 cell lines approximately 20 h after mixing. During the long-term observation, samples were maintained at 37°C in 5% CO_2 air atmosphere. The segregation into an inner core surrounded by an outer shell is clearly visible in all three mixtures: (a) MDA-MB-231 (red) encloses MCF-10A (green). (b) MDA-MB-231 (red) encloses MDA-MB-436 (blue). (c) MCF-10A (green) encloses MDA-MB-436 (blue). The scale bar applies to all images.

Furthermore, SILAC mass spectroscopy of these cell lines reveals significant differences in the proteome, especially parts and pathways of it associated with related cellular function and structures, i.e. adhesion, metabolism, cytoskeleton. SILAC analysis was able to intertwine tumour-associated proteins of cells with their found mechanical properties. We find that surface densities of adhesive molecules fail to correlate with measured cell - cell adhesion, but do correlate with cell shapes, cell stiffness and the rate at which cells sort, in accordance with an extended version of the differential adhesion hypothesis (DAH). SILAC mass spectroscopy reassembles and supports the

Criterion	TST Hierarchy
Cadherin Densities (STED)	10A > 436 > 231
Cell-Cell Adhesion (AFM)	231 > 10A > 436
Shape / Interfacial Tension	10A > 436 > 231
Segregation Experiments	436 > 10A > 231

Figure 4.18: Summary of the predictions for the tissue surface tension (TST) and therefore hierarchy of experimental data and proteomic data.

experimental findings on a proteomic level and bridges the gap from observable macro- and mesoscopic quantities, given above, down to molecular details of cells (figure 4.18). Surprisingly, the DAH does not correctly predict the final sorted state. This suggests that these tissues are not behaving as immiscible fluids, cells can be kinetically trapped and that dynamical effects such as directional motility, friction and jamming may play an important role in tissue compartmentalization across the epithelial - mesenchymal transition.

4.12   Advanced Thermorheology of Living Cells

E. Warmt, T. Kießling, S. Schmidt, J.A. Käs

Thermal alterations influence instantly biomechanical properties of living cells. This was published in 2013, showing that MCF-10A normal epithelial breast cells, behave thermorheological simple i.e. creep compliance curves superpose just by shifting the time axis [1]. Moreover, we published characteristic nuclear reshaping events at certain temperatures, influencing further cell deformability [2]. Additionally, we measured thermorheological behaviour of eight common cell types within physiologically relevant temperatures and applied thermorheological time-temperature superposition (TTS) to creep compliance curves. Our results showed that superposition is not a universal feature, and is only applicable in four of the eight investigated cell types [3]. For the other cell types, transitions of thermorheological responses around 36°C were observed. Even without a rigorous applicability of TTS to all cell types, the quality how creep curves superpose reveal valuable information about relaxation processes in response to mechanical load. For various cell lines, different thermorheological characteristics can be observed indicating differences in relevant load bearing structures. Now we focused on certain cytoskeletal structures and its influence on thermorheological cell response. With the help of various cytoskeletal drugs we strengthened or weakened the actin- and microtubule network. Preliminary data showed that superposition of creep compliance curves was easier for cells with disrupted cytoskeletal networks. This is intuitive, since cells loose particular rheological properties of individual structure filaments and behave more fluid like. The exact contribution of diverse cytoskeletal filaments to cell mechanical behaviour can be calculated by this model. So we are able to explain characteristic rheological cell response of certain cell lines due to particular cell assembly of these cell lines.
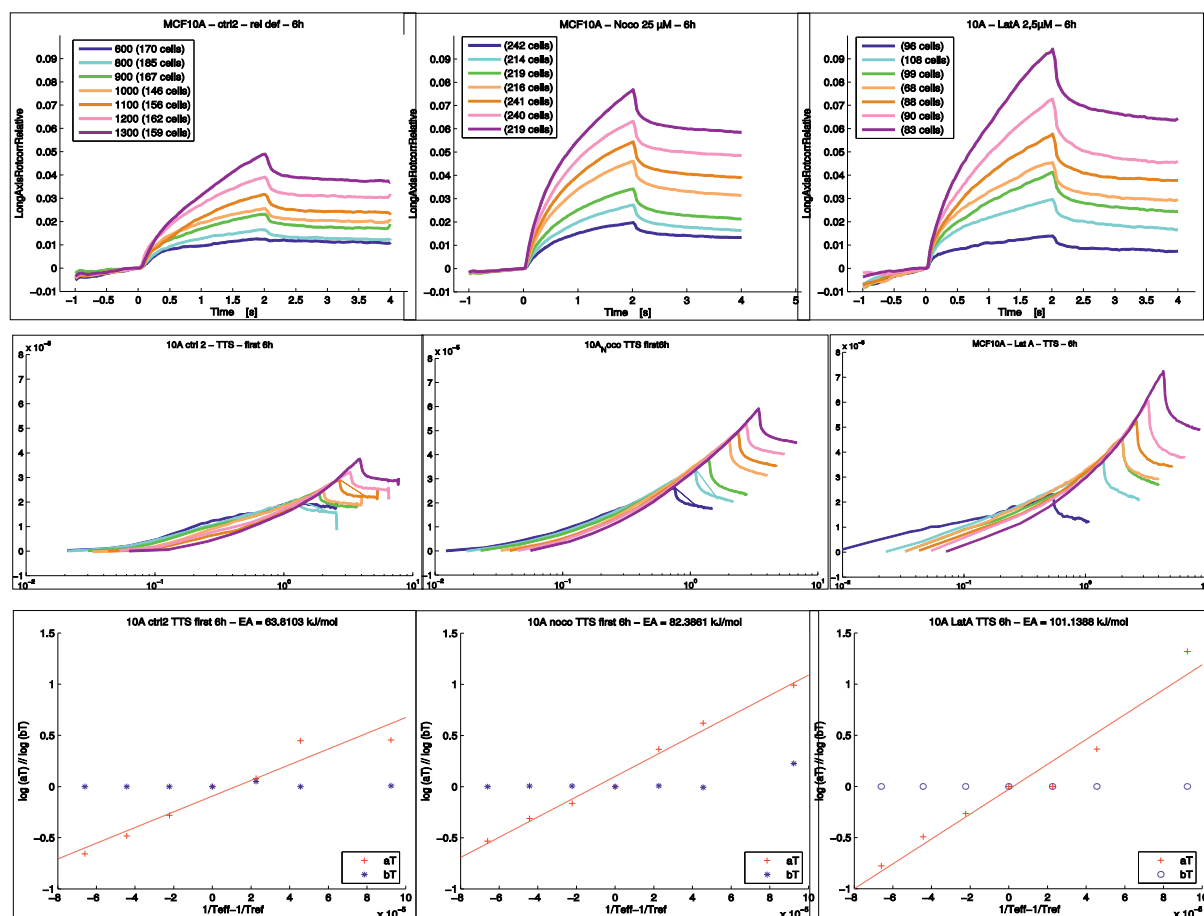
Figure 4.19: Top row: Relative Deformation of untreated (left) MCF10A cells and actin disrupted cytoskeletal networks. 25 μM Nocodazole (middle) was added for 6h and 2.5 μM Latrunculin A (right) as well for 6h. Middle row: Time-Temperature Superposition works better for cells which are treated by Nocodazole and Latrunculin A. Lower row. Arrhenius Plot of Time-Shift-Factors (red) and Modulus-Shift-Factors (blue). The fitted slop gives the Activation Energy.

[1] T. Kießling et al.: New Journal of Physics **2013** 15, 045026
[2] E. Warmt et al.: New Journal of Physics **2014** 16, 073009
[3] S. Schmidt et al.: New Journal of Physics **2015** 17, 073010

4.13 Micropatterning of reagent-free, high energy cross-linked gelatin hydrogels for bioapplications

A. Weidt, B. Heyart[*], E. Wisotzki[*], M. Zink, S.G. Mayr[*][†]

[*]Leibniz Institute for Surface Modification (IOM), Leipzig
[†]Division of Surface Physics, Felix Bloch Institute for Solid State Physics

The development of biocompatible materials for the regeneration of soft tissues is of high importance for medical applications. Materials such as collagen and gelatin show a great potential as graft materials and cell carriers, since they originate from

the extracellular matrix. An adequate structuring of hydrogels as cellular substrate is mandatory for successful cell adhesion. Here, a reagent-free method for crosslinking and subsequent micropatterning of gelatin hydrogels is demonstrated [1]. The simple and effective method of micromolding is applied to transfer structures in the μm range from a SiO_2 template during high energy electron irradiation to gelatin. Using electron irradiation, the mechanical properties of hydrogels can be tuned easily, since the number of crosslinks depends on the irradiation dose. In this way, thermally-stable substrates with well-defined storage moduli are fabricated and well conserved within 5 day storage under physiological conditions. The gel substrates exhibit a microstructure of grooves with widths of 3.75 to 170 μm and depths of several hundred nanometers, evaluated using 3D confocal microscopy. The microstructured hydrogels promote cell adhesion and contact guidance of NIH 3T3 mouse embryonic fibroblasts. Cells attach and adapt on the surfaces, and changes of the cell morphology are observed within 4 day culture in physiological conditions. The presented micropatterning technique can be adopted easily to other hydrogels giving rise to new trends in the field of tissue engineering.
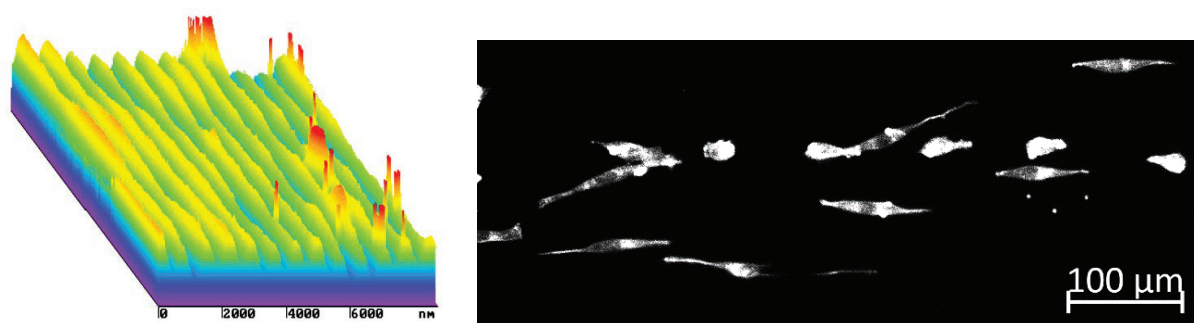
Figure 4.20: (left) Profile of 3.75 μm grooved microstructure on irradiation crosslinked gelatin hydrogels. Obtained using μsurf 3D confocal microscope. (right) NIH 3T3 fibroblasts on 40 kGy electron irradiated structured gelatin hydrogels with 3.75 μm wide grooves after 4 day incubation time. Captured with 10x magnification.

[1] B. Heyart et al.: J. of Biomedical Mat. Res. Part B: Appl. Biomaterials **2017** 00B

4.14 Employing nanostructured scaffolds for long-term adult tissue culture and investigation of tissue mechanics at the nanoscale

M. Zink, S. Rahman[*], A. Reichenbach[*], S.G. Mayr[†‡]

[*]Paul-Flechsig-Institut for Brain Research, Leipzig University
[†]Leibniz Institute for Surface Modification (IOM), Leipzig
[‡]Division of Surface Physics, Felix Bloch Institute for Solid State Physics

Tissue properties such as morphology, organization of cells and the extracellular matrix, as well as the distribution of mechanical properties can often only be accessed *ex vivo*. However, organotypic culture of adult tissues is still an unsolved task since tissue survival of adult fully differentiated tissues is limited to a few days *in vitro*. Here we show that TiO_2 nanotube scaffolds with tissue-specifically tailored characteristics can serve as ideal substrates for long-term cultures of different adult tissues with high viability for at least two weeks in contrast to tissue cultures on standard PTFE membranes [1]. Prerequisite for long-term tissue survival is an improved adhesion of the tissue to the underlying nanotube scaffold which strongly depend on the nanotube geometry in terms of tube diameter and surface roughness. Additionally, on the example of complex neural tissues such as the retina, we employ a self-designed mechanical spectroscopy setup and show that the nanotube scaffolds can be employed as vibrating reed to investigate the mechanical properties of tissue at the nanoscale, *viz.* protein level.
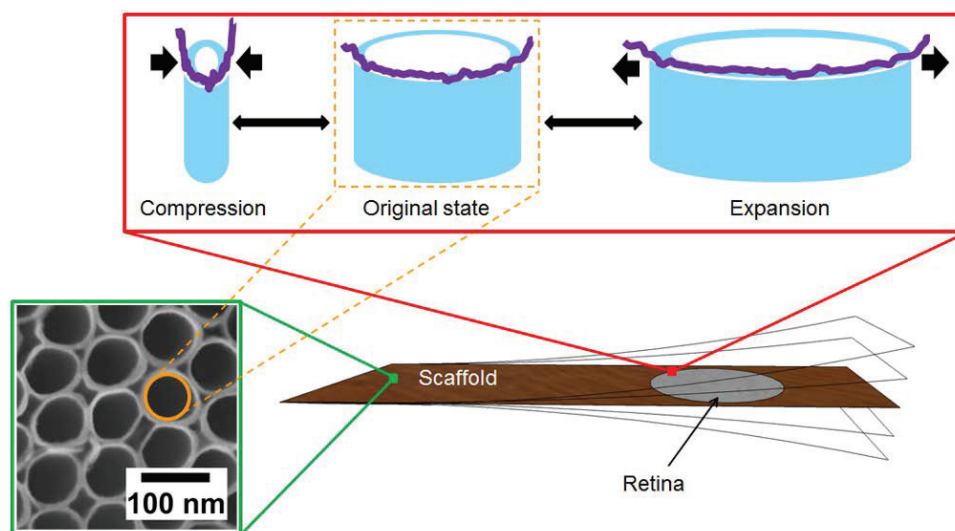
Figure 4.21: A nanotube scaffold with the retina on top is clamped at one end and excited to vibrate freely. During vibration the nanotubes are frequently compressed and stretched. Attached proteins at the nanotube-tissue interface are therefore deformed as well. Since the nanotubes have diameters similar to the attached proteins, intermolecular forces are probed during vibration. From the vibration frequency the elastic modulus of the retina can be determined.

Here the nanotube scaffold is clamped at one end and excited to perform free damped oscillations with the retina on top (fig. 4.21). The detected oscillation parameters represent a fingerprint of the frequency-dependent mechanical tissue properties

that are derived in combination with sandwich beam analysis and finite element calculations [2]. We found that the Young's modulus of the retina on the scale of 10 nm is of the order of a few GPa, much higher than values obtained on micrometer length scales. In our study, individual biopolymers and proteins on the photoreceptor side of the retina in contact with the nanostructured reed are stretched and compressed during vibration of the underlying scaffold and the acting intramolecular forces are probed at the protein level. We reveal that the Young's moduli of individual protein chains from serum - a major component of the used tissue culture medium - are about 16 times higher compared to the average modulus of the porous TiO_2 nanostructure when probed at the nanoscale (38 GPa vs. 2 GPa). In fact, computer simulations of various biomolecules already demonstrated polymer stiffnesses up to 200 GPa. Since pathology and many diseases are related to changes on molecular level, e.g. during cancer progression and remodeling of the extracellular matrix, our biotechnological approach offers new perspectives in studying the relation of tissue mechanics to tumor spreading and effect of medications.

[1] V. Dallacasagrande et al.: Adv. Mater. **2012** 2399-2403
[2] S. M. Rahman et al.: Soft Matter **2016** 12, 3431-3441

4.15   Funding

Organotypische Langzeitkultivierung von adultem Augengewebe zur Erforschung von Krankheiten und Wirkstoffen in vitro - EYECULTURE - TP 1
Dr. M. Zink
BMBF, 031A574A

4.16 Organizational Duties

Prof. J. A. Käs

- Senator der Universität Leipzig
- Member of the Organizing Committee: 7th Annual Symposium - Physics of Cancer, Leipzig, October 2016
  involved organizers: Prof. H. Herrmann (German Cancer Research Center), Dr. D. M. Smith (Fraunhofer Institute IZI)
- PWM Winterschool, Kleinwalsertal, A, March 2016
- Journal review: Nature, Science, Cell, Physical Review Letters, Biophysical Journal, Biophysica and Proceedings of the National Academy of Science, Langmuir, Angewandte Chemie, Nature Physics, Journal of Biophotonics, Cytoskeleton, Optics Express, New Journal of Physics
- Grant review: National Science Foundation, Div. of Materials Research; National Science Foundation, Div. of Cellular Organization; National Science Foundation, Div. of Computational Biology; National Science Foundation, Div. of Physics, Special Programs; Deutsche Forschungsgemeinschaft, Alexander von Humboldt Foundation, Deutsche Studienstiftung, Centre National de Recherche
- Fellow, American Physical Society
- Full Member, Saxonian Academy of Sciences

4.17 External Cooperations

Academic

- Syracuse University, USA
  Prof. M. E. Manning

- Syracuse University, USA
  Prof. M. C. Marchetti

- University of Maryland, USA
  Prof. W. Losert

- Albert Einstein College of Medicine, USA
  Prof. J. S. Condeelis

- King's College London, Biomedical Engineering Department, GB
  Prof. R. Sinkus

- Deutsche Gesellschaft für Zellbiologie (DGZ)
  Prof. Dr. H. Herrmann

- Max-Delbrück-Zentrum für molekulare Medizin
  Dr. M. Falcke

- Charité Berlin, MR Elastographie
  Prof. Dr. I. Sack

- Technische Universität Braunschweig, Zoologisches Institut
  Prof. Dr. K. Rottner

- Universität Leipzig, Klinik u. Poliklinik für Frauenheilkunde
  Prof. Dr. M. Höckel

- Universität Leipzig, Institut für Pathologie
  Prof. Dr. L.-C. Horn

- Universität Leipzig, Klinik u. Poliklinik f. Mund-, Kiefer- u. Plast. Gesichtschirurgie
  Dr. T. Remmerbach

- Universität Leipzig, Klinik u. Poliklinik f. Dermatologie, Venerologie u. Allergologie
  Prof. Dr. J. Simon

- Universität Leipzig,Translationszentrum für Regenerative Medizin
  Prof. Dr. T. Magin

- Universität Leipzig, Abteilung für Neuroradiologie
  Prof. Dr. K.-T. Hoffmann

- Universität Leipzig, Institut für Experimentelle Physik I
  Prof. Dr. C. Mierke

Industry

- RS Zelltechnik GmbH, Leipzig
  S. Rönicke, R. Stange

4.18   Publications

Journals

C. Schuldt, J. Schnauß, T. Händler, M. Glaser, J. Lorenz, T. Golde, J. A. Käs, D. M. Smith: *Tuning synthetic semiflexible networks by bending stiffness*. Phys. Rev. Lett., **117**,197801 (2016)

J. Schnauß, T. Händler, J. A. Käs: *Semiflexible biopolymers in bundled arrangement*. Polymers, **8**, 274 (2016)

M. Glaser, J. Schnauß, T. Tschirner, B. U. S. Schmidt, M. Moebius-Winkler, J. A. Käs, D. M. Smith: *Self-assembly of hierarchically ordered structures in DNA nanotube systems*. New Journal of Physics, **18**, 055001 (2016)

J. Schnauß, T. Golde, C. Schuldt, B. U. S. Schmidt, M. Glaser, D. Strehle, T. Händler, C. Heussinger, J. A. Käs: *Transition from a linear to a harmonic potential in collective dynamics of a multifilament actin bundle*, Phys. Rev. Let., **116**, 108102 (2016)

E. I. Wisotzki, R. P. Friedrich, A. Weidt, C. Alexiou, S. G. Mayr, M. Zink: *Cellular response to reagent-free electron-irradiated gelatin hydrogels*. Macromolecular Biosc., **16**, 914-924 (2016)

S. M. Rahman, A. Reichenbach, M. Zink, S. G. Mayr: *Mechanical spectroscopy of retina explants at the protein level employing nanostructured scaffolds*. Soft Matter, **12**, 3431-3441 (2016)

Talks

J. A. Käs: *Why Do Rigid Tumours Contain Soft Cancer Cells?* Institute for Bioengineering of Catalonia (IBEC)-Seminar, Barcelona, Spain, February 2016

J. A. Käs: *Multicellular Streaming in Solid Tumors*. International Symposium (SFB 755, SFB 803, SFB 937): "Biological Dynamics from Microscopic to Mesoscopic Scales", Nimbschen Abbey Grimma, February 2016

T. Golde, J. Schnauß, C. Schuldt, M. Glaser, S. Schmidt, T. Händler, C. Heussinger, J. A. Käs: *Actin bundle contractions without molecular motors*. "Physics of Development and Disease", Aspen, USA, March 2016

S. G. Mayr, M. Zink: *Intelligente Metalle und schaltbare Gummibärchen: Entwicklung neuartiger Materialien für die Medizin*. MNU Bundeskongress (Verband zur Förderung des MINT-Unterrichts), Leipzig, March 2016 (invited talk)

M. Zink: *Cell-Surface Interactions: From Protein Adsorption to Tissue Mechanics*. Fakultät für Naturwissenschaften, Universität Magdeburg, March 2016 (invited talk)

S. Pawlizak, A. W. Fritsch, S. Grosser, L. Oswald, D. Ahrens, T. Thalheim, M. L. Manning, J. A. Käs: *Cell sorting in breast cancer cell lines: Driven by differential adhesion?* PWM Winter School Kleinwalsertal, A, March 2016

J. Lippoldt, T. Möhn, J. A. Käs: *Flicker spectroscopy and the effect of cholesterol on cell membranes*. PWM Winter School Kleinwalsertal, A, March 2016

E. Warmt, S. Schmidt, T. Kießling, J. A. Käs: *Complex thermorheology of living cells*. PWM Winter School Kleinwalsertal, A, March 2016

E. W. Morawetz, L.-C. Horn, M. Höckel, J. A. Käs: *Correlation of Adhesive and Viscoelastic Tumor Markers*. PWM Winter School Kleinwalsertal, A, March 2016

J. A. Käs: *Multicellular Streaming in Solid Tumors*. DPG Spring Meeting, Regensburg, March 2016 (invited talk)

L. Oswald, S. Grosser, S. Pawlizak, A. W. Fritsch, J. A. Käs: *Liquid-like and solid-like behaviour of breast cancer cell lines in 3D aggregates*. DPG Spring Meeting, Regensburg, March 2016

S. Pawlizak, A. W. Fritsch, S. Grosser, L. Oswald, D. Ahrens, T. Thalheim, M. L. Manning, J. A. Käs: *Cell sorting in breast cancer cell lines: Driven by differential adhesion?* DPG Spring Meeting, Regensburg, March 2016

J. Schnauß: *Mechanically tunable actin networks using programmable DNA based cross-linkers*. APS Meeting, Baltimore, USA, March 2016

T. Händler, M. Glaser, T. Golde, C. Schuldt, J. Schnauß, D. M. Smith, J. A. Käs: *Mesh size of semiflexible polymer networks*. Annual conference BuildMona, Leipzig, March 2016

T. Händler, M. Glaser, T. Golde, C. Schuldt, J. Schnauß, D. M. Smith, J. A. Käs: *Mesh size of DNA networks*. Workshop: "DNA Mitteldeutschland", Jena, May 2016

J. A. Käs: *Why Do Rigid Tumors Contain Soft Cancer Cells?* Meeting: "Active and Smart Matter: A New Frontier for Science and Engineering", Syracuse, USA, June 2016 (invited talk)

A. Weidt, S. G. Mayr, M. Zink: *Organization of Proteins and Cells on Microstructured Metal Surfaces*. Soft Matter Day, Leipzig, June 2016

J. Schnauß: *Rheology of DNA and Actin Networks*. Soft Matter Day, Leipzig, June 2016

L. Oswald, S. Grosser, S. Pawlizak, A. W. Fritsch, J. A. Käs: *Fluidity and Jamming in Solid Tumours*. Soft Matter Day, Leipzig, June 2016

M. Zink, S. G. Mayr: Mechanical Spectroscopy at the protein level employing nano-structured scaffolds. Materials Sciences and Engineering (MSE) Congress, Darmstadt, September 2016

J. A. Käs: *Why Do Rigid Tumors Contain Soft Cancer Cells?* Workshop: "Nanoscale Matter - Novel Concepts and Functions" (LMU Munich), Venice, Italy, September 2016 (invited talk)

J. A. Käs: *Self-Organization and Pattern Formation in Carcinomas and their Microenvironment*. 630th Heraeus Seminar: "Patterns in Nature - Functions, Variations and Control", Bayreuth, October 2016 (invited talk)

E. W. Morawetz, L.-C. Horn, M. Höckel, J. A. Käs: *E-Cadherin Expression and Localization is Correlated to Cellular Softness in Cancer*. TIFR Centre for Interdisciplinary Sciences, Hyderabad, India, October 2016

H. Kubitschke, S. Grosser, L. Oswald, S. Pawlizak, A. W. Fritsch, J. A. Käs: *Differential Adhesion Hypothesis Revised: Is there Experimental and Proteomic Evidence?* NCBS-TIFR, Bangalore, India, October 2016

E. W. Morawetz, L.-C. Horn, M. Höckel, J. A. Käs: *E-Cadherin Expression and Localization is Correlated to Cellular Softness in Cancer*. NCBS-TIFR, Bangalore, India, October 2016

H. Kubitschke, S. Grosser, L. Oswald, S. Pawlizak, A. W. Fritsch, J. A. Käs: *Differential Adhesion Hypothesis Revised: Is there Experimental and Proteomic Evidence?* TIFR Centre for Interdisciplinary Sciences, Hyderabad, India, October 2016

J. Schnauß: *Programming the Mechanical Properties of Bionic Networks*. 7th Annual Symposium - Physics of Cancer, Leipzig, October 2016

J. A. Käs: *Why Do Rigid Tumors Contain Soft Cancer Cells?* 7th Annual Symposium - Physics of Cancer, Leipzig, October 2016

M. Zink: *Employing Nanostructured Scaffolds for Long-Term Adult Tissue Culture and Investigation of Tissue Mechanics at the Nanoscale.* 7th Annual Symposium - Physics of Cancer, Leipzig, October 2016

J. A. Käs: *Self-Organization and Pattern Formation in Carcinomas and their Microenvironment.* Seminar, Centre de Recherche, Paris, France, December 2016 (invited talk)

M. Zink: *Cell-Surface Interactions: From Protein Adsorption to Tissue Mechanics.* Fachbereich Chemie und Physik der Materialien, Universität Salzburg, December 2016 (invited talk)

M. Zink, U. Allenstein, S. G. Mayr: *Contractile cell forces deform macroscopic cantilevers and quantify biomaterial performance.* Materials Research Society Meeting, Boston, USA, December 2016

M. Zink, S. G. Mayr: *Mechanical Spectroscopy at the protein level employing nanostructured scaffolds.* Materials Research Society Meeting, Boston, USA, December 2016

Posters

E. W. Morawetz, L.-C. Horn, M. Höckel, J. A. Käs: *Correlation of Adhesive and Viscoelastic Tumor Markers.* DPG Spring Meeting, Regensburg, March 2016

E. Warmt, S. Schmidt, T. Kießling, J. A. Käs: *Complex thermorheology of living cells.* DPG Spring Meeting, Regensburg, March 2016

T. Händler, M. Glaser, T. Golde, C. Schuldt, J. Schnauß, J. A. Käs, D. M. Smith: *Mesh size of DNA nanotube networks.* DNA Nanotechnology, Jena, May 2016

S. Grosser, L. Oswald, S. Pawlizak, A. W. Fritsch, J. A. Käs: *Fluidity and Jamming in 3D Aggregates of Breast Cancer Cell Lines.* Soft Matter Day, Leipzig, June 2016

F. Sauer, S. Grosser, S. Puder, E. Morawetz, J. A. Käs, C. T. Mierke: *Influence of ECM constitution on cell migration in tuneable collagen matrices.* Soft Matter Day, Leipzig, June 2016

P. Heine, S. Grosser, J. Lippoldt, L. Oswald, J. A. Käs: *Cellular jamming, invasive behavior and streaming in cancerous and non-cancerous cell layers.* Soft Matter Day, Leipzig, June 2016

T. Händler, M. Glaser, T. Golde, C. Schuldt, J. Schnauß, D. M. Smith, J. A. Käs: *Reptation in semiflexible polymer networks.* Soft Matter Day, Leipzig, June 2016

J. Lippoldt, C. Händel, J. Schiller, T. Möhn, T. Kießling, S. Schmidt, L.-C. Horn, S. Briest, M. Höckel, J. A. Käs: *Plasma membrane softening in cancer cells.* Soft Matter Day, Leipzig, June 2016

P. Hietschold, U. Allenstein, J. A. Käs, S. G. Mayr, M. Zink: *Measurements of Contractile Cell Forces with a Bending Cantilever Setup.* Soft Matter Day, Leipzig, June 2016

E. Warmt, T. Kießling, S. Schmidt, J. A. Käs: *Advanced thermorheology of living cells.* Physics of Living Matter 11th Edition, Cambridge, UK, September 2016

H. Kubitschke, S. Grosser, L. Oswald, S. Pawlizak, A. W. Fritsch, J. A. Käs: *Proteomic Details of Differential Adhesion Hypothesis.* "Mechanobiology of Diseases", Singapore, September 2016

E. W. Morawetz, L.-C. Horn, M. Höckel, J. A. Käs: *E-Cadherin Expression and Localization is Correlated to Cellular Softness in Cancer Development.* "Mechanobiology of Diseases", Singapore, September 2016

T. Golde, M. Glaser, T. Händler, C. Schuldt, J. Schnauß, H. Herrmann, J. A. Käs: *Composite networks of actin and intermediate filaments.* 7th Annual Symposium - Physics of Cancer, Leipzig, October 2016

L. Oswald, S. Grosser, J. Lippoldt, S. Pawlizak, A. W. Fritsch, J. A. Käs: *Cellular jamming in 3D cancer aggregates.* 7th Annual Symposium - Physics of Cancer, Leipzig, October 2016

J. Lippoldt, S. Grosser, L. Oswald, P. Heine, J. A. Käs: *Connecting Cell Jamming with Adhesion, Contractility and Cell Stiffness.* 7th Annual Symposium - Physics of Cancer, Leipzig, October 2016

T. Händler, M. Glaser, T. Golde, C. Schuldt, J. Schnauß, D. M. Smith, J. A. Käs: *Reptation in semiflexible polymer networks.* 7th Annual Symposium - Physics of Cancer, Leipzig, October 2016

E. Warmt, S. Schmidt, T. Kießling, J. A. Käs: *Complex thermorheology of living cells.* 7th Annual Symposium - Physics of Cancer, Leipzig, October 2016

L. Oswald, S. Grosser, J. Lippoldt, S. Pawlizak, A. W. Fritsch, J. A. Käs: *Cellular jamming in 3D cancer aggregates.* BBZ/iDiv Poster Session, Leipzig, December 2016

J. Lippoldt, S. Grosser, L. Oswald, P. Heine, J. A. Käs: *Connecting Cell Jamming with Adhesion, Contractility and Cell Stiffness.* BBZ/iDiv Poster Session, Leipzig, December 2016

P. Hietschold, K. Bela, K. Juncheed, A. Weidt, S. M. Rahman, E. Wisotzki, M. Zink: *Junior Research Group Biotechnology and Biomedicine - From Cell Adhesion to Tissue Mechanics.* Dies Academicus Universität Leipzig, December 2016

E. Warmt, E. W. Morawetz, S. Grosser, J. A. Käs: *Myosin activity in epithelial and mesenchymal cells.* Dies Academicus Universität Leipzig, December 2016

4.19 Graduations

Doctorate

- Uta Allenstein
  Interfacing Living Cells and Fe-Pd Ferromagnetic Shape Memory Alloys: Experiments and Modeling on Different Functionalization Strategies
  29.02.2016

- Chris Händel
  Fluctuations and Oscillations in Cell Membranes
  21.03.2016

- Saddam Moyazur Rahman
  Employing a novel mechanical spectroscopy method to investigate elasticity of the retina
  24.11.2016

5

Biological Physics

5.1 Introduction

Cellular Biophysics in the Field of Cancer Research Most cancer-related deaths during the malginant cancer progression are caused by the ability of cancer cells to metastasize. The process of metastasis follows a linear propagation of several steps. It starts with the spreading of cancer cells from the primary tumor, which then migrate into the local tumor microenvironment. The cancer cells can transmigrate into blood or lymph vessels (intravasation), get transported through the vessel flow, adhere to the endothelial cell lining, grow and form a secondary tumor directly inside the vessel or the cancer cells possibly transmigrate through the endothelial vessel lining (extravasation) into the extracellular matrix of connective tissue. After this step, the cancer cells migrate further into the targeted tissue (possibly another organ), grow and form a secondary tumor (i.e. the tumor metastasizes). Despite of all current findings based on biochemistry and even the novel approaches based on genomics and proteomics cancer research did not fundamentally change cancer death rates, but still improved clinical diagnosis substantially in the field of cancer research regarding the classification and detailed staging of tumors, numerous marker proteins and mapping of specific human cancer-types. Thus, a main criticism to these methods is that the expression levels of numerous genes and molecules, which are differently regulated during cancer progression, depend on the cancer disease stage. In particular, it is still not fully understood how they regulate cancer progression. A reason may be that these genomic and proteomic based methods do not account for the localization of the molecules in special compartments such as lipid rafts, their activation or assembly state, their life-time, turn-over-, modification- and recycling rate. Thus, we and others propose that the biomechanical properties are crucial for the efficiency and speed of cancer cell invasion and subsequently, for metastases formation. In more detail, classical physical approaches will be adopted to complex soft matter such as cancer cells and novel biophysical methods will be developed in order to adopt them to cancer research. These novel physical approaches have so far changed or will still alter the direction of recent cancer research. Moreover, even the role of the endothelium during the transmigration and invasion of cells is not clear, it has been seen as passive barrier, but this could not explain all novel findings as our finding that this endothelial layer of vessels can enhance the invasiveness of cancer cells. Thus, we will investigate how cancer cells alter the structural, biochemical and mechanical properties of the endothelium to regulate their own invasiveness through

extracellular matrices and hence, through the tissue microenvironment. Moreover, we will investigate how the mechanical properties of cancer cells regulate the functional properties such as cancer cell invasion and transendothelial migration. Finally, our research will shed light on the mechanical properties of cancer cells and the interacting endothelium and will point out the importance of the mechanical properties as a critical determinant for the efficiency of cancer cell invasion and the overall progression of cancer. In conclusion, we suggest that the regulation of the endothelial cells biomechanical properties by cancer cells and the mechanical properties of cancer cells are a critical determinants of cancer cell invasiveness and may affect the future development of new cancer treatments.

Claudia Mierke

5.2   Integrin-linked kinase regulates cellular mechanics facilitating the motility in 3D extracellular matrices

T. Kunschmann, S. Puder, T. Fischer, J. Perez, N. Wilharm, C.T. Mierke,

The motility of cells plays an important role for many processes such as wound healing and malignant progression of cancer. The efficiency of cell motility is affected by the microenvironment. The connection between the cell and its microenvironment is facilitated by cell-matrix adhesion receptors and upon their activation focal adhesion proteins such as integrin-linked kinase (ILK) are recruited to sites of focal adhesion formation. In particular, ILK connects cell-matrix receptors to the actomyosin cytoskeleton. However, ILK's role in cell mechanics regulating cellular motility in 3D collagen matrices is still not well understood. We suggest that ILK facilitates 3D motility by regulating cellular mechanical properties such as stiffness and force transmission. Thus, ILK wild-type and knock-out cells are analyzed for their ability to migrate on 2D substrates serving as control and in dense 3D extracellular matrices. Indeed, ILK wild-type cells migrated faster on 2D substrates and migrated more numerous and deeper in 3D matrices. Hence, we analyzed cellular deformability, Young's modulus (stiffness) and adhesion forces. We found that ILK wild-type cells are less deformable (stiffer) and produce higher cell-matrix adhesion forces compared to ILK knock-out cells. Finally, ILK is essential for providing cellular mechanical stiffness regulating 3D motility.

5.3   Funding

Blebbing Driven or Actin Protrusive-Force Driven Cancer Cell Migration
Prof. C. T. Mierke
DFG

5.4   Organizational Duties

Prof. C. T. Mierke

- Referee: Cancer Research, Journal of Cell Science, Advanced Biomaterials, Acta Biomaterials, British Journal of Cancer, Journal of Pharmacy and Pharmacology, Molecular Vision, International Journal of Nanomedicine, Plos One, Eur. J. Biophysics
- Special Issue Guest Editor for Physical Biology

5.5 External Cooperations

Academic

- Imperial College London, Department of Materials, London, UK
  Prof. Dr.-Ing. habil. Aldo R. Boccaccini

- Netherlands Cancer Institute Amsterdam, Netherlands
  Dr. Arnoud Sonnenberg

- University of Regensburg, Institute for Molecular and Cellular Anatomy, Regensburg, Germany
  Prof. Dr. Ralph Witzgall

- Philipps-University Marburg, Department of Neurosurgery, Germany
  Prof. Dr. J. W. Bartsch

- Department of Paediatric Kidney, Hannover medical School, Germany
  Prof. Dr. Hermann Haffner , Dr. rer. nat. Wolfgang Ziegler

- University of Bonn, Institute of Genetics Actin Dynamics and Motility Unit, Germany
  Prof. Dr. Klemens Rottner

- University of Leipzig, Translational Center for Regenerative Medicine, Germany
  Prof. Dr. Thomas Magin

- University of Leipzig, Center for Biotechnology and Biomedicine (BBZ), Germany
  Prof. Dr. A. Robitzki

5.6 Publications

Journals

T. Kunschmann, S. Puder, T. Fischer, J. Perez, N. Wilharm, C. T. Mierke:*Integrin-linked kinase regulates cellular mechanics facilitating the motility in 3D extracellular matrices*, doi:10.1016/ j.bbamcr.2016.12.019

II

Institute for Experimental Physics II

6

Magnetic Resonance of Complex Quantum Solids

6.1   Introduction

The electronic properties of quantum-solids in which the electrons exhibit strong correlations with each other or with the lattice are particularly rich and will be of special importance in future functional materials. In addition, such solids are challenging for experiment, as well as theory, as the more than twenty five-year history of high-temperature superconductivity shows: we still do not understand the electronic structure of these systems. One particular aspect of strongly correlated electronic materials is their tendency towards nano-scale electronic phase separation. Even in perfect lattices, electronic nano-structures can form. The investigation of such materials requires the use of methods that can give detailed information. Here, magnetic resonance, on nuclei and electrons, is of particular interest as they not only have atomic scale resolution, but also yield bulk information in contrast to surface techniques. We explore the properties of these materials with tailored new techniques at the frontiers of magnetic resonance. For example, we are the leading laboratory when it comes to NMR at highest pressures and magnetic fields.

Jürgen Haase

6.2   NMR shift and relaxation measurements in pulsed high-field magnets up to 58 T

J. Kohlrautz, S. Reichardt, E.L. Green[*], H. Kühne[*], J. Wosnitza[*], J. Haase

[*]Dresden High Magnetic Field laboratory, Helmholtz-Zentrum Dresden-Rossendorf, Dresden, Germany

Nuclear magnetic resonance (NMR) experiments at fields up to 58 T in pulsed magnets at the Dresden High Magnetic Field Laboratory are reported. The challenge to resolve NMR shifts in these timedependent fields is addressed for the first time, and it is shown that this can indeed be accomplished with high precision with an internal reference. As a result, signal averaging is possible during a single magnetic field pulse, but also for

multiple pulses. Thus, even very weak signals can in principle be recorded and their shifts can be determined. In a second set of experiments, the measurement of nuclear relaxation is investigated. Using adiabatic inversion with the inherent time dependence of the magnetic field and small-angle inspection, it is shown that relaxation measurements are possible, as well. The shift experiments were performed with ^{27}Al NMR on a mixture of aluminum metal and a Linde type A zeolite. For the relaxation studies, ^{27}Al NMR and ^{69}Ga NMR on the metals aluminum and gallium were preformed, respectively.

6.3 Field-stepped broadband NMR in pulsed magnets and application to SrCu$_2$(BO$_3$)$_2$ at 54 T

J. Kohlrautz, J. Haase, E.L. Green[*], Z.T. Zhang[*], J. Wosnitza[*], T. Herrmannsdörfer[*], H.A. Dabkowska[†], B.D. Gaulin[†], R. Stern[‡], H. Kühne[*]

[*]Dresden High Magnetic Field laboratory, Helmholtz-Zentrum Dresden-Rossendorf, Dresden, Germany

[†]Brockhouse Institute for Materials Research and Department of Physics and Astronomy, McMaster University, Canada

[‡]National Institute of Chemical Physics and Biophysics, Tallinn, Estonia

Pulsed magnets generate the highest magnetic fields as brief transients during which the observation of NMR is difficult, however, this is the only route to unique insight into material properties up to the regime of 100 T. Here, it is shown how rather broad NMR spectra can be assembled in a pulsed magnet during a single field pulse by using the inherent time dependence of the field for the recording of fieldstepped free induction decays that cover a broad frequency range (Fig. 6.1). The technique is then applied to ^{11}B NMR of the spin-dimer system SrCu$_2$(BO$_3$)$_2$, a magnetic insulator known to undergo a series of fielddriven changes of the magnetic ground state. At peak fields of about 54 T at the Dresden High Magnetic Field Laboratory, ^{11}B NMR spectra spanning a total of about 9 MHz width are reconstructed. The results are in good accordance with a change from a high-temperature paramagnetic state to a low-temperature commensurate superstructure of field-induced spin-dimer triplets.

6.4 Perspective on the phase diagram of cuprate high-temperature superconductors

D. Rybicki[*], M. Jurkutat, S. Reichard, C. Kapusta[*], J. Haase

[*]AGH University of Science and Technology, Faculty of Physics and Applied Computer Science, Krakow, Poland

Universal scaling laws can guide the understanding of new phenomena, and for cuprate high-temperature superconductivity the influential Uemura relation showed, early on, that the maximum critical temperature of superconductivity correlates with the density of the superfluid measured at low temperatures. Here we show that the charge content
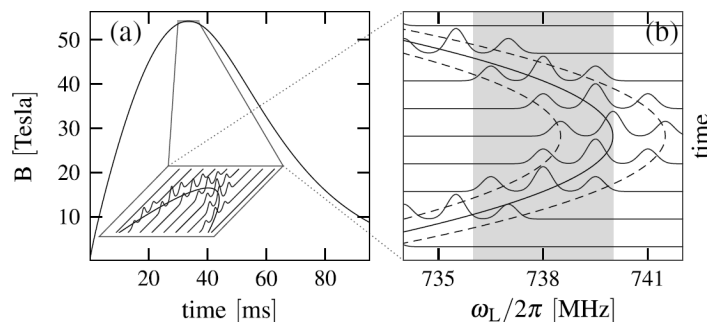
Figure 6.1: NMR in a pulsed magnet (schematic). Only near the field maximum is the time-dependence weak enough for signal observation, but the Larmor precession is still time-dependent. (a) Typical field pulse and ^{11}B spectra with three lines (spin 3/2). (b) Blow-up of spectra. As a result of the time-dependence, different parts of each spectrum can be within the bandwidth of the experiment (gray area).

of the bonding orbitals of copper and oxygen in the ubiquitous CuO_2 plane, measured with nuclear magnetic resonance, reproduces this scaling. The charge transfer of the nominal copper hole to planar oxygen sets the maximum critical temperature. A three-dimensional phase diagram in terms of the charge content at copper as well as oxygen is introduced, which has the different cuprate families sorted with respect to their maximum critical temperature. We suggest that the critical temperature could be raised substantially if one were able to synthesize materials that lead to an increased planar oxygen hole content at the expense of that of planar copper.

6.5   Charge Variations in Cuprate Superconductors from Nuclear Magnetic Resonance

S. Reichardt, M. Jurkutat, A. Erb[*], J. Haase

[*]Walther Meissner Institute for Low Temperature Research, Garching, Germany

Charge inhomogeneities in the cuprates were reported early on and have been in the focus of much research recently. Nuclear magnetic resonance (NMR) is very sensitive to local charge symmetry through the electric quadrupole interaction that must detect any static charge density variation. Recent experiments in high magnetic fields that seem to induce charge density waves in some systems have rekindled the interest in static inhomogeneities. It has long been known that excessive NMR linewidths can be observed in all cuprates, but with the exception of a few materials. However, the relation of the quadrupolar linewidths with respect to variations of the charge density in the cuprates is not understood. Here, we investigate $YBa_2Cu_3O_7$ and we find even in a moderate magnetic field that below about 200 K, i.e., well above T_c, a temperature dependent NMR linewidth appears that must be related to incipient static charge density variations. We argue that this establishes field induced charge density variation as a more general phenomenon in the cuprates (see Fig. 6.2). In view of the very recent understanding of the relation between the hole distribution in the CuO_2

plane and T_c, it is argued that charge density variations are ubiquitous, but appear not related to the maximum T_c.
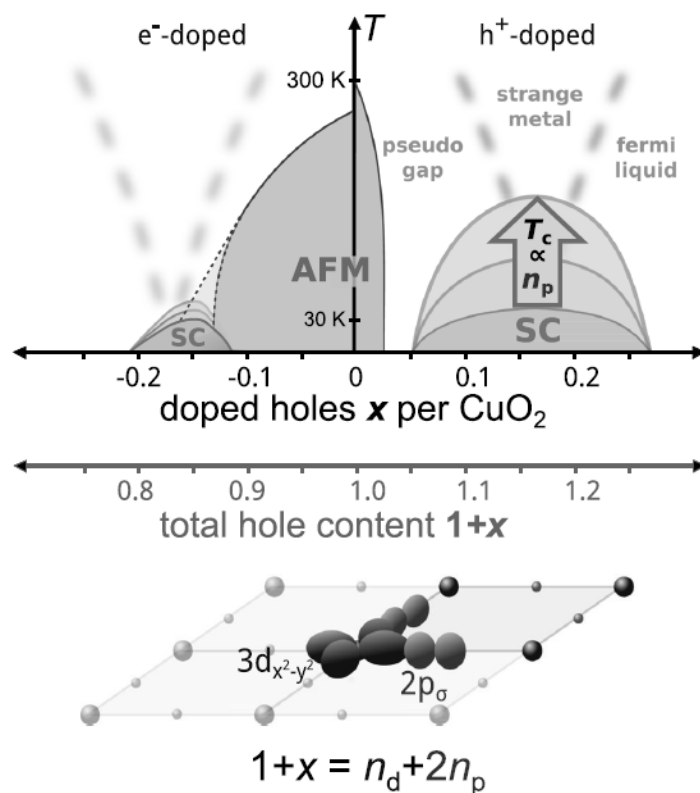
Figure 6.2: Electronic phase diagram of the cuprates with doped holes (x) as well as total planar hole content (1 + x) as abscissa. The inherent hole of the CuO_2 plane is shared differently among the bonding orbitals Cu $3d_{x^2-y^2}$ (n_d) and O $2p_\sigma$ (n_p) in different cuprate families, i.e., with $1 = n_d + 2n_p$, and doping adds or removes additional holes such that $1 + x = n_d + 2n_p$. It is found that the maximum critical temperature $T_{c,max}$ can be increased by a larger oxygen hole content n_p. Other cuprate phases, e.g. pseudogap phase, might show clear trends in this local picture as well.

6.6 ^{77}Se nuclear magnetic resonance of topological insulator Bi$_2$Se$_3$

N.M. Georgieva, D. Rybicki[*], R. Guehne, G.V.M. Williams[†], S.V. Chong[‡], K. Kadowaki[§], I. Garate[¶], J. Haase

[*]AGH University of Science and Technology, Faculty of Physics and Applied Computer Science, Krakow, Poland
[†]School of Chemical and Physical Sciences, Victoria University of Wellington, Wellington, New Zealand
[‡]Robinson Research Institute, Victoria University of Wellington, Lower Hutt, New Zealand
[§]Faculty of Pure and Applied Sciences, University of Tsukuba, Tsubuka, Japan

¶Départment de Physique and Regroupement Québécois sure les Matériaux de Pointe, Université de Sherbrooke, Sherbrooke, Canada

Topological insulators constitute a new class of materials with an energy gap in the bulk and peculiar metallic states on the surface. We report on new features resulting from the bulk electronic structure, based on a comprehensive nuclear magnetic resonance (NMR) study of ^{77}Se on Bi_2Se_3 and $Cu_{0.15}Bi_2Se_3$ single crystals. First, we find two resonance lines and show that they originate from the two inequivalent Se lattice sites. Second, we observe unusual field-independent linewidths and attribute them to an unexpectedly strong internuclear coupling mediated by bulk electrons. In order to support this interpretation, we present a model calculation of the indirect internuclear coupling and show that the Bloembergen-Rowland coupling is much stronger than the Ruderman-Kittel-Kasuya-Yosida coupling. Our results call for a revision of earlier NMR studies and add information concerning the bulk electronic properties.
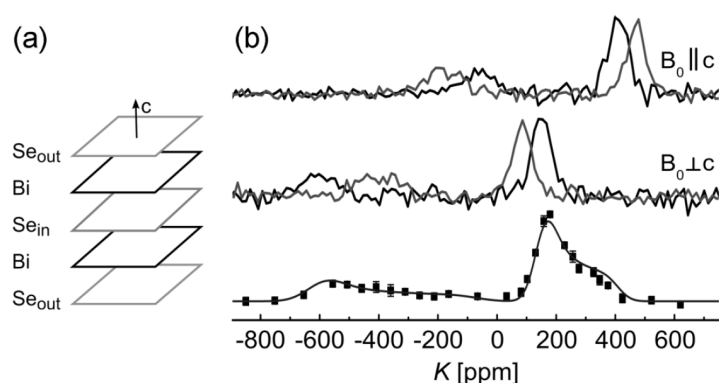
Figure 6.3: (a) Sketch of the quintuple layer. (b) ^{77}Se NMR spectra at $B_0 = 17.6$ T and room temperature of Bi_2Se_3 (black) and $Cu_{0.15}Bi_2Se_3$ (red) single crystals for two crystal orientations (top two), and of Bi_2Se_3 powder (squares) with simulation based on single crystal data (solid blue line). Shifts (K) are given with respect to $(CH_3)_2Se$.

6.7   The relation of structural mobility and water sorption of soil organic matter studied by ^{1}H and ^{13}C solid-state NMR

A. Jäger, M. Bertmer, G.E. Schaumann[*]

[*]University Koblenz-Landau, Institute for Environmental Sciences, Landau, Germany

The impact of low water contents on the molecular mobility of soil organic matter (SOM) and its most frequent components was investigated. Combined ^{1}H, ^{2}H, and ^{13}C solid-state nuclear magnetic resonance (NMR) techniques allow for an advanced insight into mechanisms of water uptake under defined atmospheres and its effect on SOMsegment mobility. The major individual organic components of two peats, a gleyic podsol and a number ofmodel substances (cutin, suberin,wood and cellulose) were

distinguishedwith respect to their contribution to the ^{1}H and ^{13}C NMR spectra. Water molecules and mobile polymer constituents of SOMcontribute to the mobile fraction in ^{1}H NMRwide line spectra. Poly(methylene), being most probably part of amphiphilic molecules, have been identified as SOMcomponents that are mobilized in the presence ofwater. Even though being of hydrophobic nature, water acts as a plasticizer on such long chain aliphatic soil components. Differential scanning calorimetry measurements of SOM samples support this insight in terms of a thermal step transition. Based on our findings, comparison of experimental results from different soils with varying water contents and soil composition should consider mobility effects of both, aliphatic moieties as well as polar moieties of SOM.

6.8 Physical long-term regeneration dynamics of soil organic matter as followed by ^{1}H solid-state NMR methods

A. Jäger, J. Schwarz[*], Y. KunhiMouvenchery[*], G.E. Schaumann[*], M. Bertmer

[*]University Koblenz-Landau, Institute for Environmental Sciences, Landau, Germany

^{1}H wide-line solid-state NMR methods have been applied to monitor long-term mobility changes in the supramolecular network of soil organic matter and water induced by short thermal treatment.NMRline widths are a direct measure of the mobility of water molecules and organic matter components. For the first time, we obtained an insight into the long-term physical mechanisms in terms of molecular mobility governing soil organic matter-water interactions. All time series reveal a systematic, attenuated proton demobilisation on time scales with a maximum of 1 year that depends on water content and type of soil. Results are discussed in the context of water molecule bridges and are compared with the results of structural transition temperatures obtained from differential scanning calorimetry measurements. The analysis is based on a porous system with random field characteristics. Two major features, a logarithmic time dependence in the first hours and a linear time dependence at longer times after the heating event, are observed in all investigated samples. In peat samples, a temporary increase of mobility was observed, the point in time depending on water content. The soil organic matter physicochemical matrix aging mechanism could also be relevant for the aging of organic chemicals in soil samples, suggesting a long-term reduction in molecular mobility.

6.9 Transport properties of hierarchical micro-mesoporous materials

D. Schneider, D. Mehlhorn, P. Zeigermann, J. Kärger, R. Valiullin

Adding mesopore networks in microporous materials using the principles of hierarchical structure design is recognized as a promising route for eliminating their transport

limitations and, therefore, for improving their value in technological applications. Depending on the routes of physico-chemical procedures or post-synthesis treatments used, very different geometries of the intentionally-added transport mesopores can be obtained. Understanding the structure-dynamics relationships in these complex materials with multiple porosities under different thermodynamical conditions remains a challenging task. In this review, we summarize the results obtained so far on experimental and theoretical studies of diffusion in micromesoporous materials. By considering four common classes of bi-porous materials, which are differing by the inter-connectivities of their sup-spaces as one of the most important parameter determining the transport rates, we discuss their generic transport properties and correlate the results delivered by the equilibrium and non-equilibrium techniques of diffusion measurements.

6.10 Linear Chains of Magnetic Ions Stacked with Variable Distance: Ferromagnetic Ordering with a Curie Temperature above 20 K

S. Friedländer, J. Liu[*], M. Addicoat[†], P. Petkov[†], N. Vankova[†], R. Rüger[†], A. Kuc[†], W. Guo[‡], W. Zhou[‡], B. Lukose[†], Z. Wang[‡], P.G. Weidler[‡], A. Pöppl, M. Ziese[§], T. Heine[†], C. Wöll[‡]

[*]Institute of Artificial Photosynthesis, Dalian University of Technology, Dalian, China
[†]Wilhelm-Ostwald-Institute of Physical and Theoretical Chemistry, Leipzig, Germany
[‡]Karlsruhe Institute of Technology, Germany
[§]Physics and Earth Sciences, Leipzig University, Leipzig, Germany

We have studied the magnetic properties of the SURMOF-2 series of metal-organic frameworks (MOFs). Contrary to bulk MOF-2 crystals, where Cu^{2+} ions form paddlewheels and are antiferromagnetically coupled, in this case the Cu^{2+} ions are connected via carboxylate groups in a zipper-like fashion. This unusual coupling of the spin 1=2 ions within the resulting one-dimensional chains is found to stabilize a low-temperature, ferromagnetic (FM) phase. In contrast to other ordered 1D systems, no strong magnetic fields are needed to induce the ferromagnetism. The magnetic coupling constants describing the interaction between the individual metal ions have been determined in SQUID experiments. They are fully consistent with the results of ab initio DFT electronic structure calculations. The theoretical results allow the unusual magnetic behavior of this exotic, yet easy-to-fabricate, material to be described in a detailed fashion.

6.11 EPR Insights into Switchable and Rigid Derivatives of the Metal-Organic Framework DUT-8(Ni) by NO Adsorption

M. Mendt, F. Gutt, N. Kavoosi[*], V. Bon[*], I. Senkovska[*], S. Kaskel[*], A. Pöppl

*Department of Inorganic Chemistry, Technical University Dresden, Germany

The metal-organic framework (MOF) DUT-8(Ni) (DUT = Dresden University of Technology) shows a structural transformation from a nonporous to a porous phase during the adsorption of gases. A rigid derivative of this material has recently been synthesized, where this 'gate pressure like' flexibility is completely absent. This rigid derivative of DUT-8(Ni) always stays in the porous phase even in the absence of any adsorbate. This motivates the present investigation of the adsorption of nitric oxide (NO) on the flexible and rigid forms of DUT-8(Ni) by continuous wave electron paramagnetic resonance (EPR) spectroscopy at X-band frequency. The EPR signal of desorbed NO is measured at moderate temperatures and the decrease of its intensity indicates the adsorption of this gas within the porous phase of DUT-8(Ni) at low temperatures. An adsorption and desorption related hysteresis loop of the intensity of this signal is observed for the flexible but not for the rigid DUT-8(Ni). This difference might reflect the difference in the flexibility of both materials. Furthermore, EPR signals with electron spin $S = 1/2$ are measured, which can likely be attributed to Ni^{2+}-NO adsorption complexes at defective paddle wheel units within the porous phase of DUT-8(Ni) with the unpaired electron sitting at the Ni^{2+} ion. The order of their g-tensor principle values allows a distinct characterization of the ligand environment of these ions. Defects for which the EPR signals indicate that at least one NDC (2,6-naphthalenedicarboxylate) ligand molecule does not coordinate to the paddle wheel are only observed for the rigid but not for the flexible DUT-8(Ni). In addition, the density of defective paddle wheel units with only one Ni^{2+} ion or a missing dabco (1,4-diazabicyclo[2.2.2]octane) ligand is indicated to be 1 order of magnitude larger in the rigid than in the flexible derivative of this MOF. The observed differences in the presence and amount of distinct defects might be related to the difference in the flexibility of both forms of the investigated material.

6.12   Diffusion in complementary pore spaces

D. Mehlhorn, D. Kondrashova, C. Küster[*], D. Enke[*], T. Emmerich[†], A. Bunde[†], R. Valiullin, J. Kärger

*Institute of Chemical Technology, University of Leipzig, Leipzig, Germany
†Institute of Theoretical Physics, University of Gießen, Gießen, Germany

The rate of mass transfer is among the key numbers determining the efficiency of nanoporous materials in their use for matter upgrading by heterogeneous catalysis or mass separation. Transport enhancement by pore space optimization is, correspondingly, among the main strategies of efficiency promotion. Any such activity involves probing and testing of the appropriate routes of material synthesis and post-synthesis modification just as the exploration of the transport characteristics of the generated material. Modelling and molecular simulation is known to serve as a most helpful tool for correlating these two types of activities and their results. The present paper reports about a concerted research activity comprising these three types of activities. Recent progress in producing pore space replicas enabled focusing, in these studies, on 'complementary' pore spaces, i.e. on pairs of material, where the pore space of one sample did just coincide with the solid space of the other. We report about the correlations

in mass transfer as observable, in this type of material, by pulsed field gradient NMR diffusion studies, with reference to the prediction as resulting from a quite general, theoretical treatment of mass transfer in complementary pore spaces.

6.13 Eu^{2+}-Containing Luminescent Perovskite-Type Hydrides Studied by Electron Paramagnetic Resonance

N. Kunkel[*], R. Böttcher, T. Pilling, H. Kohlmann[†], A. Pöppl

[*]PSL Research University, Chimie Paris Tech-CNRS, Paris, France
[†]Inorganic Chemistry, University of Leipzig, Leipzig, Germany

Metal hydrides exhibit interesting properties as hosts for Eu(II) containing luminescent compounds due to the nephelauxetic effect and the strong ligand field of the hydride anion. In order to elucidate the lattice site symmetry of europium dopants, Q-band and X-band electron paramagnetic resonance (EPR) spectra were collected on LiMH$_3$: Eu^{2+} and LiMD$_3$: Eu^{2+} (M=Sr, Ba) powders with europium concentrations between 0.0037 and 0.27 mol %. They show well resolved hyperfine splitting in the central part of the spectra due to magnetic electron spin-nuclear spin coupling of ^{151}Eu and ^{153}Eu, and are in good agreement with simulated spectra based upon cubic site symmetry. Spin Hamiltonian parameters were extracted by spectral analysis and are reported. Low intensity rhombic spectra contributions could be assigned to small amounts of MH$_2$: Eu^{2+} or the respective deuterides as impurities in the samples. The results of this EPR investigation and size considerations suggest that europium is divalent and occupies the alkaline earthmetal (M) positions in LiMH$_3$: Eu^{2+} and LiMD$_3$: Eu^{2+} (M=Sr, Ba).

6.14 Funding

Deuterium-Festkörper-NMR und ^1H MAS PFG NMR-Untersuchungen der Beweglichkeit des Wirtsgerüsts und der Gastmoleküle in nanoporösen Materialien
Prof. Dr. Jürgen Haase
DFG, HA 1893/16-1

EPR spectroscopy of paramagnetic centers and adsorption complexes in porous metal organic frameworks: Development and application of dielectric resonators and microresonators for investigations of small single crystals
Prof. Dr. Andreas Pöppl
DFG

MOFs as carrier for nitric oxide delivery in biological systems - microscopic fundamentals of adsoprtion and controlled release studied by infrared and electron and nuclear spin resonance spectroscopy
PD Dr. Marko Bertmer, Prof. Dr. Andreas Pöppl, Prof. Dr. Martin Hartmann, Prof. Dr. Michael Fröba
DFG, BE 2434/4-2, PO 426/8-2

Charakterisierung der [2+2]-Photodimerisierung von photoaktiven Substanzen auf der Basis von Zimtsäure eingebaut in Polymeren oder in supramolekularen Strukturen mit Festkörper-NMR-Spektroskopie
PD Dr. Marko Bertmer
DFG, BE 2434/2-3

Structure and Transport Characterization of Hierarchical Porous Solids
PD Dr. Rustem Valiullin
DFG

6.15 Organizational Duties

Professor Dr. Jürgen Haase
- Dean of the Faculty
- Vice Director of the Magnetic Resonance Center Leipzig
- Board Member of the Heisenberg Gesellschaft e. V.
- Full Member of the Saxonian Academy of Sciences in Leipzig
- Member of the German Physical Society
- Member of the American Physical Society
- Member of the 'ICAM Board of Goveners' of the Institute for Complex Adaptive Matter
- Referee: Physical Review, Science, IOP, German-Israeli Foundation for Scientific Research and Developement

Prof. Dr. Andreas Pöppl
- Referee: Journal of Magnetic Resonance, Journal of the American Chemical Society, Physical Chemistry Chemical Physics, Chemical Physics Letters
- Project Reviewer: German-Israeli Foundation for Scientific Research and Development

PD Dr. Marko Bertmer
- Referee: Angewandte Chemie, Chemistry of Materials, Journal of Physical Chemistry, Solid State Nuclear Magnetic Resonance

PD Dr. Rustem Valiullin
- Member of the German Physical Society
- Scientific Advisory Board of the AMPERe Bologna Conference Magnetic Resonance in Porous Media
- Chairman of the IUPAC task group Diffusion in nanoporous solids
- Editorial Boards Diffusion Fundamentals, Dataset Papers in Physical Chemistry, Fluids
- Referee: Physical Review, RSC, ACS, Elsevier

Prof. Dr. Dieter Michel
- Full Member of the Saxonian Academy of Sciences in Leipzig
- Member of the German Physical Society
- Member of the Society of German Chemists
- German Coordinator of the German-Russian Centre 'Applied and Computational Physics (ACOPhys)' at the St. Petersburg State University
- Member at the International Advisory Committee of the International Meeting of Ferroelectricity
- Member at the International Advisory Committee of the European Meeting of Ferroelectricity
- Member at the International Advisory Committee of the Conference 'NMR of Condensed Matter St. Petersburg'
- Member of the German-Israeli Foundation for Scientific Research and Developement
- Referee: Physical Review, Journal of Physics: Condensed Matter, Langmuir, Journal of Magnetic Resonance, Phys. Stat. Sol., Materials Chemistry and Physics, German-Israeli Foundation for Scientific Research and Developement

Prof. Dr. Rolf Böttcher
- Referee: Physical Review, Journal of Physics: Condensed Matter, Langmuir, Journal of Magnetic Resonance

6.16   External Cooperations

Academic

- Technical University Munich, Physics Department, Crystal Lab, Garching, Germany
  Prof. Dr. Andreas Erb

- Cavendish Laboratory, Cambridge, UK
  S. K. Goh, P. Alireza

- Washington University, St. Louis, MO, USA
  J. Schilling, M. Conradi

- Victoria University, Physics Department,Wellington, New Zealand
  Dr. Grant V. M.Williams

- Helmholtz-Zentrum Dresden-Rossendorf, Dresden, Germany
  Prof. Dr. J. Wosnitza

- University of Minnesota, School of Physics and Astronomy, USA
  Prof. Dr. M. Greven

- University of Illinois at Urbana-Champaign, Department of Physics, USA
  Prof. Dr. C. P. Slichter

- Laboratoire National des Champs Magnétiques Pulsès, Toulouse, France
  Prof. Dr. G. Rikken

- University of New South Wales, School of Physics, Sydney, Australia
  Prof. Dr. O. Sushkov

- Washington University, Department of Chemistry, St. Louis, MO, USA
  Sophia E. Hayes

- Universität Koblenz-Landau, Abteilung Chemie, Landau, Germany
  Prof. Dr. Gabriele Schaumann

- Martin-Luther-Universität Halle-Wittenberg, Halle, Germany
  Dr. H. T. Langhammer

- Kazan State University, Tartastan, Russian Federation
  Prof. Dr. E. N. Kalabukhova

- Universität Erlangen-Nürnberg, Erlangen Catalysis Resource Center - ECRC, Erlangen, Germany
  Prof. Dr. Martin Hartmann

- Université du Maine, Laboratoire de Physique de l'Etat Condenseé, Le Mans, France
  Prof. Dr. A. Kassiba

- University of Vilnius, Faculty of Physics, Vilnius, Lithuania
  Prof. Dr. J. Banys

- Argonne National Laboratory, Illinois, USA
  Prof. Dr. P. Littlewood

- Georgetown University Department of Chemistry, Washington, DC, USA
  Prof. Dr. YuYe Tong

- Max Planck Institute of Solid State Research, Stuttgart, Germany
  Prof. Dr. B. Keimer

- University of Illinois at Chicago, USA
  Prof. Dr. D. K. Morr

- IFW-Dresden, Dresden, Germany
  M. Richter, H. Eschrig

- Ruhr-University Bochum, Bochum, Germany
  R. A. Fischer

- University of Massachusetts, MA, USA
  Prof. P. Monson

- University of Giessen, Germany
  Prof. A. Bunde

Industry

- NMR-Service GmbH, Erfurt, Germany
  M. Braun

- Bruker BioSpin GmbH, Rheinstetten, Germany
  F. Engelke

- Quantachrome Ins., Boyton-Beach, FL, USA
  M. Thommes

6.17 Publications

Journals

J. Kohlrautz, S. Reichardt, E.L Green, H. Kühne, J. Wosnitza, J. Haase
NMR shift and relaxation measurements in pulsed high-field magnets up to 58 Tesla
J. Magn. Reson. **263** (2016) 1-6.

A. V. Uskov, D. Yu. Nefedov, E. V. Charnaya, J. Haase, D. Michel, Yu. A. Kumzerov, A. V. Fokin, A. S. Bugaev
Polymorphism of metallic sodium under nanoconfinement
Nano Letters **16** (2016) 791-794.

D. Rybicki, M. Jurkutat, S. Reichardt, C. Kapusta, J. Haase
Perspective on the Phase Diagram of Cuprate High-Temperature Superconductors
Nature Comm. **7** (2016) 11413.

C. Kropf, J. Kohlrautz, J. Haase, B. Fine
Anomalous longitudinal relaxation of nuclear spins in CaF_2
Fortschr. Phys. (2016) 1-5.

N.M. Georgieva, D. Rybicki, R. Gühne, G.V.M. Williams, S.V. Chong, I. Garate, J. Haase
^{77}Se nuclear magnetic resonance of topological insulator Bi_2Se_3
Phys. Rev. B **93** (2016) 195120.

J. Kohlrautz, J. Haase, E.L Green, Z.T Zhang, J. Wosnitza, T. Herrmannsdörfer, H.A Dabkowska, B.D Gaulin, R. Stern, H. Kühne
Field-stepped broadband NMR in pulsed magnets and application to $SrCu_2(BO_3)_2$ at 54 T
J. Magn. Reson. **271** (2016) 52-59.

S. Reichardt, M. Jurkutat, A. Erb, J. Haase
Charge Variations in Cuprate Superconductors from Nuclear Magnetic Resonance
J. Supercond. Nov. Magn. **29** (2016) 3017-3022.

D. I. Kolokolov, S. S. Arzumanov, D. Freude, J. Haase, A. G. Stepanov
Mobility of Stable π-Complexes of Ethylene with Ag^+ Cations in Ag/H-ZSM-5 Zeolite: A ^{2}H Solid-State NMR Study
J. Phys. Chem. C **120** (2016) 4993-5000.

A.E Khudozhitkov, H. Jobic, D. Freude, J. Haase, D. Kolokolov, A.G Stepanov
Ultra-Slow Dynamics of Framework Linker in MIL-53 (Al) as a Sensor for Different
Isomers of Xylene
J. Phys. Chem. C **120** (2016) 21704-21709.

N. Kunkel, R. Böttcher, T. Pilling, H. Kohlmann, A. Pöppl
Eu^{2+}-Containing Luminescent Perovskite-Type Hydrides Studied by Electron Para-
magnetic Resonance
Z. Phys. Chem. **230** (2016) 931-942.

M. Mendt, F. Gutt, N. Kavoosi, V. Bon, I. Senkovska, S. Kaskel, A. Pöppl
EPR Insights into Switchable and Rigid Derivatives of the Metal-Organic Framework
DUT-8(Ni) by NO Adsorption
J. Phys. Chem. C, **120** (2016), 14246-14259.

S. Friedländer, J. Liu, M. Addicoat, P. Petkov, N. Vankova, R. Rüger, A. Kuc, W. Guo,
W. Zhou, B. Lukose, Z. Wang, P. G. Weidler, A. Pöppl, M. Ziese, T. Heine, C. Wöll
Linear Chains of Magnetic Ions Stacked with Variable Distance: Ferromagnetic Order-
ing with a Curie Temperature above 20 K
Angew. Chem. Int. Ed. **55** (2016) 12683-12687.

S. Friedländer, J. Liu, M. Addicoat, P. Petkov, N. Vankova, R. Rüger, A. Kuc, W. Guo,
W. Zhou, B. Lukose, Z. Wang, P. G. Weidler, A. Pöppl, M. Ziese, T. Heine, C. Wöll
Mit variablem Abstand gestapelte lineare Ketten magnetischer Ionen
Angew. Chem. **128** (2016) 12874-12879.

M. Šimėnas, A. Ciupa, M. Mączka, G. Völkel, A. Pöppl, J. Banys
EPR of Structural Phase Transition in Manganese- and Copper-Doped Formate Frame-
work of $[NH_3(CH_2)_4NH_3][Zn(HCOO)_3]_2$
J. Phys. Chem. C **120** (2016) 19751-19758.

S. Friedländer, P. St. Petkov, F. Bolling, A. Kultaeva, W. Böhlmann, O. Ovchar, A. G.
Belous, T. Heine, A. Pöppl
Continuous-Wave Single-Crystal Electron Paramagnetic Resonance of Adsorption of
Gases to Cupric Ions in the Zn(II)-Doped Porous Coordination Polymer $Cu_{2.965}Zn_{0.035}(btc)_2$
J. Phys. Chem. C **120** (2016) 27399-27411.

M. Bertmer
Paramagnetic solid-state NMR of materials
Solid State Nucl. Magn. Reson. **81** (2016) 1-7.

Danijela Vojta, Martina Vrankic, Marko Bertmer, Gabriele E. Schaumann
Dehydration of α-oxalic acid dihydrate: Structural, spectroscopic and thermal study
with implications on the disruption of water molecular bridges in soil organic matter
Thermochim. Acta **643** (2016) 73-82.

Alexander Jaeger, Marko Bertmer, Gabriele E. Schaumann
The relation of structural mobility and water sorption of soil organic matter studied by
^{1}H and ^{13}C solid-state NMR
Geoderma **284** (2016) 144-151.

S. Kaufhold, G. Houben, J. Dietel, M. Bertmer, R. Dohrmann
Characterization of aluminum phosphate nanoparticles formed in a water well
J. Nanopart. Res. **18** (2016) 1-11.

Alexander Jäger, Jette Schwarz, Yamuna Kunhi Mouvenchery, Gabriele E. Schaumann, Marko Bertmer
Physical long-term regeneration dynamics of soil organic matter as followed by ^{1}H solid-state NMR methods
Environ. Chem. **13** (2016) 50-57.

D. Mehlhorn, D. Kondrashova, C. Küster, D. Enke, T. Emmerich, A. Bunde, R. Valiullin, J. Kärger
Diffusion in complementary pore spaces
Adsorption **22** (2016) 879-890.

D. Schneider, D. Mehlhorn, P. Zeigermann, J. Kärger, R. Valiullin
Transport properties of hierarchical micro-mesoporous materials
Chem. Soc. Rev. **45** (12) (2016) 3439-3467.

Books

M. Mendt, M. Simenas, A. Pöppl
Electron Paramagnetic Resonance; in 'The Chemistry of Metal-Organic Frameworks, Synthesis, Characterization, and Applications'
Volume 2, Ed. S. Kaskel; Wiley-VCH Verlag GmbH & Co, Weinheim, (2016), ISBN 978-3-527-33874-0, pp 629-565.

in press

Frank Bauer, Saskia Czihal, Marko Bertmer, Ulrich Decker, Sergej Naumov, Susan Wassersleben, Dirk Enke
Water-based functionalization of mesoporous siliceous materials, Part 1: Morphology and stability of grafted 3-aminopropyltriethoxysilane
Microp. Mesop. Mater.

D. Kondrashova, A. Lauerer, D. Mehlhorn, H. Jobic, A. Feldhoff, M. Thommes, D. Chakraborty, C. Gommes, J. Zecevic, P. de Jongh, A. Bunde, J. Kärger, R. Valiullin, R. Scale-dependent diffusion anisotropy in nanoporous silicon, Sci. Rep.

Talks

Jürgen Haase
Raumtemperatur-Supraleitung in den Kupraten? Klare Vorgaben fÃ¼r die Chemie mittels NMR
AC Kolloquium, München, April 2016

Michael Jurkutat
New Perspective on the Cuprate Phase Diagram and the charge distribution in the copper-oxygen plane

Superstripes 2016
Ischia, Italy, June 23-28, 2016

Seungtaik Hwang
Infrared Microimaging on Mixed Matrix Membrames (MMMs)
M4CO2 consortium meeting, Sofia, Bulgaria, December 5-6, 2016

Jürgen Haase
Multiple Electronic Components in Cuprate High-Temperature Superconductors from NMR
International Workshop, Ugo Fano Symposium, Rome, December 2016

Robin Guehne
NMR Study of Bismuth based 3D Topological Insulators
APPC-AIP Congress, Brisbane, Australia, December 2016.

Posters

Michael Jurkutat
Charge-resolved electronic phase diagram and maximum T_c of cuprate superconductors
Strong Correlations and the Normal State of the High Temperature Superconductors
MPI-PKS Dresden, Germany, May 17-27, 2016

Seungtaik Hwang
Structural characterisation of hierarchically porous silica monolith by probing the intrapore diffusion of nitrobenzene at low temperatures by means of NMR
13th International Bologna Conference on Magnetic Resonance in Porous Media (MRPM13)
Bologna, Italy, September 4-8, 2016

Seungtaik Hwang
Characterizing diffusion of guest molecules in MOF with narrow windows
5th International Conference on Metal-Organic Frameworks & Open Framework Compounds (MOF 2016)
Long Beach, California, USA, September 11-15, 2016

Anastasiia Kultaeva
EPR spectroscopy of isomorphous Metal Organic Frameworks single crystals and powders with rtl-topology
X EFEPR Conference Torino 2016

Stefan Friedländer
Continuous Wave Single Crystal Electron Paramagnetic Resonance of Cupric Ions in the Zn(II) Doped Porous Coordination Polymer $CU_{2.965}Zn_{0.035}(btc)_2$
X EFEPR Conference Torino 2016

Robin Guehne
NMR Study of Topological Insulating Bi_2Se_3, Bi_2Te_3, and Bi_2Te_2Se Single Crystals
MI/DWC/ACES Student/Postdoc symposium, Queenstown, New Zealand, June 2016.

Marufa Zahan
Influence of cation & halogen types on photoreaction of cinnamate salts studied by solid-state NMR
EUROMAR 2016, Aarhus, Denmark, July 3-7, 2016

Arafat Khan
Nitric Oxide adsorption in MIL-100(Al) MOF studied by solid-state NMR
EUROMAR 2016, Aarhus, Denmark, July 3-7, 2016

6.18   Graduations

Doctorate

- Thomas Meier

Master

- Felix Höfer
  NMR an topologischen Isolatoren (Bi_2Se_3)
  24.03.2016

- Felix Bolling
  Einkristall-EPR mit dielektrischen Resonatoren von Cu^{2+}-Ionen im MOF-Netzwerk [(Cu/Zn)$_2$(btc)$_3$]n
  Graduation Date

Bachelor

- Felix Gutt
  Untersuchung der Adsorption von NO auf ein nicht flexibles Derivat der metallorganischen Verbindung DUT-8(Ni) mittels cw ESR Spektroskopie
  Graduation Date

6.19   Guests

- Prof. Dr. Nail Fatkullin
  Kazan Federal University/Russia
  15.02.-16.02.2016

- Dr. Richard Reznicek
  Univerzita Karlova v Praze/Czech Republic
  07.03.-09.03.2016

- Sergey Sokratiin
  St. Petersburg State University/Russia
  09.03.-09.04.2016

- Prof. Dr. Nail Fatkullin
  Kazan Federal University/Russia
  10.03.-11.03.2016

- Jun.-Prof. Dr. Jens Anders
  Universität Ulm/Germany
  11.04.-12.04.2016

- Andrei Uskov
  St. Petersburg State University/Russia
  09.06.-02.07.2016

- Dr. Vladimir Ivanshin
  Kazan Federal University/Russia
  16.09.-15.12.2016

- Anastasia Antonenko
  St. Petersburg State University/Russia
  12.09.-12.11.2016

- Denis Yurievich Nefedov
  St. Petersburg State University/Russia
  24.10.2016-20.01.2017

- Timur Biktagirov
  Kazan Federal University/Russia
  05.12.-06.12.2016

7

Nuclear Solid State Physics

7.1 Introduction

Single ion implantation, e.g. through a pierced tip, has been done more or less routinely in our group since several years and leads in a large number of projects, cooperation and papers. However, the fabrication of a quantum register based on array of single atoms in a solid is more challenging. Due to the statistical nature of ion beams, the highest probability to obtain exactly one ion in a "one-shot" implantation is limited to only 37 % as given by Poisson statistics. Building a row of only 10 atoms, by chance, is therefore already very improbable since only one of 21000 of such devices ($0.37^{10} = 0.000048$) will indeed be constituted of 10 atoms, at the right places, without doubles or missing atoms, and therefore work properly. Consequently, the fabrication of a solid-state-based quantum computer with 100 or more qubits will only be possible, when each implanted ion can be detected and counted — an approach called deterministic ion implantation. A new patent mirror charge detector is actually under development to fulfill the task of deterministic ion implantation. This system is set-up in a common "joint lab" together with the Leibniz Institute of Surface Modification (IOM). In addition, we report about a new approach how graphite formed in diamond by ion beam irradiation and describe a new model about hyperpolarization of ^{13}C using NV centres in diamond. We found that a complex 4 spin interaction including the P1 centre is necessary to explain the experimental results. Additionally, we found that usual scanning electron microscopes (SEM) are able to perform implantation of N to produce very shallow NV centres. This invention is very surprising, because SEMs are already known since 1937.

Jan Meijer

7.2 Image charge detection for ion implantation

P. Räcke[*†], D. Spemann[†‡], J.W. Gerlach[†‡], B. Rauschenbach[†‡], J. Meijer[*†]

[*]Division of Nuclear Solid State Physics
[†]Leibniz Joint Lab "Single Ion Implantation", Leipzig
[‡]Leibniz Institute of Surface Modification e.V., Leipzig

In the Leibniz Joint Lab "Single Ion Implantation" we have continued building the new set-up for high precision ion implantation. The Ga liquid metal ion source was removed from a Raith ionLINE focused ion beam system and replaced with an electron beam ion source (EBIS). This enables a great variety of elements to be ionised to high charge states and accelerated. Furthermore, all structural changes are now incorporated, including the section for the image charge detector to be installed. It is planned to achieve a beam spot resolution in the nanometre range, and to implant deterministically, by counting single ions with the principle of image charge detection.

Simultaneously, a separate new set-up has been realised to be able to measure image charge signals from a large number of moving charges. For the deterministic ion implanter, sensitivity of the detector down to a single elementary charge is necessary. Before this can be realised, theoretical and practical limitations of the signal amplification and analysis process need to be evaluated. Bunches of singly charged ions appear as objects with several thousand charges. Their image charge signal can be recorded through state of the art room temperature pre-amplifier technology.

The set-up is shown in Fig. 7.1. The ion gun ionises gas (e.g. Ar) with electrons and
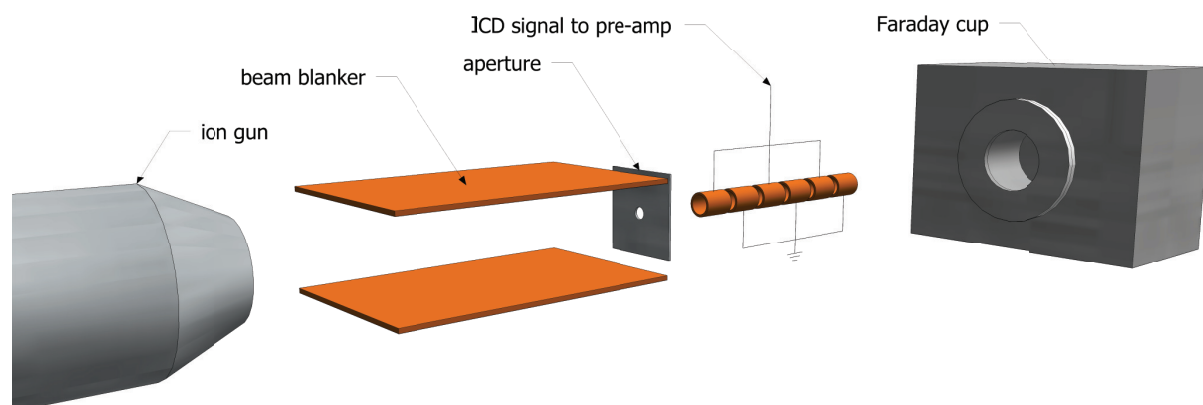
Figure 7.1: Schematic of the set-up to test the image charge detection principle and evaluate amplifier electronics.

accelerates with a potential difference of $(1-5)\,\text{kV}$. Scanning the beam over the aperture with the beam blanker, bunches of ions are sent through the image charge detector (ICD) pick-up tubes. The number of ions per bunch can be calibrated by measuring the continuous beam current in the Faraday cup. Preliminary results verify that the detection of the image charge signal is effectively a non-destructive measurement of the time of flight and the number of ions per bunch.

7.3 Investigation of the graphitisation process of ion-beam irradiated diamond using ellipsometry

T. Lühmann, R. Wunderlich, R. Schmidt-Grund[*], J. Barzola-Quiquia[†], P. Esquinazi[†], M. Grundmann[*], J. Meijer

[*]Division of Semiconductor Physics
[†]Division of Superconductivity and Magnetism

Diamond and graphite are allotropes of carbon. Graphite is characterised by sp^2-hybridised bonds, it is electrically conductive, mechanically soft and optically highly absorbent. In contrast, diamond exhibits sp^3-hybridised bonds and it is the hardest natural material, chemically inert, has a wide band gap and is consequently optically transparent over a wide spectral range. Graphite is the stable phase of carbon and diamond is formed under extreme conditions. The complete or local transformation from one allotrope to the other is possible. On the one hand, if several sp^3 bonds are cracked by an input of energy, like laser beam or particle irradiation, diamond is transformed to disordered graphite-like diamond and, following temperature annealing process, transformed to graphite. On the other hand graphite undergoes a transformation to diamond at high pressure and high temperature. The two different bonding configurations of carbon are separated by a potential barrier, which is correlated to the critical energy density $E_c = D_c \nu / X$ [1], where D_c is the critical fluence for the diamond-graphitisation, ν is the deposited energy per ion and X is the depth of the implanted ions. Different mixtures between sp^3- and sp^2-hybrid bonds are possible depending on the defect concentration. This leads to a large number of miscellaneous materials like thermally evaporated carbon [2], glassy carbon [3] and amorphous diamond [4], since mixing the two bond types and crystallinity result in different physical and chemical properties of these materials.

One possibility to induce local defects in diamond is ion beam irradiation. Controlling the energy loss of the ion beam via the ion mass or the kinetic energy and the ion fluence allows to form 3D structures inside the diamond by focusing the ion beam accordingly. The defect concentration and thus the degree of graphitisation can be controlled by the fluence of irradiation. At very high fluence a nearly complete transformation of non conductive diamond into a conductive graphite-like diamond phase [5] is possible [6–9]. This has been used to structure diamond samples, since the highly graphitised phase can be etched easily [6–10].

As a simple model, the graphitisation process can be described by the creation of sp^2-spheres inside a sp^3-matrix [1]. But so far, details of the real structure as well as the evolving macroscopic physical properties have not been studied thoroughly. In this work, we investigate buried thin film structures in diamond produced by focused He^+-ion beam irradiation. By modelling their optical response using the Bruggeman effective-medium-approximation-model (EMA) [11], in combination with Raman investigations, we were able to determine some structural properties by optical means. The determined structural parameters and the observed 3D variable-range hopping-mechanism (VRH) [1, 12–16] leads to an estimation of the localisation length parameter $\xi = 5\,\text{Å}$ and the density of states at the Fermi level (see Fig. 7.2).

[1] R. Kalish et al.: Rad. Eff. **52**, 153 (1980), doi:10.1080/00337578008210028
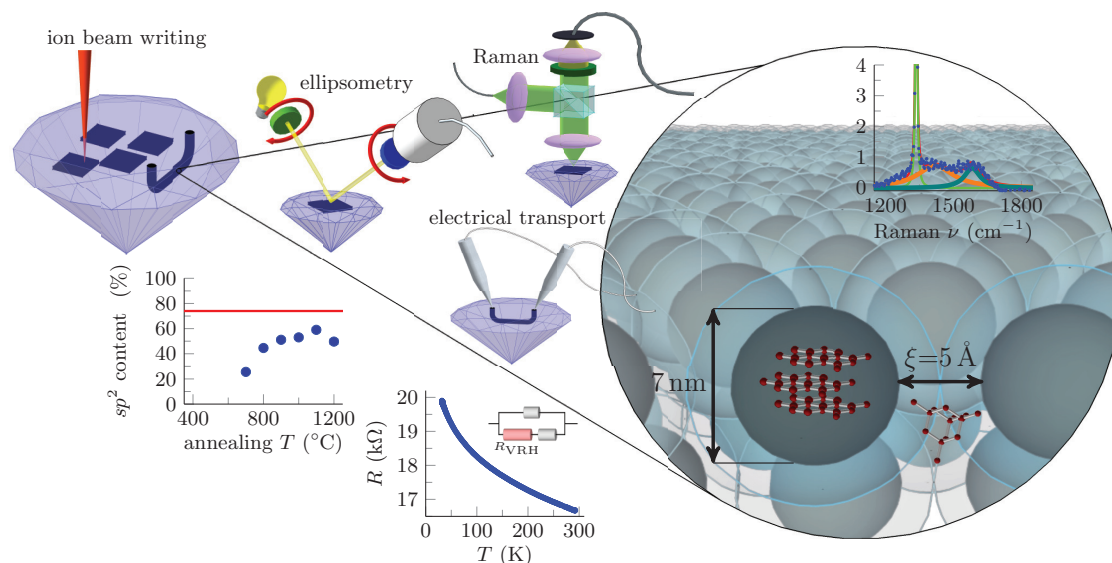
Figure 7.2: Illustration of the experiments and results. At first the graphite structures are made by high energy ion beam writing. Structural properties like the grain size and the localisation length parameter ξ were determined by combination of different methods: Raman, ellipsometry and temperature dependent electrical transport measurements.

[2] X.D. Zhu et al.: J. Phys.: Condens. Matter **14**, 5083 (2002), doi:10.1088/0953-8984/14/20/304

[3] F.R. McFeely et al.: Phys. Rev. B **9**, 5268 (1974), doi:10.1103/physrevb.9.5268

[4] A.C. Ferrari et al.: Phil. Trans. R. Soc. A **362**, 2477 (2004), doi:10.1098/rsta.2004.1452

[5] V.S. Vavilov et al.: Rad. Eff. **22**, 141 (1974), doi:10.1080/00337577408232161

[6] A.A. Gippius et al.: Diamond Relat. Mater. **8**, 1631 (1999), doi:10.1016/s0925-9635(99)00047-3

[7] P. Olivero et al.: Europ. Phys. J. B **75**, 127 (2009), doi:10.1140/epjb/e2009-00427-5

[8] P. Olivero et al.: Diamond Relat. Mater. **18**, 870 (2009), doi:10.1016/j.diamond.2008.10.068

[9] R.S. Patti: Proc. IEEE **94**, 1214 (2006), doi:10.1109/jproc.2006.873612

[10] J.D. Hunn et al.: Appl. Phys. Lett. **65**, 3072 (1994), doi:10.1063/1.112959

[11] D.A.G. Bruggeman: Ann. Phys. **416**, 636 (1935), doi:10.1002/andp.19354160802

[12] S. Prawer et al.: Phys. Rev. B **51**, 15711 (1995), doi:10.1103/PhysRevB.51.15711

[13] J.J. Hauser et al.: Solid State Commun. **18**, 789 (1976), doi:10.1016/0038-1098(76)90205-2

[14] J.J. Hauser et al.: Appl. Phys. Lett. **30**, 129 (1977), doi:10.1063/1.89323

[15] J.F. Prins: Rad. Eff. Lett. **76**, 79 (1983), doi:10.1080/01422448308209641

[16] J.F. Prins: Phys. Rev. B **31**, 2472 (1985), doi:10.1103/physrevb.31.2472

7.4   Hyperpolarisation via nitrogen–vacancy centres

R. Wunderlich, J. Kohlrautz[*], B. Abel[†], J. Haase[*], J. Meijer

[*]Division of Magnetic Resonance of Complex Solids
[†]Leibniz Institute of Surface Modification e.V., Leipzig

Hyperpolarisation at room temperature is one of the most important research fields in order to improve liquid, gas or nanoparticle tracer for Magnetic Resonance Imaging in medical applications. We utilize nuclear magnetic resonance to investigate the hyperpolarisation effect of negatively charged nitrogen–vacancy (NV) centres on ^{13}C nuclei and their spin diffusion in a diamond single crystal. Whereas the electron spins of the NV centre can be easily polarized in its $m = 0$ ground state at room temperature by irradiation with green light, the swop of the NV electron spin polarization to a ^{13}C nuclei is a complex task. We found that the coupling between the polarized NV electron spin, the electron spin of a substitutional N impurity (P1) as well as its ^{14}N nuclei and the ^{13}C nuclear spin has to be considered. Figure 7.3 shows a sketch of the model system. We show that through an optimization of this procedure, in about 2 min a signal to
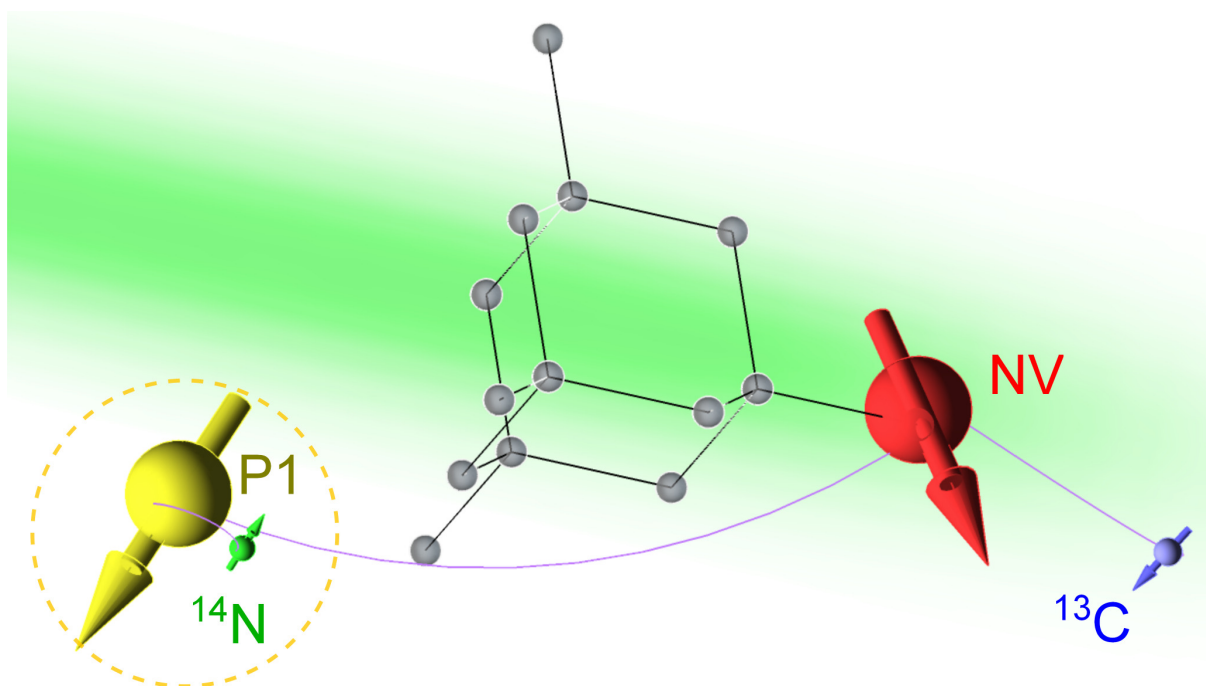
Figure 7.3: Sketch of the simulated four spin system consisting of a P1 centre electron spin coupled to its N spin and a NV centre interacting with a ^{13}C spin.

noise ratio which corresponds to a 23 h standard measurement without hyperpolarisation and an accumulation of 460 single scans can be obtained. Furthermore we were able to identify several polarisation peaks of different sign at different magnetic fields in a region of some tens of Gauss. Most of the peaks can be attributed to a coupling of the NV centres to nearby P1 centres. We formulate a new theoretical model in a framework of cross polarisation of a four spin dynamic model in good agreement with our experimental data. The results demonstrate the opportunities and power as well as limitations of hyperpolarisation in diamond via NV centres.

7.5 Nitrogen–vacancy centre creation by electron assisted implantation

S. Becker, N. Raatz, St. Jankuhn, R. John, J. Meijer

A precise and deterministic creation of NV centre is only feasible with technically advanced tools like particle accelerators which are not available in many research facilities. We developed a new method that is based on the utilization of a scanning electron microscope (SEM) for the ionization of the N atoms as well as their implantation in the diamond. In detail the process can be described as follows: The electron beam of the SEM is focused onto the sample, where the electrons accumulate because the diamond is electrically isolating. Thus, a negative electrical potential builds up, that causes an electric field. The magnitude of the potential is limited by the acceleration voltage of the electron gun of the SEM. N atoms that are channelled into the chamber interact with the electrons of the SEM beam via impact ionization, yielding N ions. The positively charged ions are then attracted by the negative potential and obtain a kinetic energy on the acceleration track to the sample that corresponds to this potential. With this obtained energy, the ions are now able to penetrate into the sample and generate vacancies, like in conventional ion implantation. A following annealing process triggers the NV centre formation. Fluorescence spectra and images recorded with a confocal microscope that is equipped with a spectrometer show that the created centres are indeed NVs (Fig. 7.4**a)** and **b)**). We proved that this NV centre creation method works actually in the way we described, by conducting this experiment with a ^{15}N isotope supply to the chamber. This isotope has a natural abundance of 0.364 % [2]. Because of the different nuclear spin of ^{14}N and ^{15}N that leads to a differing hyperfine coupling to the electron spin of the centre it is possible to distinguish between a ^{14}NV and a ^{15}NV with optically detected magnetic resonance (ODMR) (Fig. 7.4**c)**).

[1] J.R. Rabeau et al.: Appl. Phys. Lett. **88**, 023113 (2006), doi:10.1063/1.2158700
[2] D.R. Lide (Ed.): CRC Handbook of Chemistry and Physics: A Ready-reference Book of Chemical and Physical Data (CRC Press, Boca Raton 2005)

7.6 Creation of nano apertures for ion beam implantation

C. Scheuner, P. Räcke, N. Raatz, St. Jankuhn, S. Pezzagna, C. Trautmann[*], J. Meijer

[*]GSI Helmholtzzentrum für Schwerionenforschung GmbH, Darmstadt

For the creation of NV centres in diamond and other important applications, ion beams with a very small diameter are needed. This is commonly done with microprobe devices. A less expensive alternative to this is nano collimation which can be applied to several applications. Especially for applications with very low ion currents and single ion implantation this method is useful. Another possible application is the focused ion beam (FIB) technique where nowadays liquid metal ion sources are used. There a liquid metal gets ionized due to an electron spray on a very sharp tip. The advantage of this source is that it emits ions on a very small area which can be demagnified down to

a)

b)

c)
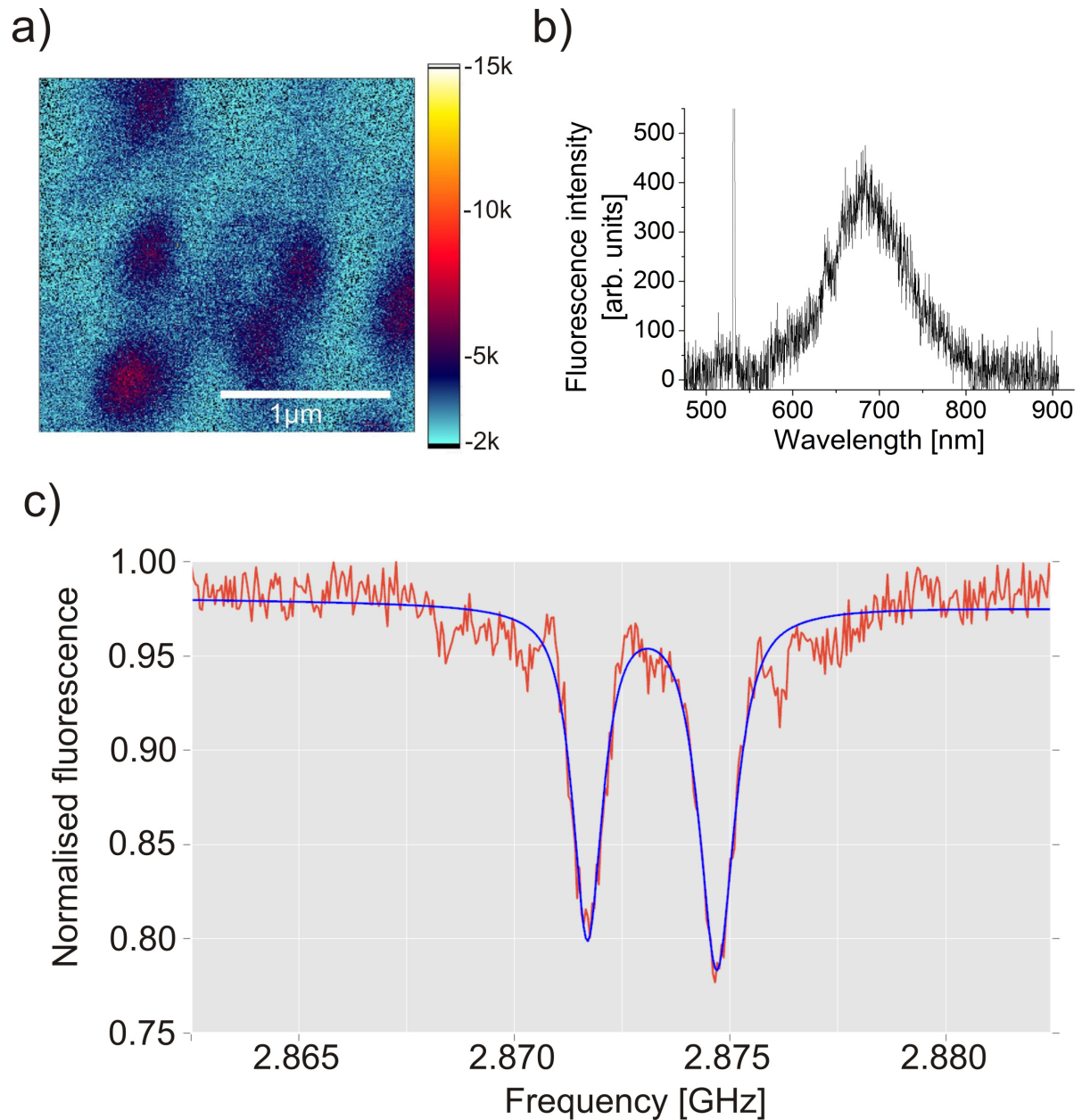
Figure 7.4: a) Fluorescence image of individual NV centre created by electron-assisted implantation. **b)** Fluorescence spectrum of one of the individual centre in **a)**, exhibiting the characteristic shape that is expected for a NV. **c)** ODMR spectrum of an individual NV centre at zero magnetic field. A dual separation of the 2.87 GHz resonance with a magnitude of 3 MHz is observable, corresponding to the hyperfine splitting expected for a [15]NV centre [1].

a few nanometres but the disadvantage is that it works just for a few chemical elements which have their melting point in a useable region. This disadvantage can be overcome for low current applications with nano collimators which are mounted behind the ion source. So there is still a small point where the ions are emitted but it is possible to use different types of ion sources, so nearly every element can be ionized.

We used two different ways to create such nano apertures for different scopes. One way is the ion track etching technique. There muscovite sheets where prepared at the GSI Darmstadt with high energetic Sm ions that penetrated the sheet and left a ion track of amorphous material. Subsequent etching with hydrofluoric acid removed this material and created diamond shaped pores. The shape of this pores origins from the crystal structure of the muscovite where are O planes that have the slowest etching rate and thus this pores have a very well defined shape and orientation, also the cross section of the pores is nearly identical. The pore size depends on the etching time and can be controlled in a certain rage. We got for one hour etching time that the two diagonals had the average length of 123 nm and 231 nm. Furthermore, the mean distance of the pores is controlled by the number of ions which penetrate the sheet because every ion leaves one track. So this can be controlled by the irradiation time. The advantage of this method is that one can archive very high aspect ratios up to 1000. This leads to nano apertures with a thickness sufficient to stop ions in the low MeV range. But the disadvantage is that the pores are randomly distributed over the irradiated area of the sheet and further collimation is needed to select a single pore.

The second method is FIB milling. There thin membranes are irradiated with a well focused beam of Ga ions. This removes material due to sputtering and thus structures can be milled in the surface (Fig. 7.5). One big advantage is that therefore arbitrary
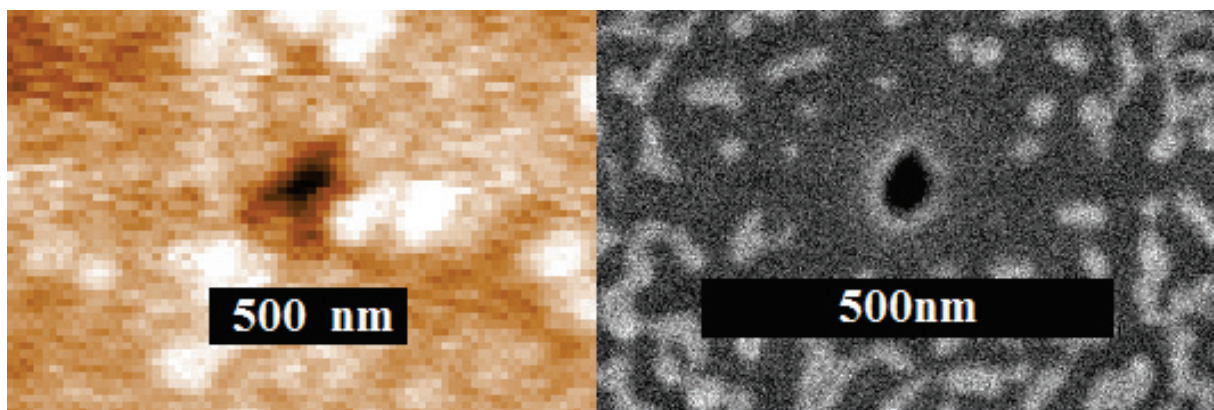
Figure 7.5: Micrograph of FIB milled pore in a Si_3N_4 membrane with a diameter of 50 nm, taken with atomic force microscopy (*left*) and scanning electron microscopy (*right*).

shapes can be written in the material and used as collimators. Furthermore, the only limitation on the collimator material is that one needs to obtain a certain sputter yield. But a limitation of this method is that for small deep pores the material that is sputtered away from the bottom of the pore is deposited at the side walls and thus the aspect ratio is limited. Meaning that for pores in the range of a few ten nanometres, the material needs to have a thickness in the order of a few hundred nanometres and thus the energy of the particles that should be collimated is limited to the lower keV range.

Another important parameter of collimators is the radiation hardness. It is planed

to study the effects of the collimator material as well as on the pore geometry with experiments and simulations and to find a well suited material for our purposes.

7.7 Quantum and classical light emitters in Si: Impurities and complex defects for nanophotonics

S. Pezzagna, M. Abbarchi[*], G. Cassabois[†], T. Herzig, I. Berbezier[*], A. Ronda[*], K. Liu[*], A. Benali[*], E. Rousseau[†], L. Doyennette[†], C. Beaufils[†], W. Redjem[†], J. Meijer

[*]Institut Matériaux-Microélectronique-Nanosciences de Provence, CNRS-UMR 7334, Aix-Marseille Université, France
[†]Laboratoire Charles Coulomb, CNRS-UMR 5221, Université de Montpellier, France

Si is the most important element when it comes to pioneering technological progress in microelectronics. Due to its several advantageous properties (semiconducting, temperature resistant, inexpensive, ultrapure, . . .) it is the main component in modern low-dimensional integrated circuits. The rapid evolution of Si-based circuits was possible due to decreasing the structure sizes on microchips ("Moore's law"). However, after five decades of increasing performance, we slowly reach the point where minimizing the structure sizes will not improve the efficiency any further. Therefore, new methods for circuit design and data exchange are required. One way to achieve this is to implement nanophotonics.

Due to its indirect bandgap, radiative transitions in Si are highly improbable. Semiconducting light emitting devices are mostly made of complex and expensive compounds. Therefore, a lot of effort was made to achieve radiation from Si itself. The most promising approach is the generation of a complex defect involving Si and C atoms, called G-centre.

Together with physicists from the Aix-Marseille University and the University of Montpellier and funded by the DFG and ANR, we investigate optimal conditions for creating G-centres with ion implantation. We use a 100 kV accelerator with a solid ion source for spatial selective implantation of C ions with different doses and energies into the Si substrate. After annealing (with RTP or oven) we create Si interstitials by high energy H or He irradiation with the LIPSION Singletron™ accelerator. Furthermore, we investigate the influence of Si nanocrystals, e.g. pillars (Fig. 7.6) and different kinds of Si crystals (in terms of crystal orientation, doping and SOI) on the photon gain. Photoluminescence measurements and potential single photon detection measurements are used to verify the results of implantation, annealing and irradiation.

The aim of this project is to find an ultra large scale integration (ULSI) method for generating efficient light emitting defects of low and high photon number in Si. By achieving this, the realisation of quantum computing and quantum cryptography will take a big step forward.
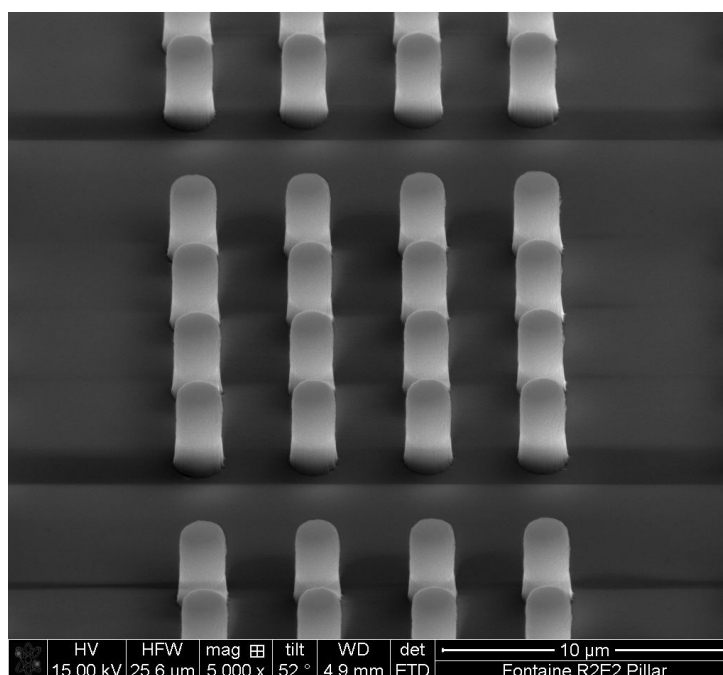
Figure 7.6: Si pillars, 5000× magnified.

7.8 Optical properties of the L1 colour centre in diamond

R. John, S. Pezzagna, J. Meijer

A large number of L1 colour centres [1] that originated from yet unknown treatment of their diamond host have been intensively studied to gather statistical knowledge about their optical properties. These include spectral emission properties with potentially vibronic structure (Fig. 7.7(a)), excited state lifetime, polarization, blinking and saturation behaviour. These measurements differ significantly from those of the ST1 colour centre [2] that is also found in the same sample, key being the $\langle 111 \rangle$ orientation of the optical dipole (Fig. 7.7(d)) compared to $\langle 110 \rangle$ for the latter [3]. Yet the property that these two types of colour centres are found in close vicinity to each other provides a strong link between these regarding their structure. Furthermore, the high variability of the spectral emission of the measured L1 centres reflected by the spread of their zero-phonon lines (ZPL) at $\approx 583(22)$ nm (Fig. 7.7(b)), and the broadening of the measured polarization angles in Fig. 7.7(d) point out a high dependence on the host structure, in this case a diamond surface damaged by ion irradiation and plasma etching, which may prove useful for surface analysis. The vibronic part of the spectral emission with its features at 15 THz and 49 THz (Fig. 7.7(c)) is still to be understood, but provides a characteristic property of theses colour centres useful for further investigations.

[1] R. John et al.: New J. Phys., submitted
[2] S.-Y. Lee et al.: Nat. Nanotechnol. **8**, 487 (2013), doi:10.1038/nnano.2013.104
[3] R. John et al.: Poster at SBDD XXI: Hasselt Diamond Workshop, Hasselt, Belgium, 09.–11.03.2016
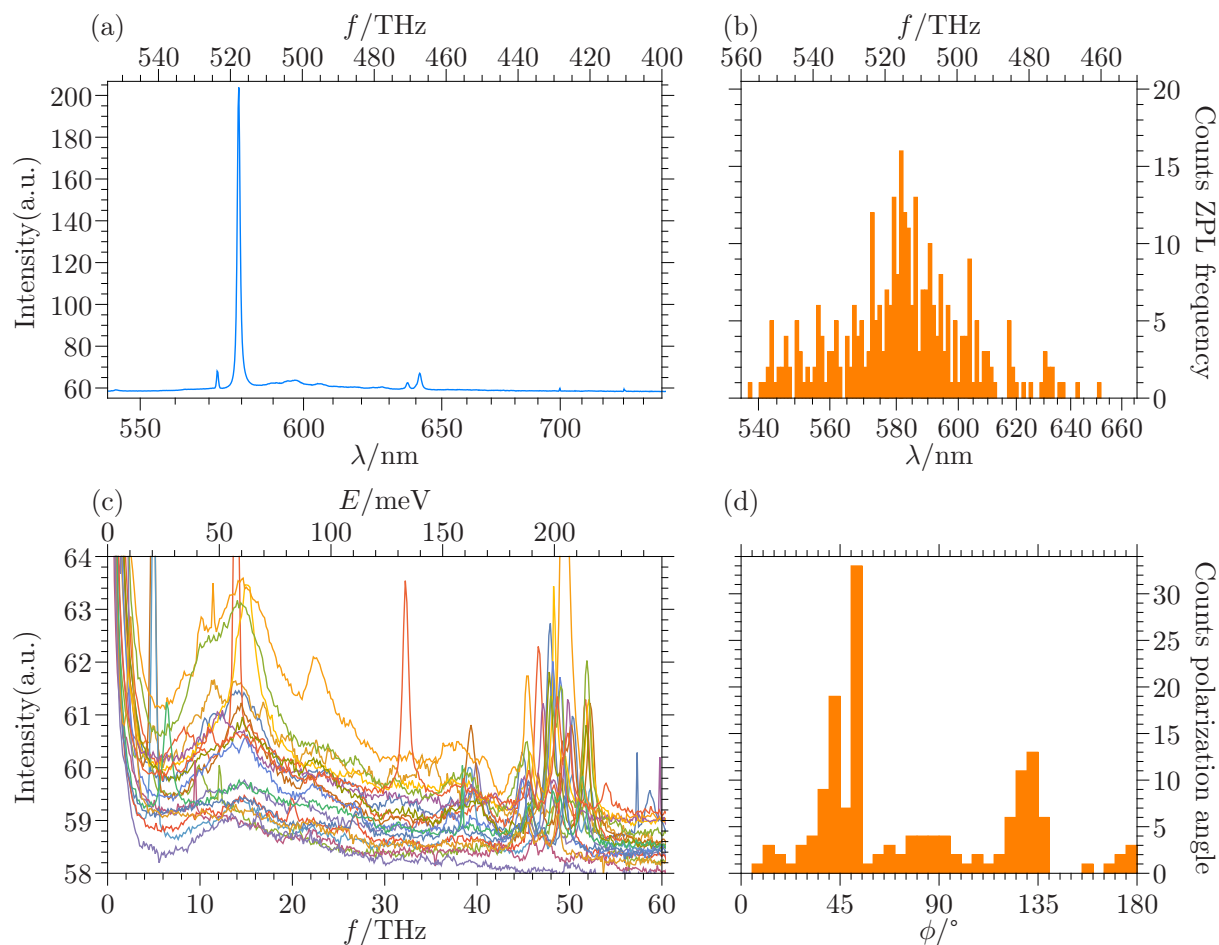
Figure 7.7: (a) Fluorescence spectrum of a characteristic L1 centre with 532 nm excitation showing a ZPL at 579.0 nm with a FWHM of 3.5 nm and potentially vibronic features at 640 nm corresponding to an energy offset of about 200 meV $\hat{\approx}$ 49 THz. **(b)** Distribution statistic of ZPLs with centre at $5\,83(\,22)$ nm. **(c)** Several spectra of L1 centres with widely spread ZPL translated to ZPL at zero frequency to visualize the potential vibronics at 15 THz and 49 THz. **(d)** Distribution statistics of angles of the linearly polarized emission of the L1 centres showing strong peaks at $\approx 45°$ and $\approx 135°$ indicating a $\langle 111 \rangle$ orientation of the optical dipole. Note the strong peak at 50° due to sample drift while the linearly polarized excitation was rotated starting from this angle.

7.9   Single ion implantation with high resolution

N. Raatz, S. Pezzagna, Y. Krivoshapkina[*], I.W. Rangelow[*], T. Jung[†], C. Becher[†], A.M. Jakob[‡], J. Meijer

[*]Institute of Micro and Nanoelectronics, TU Ilmenau
[†]Quantum Optics Group, Saarland University
[‡]Experimental Condensed Matter Physics (ECMP), University of Melbourne, Vic., Australia

One of the main projects in our group is single ion implantation. Our system to implant single ions is the nanoimplanter, a combination of low energy ion implantation and an atomic force microscope (AFM) with a pierced hollow tip [1].

The goal is to implant single ions with a resolution under 10 nm. In 2016 we started

testing a new method to make single ions visible on a sensitive resist film in cooperation with the group of I. Rangelow, Institute of Micro and Nanoelectronics in Ilmenau. The resist is very sensitive to ions or electrons. First implantations were done through a hole in an AFM tip of about 70 nm. Without developing the resist, we found a sensitivity of about 1000 ions/spot, which can be resolved in subsequent scanning with the AFM system. Figure 7.8(a) shows an AFM scan of the resist with a pattern of 9 spots, which were implanted with a fluence of 2000 ions/spot. The next step is to develop the resist and go to spots which were implanted with lower fluences until we will resolve single ion spots. Furthermore, tests will be with molecule ions in cooperation with the University of Melbourne.

We also continued implanting single N ions in photonic crystals in cooperation with the group of C. Becher, Saarland University [2]. A few years ago some nitrogen–vacancy (NV) centres were successfully found in the cavity at the centre of the photonic crystals. To have more success in the formation of NV centres which couple to the cavity modes, we implanted N ions with the help of the AFM non contact mode into a cavity. The initial AFM scan without contact reduces the risk of damaging the AFM tip and the closing of the hole in the tip due to dirt on the sample surface. Figure 7.8(b) shows an AFM scan of a typical cavity. Subsequent confocal imaging showed fluorescence of one or more NV centres, which are located in the middle of the cavitys.

In 2016 we also worked on finding standard conditions to produce very small apertures in Si_3N_4 masks. Therefore, we have thin membranes which are Au coated. To have reproducible apertures, it is necessary to use very low ion beam current. The Au coating allows the discharging of the sample as well as the focussing with very low ion beam current due to the typical island structure. We found the best results for an ion beam current of $I_{ion} = 1 \, pA$, an acceleration voltage of $U_B = 30 \, kV$, and an irradiation time of $t = 20 \, s$ for a hole about 50 nm or smaller in diameter. The masks are successfully used for creating single photon sources due to ion implantation at the University of Melbourne within the Centre of Excellence for Quantum Computation and Communication Technology (CQC^2T).
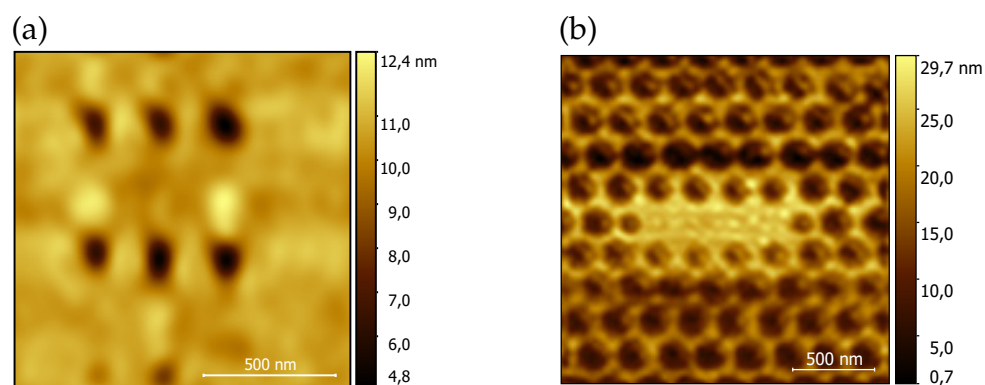
Figure 7.8: (a) AFM scan of an implanted pattern with 9 spots. Every spot is implanted with 2000 ions/spot. The hole in the tip was around 70 nm. Therefore spot = 3692 µm². **(b)** AFM scan of a typical cavity.

[1] J. Meijer et al.: Appl. Phys. A **91**, 567 (2008), doi:10.1007/s00339-008-4515-1
[2] J. Riedrich-Möller et al.: Appl. Phys. Lett. **106**, 221103 (2015), doi:10.1063/1.4922117

7.10 Funding

7.11   Organizational Duties

J. Meijer
- User Selction Panel for the Ion Beam Center: Helmholtz-Zentrum Dresden–Rossendorf
- Advisory Board: ISTAC Croatian Nuclear Science
- Programme Committee: 15th International Conference on Nuclear Microprobe Technology and Applications, Lanzhou, China, 31.07.–05.08.2016
- Referee: Several journals

R. John
- Session Chair: Annual BuildMoNa Conference, Leipzig, 14.–15.03.2016

7.12   External Cooperations

Academic

- City University of New York, College of Staten Island, Department of Engineering Science and Physics, USA
  Assoc. Prof. Dr. A.M. Zaitsev

- Centre National de la Recherche Scientifique (CNRS), École normale supérieure (ENS), Laboratoire Aimé Cotton (LAC), Cachan, France
  Prof. Dr. J.-F. Roch

- Centre National de la Recherche Scientifique (CNRS), Laboratoire des Sciences des Procédés et des Matériaux (LSPM), Fabrication Processes of Advanced Materials (PEMA), Paris, France
  Prof. Dr. J. Achard

- Commissariat à l'énergie atomique et aux énergies alternatives (CEA), Institut Rayonnement Matière de Saclay (IRAMIS), Service de Physique de l'Etat Condensé (SPEC), Quantronique, Saclay, France
  Prof. Dr. D. Esteve

- ETH Zürich, Physikdepartement, Laboratorium für Festkörperphysik, Spin Physics and Imaging, Switzerland
  Prof. Dr. C. Degen

- Fraunhofer-Institut für Angewandte Festkörperphysik Freiburg, Mikro- und Nanosensoren
  Dr. C.E. Nebel

- Humboldt-Universität zu Berlin, Mathematisch-Naturwissenschaftliche Fakultät I, Institut für Physik, AG Nanooptik
  Prof. Dr. O. Benson

- Hungarian Academy of Sciences, Wigner Research Centre for Physics, Institute for Solid State Physics and Optics, Budapest, Hungaria

- Interuniversitair Micro-Electronica Centrum (imec) Leuven, Belgium

- Julius-Maximilians-Universität Würzburg, Fakultät für Chemie und Pharmazie, Institut für Organische Chemie
  Prof. Dr. A. Krüger

- Leibniz-Institut für Oberflächenmodifizierung e.V. Leipzig
  Prof. Dr. Dr. h.c. B. Rauschenbach, Prof. Dr. B. Abel

- Leibniz-Universität Hannover, Institut für Anorganische Chemie, AK Analytik
  Prof. Dr. C. Vogt

- Ludwig-Maximilians-Universität München, Fakultät für Physik, Experimentelle Quantenphysik
  Prof. Dr. H. Weinfurter

- Max-Planck-Institut für biophysikalische Chemie Göttingen, Karl-Friedrich-Bonhoeffer-Institut, Abt. NanoBiophotonik
  Prof. Dr. Dr. h.c. St.W. Hell

- Technische Universität München, Walter Schottky Institut, E25: Spins and Defects in Semiconductors
  Prof. Dr. M.S. Brandt

- Università di Torino, Dipartimento di Fisica Sperimentale, Gruppo di Fisica dello Stato Solido
  Prof. Dr. E. Vittone

- Universität Basel, Department of Physics, Quantum-Sensing Lab, Switzerland
  Prof. Dr. P. Maletinsky

- Universität Kassel

- Universität Konstanz, Mathematisch-Naturwissenschaftliche Sektion, Fachbereich Physik, Lehrstuhl für Ultrakurzzeitphysik und Photonik
  Prof. Dr. A. Leitenstorfer

- Universität Leipzig, Medizinische Fakultät, Institut für Medizinische Physik und Biophysik
  Prof. Dr. E. Donath, Dr. I. Estrela-Lopis, Priv.-Doz. Dr. U. Reibetanz

- Universität Mainz, Fachbereich Physik, Mathematik und Informatik, Institut für Physik, Arbeitsgruppe Quanten-, Atom- & Neutronenphysik (QUANTUM)
  Prof. Dr. F. Schmidt-Kaler, Priv.-Doz. Dr. K. Singer

- Universität Stuttgart, Fakultät Mathematik und Physik, 3. Physikalisches Institut
  Prof. Dr. J. Wrachtrup

- Universität Ulm, Fakultät für Naturwissenschaften, Institut für Quantenoptik
  Prof. Dr. F. Jelezko

- Universität Ulm, Fakultät für Naturwissenschaften, Institut für Theoretische Physik, Controlled Quantum Dynamics Group
  Prof. Dr. M.B. Plenio

- University of Warwick, Department of Physics, Condensed Matter Physics, Magnetic Resonance Cluster, Coventry, UK
  Prof. Dr. M. Newton

- Universität Wien

- Westfälische Wilhelms-Universität Münster, Physikalisches Institut
  Prof. Dr. R. Bratschitsch

Industry

- ARTTIC Paris, France

- attocube systems AG München

- Element Six Ltd. Shannon, Co. Clare, Ireland

- THALES Research & Technology Palaiseau, France

7.13 Publications

Journals

P. Jamonneau, M. Lesik, J. Tetienne, I. Alvizu, L. Mayer, A. Dréau, S. Kosen, J.-F. Roch, S. Pezzagna, J. Meijer, T. Teraji, Y. Kubo, P. Bertet, J. Maze, V. Jacques: *Competition between electric field and magnetic field noise in the decoherence of a single spin in diamond*, Phys. Rev. B **93**, 024305 (2016)
doi:10.1103/physrevb.93.024305

O. Lehtinen, B. Naydenov, P. Börner, K. Melentjevic, C. Müller, L.P. McGuinness, S. Pezzagna, J. Meijer, U. Kaiser, F. Jelezko: *Molecular dynamics simulations of shallow nitrogen and silicon implantation into diamond*, Phys. Rev. B **93**, 035202 (2016)
doi:10.1103/physrevb.93.035202

M. Lesik, N. Raatz, A. Tallaire, P. Spinicelli, R. John, J. Achard, A. Gicquel, V. Jacques, J.-F. Roch, J. Meijer, S. Pezzagna: *Production of bulk NV centre arrays by shallow implantation and diamond CVD overgrowth*, phys. stat. sol. (a) **213**, 2594 (2016)
doi:10.1002/pssa.201600219

I. Lorite, Y. Kumar, P. Esquinazi, S. Friedländer, A. Pöppl, T. Michalsky, J. Meijer, M. Grundmann, T. Meyer, I. Estrela-Lopis: *Photo-enhanced magnetization in* Fe-*doped* ZnO *nanowires*, Appl. Phys. Lett. **109**, 012401 (2016)
doi:10.1063/1.4955048

C.E. Precker, P.D. Esquinazi, A. Champi, J. Barzola-Quiquia, M. Zoraghi, S. Muiños-Landin, A. Setzer, W. Böhlmann, D. Spemann, J. Meijer, T. Muenster, O. Baehre, G. Kloess, H. Beth: *Identification of a possible superconducting transition above room temperature in natural graphite crystals*, New J. Phys. **18**, 113041 (2016)
doi:10.1088/1367-2630/18/11/113041

I.P. Radko, M. Boll, N.M. Israelsen, N. Raatz, J. Meijer, F. Jelezko, U.L. Andersen, A. Huck: *Determining the internal quantum efficiency of shallow-implanted nitrogen-vacancy defects in bulk diamond*, Opt. Express **24**, 27715 (2016)
doi:10.1364/oe.24.027715

C. Schreyvogel, V. Polyakov, S. Burk, H. Fedder, A. Denisenko, F.F. de Oliveira, R. Wunderlich, J. Meijer, V. Zuerbig, J. Wrachtrup, C.E. Nebel: *Active and fast charge-state switching of single* NV *centres in diamond by in-plane* Al-*Schottky junctions*, Beilstein J. Nanotechnol. **7**, 1727 (2016)
doi:10.3762/bjnano.7.165

M. Stiller, J. Barzola-Quiquia, P. Esquinazi, D. Spemann, J. Meijer, M. Lorenz, M. Grundmann: *Strong out-of-plane magnetic anisotropy in ion irradiated anatase* TiO_2 *thin films*, AIP Adv. **6**, 125009 (2016)
doi:10.1063/1.4971794

Talks

J. Barzola-Quiquia, T. Lühmann, R. Wunderlich, M. Zoraghi, J. Meijer, P. Esquinazi
Magnetotransport properties of a disordered graphite microwire produced by He^+ *bombardment and embedded in a diamond crystal*
80. Jahrestagung der DPG und DPG-Frühjahrstagung, Regensburg, 06.–11.03.2016

F. Fávaro de Oliveira, A. Denisenko, D. Antonov, Y. Wang, S.A. Momenzadeh, A. Pasquarelli, J. Meijer, J. Wrachtrup
Engineering of spin defects in diamond within individual ion tracks
MRS Fall Meeting & Exhibit, Boston, MA, USA, 27.11.–02.12.2016

C. Giese, C. Widmann, J. Meijer, C.E. Nebel
Scalable technology development for single crystalline diamond magnetometers
SBDD XXI: Hasselt Diamond Workshop, Hasselt, Belgium, 09.–11.03.2016

P. Happel, T. Waag, M. Schimke, S. Schweeberg, A. Muzha, K. Fortak, D. Heesch, L. Klask, M. Pilscheur, F. Hoppe, T. Lenders, J. Meijer, G. Lepperdinger, A. Krüger
^{32}P-*labeled nanodiamond for biomedical applications*
SBDD XXI: Hasselt Diamond Workshop, Hasselt, Belgium, 09.–11.03.2016

P. Jamonneau, M. Lesik, J.-P. Tétienne, I. Alvizu, L. Mayer, A. Dréau, S. Kosen, J.-F. Roch, S. Pezzagna, J. Meijer, T. Teraji, Y. Kubo, P. Bertet, J.R. Maze, V. Jacques
Competition between electric field and magnetic field noise in the decoherence of a single spin in diamond
SBDD XXI: Hasselt Diamond Workshop, Hasselt, Belgium, 09.–11.03.2016

D. Lehmann
Robert Döpel: Experimenteller Kernphysiker der ersten Stunde
Joint Colloquium of Physics and Chemistry, Institute of Physics, TU Ilmenau, 07.06.2016, invited

J. Lehnert, R. John, M. Mensing, D. Spemann, S. Pezzagna, J. Meijer
Artificial defect centre in diamond with nearly phonon-free fluorescence at room temperature
SBDD XXI: Hasselt Diamond Workshop, Hasselt, Belgium, 09.–11.03.2016

J. Meijer
Functionalized single atoms by ion beam implantation
ULYSSES Kick-off Meeting, Montpellier, France, 10.–12.02.2016, invited

J. Meijer
Creation of NV centers by ion beam implantation
DIADEMS Summer School "Diamond and Spins", Cargèse, France, 26.04.–06.05.2016, invited

J. Meijer
Color center screening in diamond
MRS Fall Meeting & Exhibit, Boston, MA, USA, 27.11.–02.12.2016, invited

S. Pezzagna, D. Spemann, P. Räcke, N. Raatz, J. Gerlach, B. Rauschenbach, J. Meijer
Ions and the NV center creation efficiency
MRS Fall Meeting & Exhibit, Boston, MA, USA, 27.11.–02.12.2016, invited

D. Spemann, J. Meijer, J.W. Gerlach, P. Räcke, S. Liedtke, S. Rauschenbach, B. Rauschenbach
Concept of deterministic ion implantation at the nanoscale
XXIII. Workshop "Oberflächentechnologie mit Plasma- und Ionenstrahlprozessen", Mühlleithen, 15.–17.03.2016

M. Stiller, J. Barzola-Quiquia, P. Esquinazi, D. Spemann, J. Meijer, M. Lorenz, M. Grundmann
The influence of low-energy proton irradiation on the magnetic properties of undoped TiO_2 anatase thin films
80. Jahrestagung der DPG und DPG-Frühjahrstagung, Regensburg, 06.–11.03.2016

V. Zviagin, P. Richter, M. Bonholzer, Y. Kumar, I. Lorite, D. Spemann, J. Meijer, D.R.T. Zahn, G. Salvan, P. Esquinazi, M. Grundmann, R. Schmidt-Grund
Spectroscopic ellipsometry as a probe for structural properties of spinel ferrite thin films
7th International Conference on Spectroscopic Ellipsometry, Berlin, 06.–10.06.2016

Posters

R. John, J. Lehnert, M. Metsch, L. Rogers, S. Pezzagna, F. Jelezko, J. Meijer
ST1 colour centre in implanted and plasma treated diamond
SBDD XXI: Hasselt Diamond Workshop, Hasselt, Belgium, 09.–11.03.2016

R. John, J. Lehnert, M. Metsch, L. Rogers, S. Pezzagna, F. Jelezko, J. Meijer
ST1 colour centre in implanted and plasma treated diamond
Annual BuildMoNa Conference, Leipzig, Germany, 14.–15.03.2016

R. John, J. Lehnert, M. Metsch, L. Rogers, S. Pezzagna, F. Jelezko, J. Meijer
ST1 colour centre in implanted and plasma treated diamond
DIADEMS Summer School "Diamond and Spins", Cargèse, France, 26.04.–06.05.2016

E. Kirilina, M. Morawski, K. Reimann, I.Weigelt, St. Jankuhn, L. Müller, N. Jakubowski, N. Weiskopf
More then simply iron: Macro- to microscopic cellular iron distribution in the brain determines MR contrast
Toward a Super-Big Brain: Promisses and Pitfalls of Microstructural Imaging, Montréal, QC, Canada, 03.–05.08.2016

E. Kirilina, M. Morawski, K. Reimann, J. Dinse, P.-L. Bazin, S. Geyer, R. Trampel, L. Müller, St. Jankuhn, A. Deistung, N. Weiskopf
Imaging subcortical white matter by high resolution 7 T MRI in vivo: Towards potential U-fiber density mapping in humans
Toward a Super-Big Brain: Promisses and Pitfalls of Microstructural Imaging, Montréal, QC, Canada, 03.–05.08.2016

M. Lesik, J. Renaud, O. Salord, A. Delobbe, P. Spinicelli, S. Pezzagna, V. Jacques, A. Tallaire, J. Achard, A. Gicquel, J. Meijer, J.-F. Roch
NV center engineering using focused ion beam technique
SBDD XXI: Hasselt Diamond Workshop, Hasselt, Belgium, 09.–11.03.2016

N. Raatz, K. Groot-Berning, C. Eames, S. Pezzagna, S. Becker, St. Jankuhn, M. Holz, I.W. Rangelow, J. Meijer
Increasing the quality of single ion implantation with high spatial resolution
DIADEMS Summer School "Diamond and Spins", Cargèse, France, 26.04.–06.05.2016

P. Räcke, D. Spemann, F.-J. Schmückle, W. Heinrich, S. Liedtke, J.W. Gerlach, B. Rauschenbach, J. Meijer
Novel concept of deterministic ion implantation at the nano-scale
DIADEMS Summer School "Diamond and Spins", Cargèse, France, 26.04.–06.05.2016

R. Staacke, R. John, P. Schlupp, J. Lehnert, M. Grundmann, J. Meijer
NV-magnetometry of non-classical conduction in zinc-tin-oxide thin films
SBDD XXI: Hasselt Diamond Workshop, Hasselt, Belgium, 09.–11.03.2016

V. Zviagin, P. Richter, Y. Kumar, I. Lorite, M. Lorenz, D. Spemann, J. Meijer, D.R.T. Zahn, G. Salvan, P. Esquinazi, M. Grundmann, R. Schmidt-Grund
Spectroscopic ellipsometry and MOKE as a probe for structural properties of spinel oxide thin films
80. Jahrestagung der DPG und DPG-Frühjahrstagung, Regensburg, 06.–11.03.2016

V. Zviagin, Y. Kumar, I. Lorite, D. Spemann, J. Meijer, P. Esquinazi, M. Grundmann, R. Schmidt-Grund
Magnetic and optical properties of normal, disordered, and inverse spinel oxides
33rd International Conference on the Physics of Semiconductors, Beijing, China, 31.07.–05.08.2016

7.14 Graduations

Master

- Y. Albanay
  Theoretical and Practical Study of Deforming of Si_3N_4 Nanopores under Electron and Carbon-12 Ion Beam
  May 2016

- S. Becker
  Elektronen-assistierte Implantation in isolierenden Proben
  June 2016

Bachelor

- S. Dietel
  Charakterisierung von NV-Zentren vor und nach CVD-Wachstum
  October 2016

- J. Dwan
  A New Method for Precision Ion Implantation
  June 2016

- A.-D. Ziems
  Creation of Optical Centres in Yttrium Aluminium Garnet Crystals
  December 2016

7.15 Guests

- Dr. M. Chipaux
  University of Groningen, Department of Biomedical Engineering, Bioimaging & Bioanalysis Group
  05.07.2016

- Dr. H. Fedder
  Universität Stuttgart, 3. Physikalisches Institut
  11.–13.07.2016

- Prof. M. Gurioli
  University of Florence, Department of Physics and Astronomy
  06.09.2016

- Prof. Dr. J. Heitmann
  TU Bergakademie Freiberg, Institut für Angewandte Physik
  26.01.2016

- Dr. A.M. Jakob
  University of Melbourne, Faculty of Science, School of Physics, Experimental Condensed Matter Physics
  28.06.2016

- Priv.-Doz. Dr. Dr. M. Morawski, I. Weigelt
  Universität Leipzig, Medizinische Fakultät, Paul-Flechsig-Institut für Hirnforschung
  14.06.2016

8

Semiconductor Physics

8.1 Introduction

We are happy to present our latest research with this report and hope that you enjoy going through it. Among others, you will find novel results on exceptional points in optically anisotropic bulk materials and planar microcavities, lasing in nanostructures and electrical properties of amorphous oxides. Copper iodide was found to exhibit by far the largest figure of merit for p-type transparent conductors. Our work has also been featured on a couple of journal covers.
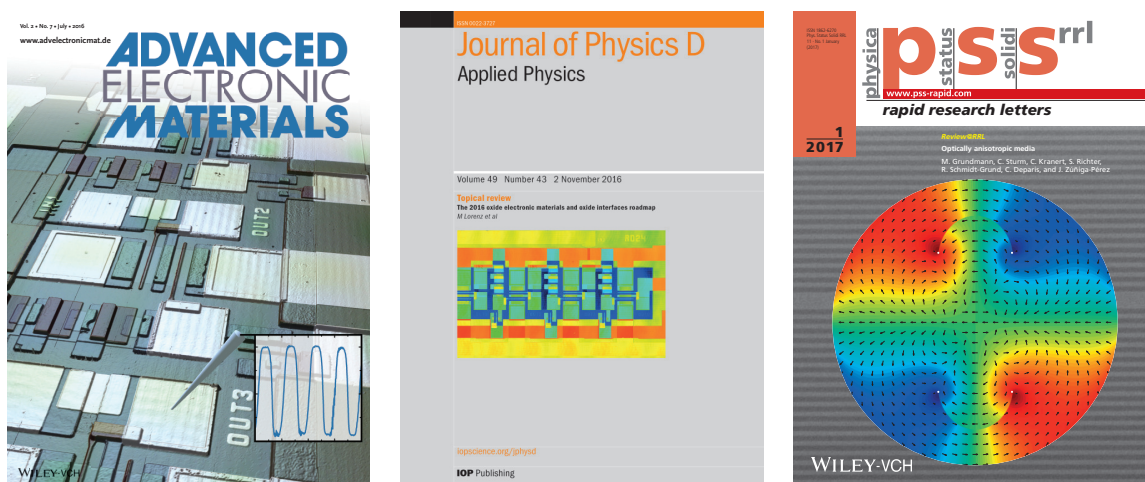
Figure 8.1: Journal covers of 2016/17 publications of the semiconductor physics group

A particularly interesting feature of anisotropic (biaxial) optical materials is the occurence of singular axes. For such axis only one polarization eigenmode exists. We have investigated such phenomenon in monoclinic gallia bulk crystals. This represents the first data on the spectral dispersion of the angular position of singular axes. We have put particular effort on the correct modeling of transmission and reflexion in the vicinity of singular axes. A related phenomenon are the polarization properties of anisotropic microcavities, i.e. cavities where the optic axis of the uniaxial cavity medium (e.g. GaN or ZnO) is inclined with respect to the mirror normal. Such medium turns out to be 'effectively' optically biaxial and the eigenmodes are generally elliptically polarized. For further details see Section 8.17.

A number of thrilling results have been obtained for amorphous oxides, namely ZTO (zinc-tin-oxide) and ZON (zinc-oxynitride), offering rather large electron mobilities. Using the composition-spread approach to combinatorial deposition, we could optimize the cation-ratio for ZTO and have realized quite good Schottky diodes. Expect further results for integrated circuits based on this technology.

From the many other results in this report I like to draw your attention to the experimental determination of the non-linear optical deformation potential of ZnO, determined from luminescence experiments on bent ZnO micro-wires (see Section 8.13).

We are largely indebted to our funding agencies in particular Deutsche Forschungsgemeinschaft (DFG). We are grateful for the continued funding of Sonderforschungsbereich SFB 762 "Functionality of Oxide Interfaces" that has been renewed (2016–2019) and our project on nanowire heterostructures in the Forschergruppe FOR 1616 "Nanowire Optoelectronics" which was extended for the second funding period (2015–2018). A project on flexible oxide electronics has started in the new DFG SPP FFlexCom (SPP 1796). The work of our students and researchers together with our academic and industrial partners near and far was fruitful and enjoyable and thus it is with pleasure that the semiconductor physics group presents their progress report.

Leipzig, *Marius Grundmann*
August 2017

8.2 Semi-transparent ZnO-based UV solar cells: Analysis of electrical loss mechanisms

R. Karsthof, H. von Wenckstern, M. Grundmann

Transparent solar cells open new fields of application for photovoltaics, such as energy harvesting on glass facades and windows, or autonomously powered mobile devices via display-integrated solar cells. In general, such devices could convert any surface into a photovoltaic power source without having an impact on the appearance of the latter. We recently reported on the successful fabrication of a semi-transparent, UV-active heterojunction solar cell, based on a pulsed laser deposition (PLD) grown zinc oxide (ZnO) absorber and a DC-magnetron sputtered nickel oxide (NiO) front contact, exhibiting a power conversion efficiency of 3.1 % with respect to the ultraviolet part of the sunlight, and 0.1 % with regard to the complete solar spectrum [1]. Although already showing superior performance in comparison with other transparent solar cells presented in scientific literature, our devices suffer from a pronounced deformation of the current-voltage characteristics under illumination. This results in lower photovoltaic performance than could be expected in a model assuming ideal superposition of (dark) injection and photocurrents, affecting open-circuit voltage V_{oc}, short-circuit current density j_{sc}, and fill factor f of the solar cell.

In this work, we have investigated the loss mechanisms causing this behavior in more detail [2]. For this purpose, we compared three different ZnO-based diode structures that can all be employed as semi-transparent UV solar cells. All three device types had the same design with respect to the back contact and absorber components: a
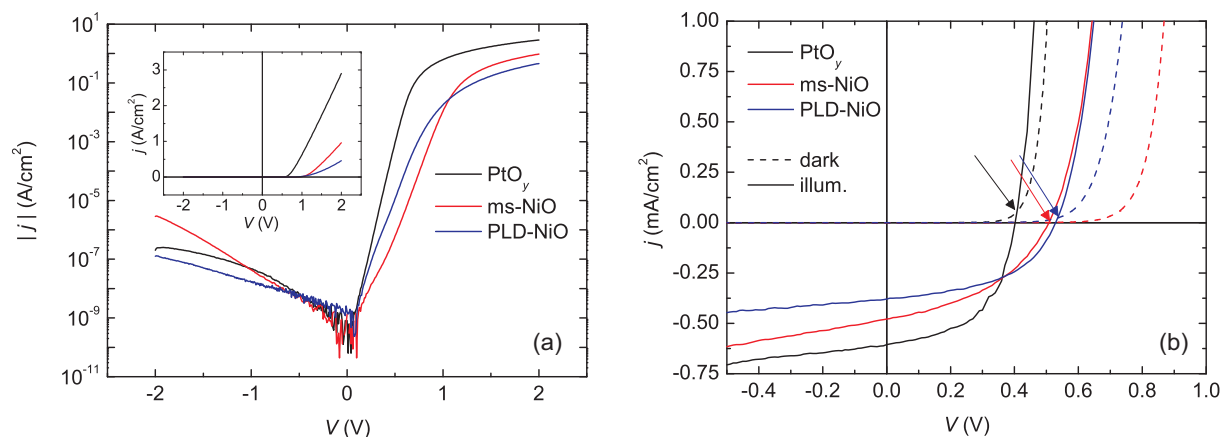
Figure 8.2: Comparison of current density-voltage (jV) characteristics of the three solar cell types using a PLD-grown NiO, DC-magnetron sputtered (ms) NiO or DC-magnetron sputtered PtO_y Schottky front contact. (a) in the dark (semilog scale), (b) dark and illuminated conditions, linear current density scale.

180 nm thick Al-doped ZnO layer was grown on a-plane oriented sapphire substrates, serving as back electrode; subsequently, a 1 μm thick, nominally undoped ZnO layer was deposited on top. The growth method for both layers was PLD, the substrate temperature was kept at 670 °C, the oxygen partial pressure was 0.02 mbar. The first diode type was identical to the one presented in Ref. [1], possessing a 16 nm thick sputtered p^+-NiO front contact. For the second type, a 100 nm thick PLD-grown p-NiO front contact was used instead, which was deposited at room temperature and at an oxygen partial pressure of 0.1 mbar. In both cases, a 3 nm thin Au capping layer was DC-magnetron sputter-deposited on top of the NiO to ensure uniform current extraction over the entire contact area. The third one employed a Schottky-type front contact made from reactively sputtered platinum oxide (PtO_y) [3].

All three device types exhibit good current rectification properties with rectification ratio of more than six orders of magnitude at ±2 V, and ideality factor of around 2 for the NiO contacts and close to 1 for the Schottky structure, in accordance with theory (Fig. 8.2(a)). Under illumination with light from a solar simulator, the diodes show comparatively distinct photovoltaic action, with the PLD-grown NiO producing the highest V_{oc} values of 530 mV, while the largest j_{sc} of 0.61 mA/cm^2 is obtained with PtO_y Schottky front contacts (Fig. 8.2(b)). For the NiO-based structures, the UV power conversion efficiency is slightly above 3 %, while the Schottky type gives around 4 %.

When the characteristics obtained under dark and illuminated conditions are compared, a significant light-induced deformation of the curves can be seen in all three cases – in particular, a strong bowing in the fourth quadrant (photovoltaic mode), responsible for a low fill factor, and an intersection of the dark and illuminated characteristics (referred to as *cross-over*) close to V_{oc} which is indicated by the arrows in Fig. 8.2(b). It can be concluded that the superposition principle described above is violated in all solar cell types. Especially the cross-over behavior can only be understood when an enhancing effect of the impinging light flux on the injection current is taken into account. For the case of Schottky diodes, this effect has already been described in the literature for GaN-based Schottky diodes [4] and can be assigned to trapping of photo-generated
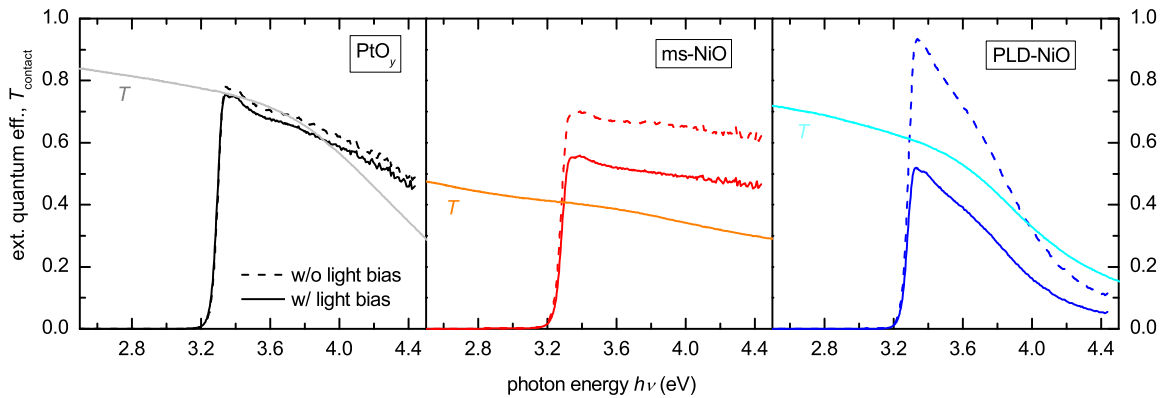
Figure 8.3: External quantum efficiency data for the three investigated solar cell types under monochromatic and white light biased conditions, measured at short-circuit, and optical transmission of the respective front contact materials

holes at the semiconductor-metal interface, reducing the built-in voltage of the junction. For the NiO-based devices, we propose a model involving an optically activated recombination channel at the NiO-ZnO interface. Electronic defect states localized at this interface provide means for carrier transport, also in the dark state, as was shown in an earlier publication [5]. Without illumination, however, this recombination is rather slow. Within the framework of our model, this is due to the fact that the rate with which an electron, once trapped at an interface defect site, is re-emitted, is low compared to the capture rate for following injected electrons, such that at higher injection levels, most of the defect states are occupied and cannot contribute to recombination. Under illumination, this situation changes because the defects are depopulated by optically enhanced emission. This will increase current flow evoked by injection, but recombination of photo-generated carriers crossing the NiO-ZnO interface as well. The latter can be seen in the data of the spectrally resolved photocurrent (more specifically, external quantum efficiency, QE). In Fig. 8.3 the QE curves for the three device types are shown under two different conditions: one is obtained by monochromatic excitation only, the other is measured while the sample is simultaneously illuminated with white light from the solar simulator (corresponding to the situation applicable to the illuminated jV measurement), referred to as *white light biasing*.

It can also be seen that the drop of the QE above the ZnO band gap energy ($\approx$ 3.3 eV) is mostly determined by absorption in the respective front contact material, as shown by the transmission (T) data plotted alongside with the QE data in Fig. 8.3. In the case of Schottky type front contacts, the light bias does not lead to differences in the measured QE within the range of measurement errors. For the NiO-based solar cells, however, a large drop of the QE is produced in this case, independent of the photon energy, and most pronounced for PLD-grown NiO where the values are approximately halved under illumination. This supports our hypothesis that interface recombination rates are enhanced by strong illumination with white light. Since the effect is not present in the Schottky device, it can be concluded that it is not related to the ZnO layer itself. To look into the light-induced recombination processes in more detail, we studied the voltage-dependent photocurrent collection of the solar cell with

the PLD-NiO, where the differences in the QE where most prominent, following the procedure described in Ref. [1]. The analysis was, again, perfomed under both weak monochromatic excitation close to the ZnO band gap energy and under intense white (solar) light illumination, and the results were compared. By using an analytical model for the collection probability, taking into account both recombination processes within the space charge region (SCR) in the ZnO and at the NiO-ZnO interface, the data could be fitted, which yielded low collection probabilities (around 50 % at short-circuit) due to high interface recombination for strong white light. In the case of weak monochromatic illumination, the collection efficiencies were significantly higher (83 % at $V = 0$ V), and losses were mostly determined by SCR recombination. These findings further support our hypothesis of an optically activated interface recombination channel.

[1] R. Karsthof, P. Räcke, H. von Wenckstern, M. Grundmann, Phys. Stat. Solidi A **213**(1), 30 (2016)
[2] R. Karsthof, H. von Wenckstern, M. Grundmann, J. Vac. Sci. Technol. B **34**(4), 04J107 (2016)
[3] A. Lajn, M. Schmidt, H. von Wenckstern, M. Grundmann, J. Electr. Mat. **40**, 473 (2011)
[4] O. Katz, V. Garber, B. Meyler, G. Bahir, J. Salzman, Appl. Phys. Lett. **79**, 1417 (2001).
[5] M. Grundmann, R. Karsthof, H. von Wenckstern, ACP Appl. Mater. Interfaces **6**, 14785 (2014)

8.3 Influence of Cation Composition on Material Properties of Amorphous Zinc-Tin-Oxide Thin Films

S. Bitter, P. Schlupp, H. von Wenckstern, M. Grundmann

The possibility of room temperature deposition makes amorphous zinc-tin-oxide (ZTO) an ideal candidate for flexible, large-area, and cost-efficient devices [1]. It consists of the non-toxic and naturally abundant elements zinc and tin. The influence of the composition on electrical and optical properties of ZTO has been reported for a few discrete cation ratios only [2, 3]. Besides the chemical composition, the oxygen pressure during growth has a strong influence on ZTO material properties as reported for e.g. pulsed laser deposition [4].
We discuss the electrical and optical properties of amorphous ZTO in dependence on the cation composition for a wide composition range and oxygen growth pressures of 0.025 and 0.030 mbar.
The ZTO thin films were deposited by a continuous composition spread (CCS) approach for PLD [5]. For that, a segmented ceramic target is rotated synchronously with a 50×50 mm^2 glass substrate. Additionally, an offset of 24 mm between the normal on the center of the substrate and the normal on the center of the target was chosen to achieve the composition gradient. Here, we present electrical properties for ZTO thin films with compositions between 0.08 and 0.82 Zn/(Zn+Sn).

Targets with different zinc to tin ratios in the segments were used to achieve larger or smaller composition gradients. Targets with a pure zinc oxide and tin oxide segment
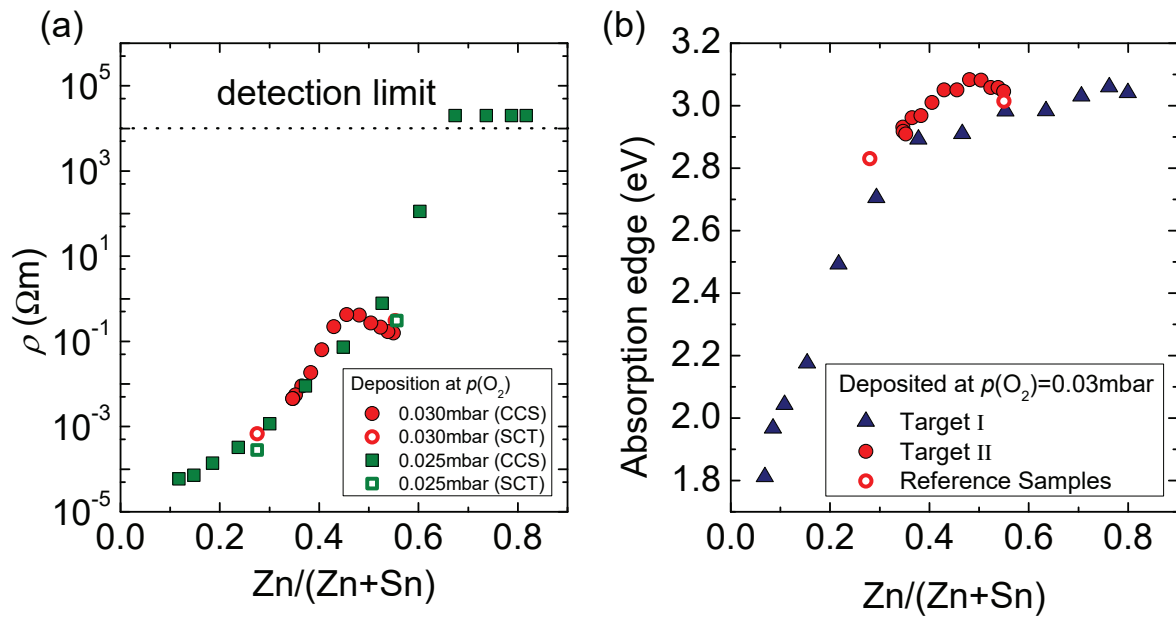
Figure 8.4: (a) Resistivity ρ determined by Hall effect measurements for different deposition pressures and targets, which can be seen in different composition ranges. These values were compared to thin films deposited from single composition targets (SCT). (b) Absorption edge for a deposition pressure of 0.03 mbar and different targets (I: segmented target with a pure SnO_2 and pure ZnO half, II: Halves with Zn/Sn ratios of 1:2 and 2:1).

resulted in thin films with a wide composition range but also a high droplet density on the thin films. The droplet density could be reduced by choosing the compositions of the target segments as 1:2 and 2:1 $ZnO:SnO_2$. The $50 \times 50\,mm^2$ samples were investigated by energy dispersive X-ray analysis to map the composition. Subsequently, the samples were divided into 5 mm wide stripes which were then broken into $5 \times 5\,mm^2$ pieces for the investigation of the electrical properties by Hall effect measurements. The resistivity and absorption edge of the thin films are depicted in Figure 8.4 in dependence on the zinc to tin ratio. The measured values for the CCS samples were compared to those of thin films deposited from standard, single composition PLD targets and a good agreement was observed.

A tuning of the free carrier density from $2 \times 10^{16}\,cm^{-3}$ to $1 \times 10^{20}\,cm^{-3}$ is possible with this approach, while the smallest measured resistivity of $5.9 \times 10^{-5}\,\Omega$m was found for 0.13 Zn/(Zn+Sn) and a deposition pressure of 0.025 mbar O_2 [6]. The absorption edge varied between 1.8 and 3 eV and increased with increasing zinc content. A further tuning of the thin film properties is possible by a variation of the deposition pressure [4]. This wide range of properties allows the fabrication of optimized devices based on this compound. All-amorphous *pn*-heterojunctions have been reported for 0.3 Zn/(Zn+Sn) already [7][8].

[1] H. Hosono *et al.*: J. Non-Cryst. Solids. **198-200**, 165 (1996)

[2] M. K. Jayaraj *et al.*: J. Vac. Sci. Technol. B **26**, 495 (2008)

[3] P. Görrn *et al.*: Advanced Materials **18**, 6, 738-741 (2006)

[4] P. Schlupp *et al.*: Mater. Res. Soc. Symp. Proc. **1633**, 101 (2014)

[5] H. von Wenckstern *et al.* CrystEngComm. **15**, 10020 (2013)

[6] S. Bitter *et al.*: ACS Comb. Sci. **18**, 4, 188-194 (2016)
[7] P. Schlupp *et al.*: Adv. Electron. Mater. **1**, 1400023 (2015)
[8] M. Grundmann *et al.*, J. Phys. D: Appl. Phys. 49, 21, 213001 (2016)

8.4   Schottky barrier diodes based on room temperature fabricated zinc tin oxide thin films

P. Schlupp, H. von Wenckstern, M. Grundmann

Low temperature fabrication of semiconductors is desirable not only because of the low costs. It also enables the use of thermally unstable but flexible substrates. Unfortunately, most semiconducting materials require a good crystalline quality and with that a high fabrication temperature in order to fulfill the requirements for most applications. Amorphous oxide semiconductors (AOS) are materials which do not underlay this contradiction. Due to their electronic structure, they exhibit good electric properties in the disordered amorphous phase [1]. Zinc tin oxide (ZTO) is a promising AOS because it consists of naturally abundant materials only. Electron mobility of $12\,\mathrm{cm^2V^{-1}s^{-1}}$ was reported while the conductivity is controllable varying the fabrication parameter [2, 3]. Schottky barrier diodes are a viable option to create rectifying contacts on semiconductor thin films and are a prerequisite for space charge region spectroscopic methods like capacitance-voltage (CV) and thermal admittance spectroscopy (TAS). They can also be used as gate contact in metal semiconductor field effect transistors (MESFET). We report on Schottky diodes using platinum metal contacts. In figure 8.5a the current density-voltage characteristics of two diodes on one and the same thin film are depicted. The grey line represents a Pt/ZTO Schottky contact. Since the leakage current is more than $10^{-3}\,\mathrm{Acm^{-2}}$ at -1.5 V and increases exponentially with increasing voltage tunneling is most likely responsible for the high leakage current. To decrease it, a thin semi-insulating ZTO layer was introduced at the platinum/ZTO interface. This reduces the leakage current of about four orders of magnitude (black line figure 8.5a). Both diodes were investigated by capacitance-voltage and thermal admittance spectroscopy. The net doping density was calculated from the CV data and is depicted in figure 8.5b. The values are between 10^{17} and $10^{18}\,\mathrm{cm^{-3}}$. A slight decrease to the surface is observed.

From TAS G/ω vs. T is obtained and depicted in figure 8.6. Both diodes show two peaks in G/ω shifting with the temperature as the probing frequency is increased. These peaks correspond to defect states in the material. The deep defect is located $215-220\,\mathrm{meV}$ below the conduction band minimum. The calculated capture cross sections are 1×10^{-14} and $1.7\times10^{-14}\,\mathrm{cm^2}$ for the diodes without and with semi-insulating ZTO layer, respectively. This is a rather high value indicating a rather large defect. Undercoordinated cation pairs are known to form deep defects [4] and are candidates for the deep defect observed. The shallow defect is within the freeze-out regime. Therefore the method of Pautrat *et al.* is applied for evaluation [5]. For that we assume that scattering at potential barriers, located at the conduction band minimum due to the different cations, is the dominant scattering mechanism in the freeze-out temperature regime [6]. Assuming a potential height of 10 to 20 meV an activation energy of 15-27 meV is obtained. Further investigations are necessary in order to obtain information about the microscopic nature of the shallow defect.

(a)   (b)
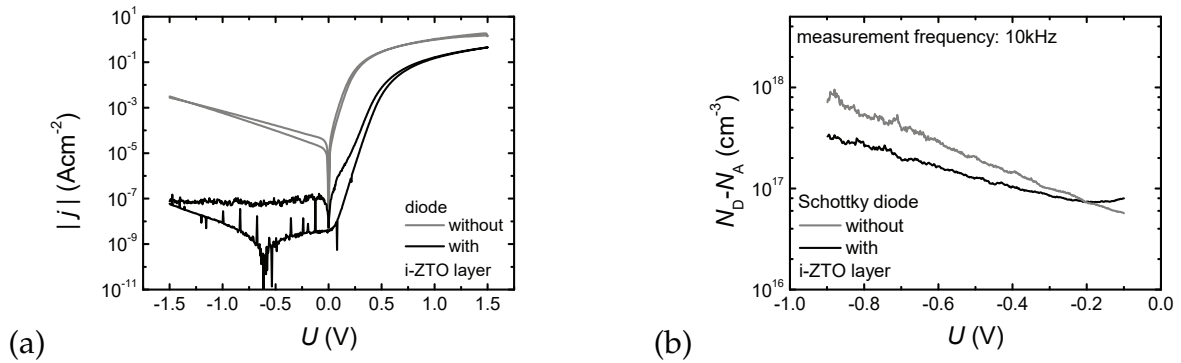
Figure 8.5: Current density-voltage characteristics of diodes without (grey line) and with (black line) a semi-insulating ZTO layer (a) and the corresponding net doping density obtained from CV (b).

(a)   (b)
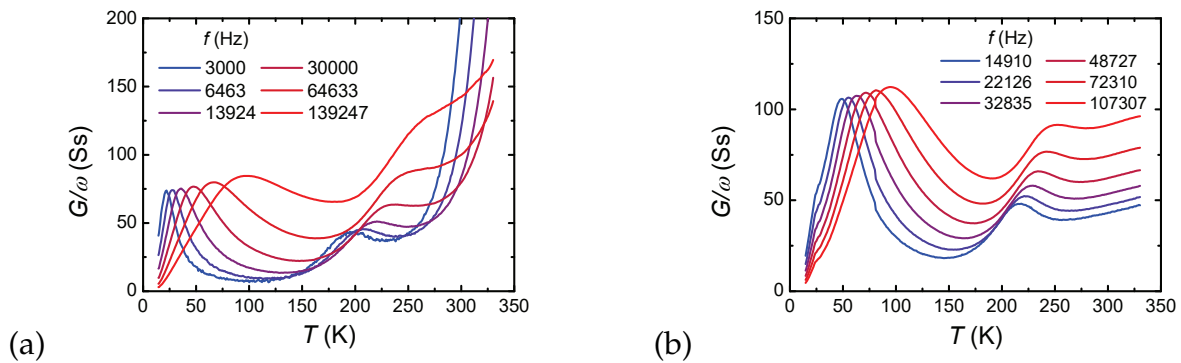
Figure 8.6: Temperature dependence of G/ω for the both diodes. The peaks shifting with the temperature indicating two defect levels.

[1] H. Hosono, N. Kikuchi, N. Ueda, H. Kawazoe: J. Non-Cryst. Solids. **198-200**, 165 (1996)

[2] M. K. Yajaraj, K. J. Saji, K. Nomura, T. Kamiya, H. Hosono: J. Vac. Sci. Technol. B **26**, 495 (2008)

[3] P. Schlupp, H. von Wenckstern, M. Grundmann: Mater. Res. Soc. Symp. Proc. **1633**, 101 (2014)

[4] W. H. Han, K. J. Chang: Phys. Rev. Appl. **6**, 044011 (2016)

[5] J.L. Pautrat, B. Katircioglu, N. Magnea, D. Bensahel, J.C.Pfister, L. Revoil: Solid-State Electron. **23**, 1159 (1980)

[6] K. Nomura, T. Kamiya, H. Ohta, K. Ueda, M. Hirano, H. Hosono: Appl. Phys. Lett. **85**, 1994 (2004)

8.5   Chemical bonding states of rf-sputtered amorphous zinc oxynitride thin films

A. Reinhardt, H. Frenzel, H. von Wenckstern, M. Grundmann, M. Welke*, R. Denecke*

*Wilhelm-Ostwald-Institut für Physikalische und Theoretische Chemie, Fakultät für Chemie und Mineralogie, Universität Leipzig

Recently, amorphous zinc oxynitride (a-ZnON) has attracted much attention as active channel material for high-performance thin-film transistors with superior field-effect mobilities [1]. However, the electrical properties of room-temperature deposited thin films depend significantly on the anion content and are also affected by moderate annealing temperatures [2]. Additionally, chemical stability is a remaining issue for reliable device production.

In order to understand changes in electrical properties, we have investigated the chemical bonding states of as-deposited, annealed and aged ZnON thin films by means of X-ray photoelectron spectroscopy (XPS). The surface sensitive XPS measurements were performed in UHV ($< 5 \times 10^{-9}$ mbar) using Al K_α radiation ($h\nu = 1486,7$ eV). The C 1s line attributed to aliphatic carbon with a binding energy of 285 eV has been used to calibrate the spectrometer. The ZnON thin films were radio-frequency sputtered at room temperature from a metallic zinc target in a reactive atmosphere consisting of Ar, N_2 and O_2 at a total gas pressure of 4×10^{-3} mbar. XPS measurements were performed directly after thin film deposition (as-dep.) and repeated after two weeks (aged). Additionally, XPS spectra of an aged (5 months) thin film, which was annealed directly after thin film deposition, were obtained for comparison. The annealing was performed for 1h in N_2 atmosphere at about 200 °C. X-ray diffraction measurements confirmed that the investigated ZnON thin films are X-ray amorphous.

The annealed as well as the aged ZnON thin film reveal an increased conductivity compared to the as-deposited films. This increase is due to an increased electron concentration as well as mobility, as indicated by means of Hall effect measurements (Tab. 8.1). While the change in carrier concentration is more pronounced for the annealed thin films, their electrical properties remain stable over months.

As indicated by XPS, only the as-deposited ZnON thin film appears to contain a few Zn–N bonds at the surface (Fig. 8.7(a) and 8.7(g)). After two weeks air exposure the Zn–N peak is reduced owing to a decreased nitrogen content (Fig. 8.7(h)). The annealed ZnON thin film also show a decreased Zn–N peak intensity compared to the as-deposited film (Fig. 8.7(i)). Besides, the Zn–O peak becomes more pronounced and the peak attributed to absorbed oxygen species is significantly reduced as a result of annealing (Fig. 8.7(f)).

In summary, the altered electrical properties of aged ZnON thin films can be attributed to nitrogen loss. Presumably, additional doping owing to adsorbed species from ambient is present. Annealing cannot prevent nitrogen loss from the surface, but the resulting ZnO surface is more stable against adsorption, which leads to improved long-term stability of ZnON thin films.

[1] Kim *et al.*, Sci. Rep. **3**, 1459 (2013)
[2] Reinhardt *et al.*, Phys. Status Solidi (A) **213** (7), 1767–1773 (2016)

Table 8.1: Electrical properties determined by Hall effect measurements: electrical conductivity σ, electron concentration n and Hall mobility μ.

	σ (S/cm)	n (cm^{-3})	μ (cm^2/Vs)
as-dep.	39,4	$5,3 \times 10^{18}$	46
after 5 months	61,0	$7,3 \times 10^{18}$	52
annealed	299,4	$3,4 \times 10^{19}$	55
after 5 months	295,3	$3,3 \times 10^{19}$	56

8.6 Electronic defects in In$_2$O$_3$ and In$_2$O$_3$:Mg thin films on *r*-plane sapphire

D. Splith, F. Schmidt, S. Müller, H. von Wenckstern, M. Grundmann

In$_2$O$_3$ is a material mostly known in its highly conducting, tin-doped form, being used as a transparent conducting oxide, e. g. as an electrode in displays or in thin film solar cells or as a contact layer in touch screens. However, interest in the semiconducting properties of In$_2$O$_3$ arose in the last years. Recently, first rectifying diodes using Schottky contacts (SCs) [1] as well as *pn*-heterojunctions [2] were realized on In$_2$O$_3$ thin films on yttria-stabilized zirconia substrates. Since In$_2$O$_3$ tends to form a surface electron accumulation layer (SEAL) due to its branch point energy lying in the conduction band [3], a reactive sputtering process is needed in order to fabricate SCs. Using such contacts, first space-charge-region based defect-spectroscopic measurements were made possible.

In this study we investigated electronic defects in nominally undoped and Mg-doped In$_2$O$_3$ thin films grown by pulsed laser deposition on *r*-plane sapphire using thermal admittance spectroscopy (TAS) and deep-level transient spectroscopy (DLTS) [4].

From Hall-effect measurements, the influence of the Mg-doping on the free charge carrier density was investigated. Nominally undoped In$_2$O$_3$ shows a high free electron concentration above 1×10^{19} cm^{-3}. Since Mg acts as an acceptor in In$_2$O$_3$, the free carrier concentration is reduced with increasing Mg content. In order to obtain SCs with low series resistance for defect spectroscopy, the Mg-doped or nominally undoped thin films were grown on top of a highly conducting Sn-doped In$_2$O$_3$ layer, acting as a back contact layer. In Fig. 8.8 (a) the IV characteristics of reactively sputtered Pt-SCs fabricated on such samples are shown for different Mg contents. The performance of these SCs strongly depends on the Mg content: while almost no rectification can be observed on samples without Mg-doping, rectification ratios of 570 were observed on the sample with 1 wt.% MgO.

TAS and DLTS measurements were performed for the nominally undoped sample and a 1 wt.% MgO-doped thin film. For the sample without Mg doping, one defect is visible in the TAS measurement. The position of the peak was determined for different measurement frequencies and plotted in an Arrhenius diagram depicted in Fig. 8.8 (b) (open symbols labeled E2). For the Mg-doped sample, two defects were found (solid symbols labeled E2 and E1). Unfortunately, DLTS measurements on the nominally undoped sample are not possible due to the high reverse current. For the Mg-doped
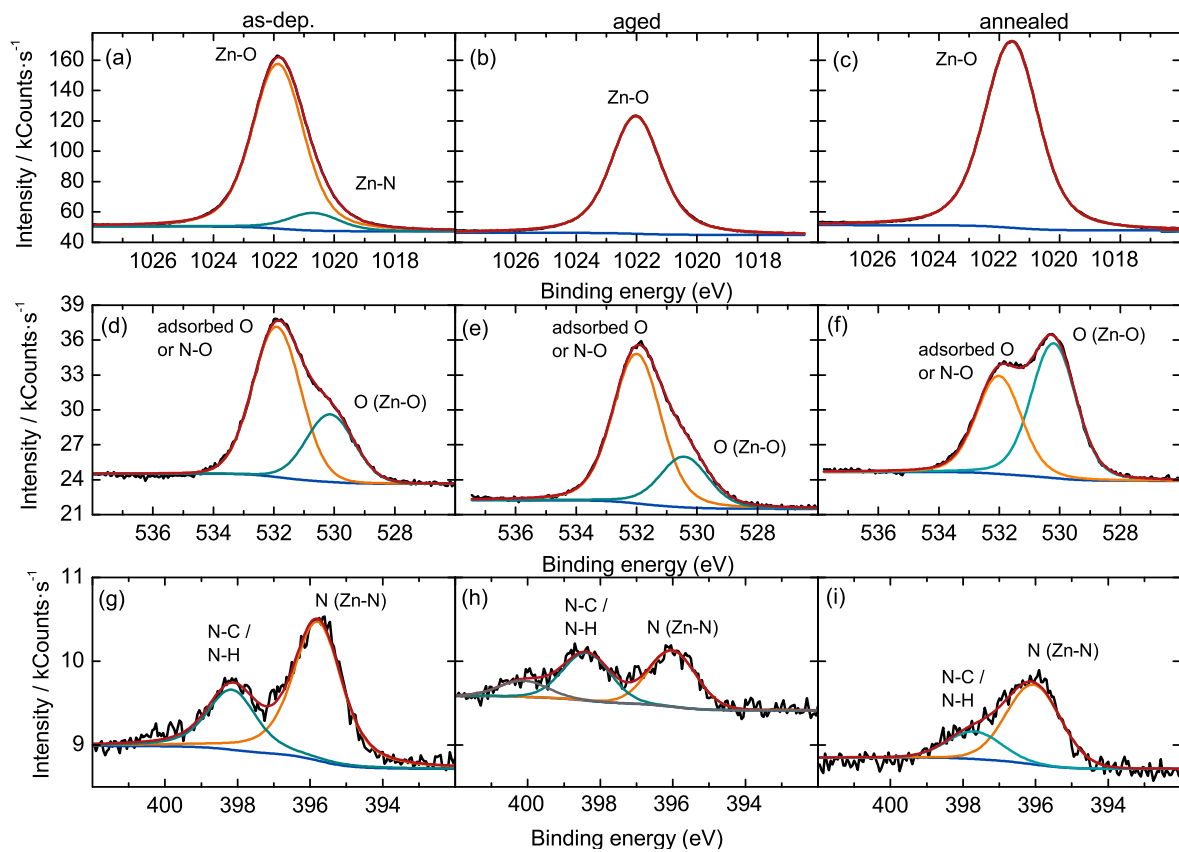
Figure 8.7: XPS spectra of the (a)-(c) zinc $2p_{3/2}$ core level, (d)-(f) oxygen 1s core level and (g)-(i) nitrogen 1s core level for as-deposited, aged (after 2 weeks air exposure) and annealed ZnON thin films.

sample, the DLTS measurement shows three defects, which are also depicted in the Arrhenius plot (solid symbols labeled E3, E4 and E5). From a linear fit we can determine the thermal activation energy E_t as well as the apparent capture cross-sections σ_n, which are summarized in table 8.2. Due to the similar defect parameters of E2 in both samples, we assume that this is the same defect. E1 is only visible in the Mg-doped sample, possible candidates for this defect are therefore interstitials of Mg or In. However, further investigations are necessary in order to clarify the chemical nature of this defect and the other defects observed.

[1] H. von Wenckstern *et al.*, APL Mat. **2**, 046104 (2014)
[2] H. von Wenckstern *et al.*, Adv. Electron. Mater. **1**, 1400026 (2015)
[3] P. King *et al.*, Phys. Rev. Lett. **101**, 116808 (2008)
[4] F. Schmidt *et al.*, Phys. Status Solidi B **252**, 10: 2304-2308 (2015)

defect	MgO (wt.%)	method	E_t (meV)	σ_n (cm^2)
E1	1.0	TAS	91	$4.6 \cdot 10^{-18}$
E2	0.0	TAS	189	$1.7 \cdot 10^{-16}$
E2	1.0	TAS	204	$4.6 \cdot 10^{-16}$
E3	1.0	DLTS	283	$4.9 \cdot 10^{-13}$
E4	1.0	DLTS	405	$1.9 \cdot 10^{-13}$
E5	1.0	DLTS	569	$4.2 \cdot 10^{-11}$

Table 8.2: Parameters of the defects found in the Mg-doped and nominally undoped sample by TAS and DLTS measurements

8.7 Room-temperature domain-epitaxy of p-type transparent conductive semiconductor copper iodide thin films for transparent CuI/ZnO heterojunctions

C. Yang, M. Kneiß, M. Lorenz, M. Grundmann

Over the last decade transparent conductive materials (TCMs) had a dramatic increase in interest in the field of optoelectronics. Most attention has been paid to n-type wide bandgap semiconductors including In_2O_3, SnO_2, ZnO, TiO_2 and their doped versions. However, the lack of suitable p-type TCMs has been the main obstacle in front of either passivate or active electronic applications. Copper iodide in the zincblende ground-state phase (γ-CuI) has p-type conductivity with a high Hall mobility (>40 cm^{2}V$^-$1s$^-$1 in bulk), a wide band gap (3.1 eV) with a direct band structure, and a large exciton binding energy (62 meV). These advantageous properties make it one of the most promising p-type TCMs [1].

It is a challenge to grow epitaxial thin films of CuI due to the lack of lattice-matched substrates. Here, we report the room-temperature heteroepitaxial growth of CuI on various substrates by reactive sputtering technique [2]. In such heteroepitaxial growth the formation of rotation domains is observed and hereby systematically investigated in
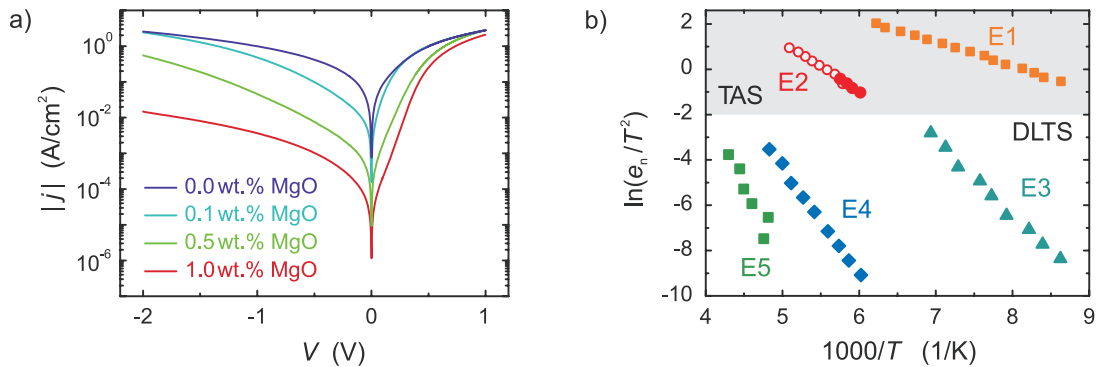
Figure 8.8: (a) current density - voltage characteristic of reactively sputtered Pt-SCs on In_2O_3 thin films with different Mg content. (b) Arhenius-plot of all defects found in Mg-doped (solid symbols) and nominally undoped (open symbols) In_2O_3 thin films by either TAS (gray area) or DLTS measurements.

accordance with existing theoretical study of domain-epitaxy [2, 3]. The rotational symmetries of the substrates used in this study are n = 2, 3, 4 and 6, namely for a-sapphire [$Al_2O_3(11\bar{2}0)$], NaCl(111), NaCl(001), c-sapphire [$Al2O3(0001)$], respectively. As depicted in Fig. 8.9 (a), the heteroepitaxial relationships can be deduced as CuI[$1\bar{1}0$](111) ∥ Al_2O_3[0001]($11\bar{2}0$), CuI<$11\bar{2}$>(111) ∥ NaCl[$11\bar{2}$](111), CuI<$11\bar{2}$>(111) ∥ NaCl[110](001), and CuI<$11\bar{2}$>(111) ∥ Al_2O_3[$1\bar{1}00$](0001). The formation of these different rotation domains can be explained using atomic configurations as sketched in Fig. 8.9 (b).
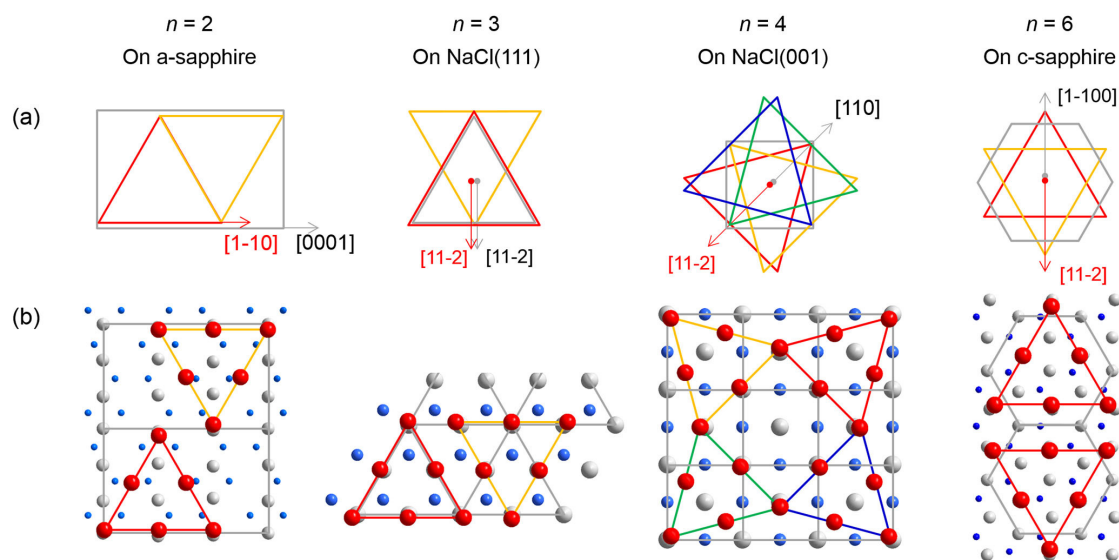
Figure 8.9: (a) Schematic alignment and (b) atomic configurations of CuI crystallites epitaxially grown on NaCl and sapphire substrates. In (b) blue sphere: cation of substrate material; grey sphere: Anion of substrate material; red sphere: I^- of CuI epilayer.

The controllable epitaxy of CuI thin films allows for the combination of p-type CuI with suitable n-type TCMs with the purpose to fabricate epitaxial thin film heterojunctions. Such heterostructures have superior properties to structures without or with weakly ordered in-plane orientation. Based on these results, bipolar heterodiodes were fabricated from epitaxial p-CuI/n-ZnO on a-sapphire heterostructures, as shown in Fig. 8.10. The obtained epitaxial thin film heterojunction of p-CuI(111)/n-ZnO(00.1) exhibits a high rectification up to 2×10^9 (±2 V), a 100-fold improvement compared to diodes with disordered interfaces [2, 4]. This value presents by far the highest rectification of crystalline diodes involving oxide semiconductors. The low growth temperature (room temperature) and the use of sputtering technique make it a facile way to produce large area CuI epilayers for applications in transparent electronics.

[1] M. Grundmann et al., Phys. Status Solidi A **210**, 1671-1703 (2013), doi:10.1002/pssa.201329349
[2] C. Yang et al., Sci. Rep. **6**, 21937 (2016), doi:10.1038/srep21937
[3] M. Grundmann et al., Phys. Rev. Lett. **105**, 146102 (2010), doi:10.1103/PhysRevLett.105.146102
[4] F. L. Schein et al., Appl. Phys. Lett. **102**, 092109 (2013), doi:10.1063/1.4794532
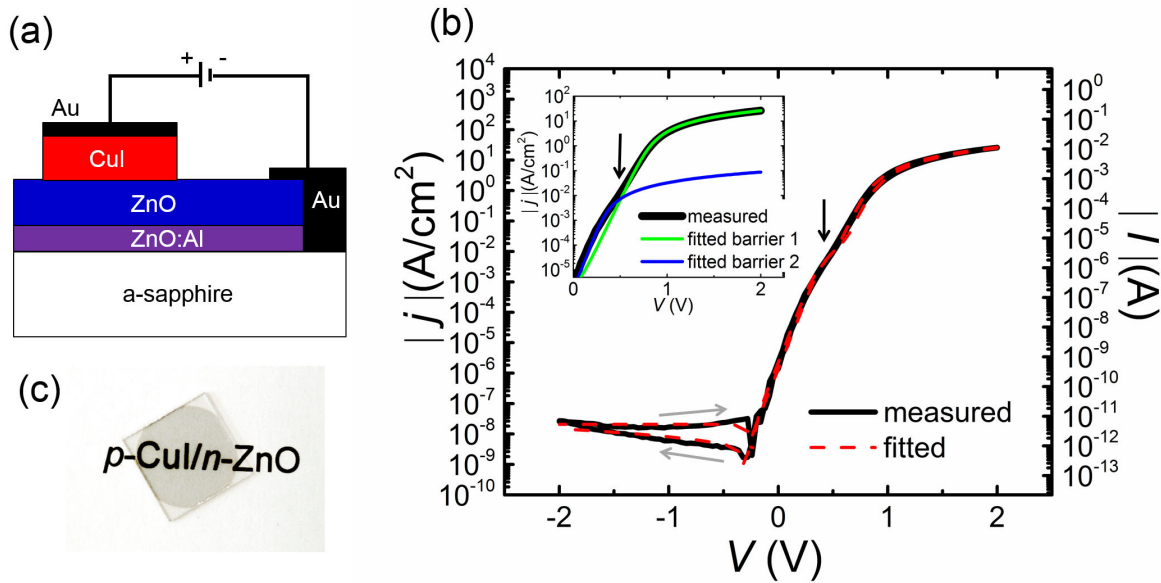
Figure 8.10: (a) Schematic of the CuI/ZnO diode structure, (c) photograph of CuI/ZnO bilayer on a-sapphire substrate, and (b) Current density vs. voltage characteristic of CuI/ZnO diode. The inset depicts the characteristics of the fitted multiple barriers near the kink region. Black arrow: kink at 0.6 V probably related to inhomogeneous diode properties. Grey arrow: voltage sweeping direction.

8.8 Boosting the Figure of Merit of p-Type Transparent Conductors: Degenerate Copper Iodide Thin Film Synthesized at Room Temperature

C. Yang, M. Kneiß, M. Lorenz, M. Grundmann

Transparent conductors (TCs) are well known for their wide use in passive electronic applications, such as transparent electrodes for solar cells, flat-panel displays and light emitting diodes. However, the lack of high-performance p-type TCs has been the main obstacle for both passive and active electronic applications. A high-conductivity, high optical transmittance material with corresponding low-temperature synthesis techniques is desired for practical use.

In this study, we overcome the challenge in achieving simultaneously high conductivity and transparency for p-type TCs by developing the degenerate wide bandgap semiconductor CuI. We propose industrially applicable techniques including room-temperature physical deposition by reactive sputtering for thin film growth and iodine-doping of CuI. The obtained degenerate CuI polycrystalline thin films exhibit record high p-type conductivity of 156 S/cm for undoped CuI and 283 S/cm for I-doped CuI. At the same time, the films appear clear and exhibit a high transmission of 60−85 % in the visible spectral range. In Fig. 8.11 we summarize the electrical conductivity (σ) and visible transmittance (T_{vis}) (i.e. the transmittance averaged over the visible spectral range 400−800 nm) for CuI thin films as well as for other TCs. For the purpose of achieving simultaneously high σ and T_{vis}, there is obviously a huge gap between p- and n-type TCs. It is now filled by CuI. For a high $T_{vis} > 70$ %, our p-type CuI thin films
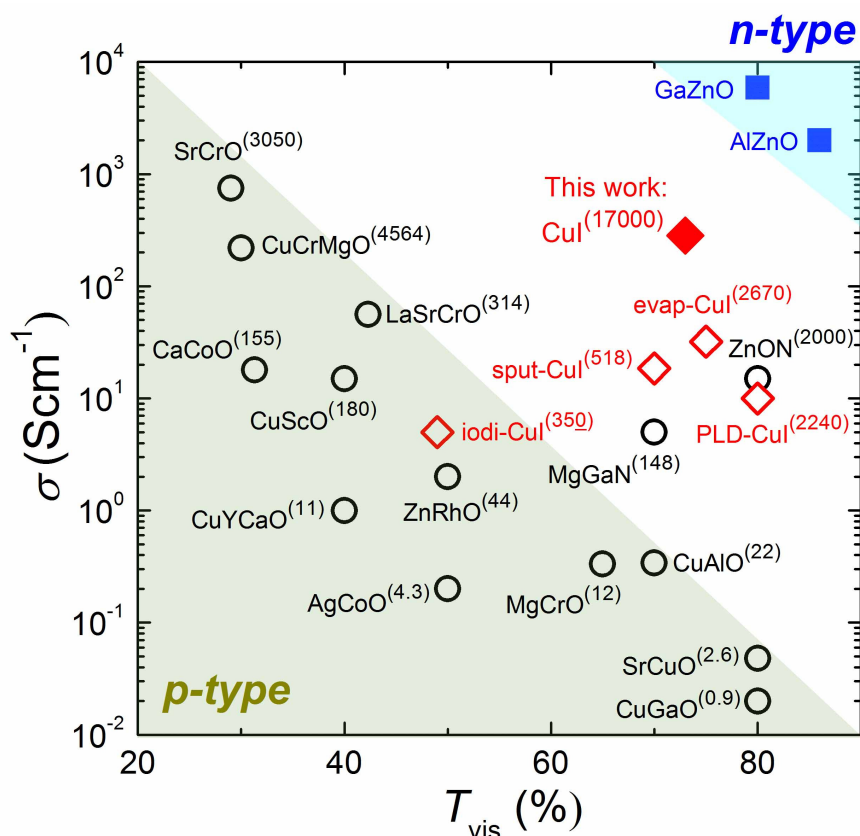
Figure 8.11: Graphical representation of room-temperature σ and averaged T_{vis} for CuI thin films (red rhombuses), other p-type (black circles) and n-type TCs (blue squares).

exhibit a very high conductivity, two or three orders of magnitude higher than that of any other p-type TC of such transparency.

The realization of such simultaneously high conductivity and transparency boosts the figure of merit (FOM) of a p-type TC. As shown in Fig. 8.12, the FOM for p-type TCs has improved over the years from 1996 until now. Except for CuI, the FOM for most p-type TCs is lower than 200 MΩ^{-1} unless sacrificing their transmittance below 50 %. In contrast, the as-deposited CuI in this study shows an FOM about 50 times higher, up to 9500 MΩ^{-1}, while providing a high Tvis above 70 %. This FOM value can be further doubled to 17000 MΩ^{-1} without affecting the transparency by iodine doping. These results demonstrate the superior TC performance of our CuI thin films with respect to all measures. The CuI reported here exhibits significantly higher FOM (10 times) compared to previously reported CuI and p-type ZnO, and even 100 times greater compared to any other p-type TC.

Our results underscore the great potential of CuI applied as p-type transparent electrodes [1]. It is also compatible with many other n-type TCs for active device structures, such as transparent CuI/ZnO bipolar diodes [2]. Besides diodes, CuI/n-type TC tunneling contacts also appear attractive and could be a further direction of research. The sputtering technique at room temperature used here can be upscaled for applications of CuI in transparent electronics. These results may motivate further systematic studies of CuI as one of the most promising p-type TCs [3].

[1] C. Yang et al., PNAS **113**, 12929-12933 (2016), doi:10.1073/pnas.1613643113
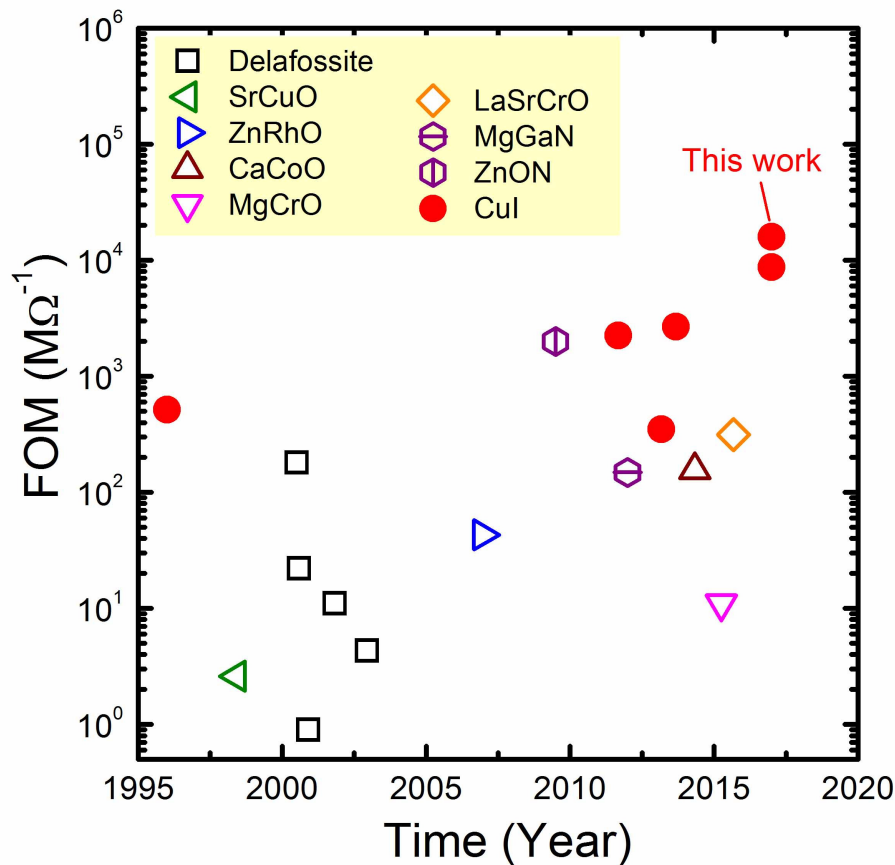
Figure 8.12: Graphical representation of FOM over time for p-type TCs with T$_{vis}$ > 30%.

[2] C. Yang et al., Sci. Rep. **6**, 21937 (2016), doi:10.1038/srep21937

[3] M. Grundmann et al., Phys. Status Solidi A **210**, 1671-1703 (2013), doi:10.1002/pssa.201329349

8.9   Exchange bias in LaNiO$_3$ / LaMnO$_3$ superlattices

H.M. Wei, J. Barzola-Quiquia[*], T. Höche[†], C. Patzig[†], M. Lorenz, and M. Grundmann

[*]Division of Superconductivity and Magnetism, Institute für Experimentelle Physik II, Universität Leipzig

[†]Center for Applied Microstructure Diagnostics, Fraunhofer-Institut für Mikrostruktur von Werkstoffen und Systemen, Halle/S.

The exchange bias (EB), exhibiting a shift of the center of the magnetic loop along the magnetic field axis, has tremendous utility in magnetic recording, magnetic tunnel junctions, and giant magnetoresistance sensors [1]. For a long time, it has been known in many different systems containing interfaces between ferromagnetic and antiferromagnetic materials [2]. Recently, we observed an unexpected EB effect in superlattices (SLs) composed of layers of paramagnetic LaNiO$_3$ (LNO) and ferromagnetic LaMnO$_3$

(LMO). The SLs are grown by PLD with structure of $LMO_n+[LNO_m/LMO_n]_l$ SLs (m and n indicate the number of unit cells, respectively, therafter referred to as $[m/n]_l$). The stacking periodicity is repeated l times to adjust the total SL thickness. Two kinds of $SrTiO_3$ (STO) single crystals with orientations of (001) and (111) are used as substrates.
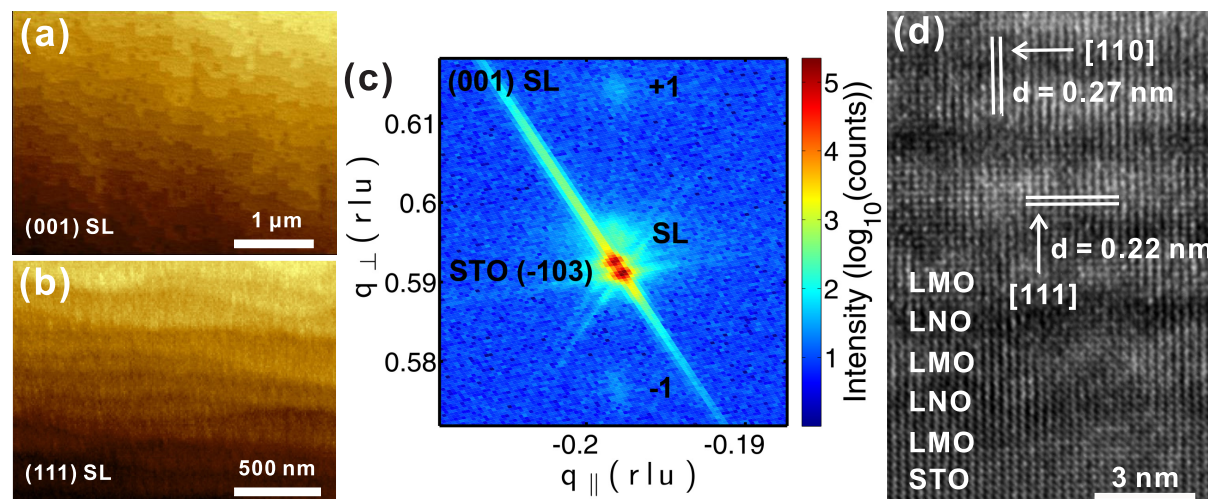
Figure 8.13: AFM images of $[2/2]_6$ LNO/LMO SLs deposited on (a) STO (001) and (b) STO (111) substrates. (c) XRD RSM with indicated reflection of $[8/2]_{10}$ SL grown along (001) orientation. (d) TEM image of the $[7/7]_{10}$ SL grown on STO (111) substrate.

Fig. 8.13 (a) and (b) display AFM images of $[2/2]_6$ SLs deposited on STO (001) and STO (111) substrates, respectively. The SLs show monolayer terraces with low roughness of 0.095 nm for (001) and 0.1115 nm for (111). The steps height are 0.39 nm and 0.22 nm, corresponding to one unit cell for (001) and (111) orientation, respectively. The in-plane epitaxial relationship between SLs and substrates is analyzed by X-ray diffraction (XRD) reciprocal space map (RSM). Taking the $[8/2]_{10}$ SL, for example, the in-plane lattice match can be deduced from the vertical alignment of the SL and substrate peaks as shown in Fig. 8.13 (c). In addition, the SL period can be calculated from the distance between two adjacent satellite peaks. More accurate structural parameters are obtained by high-resolution transmission electron microscopy (TEM). As shown in Fig. 8.13 (d), 10 double layers LNO/LMO with thickness of about 3 nm were confirmed, corresponding to the designed (111)-oriented $[7/7]_{10}$ SL structure. The inter-planar spacing along the growth direction is 0.22 nm, whose value is equal to the steps height of one unit cell measured by AFM. The in-plane lattice parameter of SL is about 0.27 nm, further confirming the lattice match between SL and substrate.

The magnetic properties of SLs are measured using superconducting quantum interference device (SQUID) and double checked by the vibrating sample magnetometer of a physical property measurement system (PPMS-9) from Quantum Design, Inc. Fig. 8.14 (a) presents hysteresis loops of (111)-oriented SL at 2 K after field-cooling from room temperature in the presence of ± 1 T fields. The shift of the hysteresis loops along the magnetic field axis is clearly visible. This behavior is a classic signature of EB effect. Different from the previous study by Gibert *et al.* [3], the EB is also present in the (001)-oriented SL with a clear shift of the hysteresis loops at different measured temperatures as shown in Fig. 8.14 (b). In order to further understand the EB effect, temperature-dependent zero-field-cooling (ZFC) and field-cooling (FC) magnetization
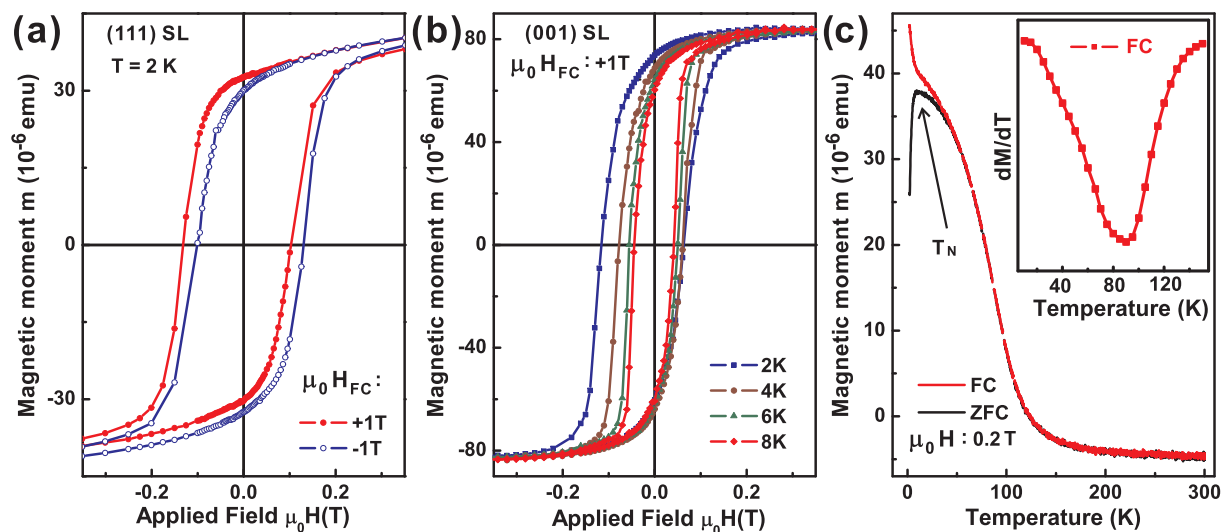
Figure 8.14: (a) Magnetic hysteresis loops at 2 K for the (111)-oriented $[7/7]_{13}$ SL after field-cooling at two different fields $\mu_0 H_{FC} = \pm 1$ T. (b)Hysteresis loops for the (001)-oriented $[5/5]_{10}$ SL at different constant temperatures after cooling the sample with a field of +1 T. (c) Magnetic moment versus temperature of (111)-oriented SL in the ZFC and FC states at a field of 0.2 T. The inset is dM/dT versus temperature of FC curve.

measurements have been performed. As shown in Fig. 8.14 (c), the ZFC and FC curves show different behavior at low temperatures, suggesting that the sample contains two magnetic phases with different magnetocrystalline anisotropy [4]. Since the difference in the magnetic moment measured in ZFC and FC sequences was insignificant in LMO/LaAlO$_3$ SLs, we conclude that the EB observed in LNO/LMO SLs is related to the interfaces between the two components. In addition, the Curie temperature of SL was obtained to be 90 K from the minium of the dM/dT curve as shown in the inset of Fig. 8.14 (c). If we define the characteristic Néel temperature (T_N) where the ZFC magnetic moment shows a maximum, a temperature of 10 K was obtained.

[1] R. L. Stamps: J. Phys. D: Appl. Phys. **33**, R247-R268 (2000), doi:10.1088/0022-3727/33/23/201
[2] J. Nogués et al.: J. Magn. Magn. Mater. **192**, 203-232 (1999), doi:10.1016/S0304-8853(98)00266-2
[3] M. Gibert et al.: Nature Mater. **11**, 195-198 (2012), doi:10.1038/nmat3224
[4] M. Lorenz et al.: CrysEngComm **14**, 6477-6486 (2012), doi:10.1039/C2CE25505G

8.10 Effect of Bi-content and Gd-doping on the multi-ferroic properties of BaTiO$_3$-BiFeO$_3$ superlattices

S. Hohenberger, M. Lorenz, V. Lazenka*, K. Temst*, M. Grundmann

*Institute for Nuclear and Radiation Physics, KU Leuven, Belgium

Periodic thin film multilayers of $BaTiO_3$ (BTO) and $BiFeO_3$ (BFO) show vastly increased magnetoelectric (ME) coupling, compared to single phase materials [1]. These layered epitaxial thin films combine the ferroelectric BTO and the only known single phase room temperature multiferroic BFO. Our previous work suggests that the exceptionally large ME voltage coefficients of up to 49 V/cmOe at 300 °C in these films is linked to epitaxial strain at the interfaces [2]. However, the exact origin of the magnetoelectric coupling mechanism still requires further investigation. Additionally, the ferroelectric and magnetic performance of these films have to be improved to pave the way for practical applications.

In single phase films of BFO, a common route is to enrich the Bi-content in the ablation target to account for the inherent volatility of Bi [3] and thus reduce the defect density and reduce leakage current. In another approach, substituting Bi in BFO with rare earth ions such as La, Nd, or Gd has been shown [4] to increase the saturation magnetization and decrease the roughness of single phase $Bi_{1-x}RE_xO_3$ films deposited on STO.

Samples consisting of 15 double layers of 15 nm BTO and 5 nm - 50 nm BFO were fabricated by pulsed laser deposition on un-doped and Nb-doped, (001)-oriented $SrTiO_3$ (STO) single-crystal substrates at 650 °C and 0.25 mbar oxygen partial pressure. The substrates were etched and annealed prior to deposition, creating TiO_2-terminated, single unit-cell stepped surfaces. The composition of the BFO films was varied by altering the proportions of Bi_2O_3, Gd_2O_3, and Fe_2O_3 powders used in the target synthesis, yielding the nominal compositions $Bi_{1.1}FeO_3$ and $Bi_{0.95}Gd_{0.05}FeO_3$.

X-ray diffraction experiments show the high crystalline quality of the deposited films. As depicted in the reciprocal space maps (RSM) in fig. 8.15, superlattice fringe peaks are clearly visible to seventh order and higher, indicating sharp, coherent interfaces. Furthermore, RSM measurements in the vicinity of asymmetric substrate peaks (not shown here) indicate a relaxed growth of the superlattices with respect to the substrates. Fig. 8.16 (a) highlights the pronounced enhancement of the magnetic properties of BTO-BFO superlattices by Gd-doping. While at room temperature the superlattice with $Bi_{1.1}FeO_3$ saturates at 1.5 emu/cm^3, the sample with $Bi_{0.95}Gd_{0.05}FeO_3$ shows an enhanced saturation magnetization of 2.2 emu/cm^3. Whereas the highest difference in magnetic saturation was measured in samples with large BFO thickness relative to the BTO thickness, samples with low BFO thickness showed the both the largest values and most pronounced differences for the ME voltage coefficients. Depicted in fig. 8.16 (b) are temperature-dependent measurements of the ME voltage coefficients of two such samples with low BFO thickness, with the $Bi_{1.1}FeO_3$ sample reaching 34 V/cmOe at 300 K, and the $Bi_{0.95}Gd_{0.05}FeO_3$ sample reaching 51 V/cmOe.

In summary, high quality multiferroic superlattices of BTO and BFO were fabricated on STO single crystalline substrates. Variation of the Bi content and doping with Gd were shown to be promising approaches to further push the boundaries of magnetoelectric coupling in composite multiferroic materials.

[1] M. Lorenz *et al.*, J. Phys. D: Appl. Phys. **47**, 135303 (2014)
[2] M. Lorenz *et al.*, Adv. Mater. Interfaces **3**, 1500822 (2016)
[3] J. Wu *et al.*, ACS Appl. Mater. Interfaces **4**, 1182 - 1185 (2012)
[4] V. Lazenka *et al.*, J. Phys. D: Appl. Phys. **46**, 175006 (2013)
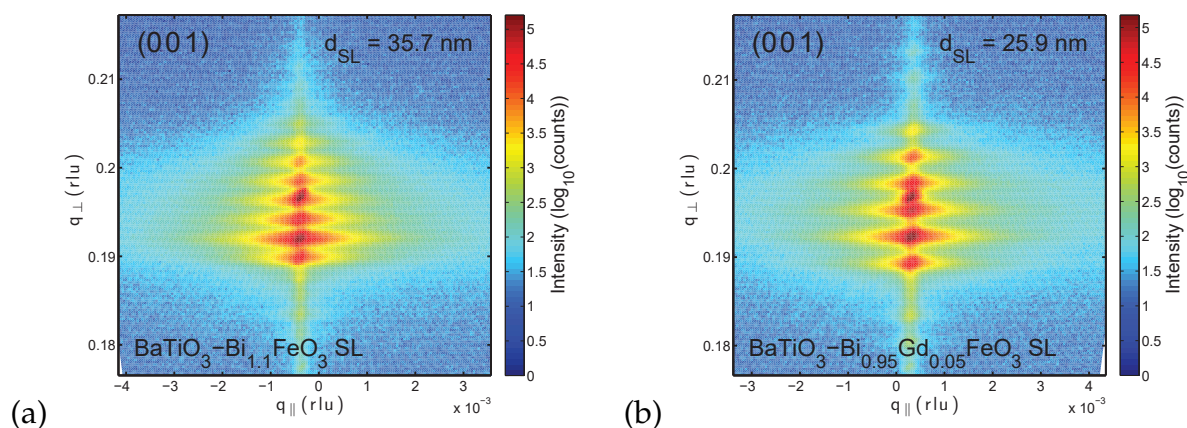
Figure 8.15: Reciprocal space maps around the (001) STO substrate peak of superlattices 15× $BaTiO_3$ and (a) $Bi_{1.1}FeO_3$ and (b) $Bi_{0.95}Gd_{0.05}FeO_3$. The inserted superlattice periodicities d_{SL} were calculated from the spacing of the fringe peaks.
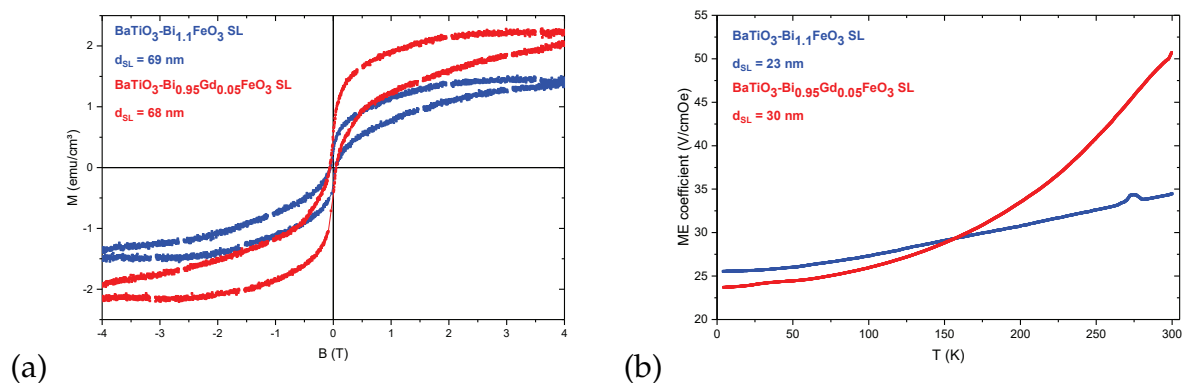
Figure 8.16: (a) Room temperature magnetic hysteresis measurements of two superlattices with high BFO layer thickness; (b) T-dependent ME voltage coefficient measurements of two superlattices with low BFO layer thickness. BTO layer thickness is kept constant at ca. 15 nm for all samples.

8.11 Optical properties of CuI-based inorganic-organic hybrid materials

L. Trefflich, G. Benndorf, M. Wille, R. Schmidt-Grund, H. Krautscheid[*], M. Grundmann

[*]Institut für Anorganische Chemie, Universität Leipzig, Johannisallee 29, 04310 Leipzig, Germany

In recent years, a lot of research has been done in the field of phosphors for white light generation. However, nearly all of them suffer from doping with rare-earth elements [1], which can be problematic because of their environment unfriendly mining and possible supply issues. A promising replacement are CuI-based lighting phosphors due to their optical tunability, facile synthesis and high quantum yield of up to 95 % [2]. We studied the optical as well as electrical properties of (CuI)-based inorganic-organic hybrid materials for application in rare earth free white light LEDs and electrically driven
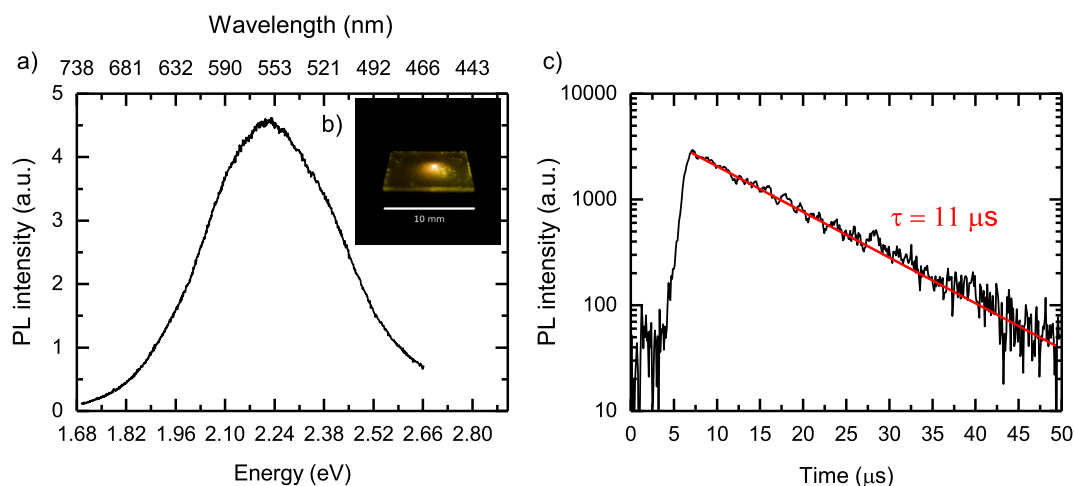
Figure 8.17: a) Photoluminescence spectrum of $Cu_2I_2(3-pc)_4$ shows spectrally broad emission around 550 nm, which results in bright orange light clearly visible to the naked eye (b). c) Timeresolved photoluminescence spectroscopy shows a decay time of around 10 μs as well as a monoexponential decay in the time range up to 50 μs.

inorganic-organic solid state lasers. Therefore we deposited approximately 170 nm thin films of $Cu_2I_2(3-pc)_4$ ($3-pc$ means 3-Picoline) via spincoating on Si + SiO_2 and c-plane sapphire substrates and investigated their optical properties as well as temporal dynamics using photoluminescence spectroscopy. We found spectrally broad photoluminescence emission around 550 nm resulting in intense orange visible light emission (Figure 8.17). This luminescence is most likely caused by recombination of electrons and holes in the LUMO and HOMO bands respectively [3]. The luminescence shows a monoexponential decay with a dacay time of around 10 μs. This is roughly two orders of magnitude shorter than the lifetime of currently used phosphores [4], demonstrating the applicational potential of this material class.

[1] K. Li *et al.:* J.Mater.Chem.C **4**, 5507 (2016), doi:10.1039/C6TC00436A.
[2] W. Liu *et al.:* J. Am. Chem. Soc. **137**, 9400, (2015), doi:10.1021/jacs.5b04840.
[3] A. Moliton: Optoelectronics of Molecules and Polymers, Springer, 2006
[4] M. Janulevicius *et al.:* Sci. Rep. **6**, 26098 (2016), doi:10.1038/srep26098.

8.12 Growth kinetics of ZnO nanowires grown by pulsed laser deposition

A. Shkurmanov, C. Sturm, H. Hochmuth, M. Grundmann

The exploitation of ZnO nanostructures such as nanowires (NWs) for devices is already demonstrated for a wide variety of applications as light emitters, electromechanical resonators, pressure and 3D imaging sensors. However, the functionality of these devices depends strongly on the NW geometrical characteristics [1]. For instance, thick NWs with a diameter of few μm are preferred for applications which are based on compression, e.g. caused by an externally applied pressure, whereas thin NWs with a diameter
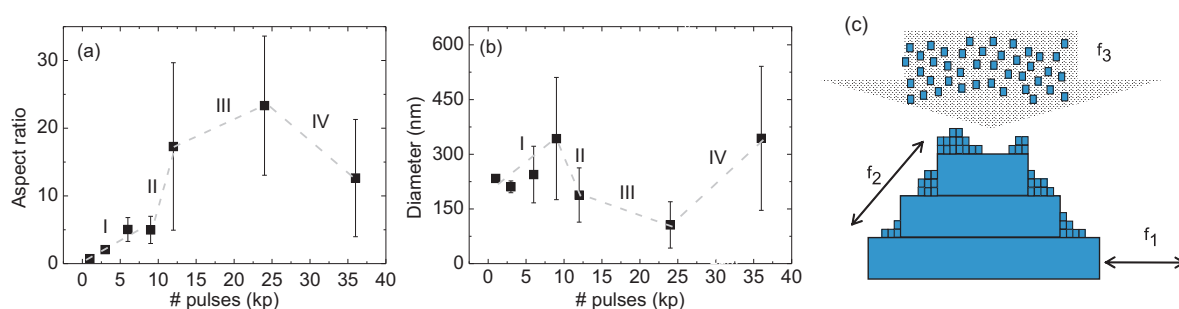
Figure 8.18: Median values of aspect ratio (a) and diameter (b) of nanowires, grown on pure ZnO layer, as functions of number of laser pulses. First 3000 pulses corresponds to the formation of ZnO seeds for further growth of nanowires. A scheme of the NW growth by interraction of three flows of the ZnO particles (c).

of a few nm offer a large surface-to-volume ratio, making them interesting for bending sensitive applications [2, 3]. Thus the understanding of the growth kinetics in order to control the shape of the NWs is important [4].

In order to investigate the growth process of ZnO NWs by using undoped ZnO seed layers and a growth temperature of $T \approx 950\,°C$, we fabricated a series of NWs which differ in the amount of deposited ZnO material. This was achieved by varying the number of laser pulses from 3000 to 36 000. The first 3000 pulses are responsible for the growth of the pyramidal nucleation seeds. For larger pulse numbers the growth of the NWs is then obtained on top of the seeds. The NW aspect ratio and diameter are presented in Fig. 8.18 as a function of the laser pulse number. For the applied pulses in the range of $3000 - 9000$ (regime I), the length of the NWs increases whereas the NW diameter remains almost constant. A larger number of laser pulses in the range of $9000 - 12\,000$ (regime II) leads to an increase of the length and decrease of the diameter. When $12\,000 - 24\,000$ (regime III) pulses were applied, the length and the diameter increases and decreases further, respectively, but at a lower rate. For larger number of laser pulses (over 24 000 pulses, regime IV) we observe that in some cases of growth, the diameter increases whereas the length decreases with number of pulses.

The observed behavior of the NW developing might be caused by interaction of three flows of particles (Fig. 8.18c) [4]. The first one (f_1), the flow of the deposited particles on the seed layer, is responsible for formation the nucleation seeds. The second flow (f_2) is a movement of the particles on the facets of the NW and responsible for the length and diameter developing. The third (f_3) is a constant flow of particles which are deposited from the target to the substrate and arrive directly to the NW facets.

[1] M. Riaz *et al.:* Adv. Funct. Mater. **21**, 628 (2011), doi:10.1002/adfm.201001203.

[2] Z. L. Wang: MRS Bulletin **37**, 814 (2012), doi:10.1557/mrs.2012.186.

[3] C. Pan *et al.:* Nat. Photonics **7**, 752 (2013), doi:10.1038/NPHOTON.2013.191.

[4] A. Shkurmanov *et al.:* Procedia Engineering **168**, 1156 (2016), doi:10.1016/j.proeng.2016.11.387.
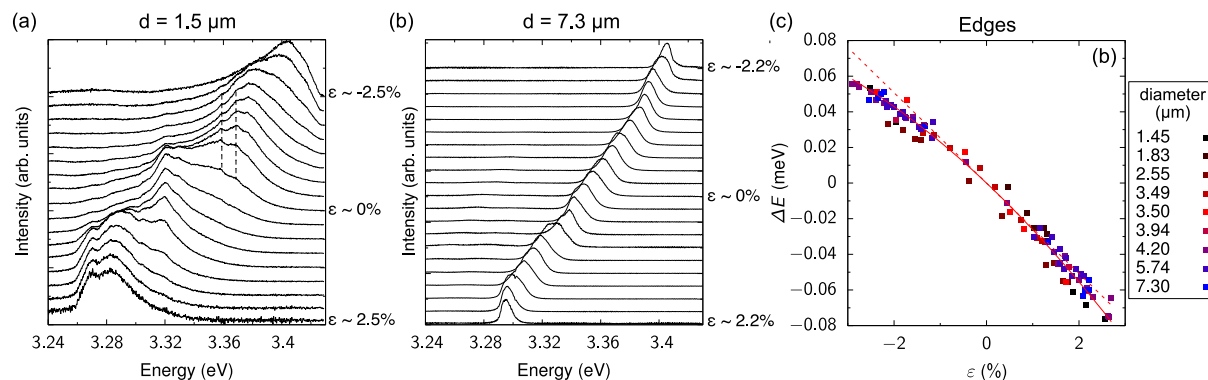
Figure 8.19: Cathodoluminescence spectra of linescans across the wires perpendicular to the wire c-axis for bent microwires with a diameter of (a) $d = 1.5\,\mu m$ and (b) $d = 7.3\,\mu m$ The vertical dashed lines in (a) depict exemplarily the spectral positions of two modes. (c) Shift of the emission energy as a function of the strain (ϵ) determined at the tensile and compressive strained edges of the microwires of different diameters and different bending radii. The red dashed and solid lines represent the fit by a polynomial of the first and second order, respectively.

8.13 Non-linear optical deformation potentials in uniaxially strained ZnO microwires

C. Sturm, M. Wille, J. Lenzner, S. Khujanov, M. Grundmann

ZnO microwires are ineresting building blocks for the realization of low dimensional devices, e.g. pressure sensors with high spatial resolution [1]. The presence of strain leads to a change of the electrical and optical properties, especially the band gap energy. It can be exploited in order to tune the emission properties, therefore the optical deformation potentials were investigated in the last years in detail (e.g. Ref. [2]). However, these investigations are mainly limited to small strain values and only linear optical deformation potentials were reported.

For the determination of the optical non-linear deformation potential, we fabricated ZnO microwires with diameters in the range $d = 1.5 - 7.3\,\mu m$ by vapour phase transport method. Selected microwires were transferred onto a Si substrate and bent. By doing so we induced an uniaxial strain of up to $\pm 2.9\,\%$. The optical properties of these bent microwires were investigated by cathodoluminescence spectroscopy at $T = 10\,K$. Exemplary emission spectra are shown in Fig. 8.19(a,b) for two microwires with a diameter of $d = 1.5\,\mu m$ and $d = 7.3\,\mu m$. The presence of the rich mode structure, which is observable for the thin microwire, we attribute to the fact that in these microwires the photon density of states is not monotonically increasing and exhibit minima and maxima at certain energies. At these energies the recombination of the excited charge carriers is suppressed or rather enhanced, similar to the Purcell effect in resonators. For the thick microwires, the photon density of states is almost increasing with energy and thus the Purcell effect is less pronounced.

The change in the emission energy as a function of induced strain for different microwire diameters is shown in Fig. 8.19c. At the compressive and tensil strained edge of the microwire the photon density of states is less modified with regard to the free space such that the emission spectrum resembles almost the gain spectrum of the ma-

terial [3]. We thus consider only the emission from these two edges by applying scans along the wire covering positions with different bending radii. Note, the energy shift determined by this method is in excellent agreement with that, which can be obtained from linescans across the thick wire from the tensile to the compressive strained edge [3]. For small strain values ($\|\epsilon_c\| \lesssim 1.5\%$), we observe a almost linear dependence of the emission energy on the applied strain. This is in agreement with our previous experiments [4]. However, for larger strain values, a non-linear energy shift is observable and its magnitude depends on the sign, i.e. tensile and compressive, of the strain. In order to deduce the optical deformation potentials we described the observed energy shift by a polynomial of second order, i.e. $\Delta E = D_1 \epsilon + D_2 \epsilon^2$. The linear and non-linear optical deformation potentials are then determined to be $D_1 = (-2.50 \pm 0.05)\,\text{eV}$ and $D_2 = (-15.0 \pm 0.5)\,\text{eV}$, respectively. This agrees very well with those which are deduced from theoretical calculations [5]. In this publication, optical deformation potentials were determined to be $D_1 = -2.2\,\text{eV}\ldots-4.1\,\text{eV}$ and $D_2 = -6.7\,\text{eV}\ldots-19.2\,\text{eV}$, depending on the applied method.

[1] Z. L. Wang: Mat. Sci. Eng. R **64**, 33 (2009), doi:10.1016/j.mser.2009.02.001.
[2] K. Watanabe *et al.*: ACS Nano **9**, 2989 (2015), doi:10.1021/nn507159u.
[3] C. Sturm *et al*: Appl. Phys. Lett. **110**, 062103 (2017), doi:10.1063/1.4975677.
[4] C. P. Dietrich *et al*: Appl. Phys. Lett. **101**, 141116 (2012), doi:10.1063/1.4757572
[5] W. A. Adeagbo *et al.*: Phys. Rev. B **89**, 195135 (2014), doi:10.1103/PhysRevB.89.195135.

8.14   Growth and characterisation of MgO/TiN superlattices

F. Jung, V. Zviagin, M. Bonholzer, C. Sturm, J. Lenzner, S. Selle*, R. Schmidt-Grund, M. Lorenz, M. Grundmann

*Nanomaterialien und Nanoanalytik, Center für Angewandte Mikrostrukturdiagnostik CAM, Fraunhofer-Institut für Mikrostruktur von Werkstoffen und Systemen IMWS, Walter-Hülse-Straße 1, 06120 Halle, Germany

We investigated the growth and structural properties of MgO/TiN-based multilayers and superlattices with a lattice periodicity of a few nanometers. Planar periodic nanostructures comprising of a plasmonic and a dielectric component are expected to exhibit a hyperbolic dispersion, i.e. different signs for the effective dielectric functions in the direction of layer growth $\epsilon_\perp$ and in the layer plane $\epsilon_\parallel$. These materials are referred to as hyperbolic metamaterials [1]. Such structures, with titanium nitride as plasmonic component, have already been realised by Naik *et al.* [2].

Single layers of titanium nitride and magnesium oxide were ablated on MgO(100)-substrates with a miscut of less than 0.1° from sintered targets in an argon atmosphere using pulsed laser deposition (PLD). TiN single layers with high crystalline quality have been successfully fabricated in our group by M. Bonholzer *et al.* [3]. The growth was monitored in-situ by reflection high-energy electron diffraction (RHEED). From the RHEED oscillations and diffraction patterns, the thickness of the layers and the growth mode were derived, respectively. RHEED oscillations were observable up to
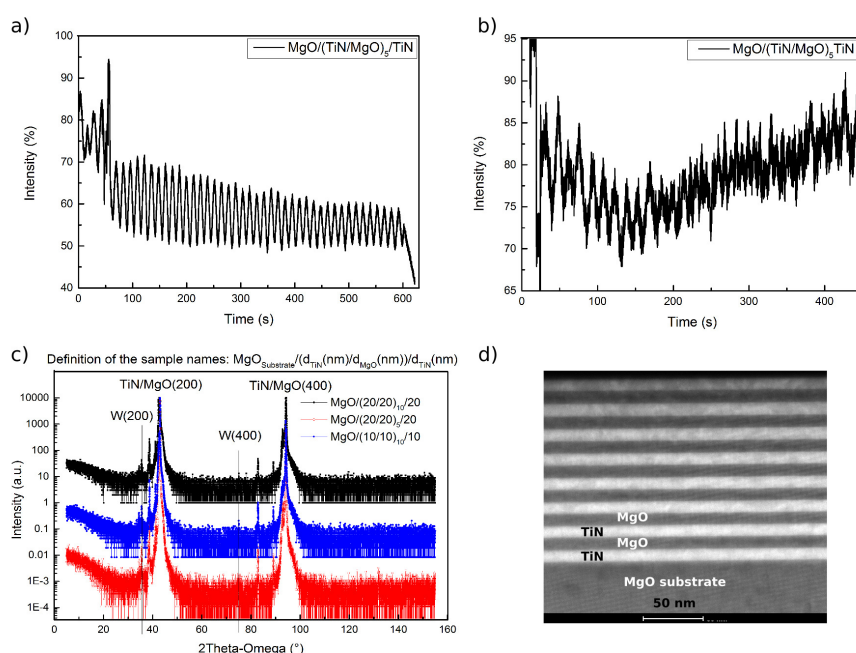
Figure 8.20: a) and b): RHEED oscillations during the growth of the first and the eleventh single layer in a MgO/TiN-superlattice structure, respectively. From the number of the intensity maxima, the thickness of the layers was calculated. c): XRD 2θ-ω-scans with different diffraction peaks. The unlabeled peaks are the K_β-, L_{α_1}-, L_{α_2}-, K_{α_1}- and K_{α_2}-peaks of the (200) and (400)-orientation of the superlattice respectively. Data is presented for three samples with different number of layer pairs as indicated in the graphs. d): High-angle annular dark-field imaging (HAADF) HRSTEM image of a TiN/MgO superlattice on MgO(100)-substrate with seven layers of MgO and one layer of TiN (measured at the CAM of the IMWS in Halle).

a total lattice thickness of approximately 110 nm with single layer thicknesses of TiN and MgO layers of approx. 10 nm, indicating a Frank-van-der-Merwe growth mode (Fig. 8.20(a),(b)).

Superlattices were grown with a number of three to ten layer pairs of titanium nitride and magnesium oxide. X-ray reflectivity (XRR), X-ray diffraction 2θ-ω scans and reciprocal space maps revealed homogeneous layer thicknesses and an epitaxial growth of the multilayer samples, as well as a small amount of tungsten, originating from inpurities in the sintered TiN-targets (Fig. 8.20(c). By modeling the XRR data, the layer thicknesses of individual layers in the superlattice were determined and this information was used to achieve a uniform layer thickness. High-resolution transmission electron microscopy, high-resolution scanning electron microscopy (HRSTEM), scanning electron microscopy-energy-dispersive X-ray spectroscopy and nanobeam diffraction studies have been performed, yielding very smooth interfaces and a almost perfect crystal structure throughout the entire layer stack (Fig. 8.20(d)).

Ellipsometry was applied to both, single- and multilayers, in order to judge the quality of their optical properties. For the optical figure of merit (*FOM*) of the TiN layers, defined by $FOM = -\epsilon'/\epsilon''$, where ϵ' and ϵ'' are the real and the imaginary part of the dielectric function, we reached up to now $FOM = 4$. Current research is focused on improving the optical properties of the TiN films in order to beat the best values

known from literature (*FOM* = 4 [1]). This should be achieved by a systematic study of the dependence of the optical properties on growth parameters during PLD.

[1] G.V. Naik *et al.*: Optical Materials Express **2**, 478 (2012), doi:10.1364/OME.2.000478.
[2] G.V. Naik *et al.*: PNAS **111**, 7546 (2014), doi:10.1073/pnas.1319446111.
[3] M. Bonholzer *et al.*: Physica Status Solidi A **211**, 2621 (2014), doi:10.1002/pssa.201431458.

8.15 Model dielectric function analysis of normal and inverse Spinel Ferrites in relation to their magnetic and structural properties

V. Zviagin, P. Huth[*], Y. Kumar, I. Lorite, M. Bonholzer, A. Setzer, K. Fleischer [†], R. Denecke,[*] P. Esquinazi, M. Grundmann, R. Schmidt-Grund

[*]Universtät Leipzig, Wilhelm-Ostwald-Institut für Physikalische und Theoretische Chemie, Linnéstr. 2, Germany.

[†]School of Physics, Trinity College Dublin, Dublin 2, Ireland
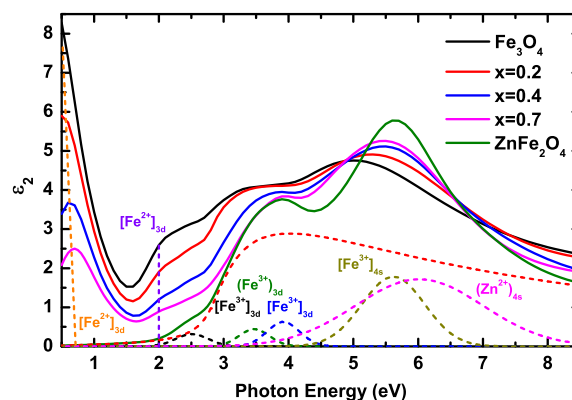
Figure 8.21: Model dielectric function (ε_2) calculated from SE for $Zn_xFe_{3-x}O_4$ composites with the corresponding Zn concentrations x as indicated. Dashed model oscillator functions corresponding to involved cations are depicted for $x = 1$ MDF, while the dashed straight lines below 2.0 eV show the oscillator position involving Fe^{2+} for $x < 1$. Square brackets and parentheses correspond to octahedrally and tetrahedrally coordinated cations, respectively.

Transition metal spinel oxides have played a vital role in technologically advancing the semiconductor industry and continue to do so as a result of their versatile application potential, namely high-frequency and high-power applications, detectors, sensors, microwave and spintronic devices [1]. With a chemical formula AB_2O_4, spinel ferrites have $(A^{2+}_{1-x}B^{3+}_x)[A^{2+}_xB^{3+}_{2-x}]O^{2-}_4$ ion distribution where x is the inversion parameter and tetrahedral and octahedral crystal lattice sites are denoted by parentheses and square brackets, respectively. Depending on the choice of A and B elements as well as growth parameters, namely temperature and pressure, synthesis of normal, disordered and inverse spinel structures with variable magnetic and electronic properties is possible.
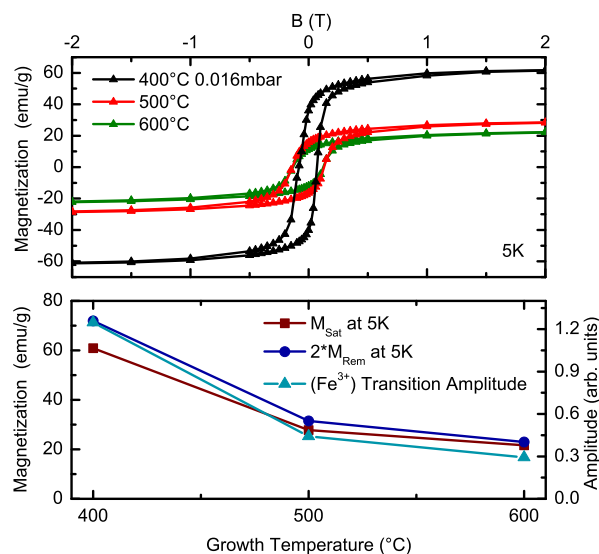
Figure 8.22: (Top) Magnetization as a function of applied magnetic field measured at 5 K. (Bottom) Saturation and twice of remanence magnetization as well as the amplitude of transition involving tetrahedral Fe^{3+} cations obtained from the model dielectric function versus growth temperature.

It is only recently that spectroscopic methods have been applied to investigate mechanisms responsible for the mentioned tuneable magnetic properties in $ZnFe_2O_4$ (ZFO) [2]. The model dielectric function (MDF) was obtained by spectroscopic ellipsometry in a wide spectral range $(0.5-8.5)$ eV. From the MDF, we were able to determine the possible cation occupancy as well as the degree of inversion in ZFO and Fe_3O_4 (FFO) spinel ferrites based on the electronic transitions assigned from literature and give a explanation for the magnetic response measured by superconducting quantum interference device (SQUID) [3, 4]. Although optical properties of magnetite have been thoroughly investigated, the controversy over the validity of the assigned optical transitions still remains. In the visible and infrared ranges of the FFO spectrum, spin- and parity-forbidden transitions between the levels of 3d ions in the internal crystal field are apparent [5].

In order to confirm the transitions assigned to both normal ZFO spinel and inverse FFO spinel and to investigate the intermediate structure, composite thin films, $Zn_xFe_{3-x}O_4$ with x varying from $(0-1)$, were grown on (100) MgO substrate in Argon atmosphere at 500 °C by pulsed laser deposition (PLD). In the MDF, transitions involving cations, as indicated in (Fig. 8.21), were assigned. Below 4.5 eV, the transitions were found to be either inter-valence or inter-sublattice charge transfer transitions between 3d bands of Fe^{2+} and Fe^{3+} tetrahedrally and octahedrally coordinated cations. Above this energy, the transitions are mostly between O_{2p} and 4s orbitals of Fe^{2+}, Fe^{3+} and Zn^{2+} cations. Depending on the Fe^{2+} concentration and equivalently the oscillator strength of the transitions located at 0.8 eV and 2.0 eV, a change from disordered normal to disordered inverse spinel is visible between $x = 0.5$ and 0.2. Magnetic response shows expected behaviour at the extremes, but little difference for films with intermediate Zn^{2+} concentrations. Further methods such as magneto-optical Kerr effect as well as
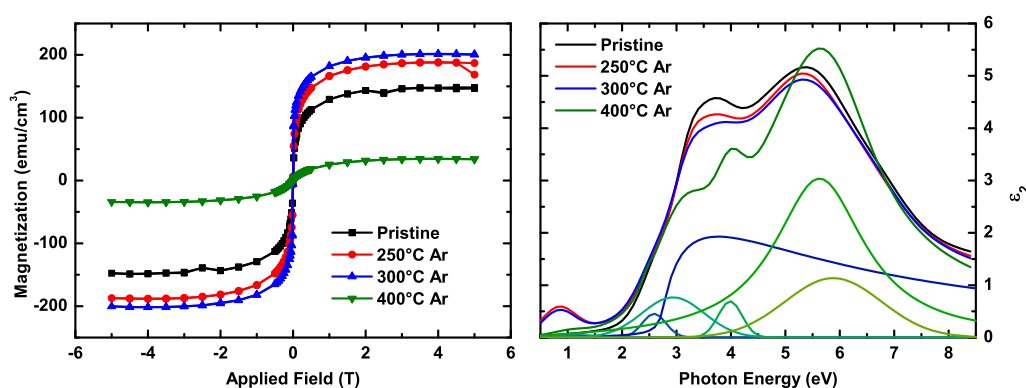
Figure 8.23: (Left) Magnetic response as a function of applied magnetic field for a ZFO thin film annealed in Argon atmosphere at temperatures indicated. (Right) Model dielectric function, (ε_2), obtained by SE for the same thin film.

X-ray photoelectron spectroscopy were employed for obtaining further information on the thin film composition.

ZFO thin films, of 40 nm, were deposited by PLD on (100) $SrTiO_3$ (STO) substrate at temperatures ranging from $400-600\,°C$ and at highest O_2 pressure in order to avoid oxygen vacancies as well as to have the lowest concentration of Fe^{2+} [6]. While little difference in the MDF as well as the magnetic response was seen for thin films grown at 500 °C and 600 °C, the film grown at lowest temperature, 400 °C, showed the greatest amount of disorder. The increase in amplitude of the transition involving tetrahedral Fe^{3+} with decrease in deposition temperature correlates directly to the increasing ferrimagnetic response measured at 5 K, as depicted in (Fig. 8.22) [4]. Mechanism behind this effect is likely due to the dominating magnetic coupling between the octahedral and tetrahedral lattice sites for the thin film grown at lowest temperature.

A further study has been conducted in order to investigate the influence of annealing temperature as well as environment on the structural and magnetic properties. ZFO thin film, grown at 300 °C on STO by PLD exhibited similar properties as described above. While annealing the film in Argon atmosphere resulted in the increase of the low energy peak, Fig. 8.23 (right), thus the increase in Fe^{2+} concentration, annealing the film in Oxygen atmosphere showed little change in the MDF up to the growth temperature of 300 °C. For both of the thin films, a clear change in the MDF as well as the magnetization response is visible between temperatures of 300 °C and 400 °C, suggesting a transition in the crystal structure from disordered to ordered normal spinel.

[1] R. Valenzuela: Phys. Res. Int. **2012**, 591839 (2011), doi:10.1155/2012/591839.
[2] C. E. Rodriguez Torres *et al.*: Phys. Rev. B **84**, 064404 (2011), doi:10.1103/PhysRevB.84.064404.
[3] V. Zviagin *et al.*: Phys. Status Solidi B, **253**, 3 (2015), doi:10.1002/pssb.201552361.
[4] V. Zviagin *et al.*: Appl. Phys. Lett. **108**, 13 (2016), doi:10.1063/1.4944898.
[5] G. S. Krinchik *et al.*: Sov. Phys. JETP **45**, 366 (1977).
[6] E. Liskova-Jakubisova *et al.*: J. Appl. Phys. **117**, 17B726 (2015), doi:10.1063/1.4916936.

8.16 Temperature dependence of the dielectric tensor of monoclinic Ga_2O_3

C. Sturm, V. Zviagin, R. Schmidt-Grund, M. Grundmann

The large band gap energy of about 4.8 eV [1] makes Ga_2O_3 interesting as transparent conductive oxide (TCO), since even in the presence of defects or impurities, e.g. caused by doping, a high transmissivity can be obtained in the visible and even in the UV-A/B spectral range. At ambient conditions Ga_2O_3 crystalizes in a monoclinic crystal structure. In this case the dielectric function (DF) is a tensor with four complex quantities. Recently these quantities were determined by generalized spectroscopic ellipsometry for the infared [2, 3] up to the UV spectral range [1, 2] at room temperature.

For the determination of the temperature dependence of the dielectric function of Ga_2O_3 we investigated two bulk single crystals in the temperature range $T = 10-300$ K by generalized spectroscopic ellipsometry. For the lineshape analysis of the experimentally determined Mueller matrix spectra we described the dielectric tensor of Ga_2O_3 by a model dielectric function taking into account oriented excitonic dipole transitions [2]. The contribution of each excitonic transition to the dielectric function (DF) was described by a model function developed by Tanguy [4]. A detailed description of the model and the used model functions is given in Ref. [2].

In doing so, we found that the change of the DF as a function of temperature is mainly determined by the red shift of the exciton transition energies with increasing temperature (Fig. 8.24a). A strong enhancement or narrowing of the transition peaks is not observable. This indicates that the oscillator strength as well as the broadening are almost independent of the temperature. Since the exciton transition energy is connected to the band gap by the exciton binding energy, the observed temperature dependence can be described by a Bose-Einstein-Model introduced by Viña *et al.* [5] (Fig. 8.24b). The electron-phonon coupling strength and averaged energy of the phonons which are involved in the electron-phonon coupling was determined to be about 1 meV K^{-1} and 56 meV, respectively. This energy agrees very well with the bary center of the phonon density of states calculated by density functional theory [6]. The deduced broadening as a function of temperature is shown in Fig. 8.24c. The increase in broadening with increasing temperature can be attributed to a dephasing caused by the interaction with LO-phonons with an average energy of about 21 meV. Interestingly, the determined zero temperature broadening of the excitonic transition increases with increasing transition energy. The reason for this behaviour is not fully understood up to now.

[1] C. Sturm *et al.*: APL Materials **3**, 106106 (2015), doi:10.1063/1.4934705.

[2] C. Sturm *et al.*: Phys. Rev. B **94**, 035148 (2016), doi:10.1103/PhysRevB.94.035148.

[3] M. Schubert *et al.*: Phys. Rev. B **93**, 125209 (2016), doi:10.1103/PhysRevB.93.125209.

[4] C. Tanguy: Phys. Rev. Lett. **75**, 4090 (1995), doi:10.1103/PhysRevLett.75.4090; Phys. Rev. Lett. **76**, 716 (1996), doi:10.1103/PhysRevLett.76.716; Phys. Rev. B **60**, 10660 (1999), doi:10.1103/PhysRevB.60.10660.

[5] L. Viña *et al.*: Phys. Rev. B. **30**, 1979 (1984), doi:10.1103/PhysRevB.30.1979.

[6] S. Yoshioka *et al.*: J. Phys.: Condens. Matter **19**, 346211 (2007), doi:10.1088/0953-8984/19/34/346211.
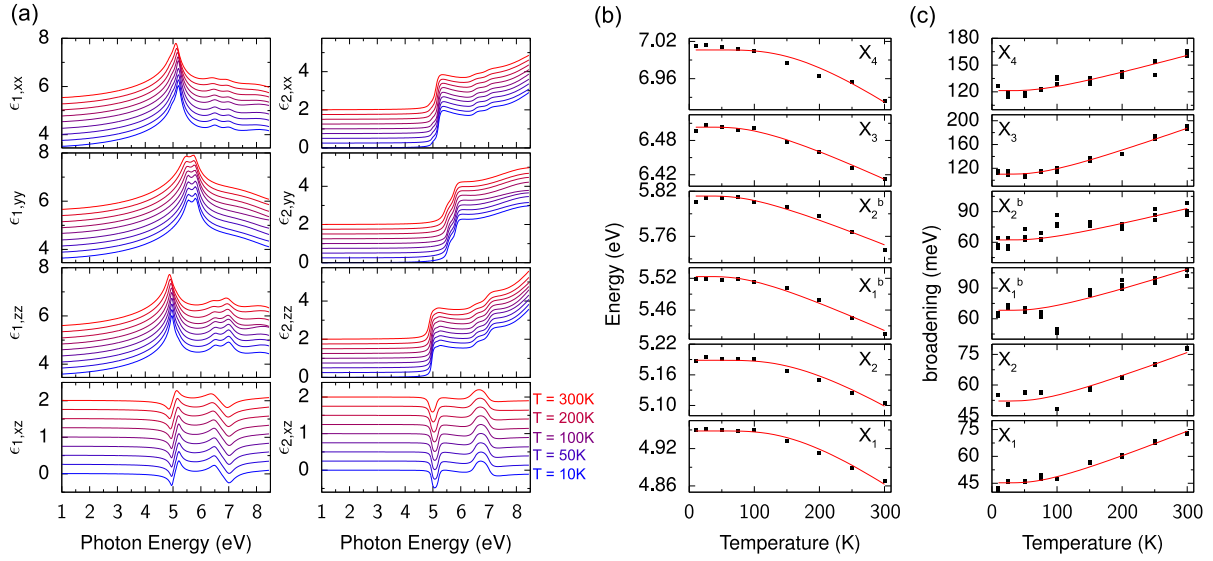
Figure 8.24: (a) Experimentally determined components of the dielectric tensor as a function of temperature. The functions were shifted vertically with respect to each other for a better clarity. (b, c) Energy (b) and broadening (c) of the excitonic transitions as a function of the temperature. The symbols and the red solid lines represent the experimentally determined values and the calculated dependence taking into account the coupling with phonons. The nomenclature of the exciton transitions (X_i^j) is taken from Ref. [1].

8.17 Exceptional points in dispersive and absorbing structures - biaxial Ga$_2$O$_3$ and anisotropic microcavities

S. Richter, C. Sturm, T. Michalsky, B. Rosenow*, M. Grundmann, R. Schmidt-Grund

*Universtät Leipzig, Institute for Theoretical Physics, Brüderstr. 16, 04103 Leipzig, Germany

Optically biaxial (orthorhombic, monoclinic or triclinic) systems reveal two classic optic axes in the transparent spectral range, i.e. there exist two distinct directions for which the light propagation is independent of the light polarization. However, as W. Voigt noted already in 1902 [1], the two classic optic axes split into four singular optic axes in the absorptive spectral range which he named "Windungsachsen". Along a singular axis, only left- or right-circularly polarized light is allowed to propagate, which is the so-called Voigt wave.

Biaxiality can be observed in different systems such as ansiotropic bulk crystals or anisotropic layered structures. In any case, the singular axes can be mathematically described as so called *exceptional points* (EP) [2–4]. EPs are characterized by a one-dimensional eigenspace of the propagation operator. For a complex symmetric matrix like the dielectric tensor this yields directly eigenstates describing a circular light polarization. Generally, the requirement for such a matrix operator is its non-Hermiticity. This again requires non-vanishing imaginary parts of the matrix entries and (for real diagonal elements) non-vanishing complex off-diagonal elements. Both result from biaxility along with absorption or dissipation.
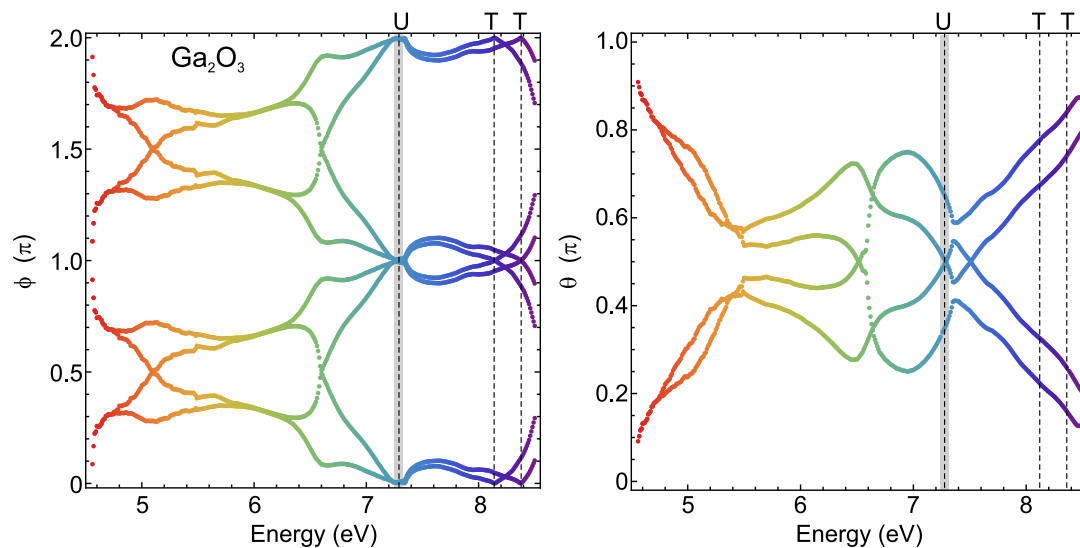
Figure 8.25: Orientation of the singular optic axes as a function of energy. The angles ϕ (left) and θ (right) denote the azimuthal and polar angle, respectively. The almost uniaxial point (U) and the two triaxial points (T) are indicated by dashed lines.

8.17.1 Singular optic axes in bulk crystals

In the absorption regime, the change of the polarization for a propagation along a certain direction is given on the one hand by the phase change, caused by the real part of the dielectric tensor, and on the other hand by the polarization dependent attenuation, caused by the imaginary part. For optically biaxial materials, the orientation of the dielectric axes of the real and imaginary part and the ratio of the major axes of the corresponding ellipsoid do not coincide with each other. The interplay between both effects leads to the formation of the singular optic axes. Interestingly, in contrast to the transparency regime, the crystal symmetry of biaxial materials can be distinguished by the properties of the singular optic axes, which also reflects the different symmetry of the dielectric tensor for these crystal systems. For instance, for orthorhombic crystals, the orientation of the dielectric axis for the real and imaginary parts of the dielectric tensor coincide with each other. However, the ratio of the major axes of the corresponding ellipsoids differ from each other. Thus four singular optic axes are formed on the surface of a cone and the corresponding Voigt waves propagate with the same velocity [5]. In contrast to that, for a triclinic material all major axes differ in orientation and ratio between the real and imaginary part, so that the symmetry in the orientation of the singular optic axes is lifted and all four Voigt waves propagate with a different velocity.

For the energy dependence of the orientation of the singular optic axes for orthorhombic and monoclinic crystals, we provided analytical expression which can be found in Ref. [5] and proved that only 4 singular optic axes in maximum can exist. As a model material, the orientation of these axes in monoclinic Ga_2O_3 was investigated in detail. The dielectric function of this material was determined by generalized spectroscopic ellipsometry [6, 7]. The calculated orientation of the singular optic axes is shown in Fig. 8.25. It was found that in the energy range $E \approx 7.23-7.33$ eV all four singular optic axes are oriented almost parallel to the [010]-direction so that the crystal in this regime behaves almost like an optically uniaxial material. Another interesting
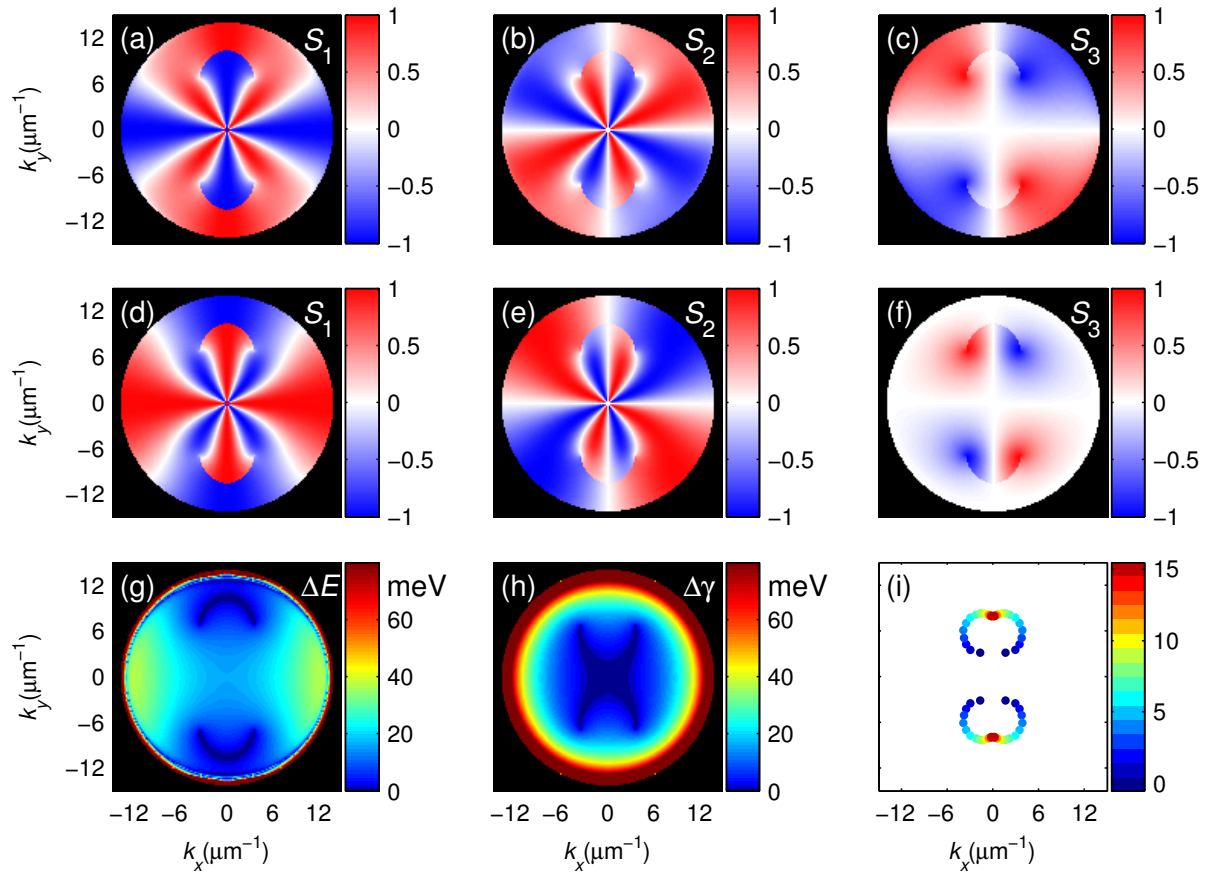
Figure 8.26: Characteristics of the cavity photon modes of a $\lambda/2$ microcavity, depending on the in-plane wavevector $\vec{k}_\parallel$. 5 DBR layer pairs with central wavelength (at normal incidence) 496 nm are assumed while the cavity thickness is 130 nm with $n_\parallel = 2.26$ and $n_\perp = 2.20$. (a-f): Mode polarization as Stokes vector, for the energetically higher ((a-c)) and lower ((d-f)) mode. (g,h): Difference of the real (E) and imaginary ($\gamma =$ HWHM) parts of the complex mode energy. (i): Position of EPs with varying number of DBR layer pairs as indicated by the colorbar.

situation was found for energies $E \approx 8.14$ eV and $E \approx 8.37$ eV. At these energies, two singular optic axes coincide with each other, forming a conventional "absorbing" optic axis which coexists with two singular optic axes. At this energy the material can be considered triaxial.

8.17.2   Anisotropic planar microcavities

Orthorhombic or monoclinic symmetries can be implemented in stratified structures, if layers of optically uniaxial materials are used. One such example is a planar microcavity with uniaxial cavity layer embedded between distributed Bragg reflectors (DBR). Such a microcavity reveals photonic modes ("cavity modes") which can reveal EPs in the momentum space even if only transparent media are used [8]. The above described imaginary contribution to the propagation operator is then provided by photonic loss, i.e. mode broadening. A complex mode energy requires a non-Hermitian transmission Jones matrix.

Planar microcavities are in principle well studied but, if the optic axis of a uniaxial cavity layer is arbitrarily oriented, often used separation of the mode computation into transversal electric (*TE*) and magnetic (*TM*) polarization is no longer valid. Instead, modes become generally elliptically polarized and do not even need to be orthogonal to each other. In such cases, deriving analytical formulae becomes very complex. Hence we performed numerical computations using a 4×4 transfer matrix formalism to obtain complex mode energies and mode polarizations, depending on the in-plane momentum $\vec{k}_{\parallel}$.

As model system we assumed a $\lambda/2$ microcavity consisting of a uniaxial cavity layer with optic axis aligned in the cavity plane. An example is shown in Fig. 8.26. As for cylindrically symmetric microcavities, the $\lambda/2$ mode is split into two modes. The modes can degenerate in (real) energy or broadening at certain in-plane wavevectors $\vec{k}_{\parallel}$ (Fig. 8.26 (g),(h)). At four finite values of $\vec{k}_{\parallel}$, EPs occur, characterized by either left or right circularly polarized light (Fig. 8.26 (c),(f)). In particular, they occur pairwise, and a pair of EPs establiches a vortex center for the linear polarization. Such characteristics are similar to the singular optic axes. In order to observe EPs, a slight detuning between the DBRs' central wavelength and the optical cavity thickness is necessary to observe EPs. Otherwise, they move out of the vacuum light cone. Furthermore, dissipation, which is controlled by the number of DBR layer pairs, determines the exact position of the EPs in momentum space, as Fig. 8.26 (i) depicts.

[1] W. Voigt: Philos. Mag. **4**, 90 (1902) / Gött. Nachr. 1, 48 (1902), doi:10.1080/14786440209462820.

[2] M. Grundmann *et al.*: Phys. Status Solidi RRL **11**, 1 (2016), doi:10.1002/pssr.201600295.

[3] M.V. Berry and M.R. Dennis: Proc. R. Soc. Lond. A **459**, 1261 (2003), doi:10.1098/rspa.2003.1155.

[4] W.D. Heiss: J. Phys. A: Math. Theor. **45**, 444016 (2012), doi:10.1088/1751-8113/45/44/444016.

[5] C. Sturm and M. Grundmann: Phys. Rev. A **93**, 053839 (2016), doi:10.1103/PhysRevA.93.053839.

[6] C. Sturm *et al.*: APL Materials **3**, 106106 (2015), doi:10.1063/1.4934705.

[7] C. Sturm *et al.*: Phys. Rev. B **94**, 035148 (2016), doi:10.1103/PhysRevB.94.035148.

[8] S. Richter *et al.*: Phys. Rev. A **95**, 023836 (2017), doi:10.1103/PhysRevA.95.023836.

8.18   Lasing processes in Microcavities

R. Schmidt-Grund, M. Wille, T. Michalsky, S. Lange, E. Krüger, L. Trefflich, C. Sturm, S. Richter, O. Herrfurth, S. Blaurock*, V. Gottschalch*, V. Zviagin, M. Kneiß, G. Benndorf, H. Krautscheid*, M. Grundmann

*Institut für Anorganische Chemie, Universität Leipzig, Johannisallee 29, 04310 Leipzig, Germany

Like in the past years, also in 2016, we intensively investigated ZnO-based microcavities (MC), but also extended our investigations to the recently upcoming material CuI, which is very promising for opto-electronic applications due to its very high exciton

oscillator strength [1]. MC physics is in focus of current research because it still provides new and facinating fundamental physical effects like quantum-optical properties in the strong light-matter coupling regime or even topological non-trivial states [2]. Further, MCs are of considerable interest for applications in quantum-information technology or optoelectronic devices like laser structures.

We continued our research on nano- and microwire based structures yielding versatile optical mode properties enabling different regimes of light-matter interaction. Particularly, we investigated lasing due to emission from electron-hole-plasma and exciton-scattering states as gain in ZnO and CuI nano- and microstructures and could explain different lasing mode energies, observed for different structures by spatially different absorption properties caused by the excitation geometry (cf. Sects. 8.18.1-8.18.3). Further we succeeded in the observation of the propagation of coherent whispering gallery mode polariton states in a microwire of more than $10\,\mu\mathrm{m}$ in diameter at room temperature by ps-resolved real- and momentum-space imaging spectroscopy and could prove by interferometry their spatial coherence over distances of at least $20\,\mu\mathrm{m}$ (Sect.8.18.3).

In order to conclusively deduce if the excited state in MCs are thermal, coherent, single-photon sources, or entangled, the photon statistics or rather the second-order temporal correlation function of the emitted light has to be measured. In 2016, we thus started to build up a Hanbury-Brown & Twiss (HBT) setup and obtained first results from ZnO single crystals and microwires in regimes of thermal and coherent (lasing) emission (Sect.8.18.4).

8.18.1   Lasing in cuprous iodide microwires

The synthesis of cuprous iodide (CuI) micro- and nanostructures is almost unexplored in contrast to other compound semiconductors such as zinc oxide (ZnO), cadmium sulfide (CdS), gallium nitride (GaN) and gallium arsenide (GaAs). However, CuI is a promising material for future optoelectronic devices due to its intrinsic p-type conductivity, its high oscillator strength of the exciton resonance expressed by its large longitudinal-transversal splitting, and its rich variety of intense optical recombination channels including pronounced phonon replica in the near ultraviolet (NUV) range.

Here, we demonstrate lasing emission of single CuI microwires under optical excitation. We succeeded with the synthesis of high quality CuI microwires. These microwires grow self-organized in zincblende γ-CuI phase and exhibit a balanced stoichiometry of Cu : I = 1 : 1. Figure 8.27(a) shows an SEM image of an exemplary microwire with a length of $l = 49\,\mu\mathrm{m}$ and a diameter of $d = 4.0\,\mu\mathrm{m}$. Conspicuously, the microwire surface is smooth and free of any structural defects. Having a closer look, a rounded triangular shape of the microwire cross section was found, which indicates that the (111) direction of zincblende CuI is the preferred growth direction.

Excitation density dependent μ-PL spectra of this microwire at a temperature of $T = 10\,\mathrm{K}$ are shown in Fig. 8.27(b). In the low excitation density regime (black line) the emission of acceptor bound excitons (A^0X) and further defect bound excitons (DBX) as well as their LO-phonon replica, and an additional emission band in the energy range of $3.029 - 3.035\,\mathrm{eV}$ can be observed. This probably originates from inelastic exciton-exciton scattering (P-band), where the radiatively decaying exciton emits a photon and scatters another exciton into a higher excited state [3]. Tanaka et al. already demonstrated
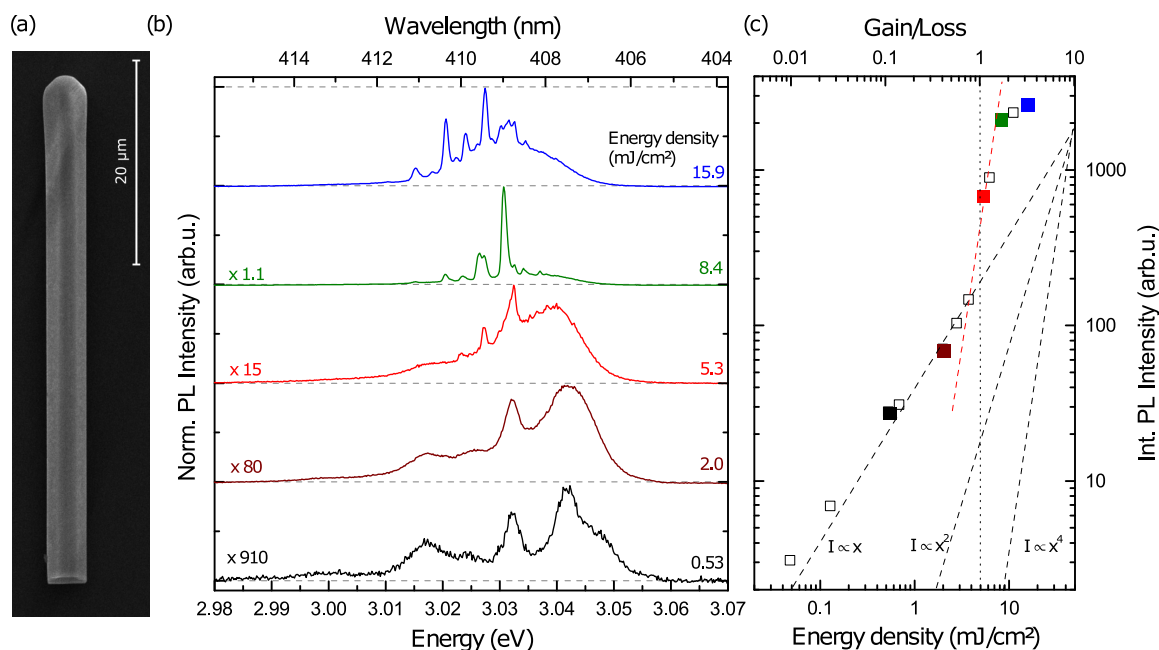
Figure 8.27: (a) Scanning electron microscope (SEM) image of an exemplary CuI microwire ($l = 49\,\mu$m, $d = 4.0\,\mu$m). (b) The excitation density dependent μ-PL spectra of the respective microwire at 10 K using the 355 nm line of a NdYag laser reveals a transition from broad spontaneous emission (see black and brown line) to sharp mode emission (see green and blue line) in the laser regime. (c) Double-logarithmic plot of the integrated μ-PL intensity in dependence on the energy density of the excitation laser pulse indicates a laser threshold of $E_{\mathrm{Th}} \sim 5\,\mathrm{mJ/cm}^2$.

P-band-correlated optical gain of $\sim 400\,\mathrm{cm}^{-1}$ by stripe length technique and the accompanied stimulated emission in CuI thin films [4]. With increasing excitation density, the initially strongest emission bands saturate and at an excitation density of around $5.3\,\mathrm{mJ/cm}^2$, narrow modes appear in the spectral vicinity of the P-band emission. With further increasing excitation density, additional modes appear at lower energies and cover a spectral range from $3.015 - 3.035\,\mathrm{eV}$ for the highest density of $15.9\,\mathrm{mJ/cm}^2$ (blue line in Fig. 8.27(b)). Figure 8.27(c) depicts the emitted integrated PL intensity from the microwire as a function of excitation density. The double-logarithmic plot depicts a distinct S-shape course which represents the threshold behavior of the underlying laser transition. Below the laser threshold of around $E_{Th} = 5\,\mathrm{mJ/cm}^2$, the emission intensity increases linearly with the excitation density. In the threshold regime, the slope becomes strongly nonlinear ($I \sim x^4$) and declines back to a linear slope in the lasing regime. This observation clearly demonstrates lasing in our microwires.

8.18.2   Absorptive lasing mode suppression in ZnO nano- and microcavities

In literature, lasing modes in ZnO micro- and nanostructures were observed to emerge in different spectral ranges without a conclusive explanation for the observed mode energies. In this study (details can be found in ref. [5]), we conclusively explain the different lasing mode energies. In order to do this, we studied the influence of the
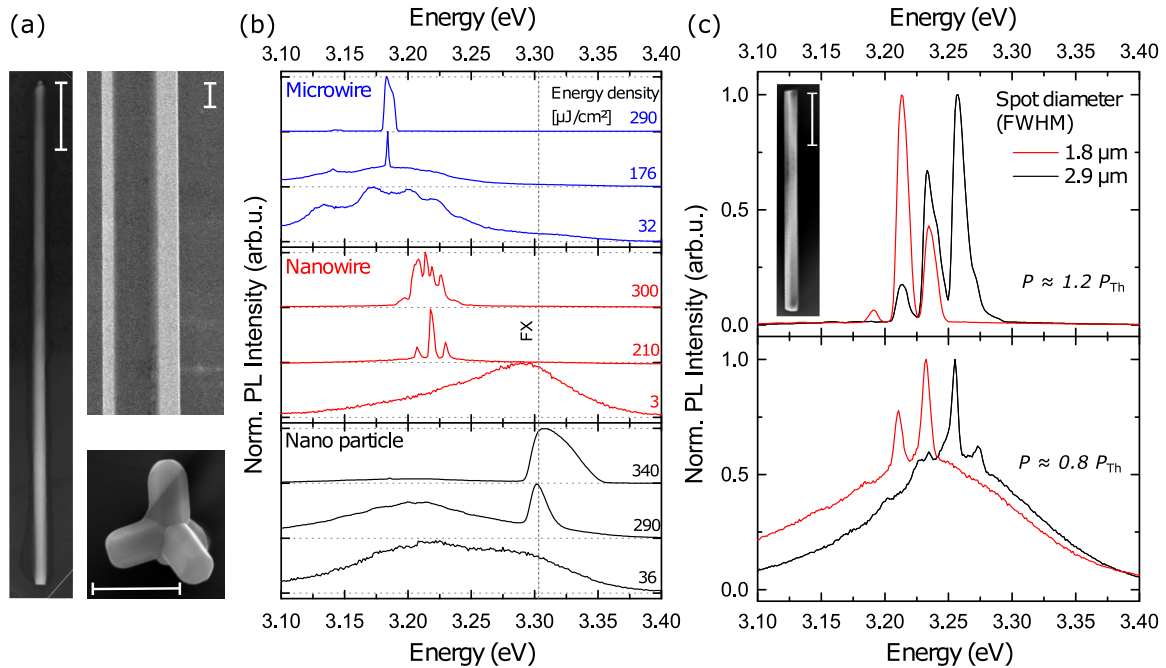
Figure 8.28: (a) Scanning electron microscope images (SEM) of a ZnO nanowire ($L = 7.9\,\mu m$, $d = 165-190\,nm$, microwire ($d = 3.5\,\mu m$) and a tetrapod-like nano particle (leg length of $\sim 800\,nm$ and leg diameter of $\sim 450\,nm$). The white bars have a length of $1\,\mu m$. (b) Room temperature PL spectra for three different structure types and three excitation powers reveal lower lasing mode energies for larger structure dimensions. The structures were excited with a frequency doubled Ti:Sa laser ($\lambda_{ex} = 355\,nm$, $t_{pulse} = 2\,ps$). (c) Lasing emission spectra of a ZnO nanowire (see inset: $L = 4.2\,\mu m$, $d = 245\,nm$), shown for two excitation spot diameters of $1.8\,\mu m$ (red) and $2.9\,\mu m$ (black). The excitation with a larger spot size leads to a mode enhancement on the high energy side of the spectrum.

excitation conditions in correlation with the size and geometry of the active medium on the laser mode energy. Therefore, we compare the lasing mode energies of different single micro- and nanostructures, as they are depicted in Fig 8.28(a), and discuss the results in terms of the spatial gain region, which results from the spatial inhomogeneity of the excitation spot and the limited penetration depth of the exciting laser light.

Figure 8.28(b) shows the room temperature emission spectra of the three investigated nano- and microstructures for different excitation energy densities. All three structures exhibit lasing emission under high excitation which expresses through sharp lines in the emission spectra and through a nonlinear increase of emission intensity in the threshold regime. The lasing thresholds are similar and vary from $\sim 180\,\mu J/cm^2$ for the investigated microwire to $\sim 190\,\mu J/cm^2$ for the nanowire and to $\sim 270\,\mu J/cm^2$ for the tetrapod-like nanoparticle. However, the lasing mode energies are different for the different structures. The lasing mode energy of the microwire is around $3.18\,eV$. It turns out that smaller structures like nanowires exhibit lasing modes at higher energies, here in an energy range from $3.19-3.23\,eV$. Tetrapod-like particles show even higher emission energies in a range of $3.30-3.35\,eV$.

Furthermore, it was found, that the emission energy of single nanowires is slightly tuneable by changing the spot size of the excitation laser. Figure 8.28(c) depicts the lasing emission spectra of a $\sim 4.2\,\mu m$ long nanowire (see inset) slightly below and above the
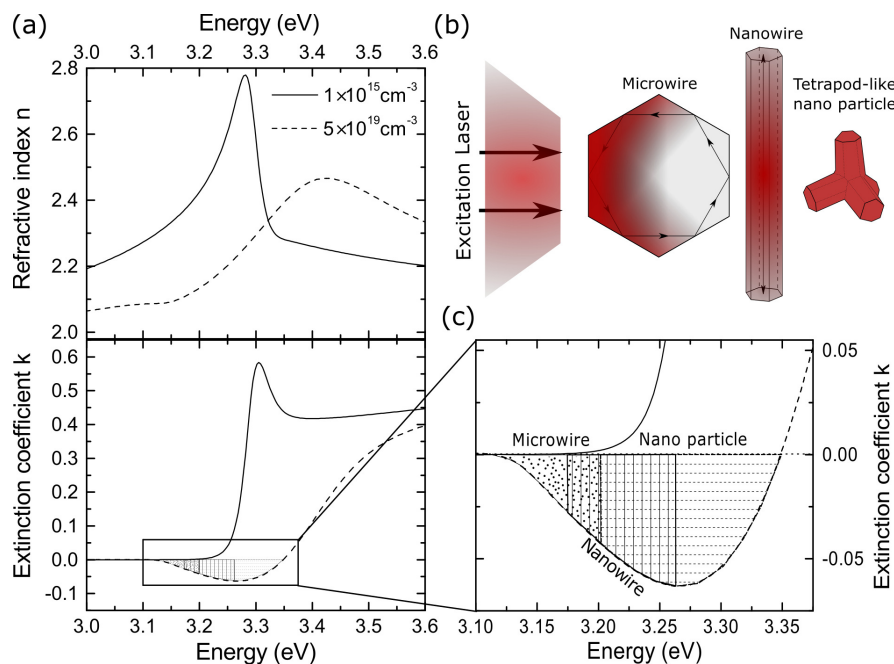
Figure 8.29: (a) Calculated carrier density dependent complex refractive index for 1×10^{15} cm^{-3} (solid line) and 5×10^{19} cm^{-3} (dashed line). (b) Sketch of the spatial gain regions in different nano- and microstructures (microwire, nanowire, nanoparticle) under excitation with a gaussian laser profile. Red color indicates high carrier densities and thus high gain whereas white color indicates regions without any excited carriers. (c) Sketch of differently hatched energy ranges in the enlarged gain spectra for a carrier density of 5×10^{19} cm^{-3}, for which lasing was observed for different nano- and microstructures in literature.

respective threshold power for different excitation spot sizes (red for ∼ 1.8 µm and black for ∼ 2.9 µm). Note, additional modes appear on the high energy side of the spectra in the case of a larger excitation spot (black lines).

The different lasing mode energies of the respective micro- and nanostructures can be well explained by considering the spectral gain profile of the semiconductor material under high excitation and the spatial distribution of electronically inverted regions in the respective structures. The complex refractive index for carrier concentrations of 1×10^{15}cm^{-3} and 5×10^{19}cm^{-3}, which represent the cases of excitation far below and slightly above the Mott density, respectively, is depicted in Fig. 8.29(a) . The excitonic resonance/absorption, visible as a pronounced peak for low carrier concentration, vanishes at high carrier concentrations, accompanied by the formation of optical gain for energies between 3.1 eV and 3.35 eV. To obtain further insight into the carrier density dependent complex refractive index and its temporal dynamics after a high power excitation pulse, the reader is referred to reference [6]. The spectral gain range is shown magnified in Fig. 8.29(c). Each of the differently highlighted areas represents a variety of experimentally observed lasing energies for the respective microwires, nanowires/nanobelts and nanoparticles/tetrapods. Obviously, particles of smaller size exhibit lasing modes with higher energies compared to several µm-long nanowires and µm-thick microwires.

This behavior can be explained by considering the spatial absorption profile of the excitation laser light in the respective structures, see Fig. 8.29(b). Depending on the
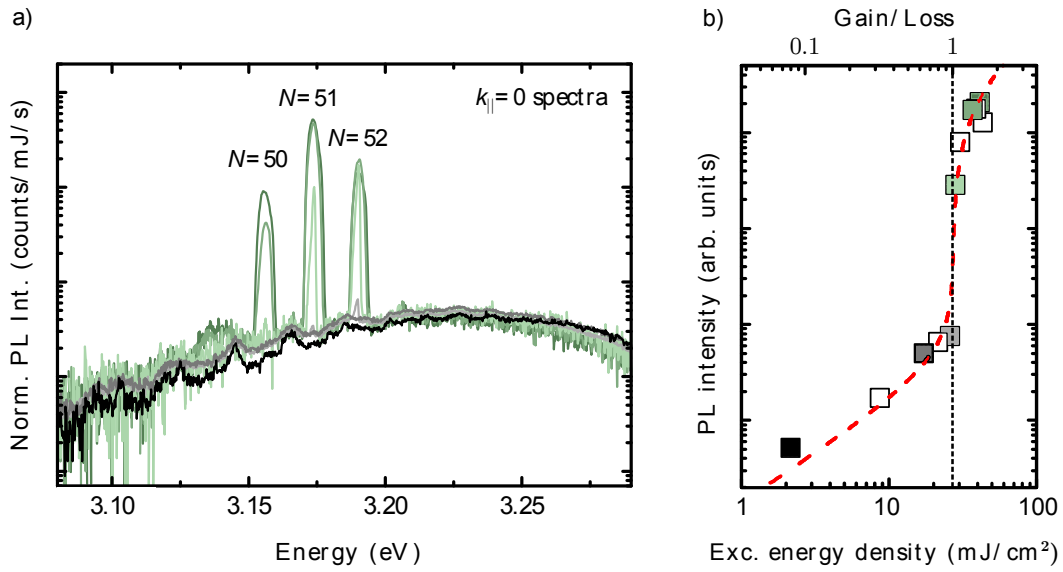
Figure 8.30: a) Excitation density dependent spectra at room temperature for $k_{\parallel} = 0$, normalized to the applied pump energy density. With increasing excitation density, the WGMs with mode numbers $N = 50, 51, 52$ exhibit a super-linear increase in intensity while the underlying PL signal slightly shifts to lower energies. b) The log-log plot of PL intensity vs. excitation energy density exhibits a distinct S-shape behavior. The dashed red line corresponds to the adapted multimode laser model [8] with a threshold density of 27 mJ/cm^2.

structure size, a certain structure volume remains weakly or even non-excited after excitation (backside of microwires, endfacet near regions of nanowires). This leads to mode absorption outside of the spatial gain region. For hexagonal microwires with diameters of several microns, the effect is most pronounced due to the small gain region close to the front facet. In the case of lasing nanoparticles, the carrier concentration is spatially homogeneous. Hence, gain distribution correlated absorption effects are negligible and lasing modes are observable in the center and on the high energy side of the gain profile. Nanowires behave in an intermediate fashion due to the weaker excitation in the end facet near region. By changing the spot size, the length of absorbing end facet region was varied. As a consequence, we observed lasing modes on the high energy side of the emission spectra in the case of homogeneous carrier density distribution, i.e. larger spot size. For a smaller spot size, high energy lasing modes are suppressed outside of the transparency region.

8.18.3 Spatial and temporal evolution of coherent polariton modes in ZnO microwire cavities

We investigated the spatial and temporal behaviour of coherent whispering gallery modes (WGMs) in ZnO microwires after excitation with a fs-laser pulse at room temperature. The estimation of the carrier density ($n_{th} \approx 5 \times 10^{20}$ cm^2) at the threshold excitation power density of $I_{th} = 27$ mJ/cm^2 reveals that the gain process responsible for the build up of the coherent states is connected to the (stimulated) recombination in an electron-hole plasma [7]. Excitation energy density dependent photoluminescence
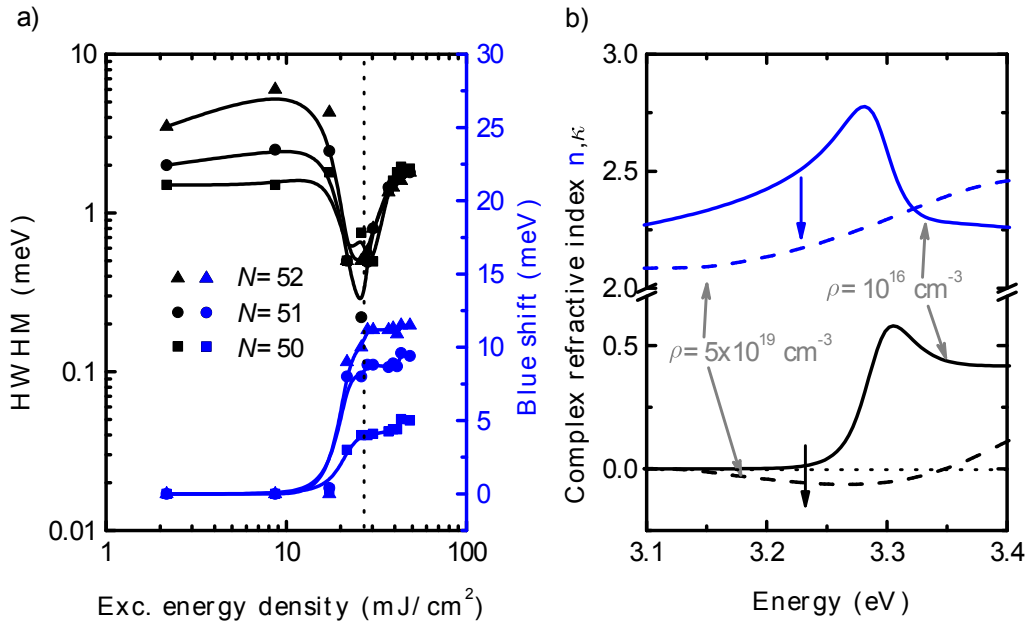
Figure 8.31: a) WGM broadening (HWHM; black symbols) and blue-shift (blue symbols) for the three dominating WGMs ($N = 50, 51, 52$) from Fig. 8.30 a) in dependence on the excitation energy density. The lines are a guide to the eye. b) Calculated refractive indices (blue) and extinction coefficients (black) for carrier densities far below (straight lines) and above (dashed lines) the Mott density. The dotted line indicates zero extinction. After [6, 9].

(PL) spectra and a corresponding fit with a multi-mode laser model [8] are shown in Fig. 8.30.

Regarding the WGMs which exhibit a nonlinear increase in intensity, the increasing excitation energy density leads to a blue shift of these modes and to a minimimum linewidth at the nonlinear threshold, as shown in Fig. 8.31 a). The blue shift ΔE can be explained with the change in the carrier density dependent refractive index Δn. As the WGM resonance energies are indirectly proportional to the refractive index of the cavity material, for small changes of the refractive index the blue shift can be expressed as

$$\Delta E \approx -E_0 \frac{\Delta n}{n_0 + \Delta n}. \tag{8.1}$$

The subscript 0 indicates the low carrier density limit for the corresponding quantities. In Fig. 8.31 b) the modeled complex DF [6, 9] is plotted for carrier densities below and beyond the Mott carrier density. It can be seen that in the high carrier density limit the refractive index is reduced in the spectral range of interest (energetically below the exciton groundstate resonances at 3.3 eV . This is a direct consequence of the screening of the excitonic oscillator strength and leads to the aforementioned blue shift. A quantitative comparison between theory and experiment is hardly possible as only a small part of the closed light path in the cavity is pumped (see Fig. 8.36 a)) and the carrier diffusion length, determining the carrier density, remains an unknown parameter so far.

But, if we assume that the modeled change in DF gives reasonable values, it is possible to estimate the carrier diffusion length L_d via the measured blue shift. Therefore
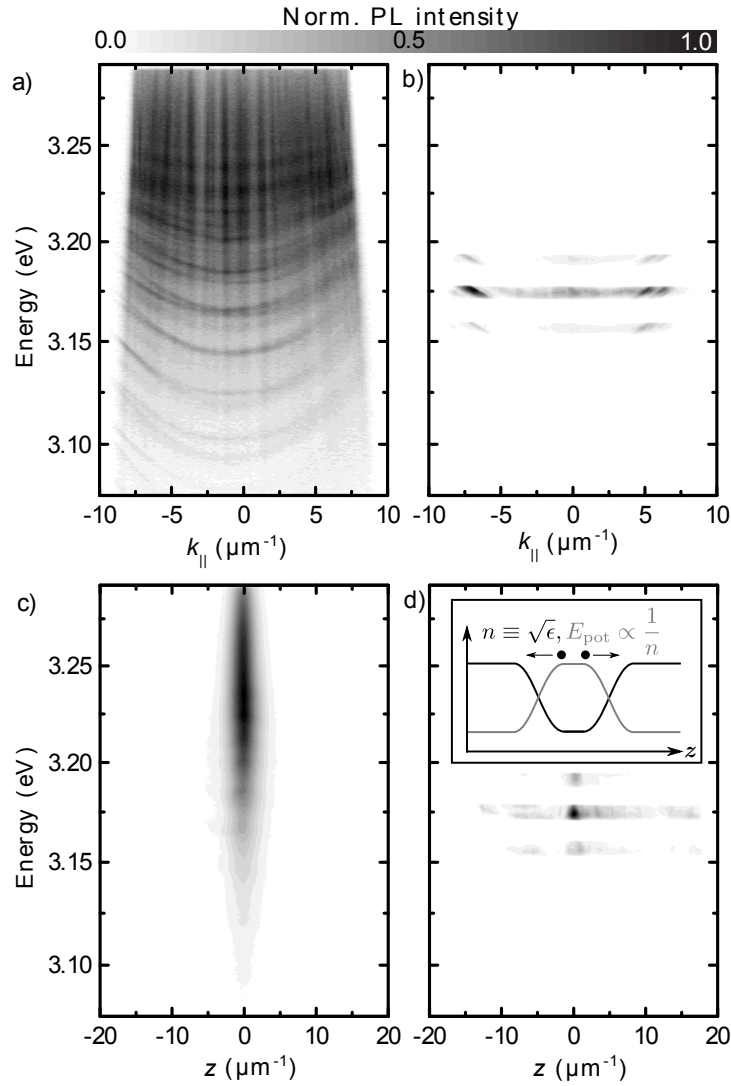
Figure 8.32: Energy resolved *k*- and real space images below ((a) and (c)) and above ((b) and (d)) threshold. The spatial direction (*z*) as well as the in-plane wavevector projection ($k_{\parallel}$) are measured along the wire axis. The inset in d) shows a sketch of the spatially varying DF (black) together with the resulting repulsive potential (gray) seen by the WGM-polaritons.

we have to replace Δn in equation (8.1) with $\Delta n L_{\mathrm{d}}/L_{tot}$. The quantity L_{tot} is the resonator length which is known from modeling the WGM energies for the investigated sample ($L_{tot} = 9.0\,\mu$m). The three lasing modes ($N = 50, 51, 52$) and their corresponding blue shifts give three different values for L_{d} namely $(0.1, 0.2, 0.3)\,\mu$m. This might be an indication that the modeled DF differs from the real one as similar values for L_{d} are expected. Additionally, the blue shift is obtained from time integrated measurements after fs-excitation introducing further uncertainties [6].

Regarding the WGM linewidth, their reduction in the vicinity of the threshold is typical for the onset of lasing as in this situation, the material gain (negative κ, see Fig. 8.31 b)) compensates all resonator losses, which predominantly determine the WGM linewidth [10]. The increase in linewidth beyond threshold is mostly determined by the pulsed excitation conditions in combination with the time integrated measurement scheme applied here. Therefore, after each single excitation pulse, the carrier
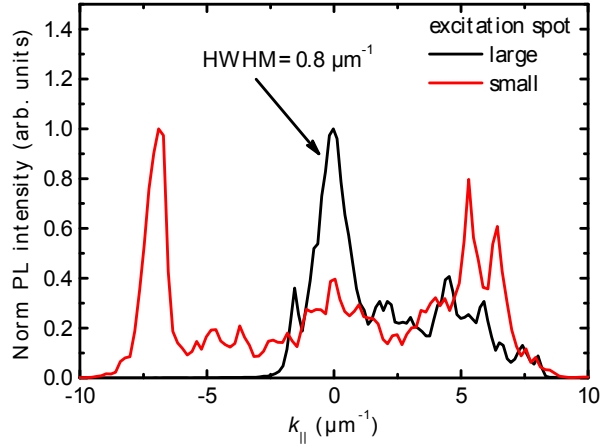
Figure 8.33: *k*-space mode distribution in dependence on the excitation spot size beyond the nonlinear threshold. A small (submicron) excitation spot (red) size results in the appearance of the coherent modes from the dispersion of the unperturbed WGMs at $k_\parallel > 0$, whereas a large (micron) exciton spot (black) (≈ 1.5 μm FWHM) results in coherent states distributed around $k_\parallel = 0$. Here, the large excitation spot leads to a $k_\parallel$-distribution with a HWHM of 0.8 μm^{-1}.

density changes in time, resulting in different blue shifts over which is integrated, affecting the measured (time integrated) linewidth [6].

The energetically resolved real and *k*-space distribution of the WGM PL emission below and above threshold are shown in Fig. 8.32. Above threshold, the emission stems from distinct points of the dispersion relation $E_{WGM}(k_\parallel)$ ($k_\parallel$ is the in-plane wavevector) of the WGMs in the low density limit. These points indicate the intersections of the blue shifted WGM ground state energies with their correspondig dispersion relation. In the frame of exciton-polariton Bose-Einstein condensation this was explained [11] with the conversion of potential energy (due to repulsive polariton-polariton interaction, given by ΔE) in kinetic energy ($(\hbar k_\parallel)^2/(2m_{eff})$) of the quasiparticles. Second, in the photonic crystal approach, the optical potential for photons (as quasiparticles) is defined by $1/\varepsilon$ (ε is the actual value of the dielectric function), thus photons are accelerated to regions with higher ε. Third, this effect can also be explained under ray-optical consideration [12], where the locally varying refractive index leads to a change of the $k_\parallel$-component of the wavevector as light rays tend to bend into the direction of higher refractive index (cf. inset in Fig. 8.32d)). The maximum achievable in-plane wavevector component $k_{\parallel max}$ for a mode generated at $k_\parallel = 0$ in dependence on the refractive index change Δn is given by:

$$k_{\parallel max} \simeq \frac{2\pi}{\lambda_0}\sqrt{2n_0|\Delta n|} \simeq \frac{2\pi}{\lambda_0}\sqrt{2n_0^2\left|\frac{\Delta E}{\Delta E + E_0}\right|}, \qquad (8.2)$$

with λ_0 being the vacuum wavelength of the corresponding mode. Independent of the picture which is chosen (interacting particles with effective mass m_{eff} or light rays in a polarizable medium where the χ^3 susceptibility (carrier dependent refractive index) is taken into account), the spatially narrow excitation leads to an acceleration of the coherent states away from the excitation center. This is directly reflected in the real space emission pattern, as sown in Fig. 8.32, where below threshold, the contribution of low $k_\parallel$ states results in effectively lower spatial expansion compared to the lasing
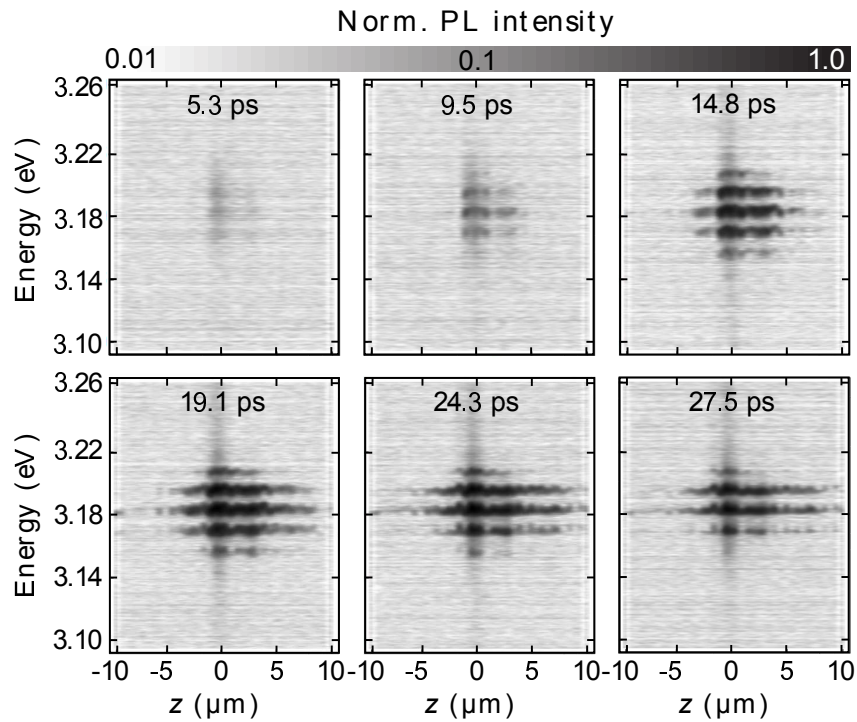
Figure 8.34: Spectrally resolved spatiotemporal evolution of coherent WGMs after fs-excitation with a large (micron) excitation spot. The time steps are given in the corresponding image. The absolute value of the time scale does not represent the time difference to the excitation laser pulse.
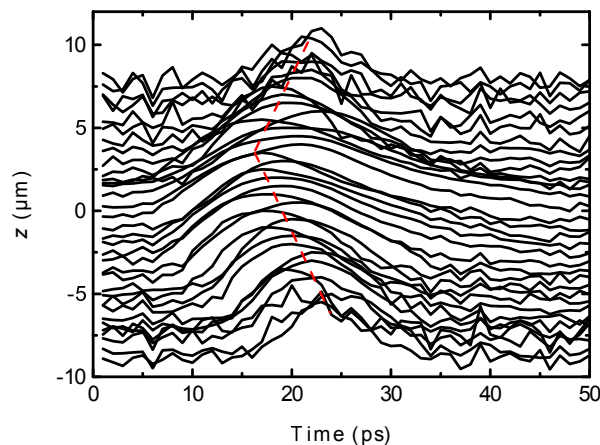
Figure 8.35: Spatiotemporal expansion of a single coherent WGM ($E = 3.188$ eV, compare Fig. 8.34) after fs-excitation with a large (micron) exciton spot. The measured velocity is $v_{\text{meas}} \approx 1.5$ μm/ps, corresponding to an average wavenumber of $k_{\|,\text{meas}} \approx 0.4$ μm^{-1}. The log-spectra are normalized to their corresponding maximum and shifted with a constant offset, corresponding to a spatial separation of 0.5 μm.
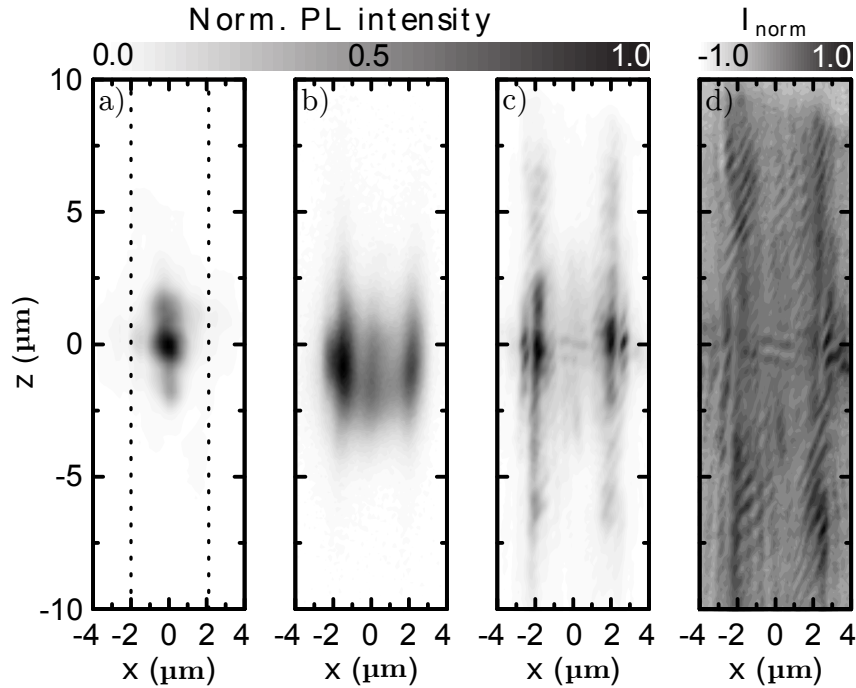
Figure 8.36: Spatial coherence: a) Pump laser beam reflection from the wire surface. b) Interferogram of the PL signal from the wire surface below threshold. c) Interferogram of the PL signal from the wire surface beyond threshold. d) Normalized intensity of the interferogram depicted in c).

case. There, the high $k_\parallel$ states dominate the emission resulting in an effectively larger spatial expansion.

In order to resolve the spatial expansion of the coherent WGMs in time, we combined the micro imaging setup with a streak camera. For technical reasons the spatiotemporal resolution of the high $k_\parallel$ states, depicted in Fig. 8.32 b), could not be achieved. Thus, we used a larger excitation spot in order to generate coherent states distributed around $k_\parallel = 0$, as shown in Fig. 8.33, with a HWHM of $0.8\,\mu\mathrm{m}^{-1}$. The reconstructed spectrally resolved real space images for different time steps are shown in Fig. 8.34, revealing the spatial expansion of the lasing modes with increasing time after excitation with a fs-laser pulse. Investigating a single mode (see Fig. 8.35), a velocity $v_\mathrm{meas} \approx 1.5\,\mu\mathrm{m/ps}$ could be measured which corresponds to wavenumber of $k_{\parallel,\mathrm{meas}} \approx 0.4\,\mu\mathrm{m}^{-1}$. This value is smaller than expected from the HWHM in the k-space distribution and may be a result of the fact that WGMs accelerate in the spatially varying potential, whose size is given by the carrier diffusion length here. Due to trigger jitter of the streak camera system, this acceleration process appears to be hidden.

In order to investigate the spatial coherence properties of the WGM states a Michelson interferometer was put in the collimated beam behind the microscope objective. One arm of the interferometer was equipped with a retro-reflector, which acts as an inverter for the image of the sample surface. In Fig. 8.36 the results are shown. In order to determine the excitation spot size in our experiments, the spatially resolved reflection of the excitation laser light was imaged on the CCD using only one arm of the interferometer. The result is depicted in Fig. 8.36 a), from which an oval excitation spot size can be determined. The two diameters of the excitation spot (FWHM) are $0.70\,\mu\mathrm{m}$
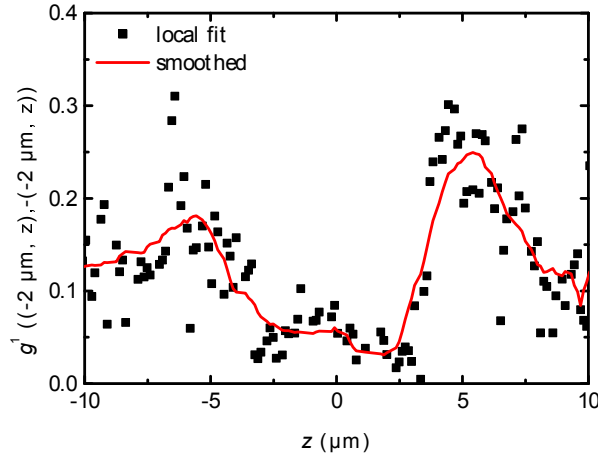
Figure 8.37: Spatial coherence $g^1(\vec{x}, -\vec{x})$ extracted from the $x = -2\mu$m line (wire-edge) as presented in the normalized intensity pattern in Fig. 8.36 d). The symbols represent a local fit for $g^1((-2\,\mu\text{m}, z), -(-2\,\mu\text{m}, z))$ over one period of the interference pattern. The red line is a smoothed plot (Savitzky-Golay) of the data and represents a guide to the eye. The minimum of the spatial coherence in the observable range can be found close to the excitation center around $z = 0\ \mu$m.

along the wire axis and 0.38 µm perpendicular to the wire axis, respectively, resulting in an excited area of approximately 0.28 µm². Below threshold (see interferogram in Fig. 8.36 b)), the spontaneous PL emission can be observed from the wire surface and edges with a spatial extension of about 4 µm (FWHM), exceeding the excited area. The interferogram shows no fringes as the emission is dominated by spontaneous excitonic recombination which is spectrally broad (FWHM≈ 100 meV) at room temperature. The situation changes if the excitation energy density is beyond threshold (see Fig. 8.36 c)), where the wire emission is dominated by WGMs coupling out of the wire edges. Here, clear interference fringes appear. In Fig. 8.36 d) the normalized intensity $I_{\text{norm}}(\vec{x})$ calculated after equation:

$$I_{\text{norm}}(\vec{x}) = \frac{I_{\text{interf}}(\vec{x}) - I_1(\vec{x}) - I_2(-\vec{x})}{2\sqrt{I_1(\vec{x})I_2(-\vec{x})}} = g^1(\vec{x}, -\vec{x})\cos\left(\vec{k}_{\text{interf}}\vec{x} + \phi\right) \tag{8.3}$$

is plotted, where I_1, I_2 and I_{interf} describe the intensity patterns of the single arms and their combined image, respectively. The quantities $\vec{k}_{\text{interf}}$ and ϕ describe the setup-defined interference wavevector and phase. The amplitude of the interference fringes of the normalized intensity gives the first order spatial coherence function $g^1(\vec{x}, -\vec{x})$ and it is obvious that the coherence is highest at the wire edges away from the excitation center (see also Fig. 8.37). This can be attributed to the fact that at the excitation center, a non-vanishing population of uncoherent states is present, lowering the coherence. Contrarily, away from the excitation center, only the emission from the highly coherent propagating WGM states is detectable . The reason for g^1 being always noticeably below 1 can be found mainly in the fact that during the measurements vibrations of the sample were unavoidable introducing intensity fluctuations in emission on the one hand and a smearing of the interference fringes on the other. Furthermore, the single (interferometer-) arm measurements had to be performed separately which together with the intensity fluctuations result in an uncertainty in the normalized intensity which, of course, affects the spatial coherence g^1.
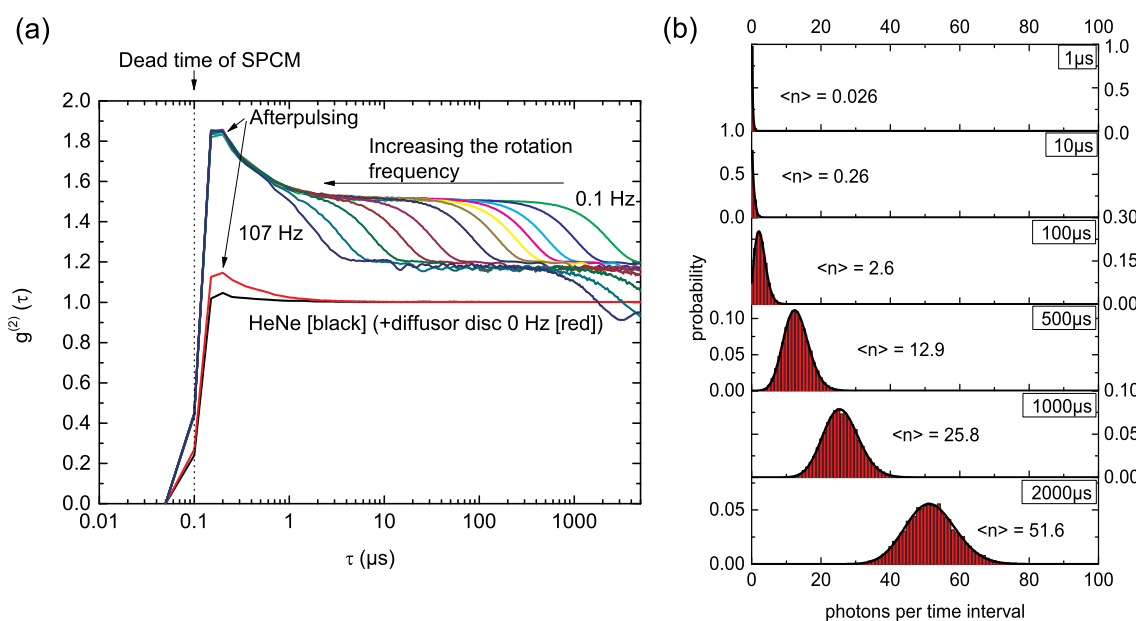
Figure 8.38: (a) Experimental results of $g^{(2)}(\tau)$ obtained from a *cw*-HeNe laser (black line) and from a pseudothermal light source simulated by scattering the HeNe emission on a rotating diffusor disc for different rotation frequencies and thus for different correlation time τ_c (colored lines). (b) Measured photon statistic of the HeNe laser (red bars) calculated with different time windows (indicated in the right corners) and therefore varying mean photon numbers $< n >$. Black lines indicate a least-squares fit with a poisson distribution.

In summary we have shown how to generate and manipulate propagating coherent WGM states at room temperature and investigated their spatial coherence properties.

8.18.4 Buildup of a photon correlation measurement setup and first results for the thermal and lasing regime in ZnO

In order to unambiguously prove if light is emitted by coherent or thermal states investigation of the second order temporal correlation function $g^{(2)}(\tau)$ is indispensable. This is true at least for the case of sufficiently narrow spectral bandwidth of thermal light, as it is the case for emission out of whispering gallery modes in the low-excitation density regime in our high-quality microwire cavities. For characterization of the statistics of light emitted from such structures and assignement of the regime around the lasing threshold to be amplified spontaneous emission or photon/polariton lasing, we built up an intensity interferometer according to Hanbury-Brown & Twiss (HBT). Photoluminescence of the sample is spectrally filtered by a monochromator, split by a 50:50 beam splitter, and focussed onto single photon avalanche photo diodes (SAPDs). The electrical pulses of the detectors are transferred to a single photon counting module (SPCM) where they act as start/stop signals for a time-correlated single photon counting (TCSPC) unit.

We tested the functionality of the setup by measuring $g^{(2)}(\tau)$ for a *cw*-HeNe laser and a quasi-thermal lightsource using only one of the detectors as shown in Fig. 8.38(a). Due to the dead time of the detection electronics, only subsequent events with a time
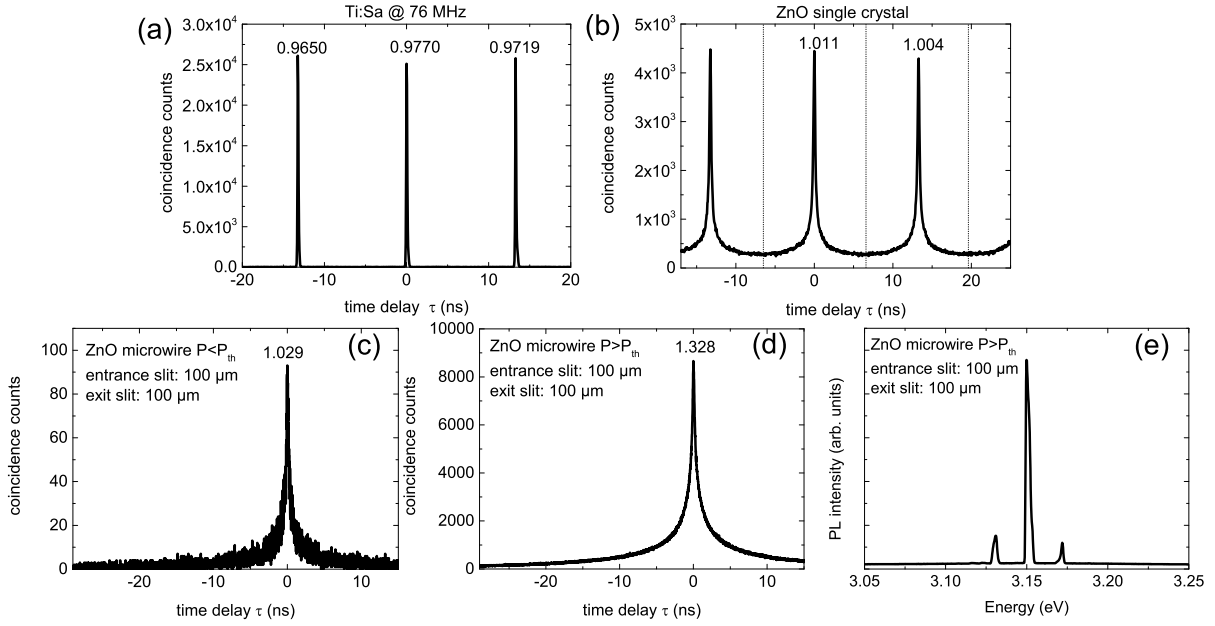
Figure 8.39: Photon coincidence counts obtained from (a) pulsed Ti:Sa laser, (b) PL of a ZnO single crystal, PL of a ZnO microwire below (c) and above (d) lasing threshold with the corresponding spectrum (e). The numbers above the peaks indicate the value of $g^{(2)}$ for the time delay at the maximum of the peak.

difference of at least 100 ns can be observed. The laser emission shows the theoretically predicted behavior of $g^{(2)}(\tau) \approx 1$. The small peak at 150 ns is due to afterpulsing of the SAPD. The corresponding photon statistic is Poisson-like, as can be seen in Fig. 8.38(b). A pseudothermal light source was used to simulate the correlation properties of natural thermal light, but with adjustable coherence time [14]. Here, the HeNe emission is scattered by a rotating diffusor disc, thus inducing temporal decoherence, where the coherence time τ_c can be adjusted by the rotation frequency. We found a dependence $g^{(2)}(\tau) \propto a + b \cdot \exp^{-c\left(\frac{\tau}{\tau_c}\right)^2}$ with $a, b, c, \tau_c > 0$, which is typical for thermal behavior. $g^{(2)}(\tau)$ does not reach 1 for $\tau \to \infty$ due to the inhomogeneous roughness distribution of the diffusor disc.

The photon statistics (photon coincidence rates) of the emission from a ZnO bulk single crystal as well as microwire excited with a pulsed Ti:Sa laser below and above the nonlinear threshold power density is shown in Fig. 8.39. The emission from the Ti:Sa laser shows, as expected, $g^{(2)}(\tau) \approx 1$ (Fig. 8.39(a)). The emission from the ZnO bulk single crystal at low excitation power (Fig. 8.39(b)) shows, with respect to the laser, a broadened temporal behaviour due to the decay of free excitons with a time constant of about 100 ps. Evaluation of $g^{(2)}$ at $\tau = 0$ provides a value of 1.01, indicating a coherent state. However, one would expect the semiconductor to be in a thermal state. A possible explanation can be found in the ratio of the temporal resolution of the setup to the correlation time of the emitted photons which gives approximately 10 %. Thereby the correlation time is given by the exciton linewidth according to the Wiener-Khinchin theorem, which is determined at room temperature by the strongly inhomogeneous decay properties of the excitons. This corresponds to an averaging of the measured signal over uncorrelated decay channels over the entire inhomogeneous exciton life-

time. We found the same behaviour for the ZnO microwire at excitation power below threshold (Fig. 8.39(c)). Above threshold (Fig. 8.39(d)), we found $g^{(2)}(\tau = 0) = 1.328$. This is counter-intuitive, as one would expect values larger 1 below threshold and equal to 1 above threshold. One possible explanation might be that the wire is in a transition regime between spontaneous and stimulated emission, where amplified spontaneous emission can be expected to contribute. Here, non-linear emission intensity increase takes place, but the material is mainly still in the thermal regime, but with strongly decreased effective exciton lifetime due to increased exciton-exciton scattering [6]. This effect reduces the inhomogeneous character of the excitonic decay by preferring one decay channel, thus increasing the correlation time to be similar to the current resolution of the setup, such that correlation effects are visible.

In the next step we will increase the time resolution of the setup by perfecting the two-detector correlation setup.

[1] M. Grundmann *et al.*: Phys. Status Solidi A **210**, 1671 (2013), doi:10.1002/pssa.201370056.
[2] L. Lu *et al.*: Nat. Photonics **8**, 821 (2014), doi:10.1038/nphoton.2014.248.
[3] C. Klingshirn: Physics Reports **70**, 315 (1981), doi:10.1016/0370-1573(81)90190-3.
[4] I. Tanaka and M. Nakayama: J. Appl. Phys **92**, 3511 (2002), doi:10.1063/1.2226992.
[5] M. Wille *et al.*: Appl. Phys. Lett. **109**, 061102 (2016), doi:10.1063/1.4960660.
[6] M. Wille *et al.*: Nanotechnology **27**, 225702 (2016), doi:10.1088/0957-4484/27/22/225702.
[7] C. Klingshirn *et al.*: Phys. Rev. B **75**, 115203 (2007), doi:10.1103/PhysRevB.75.115203.
[8] L.W. Casperson: J. Appl. Phys. **46**, 5194 (1975), doi:10.1063/1.328660.
[9] M.A.M. Versteegh *et al.*: Phys. Rev. B **84**, 035207 (2011), doi:10.1103/PhysRevB.84.035207.
[10] J. Wiersig: Phys. Rev. A **67**, 023807 (2003), doi:10.1103/PhysRevA.67.023807.
[11] M. Wouters *et al.*: Phys. Rev. B **77**, 115340 (2008), doi:10.1103/PhysRevB.77.115340.
[12] T. Michalsky: PhD-Thesis, Universität Leipzig (2017).
[13] R. Glauber: Phys. Rev. **130**, 2529 (1963), doi:10.1103/PhysRev.130.2529.
[14] W. Martienssen et al.: American Journal of Physics **32**, 919 (1964), doi:10.1119/1.1970023.

8.19   Development of a femtosecond time-resolved spectroscopic ellipsometry setup

S. Richter, O. Herrfurth, M. Rebarz*, S. Espinoza*, M. Kloz*, T. Michalsky, C. Sturm, M. Grundmann, J. Andreasson*, R. Schmidt-Grund

*ELI beamlines, Za Radnicí 835, Dolní Břežany, Czech Republic

Time-resolved spectroscopic ellipsometry (SE) was recently reported to provide a time-resolution below picoseconds [1]. However, electronic dynamics occur on a even shorter time scale. Further, the UV spectral range could not be accessed up to now. This spectral range is of special interest for wide-gap semiconductor materials such as ZnO, which are promising for the application in optoelectronic devices. In particular, it is still a topic of current research to explore the dielectric functions of semiconductors at short

time scales after intense optical excitation and to understand the physical processes underlying the transient optical properties.

A successful way to obtain the desired time-resolution is provided by pump-probe techniques. Thereby, the temporal resolution is determined by the pump and probe pulse width. As a result of first experiments at Universität Leipzig [2], a pump-probe femtosecond time-resolved SE setup was established in cooperation with the group of Jakob Andreasson (RP4, ELI Beamlines, Czech Republic). An amplified Ti:Sa laser (35 fs, 6 mJ,1 kHz) was employed. Its third harmonic was used as pump and a small part of the laser power was used to create a continuum white light probe beam using a CaF_2 crystal, which allows to probe a spectral range from NIR to 3.6 eV with a single shot. Different polarization states were measured in polarizer-sample-compensator-analyzer (PSCA) configuration for certain compensator positions with an estimated time resolution of 200 fs. The signal-to-noise ratio could be greatly improved by the application of a two-chopper technique coupled to the CCD detector, which allows to measure quasi real-time correction spectra for fluctuations of both pump and probe pulse.

The pseudo dielectric function of a c-plane ZnO single crystal, calculated from pump-probe SE measurements, is shown in Fig. 8.40 for several relative delays between pump and probe pulse. The highest induced charge carrier density amounts to 8×10^{-18} cm^{-3}. One can clearly see that at early times the exciton resonance peak around 3.3 eV is suppressed, which can be explained by the screening of excitons due to the high charge carrier density, induced by the pump pulse. The spectral minimum of the imaginary part of the pseudo dielectric function ($< \epsilon_2 >$) being present in the $1 - 15$ ps range hints to the occurrence of optical gain. For longer times, the decreasing charge carrier density allows re-appearance of the excitonic peak. In the next step, modelling of such data will yield the dielectric function of semiconductors as a function of charge carrier density and more insight into relaxation and scattering processes will be obtained.

[1] F. Boschini, et al.: Review of Scientific Instruments 86 (2015), 013909, doi:10.1063/1.4906756.

[2] M. Grundmann: The Semiconductor Physics Group of Universität Leipzig, Report 2015.

8.20 Polarization patterns of the sky

M. Scholz[*], S. Richter, T. Michalsky, L. Trefflich, R. Schmidt-Grund

[*]Gymnasium Engelsdorf, Arthur-Winkler-Str. 6, 04319 Leipzig, Germany

Sunlight which is scattered from molecules in the atmosphere becomes linearly polarized. This is a consequence of Rayleigh scattering based on excited molecular dipoles. The orientation of the linear polarization observed on earth should hence be described by concentric circles around the sun. The degree of polarization is expected to be maximum for a viewing angle of 90° with respect to the sun, leaving light unpolarized which arrives directly from the sun or anti-sun direction. However, multiple Rayleigh scattering processes result in linearly polarized light with polarization orientation exactly perpendicular to that of single Rayleigh scattering. The (incoherent) superposition
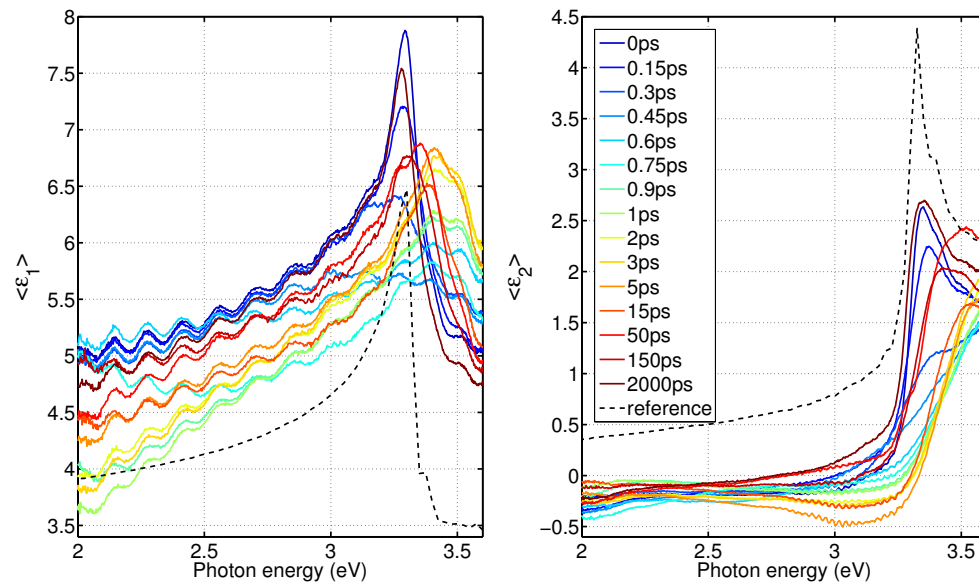
Figure 8.40: As-measured time-resolved pseudo dielectric function of a *c*-plane ZnO single crystal calculated from pump-probe SE measurements. The maximal created charge density amounts to 8×10^{-3} cm^{-3}. Please note, the oscillations visible at low energies are experimental artifacts which are not corrected for yet.

of the light of both scattering processes yields the appearance of unpolarized points at the sky, which differ from the sun and anti-sun directions [1]. In particular, there are four points aligned on a great circle covering sun, anti-sun and zenith positions [2]. The Babinet and Brewster points are situated above and below the sun, respectively. The Arago and second Brewster points are situated above and below the anti-sun position, respectively. Hence, they cannot be observed at the same time. The exact positions depend on the sun´s elevation, wavelength and albedo. The unpolarized points are vortex centers for the linear polarization orientation.

During a two-weeks internship in September, the polarization of the sky was investigated using a commercial digital camera with fisheye objective, equipped with rotatable linear-polarization filter. Light intensity values were re-calculated from the red, green and blue color channel values of the images and the polarization was evaluated from sets of images. The expected polarization patterns, including the Babinet and Arago points, could be observed during the day and around sunset, respectively. The degree of polarization was found to be highly dependent on the wavelength. Brewster points could not be observed because they occur too near to the horizon and are hence prone to atmospheric distortions. Distortions in the polarization pattern are also caused by clouds. Even clouds which are hardly visibly by eye can be clearly detected in polarization images. Additionally, right- and left circular polarization filters have been used to investigate the circular degree of the sky polarization. Circular polarization is expected to arise from Mie scattering processes, mainly caused by aerosols. Relevant circular polarization patterns could only be found during twilight, probably caused by atmospheric haze. Finally, also polarization of the moon-lit sky was detected, which is similar to that of the sun-lit sky, as illustrated in Fig. 8.41.

[1] S. Chandrasekhar: *Radiative Transfer* (Oxford 1950).
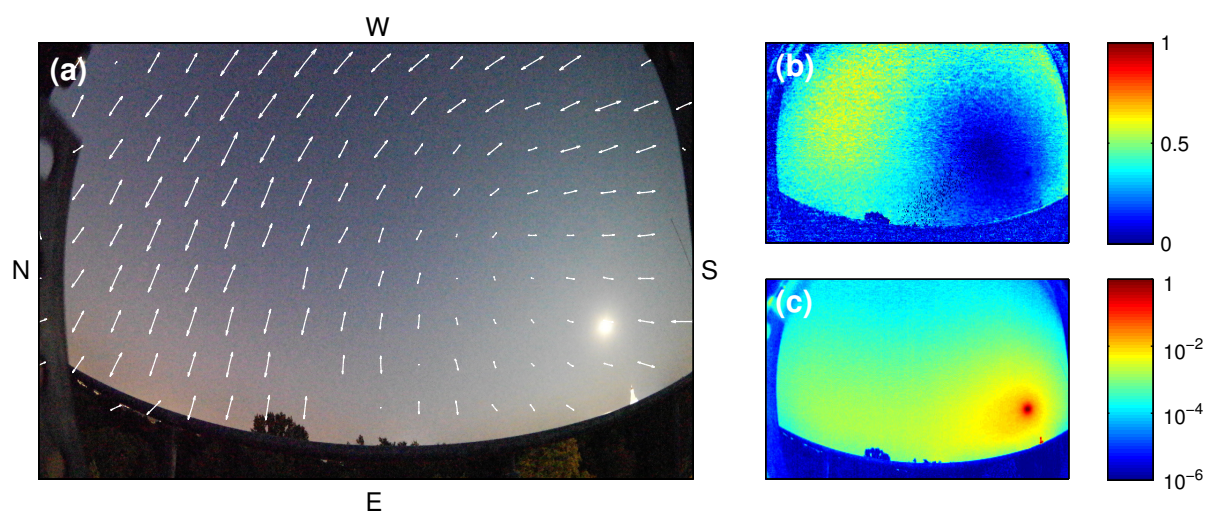
Figure 8.41: Polarization of the moon-lit sky on September 19th 2016, 20:25, Linnéstr. 3, Leipzig (51.33°N, 12.39°E). The camera was tilted towards the eastern horizon (E, bottom side; Russian orthodox church visible at the horizon). (a) photograph with arrows depicting the orientation and degree (arrow length) of the linear polarization, (b) degree of linear polarization and (c) brightness for the blue color channel. The unpolarized Babinet point (see (b)) is distinct from the position of the moon (brightest point).

[2] G. Horváth *et al.*: J. Opt. Soc. Am. A **19**, 2085 (2002), doi:10.1364/JOSAA.19.002085.
[3] J. Gál *et al.*: J. Geophys. Res. **106**, 22647 (2001), doi:10.1029/2000JD000085.

8.21   Funding

Extrem verzerrte Nano- und Mikrodrähte
Prof. Dr. M. Grundmann
DFG GR 1011/23-1

Quantum Gases and Liquids in Semiconductor Rods conformally coated with Bragg Mirrors
Dr. R. Schmidt-Grund, Prof. Dr. M. Grundmann
DFG SCHM 2710/2-1, SCHM 2710/2-2, TP P1 within FOR 1616 *Dynamics and Interactions of Semiconductor Nanowires for Optoelectronics*

Whispering Gallery Moden: Einfluss der Resonatorform auf Lasing-Eigenschaften
Prof. Dr. M. Grundmann
DFG GR 1011/26-1

Amorphe Spinelle als p-Typ Halbleiter
Prof. Dr. M. Grundmann
DFG GR 1011/27-1

Cupferiodid: Epitaxie, Dioden und Ferromagnetismus
Prof. Dr. M. Grundmann
DFG GR 1011/28-1

Dioden auf der Basis von MBE und MoVPE oxid-Dünnfilmen
Prof. Dr. M. Grundmann
DFG GR 1011/30-2

Flexible analoge und digitale Grundschaltungen in amorphen Metalloxiden
Prof. Dr. M. Grundmann
DFG GR 1011/31-1, within SPP *High Frequency Flexible Bendable Electronics for Wireless Communication Systems (FFLexCom)*

Graduiertenschule: Wolken, Aerosole und Strahlung am Beispiel des Mineralstaubes
Prof. Dr. M. Grundmann, Prof. Dr. A. Macke (Leibniz-Institut für Troposphärenforschung e. V.)
SAW-2012-IfT-4

Transparente MESFET für digitale Anwendungen
Prof. Dr. M. Grundmann, Dr. H. Frenzel
BMBF 03V0509

SolarSens: Herstellung von wellenlängenselektiven DUV-Photoelektroden,
Dr. H. von Wenckstern
BMBF 01DR15008

High-resolution fingerprint sensing with piezoelectric nanowire matrices: PiezoMat
Prof. Dr. M. Grundmann
European Union, Seventh Framework Programme 611019

LOMID - Large cost-effective OLED microdisplays and their applications
Prof. Dr. M. Grundmann, Dr. H. von Wenckstern
European Union, Horizon 2020 644101

8.22   Organizational Duties

M. Grundmann

- Prodekan Forschung der Fakultät für Physik und Geowissenschaften
- Direktor des Instituts für Experimentelle Physik II
- Stellvertretender Sprecher der Graduiertenschule "Leipzig School of Natural Sciences - Building with Molecules and Nano-objects" (BuildMoNa), http://www. build-mona.de
- Stellvertretender Sprecher des Sonderforschungsbereiches "Funktionalität Oxidischer Grenzflächen" (SFB762), http://www.physik.uni-halle.de/sfb762
- Stellvertretender Sprecher der Forschergruppe FOR 1616, http://www.for1616.uni-jena.de
- Sprecher der Fächerübergreifenden Arbeitsgemeinschaft Halbleiterforschung Leipzig (FAHL), http://www.uni-leipzig.de/~fahl
- Mitglied des wissenschaftlichen Beirats des Leibniz-Instituts für Oberflächenmodifizierung e. V., Leipzig (IOM)
- Member Editorial Board: Physica Status Solidi (a), (b), RRL
- Member International Advising Board: Advanced Electronic Materials
- Project Reviewer: Deutsche Forschungsgemeinschaft (DFG), Alexander von Humboldt-Stiftung (AvH), Schweizerischer Nationalfonds zur Förderung der wissenschaftlichen Forschung (FNSNF), Fonds zur Förderung der Wissenschaften (FWF), EU, Österreichische Forschungsförderungsgesellschaft mbH (FFG), Agence Nationale de la Recherche (ANR, France)
- Referee: Applied PhysPhysics Letters, Electronics Letters, Journal of Applied Physics, Nature, Physica E, Physical Review B., Physical Review Letters, Physica Status Solidi, Advanced Materials, u.a.

M. Lorenz

- Editorial Board Member Journal of Physics D: Applied Physics (IOP, Bristol, U.K.)
- Project referee: Deutsche Forschungsgemeinschaft (DFG), Czech Science Foundation, Technology Foundation STW (The Netherlands)
- Referee: ACS Applied Materials Interfaces, Advanced Materials, Advanced Functional Materials, Applied Physics Letters, Chemical Physics Letters, Crystal Growth and Design, IEEE Photonics Technology Letters, Journal of the American Ceramic Society, Journal of Applied Physics, Journal of Materials Chemistry C, Journal of Physical Chemistry, Journal of Physics D: Applied Physics, Journal of Solid State Chemistry, Journal of Vacuum Science and Technology A, Physica Status Solidi C, Physica Statur Solidi Rapid Research Letters, Thin Solid Films

H. von Wenckstern

- Project Reviewer: U.S. Department of Energy – Office of Science, National Research Fondation RSA
- Referee: Applied Physical Letters, Journal of Applied Physics, Thin Solid Films, Solid State Electronics, Physica Status Solidi, Journal of Electronic Materials, Turk. Journal of Physics, Journal of Material Sciences, u.a.

R. Schmidt-Grund

- Vice Chair of the German Association on Ellipsometry (Arbeitskreis Ellipsometrie – Paul Drude e.V.)
- Project Reviewer: Deutsche Forschungsgemeinschaft (DFG), US Department of Energy – Office of Science
- Referee: Thin Solid Films, Current Applied Physics, Physica Status Solidi C, Nature Communications, Applied Physics Letters, Optics Express, Journal of Electromagnetic Waves and Applications, Optical Materials, ACS Applied Materials & Interfaces

H. Frenzel
- Referee: IEEE Electronic Device Letters, Thin Solid Films, Applied Physics Letters, ETRI Journal, Journal of Applied Physics, Japanese Journal of Applied Physics, Advanced Materials, Physica Status Solidi (a)

8.23 External Cooperations

Academic

- Leibniz-Institut für Oberflächenmodifizierung e. V., Leipzig, Germany
  Prof. Dr. B. Rauschenbach, Prof. Dr. S. Mayr, Dr. J. Gerlach, Dr. C. Bundesmann, Dr. A. Lotnyk

- Universität Leipzig, Fakultät für Chemie und Mineralogie, Germany
  Prof. Dr. H. Krautscheid, Prof. Dr. R. Denecke

- Universität Halle-Wittenberg, Germany
  Prof. Dr. I. Mertig, Prof. Dr. W. Widdra, Prof. Dr. S.G. Ebbinghaus, Prof. Dr. W. Hergert

- Max-Planck-Institut für Mikrostrukturphysik, Halle/Saale, Germany
  Dr. O. Breitenstein, Dr. A. Ernst, Dr. P. Werner, Prof. Dr. D. Hesse

- Forschungszentrum Dresden-Rossendorf, Germany
  Prof. Dr. M. Helm, Dr. K. Potzger

- Technische Universität Berlin, Germany
  Prof. Dr. D. Bimberg, Prof. Dr. A. Hoffmann

- Universität Magdeburg, Germany
  Dr. J. Bläsing, Prof. Dr. J. Christen

- Universität Jena, Germany
  Prof. Dr. C. Ronning

- University of Pretoria, South Africa
  Prof. F. D. Auret

- University of Canterbury, Christchurch, New Zealand
  Prof. Dr. M. Allen

- Centre de Recherche sur l' Hétéro-Epitaxie et ses Applications (CNRS-CRHEA), Valbonne, France
  Dr. J. Zúñiga-Pérez, Dr. Guy Feuillet

- Western Michigan University, USA
  Prof. Dr. S. M. Durbin

- Katholieke Universiteit Leuven, Belgium
  Dr. V. Lazenka, Prof. Dr. K. Temst

Industry

- Freiberger Compound Materials GmbH, Freiberg, Germany
  Dr. G. Leibiger

8.24 Publications

Journals

S. Bitter, P. Schlupp, M. Bonholzer, H. von Wenckstern, M. Grundmann: *Influence of the cation ratio on optical and electrical properties of zinc-tin-oxide thin films from pulsed-laser deposition*, ACS Comb. Sci. **18**(4), 188-194 (2016)

L. Brillson, W.T. Ruane, H. Gao, Y. Zhang, J. Luo, H. von Wenckstern, M. Grundmann: *Spatially-Resolved Cathodoluminescence Spectroscopy of ZnO Defects*, Mat. Sci. Semic. Process. **57**, 197-209 (2016)

M. Grundmann, F.Klüpfel, R. Karsthof, P. Schlupp, F.-L. Schein, D. Splith, C. Yang, S. Bitter, H. von Wenckstern: *Oxide Bipolar Electronics: Materials, Devices and Circuits*, J. Phys. D: Appl. Phys. **49**(21), 213001 (25 pages) (2016)

M. Grundmann, J. Zúñiga-Pérez: *Pseudomorphic ZnO-based heterostructures: from polar through all semipolar to nonpolar orientations*, phys. stat. sol. (b) **253**(2), 351-360 (2016)

M. Grundmann, C. Sturm: *The Singular Optical Axes in Biaxial Crystals and Analysis of Their Spectral Dispersion Effects in β-Ga_2O_3*, arxiv: 1601.03760 (7 pages) (2016)

M. Jenderka, S. Richter, M. Lorenz, M. Grundmann: *Fundamental absorption edges in heteroepitaxial $Y_1Bi_1O_3$ thin films*, arxiv: 1606.03945 (2016)

M. Jenderka, S. Richter, M. Lorenz, M. Grundmann: *Fundamental absorption edges in heteroepitaxial $YBiO_3$ thin films*, J. Appl. Phys. **120**, 125702 (4 pages) (2016)

R. Karsthof, H. von Wenckstern, M. Grundmann: *Semi-transparent ZnO-based UV-active solar cells: Analysis of electrical loss mechanisms*, J. Vac. Sci. Technol. B **34**, 04J107 (8 pages) (2016)

R. Karsthof, P. Räcke, Z. Zhang, H. von Wenckstern, M. Grundmann: *Semi-transparent n-ZnO/p-NiO UV solar cells*, phys. stat. sol. (a) **213**(1), 30-37 (2016)

R. Khazaka, M. Grundmann, M. Portail, P. Vennéguès, M. Zielinski, T. Chassagne, D. Alquier, J.-F. Michaud: *Realization of minimum number of rotational domains in heteroepitaxied Si(110) on 3C SiC(001)*, Appl. Phys. Lett. **108**, 011608 (4 pages) (2016)

F.J. Klüpfel, H. von Wenckstern, M. Grundmann: *Ring Oscillators based on ZnO Channel JFETs and MESFETs*, Adv. Electron. Mater. **2**(7), 1500431 (5 pages) (2016)

C. Kranert, C. Sturm, R. Schmidt-Grund, M. Grundmann: *Raman tensor elements of β-Ga_2O_3*, Sci. Rep. **6**, 35964 (9 pages) (2016)

C. Kranert, C. Sturm, R. Schmidt-Grund, M. Grundmann: *Raman tensor elements of β-Ga_2O_3*, arxiv: 1606.07409 (2016)

C. Kranert, C. Sturm, R. Schmidt-Grund, M. Grundmann: *Raman Tensor Formalism for Optically Anisotropic Crystals*, Phys. Rev. Lett. **116**, 127401 (5 pages) (2016)

M. Lorenz, V. Lazenka, P. Schwinkendorf, M.J. Van Bael, A. Vantomme, K. Temst, M. Grundmann, T. Höche: *Epitaxial coherence at interfaces as origin of high magnetoelectric coupling in multiferroic BaTiO₃ - BiFeO₃ superlattices*, Adv. Mater. Interf. **3**(11), 1500822 (7 pages) (2016)

M. Lorenz, M.S. Ramachandra Rao, T. Venkatesan, E. Fortunato, P. Barquinha, R. Branquinho, D. Salgueiro, R. Martins, E. Carlos, A. Liu, F.K. Shan, M. Grundmann, H. Boschker, J. Mukherjee, M. Priyadarshini, N. DasGupta, D.J. Rogers, F.H. Teherani, E.V. Sandana, P. Bove, K. Rietwyk, A. Zaban, A. Veziridis, A. Weidenkaff, M. Muralidhar, M. Murakami, S. Abel, J. Fompeyrine, J. Zuniga-Perez, R. Ramesh, N.A. Spaldin, S. Ostanin, V. Borisov, I. Mertig, V. Lazenka, G. Srinivasan, W. Prellier, M. Uchida, M. Kawasaki, R. Pentcheva, P. Gegenwart, F. Miletto Granozio, J. Fontcuberta, N. Pryds: *The 2016 oxide electronic materials and oxide interfaces roadmap (ch. 3, M. Grundmann: Bipolar oxide devices)*, J. Phys. D: Appl. Phys. **49**(43), 433001 (53 pages) (2016)

M. Lorenz, G. Wagner, V. Lazenka, P. Schwinkendorf, M. Bonholzer, M.J. Van Beal, A. Vantomme, K. Temst, O. Oeckler, M. Grundmann: *Correlation of high magnetoelectric coupling with oxygen vacancy superstructure in epitaxial multiferroic BaTiO₃-BiFeO₃ composite thin films*, Materials 9, **44** (13 pages) (2016)

I. Lorite, Y. Kumar, P. Esquinazi, S. Friedländer, A. Pöppl, T. Michalsky, J. Meijer, M. Grundmann, T. Mayer: *Photo-enhanced magnetization in Fe-doped ZnO nanowires*, Appl. Phys. Lett. **109**, 012401 (4 pages) (2016)

I. Lorite, Y. Kumar, P. Esquinazi, S. Friedländer, A. Pöppl, T. Michalsky, J. Meijer, M. Grundmann, T. Meyer, I. Estrela-Lopis: *Photo-enhanced magnetization in Fe-doped ZnO nanowires*, arxiv: 1606.06955 (2016)

A. Mavlonov, S. Richter, H von Wenckstern, R. Schmidt-Grund, M. Lorenz, M. Grundmann: *Temperature dependent self-compensation in Al and Ga-doped Mg0.05Zn0.95O thin films grown by pulsed laser deposition*, J. Appl. Phys. **120**, 205703 (6 pages) (2016)

T. Michalsky, H. Franke, R. Buschlinger, U. Peschel, M. Grundmann, R. Schmidt-Grund: *Coexistence of strong and weak coupling in ZnO nanowire cavities*, arxiv: 1602.06804 (2016)

T. Michalsky, H. Franke, R. Buschlinger, U. Peschel, M. Grundmann, R. Schmidt-Grund: *Coexistence of strong and weak coupling in ZnO nanowire cavities*, Eur. Phys. J. Appl. Phys. **74**, 30502 (10 pages) (2016)

H. Modarresi, V. Lazenka, E. Menéndez, M. Lorenz, M. Bisht, A. Volodin, C. Van Haesendonck, M. Grundmann, M.J. Van Bael, K. Temst, A. Vantomme: *Induced ferromagnetism and magnetoelectric coupling in ion-beam synthesized BiFeO3-CoFe₂O₄ nanocomposite thin films*, J. Phys. D: Appl. Phys. **49**(32), 325302 (6 pages) (2016)

K. Narushima, Y. Ashizawa, K. Brachwitz, H. Hochmuth, M. Lorenz, M. Grundmann, K. Nakagawa: *Magnetic activity of surface plasmon resonance using dielectric magnetic materials fabricated on quartz glass substrate*, Jpn. J. Appl. Phys. **55**(7S3), 07MC05 (4 pages) (2016)

A. de Pablos-Martin, G. Benndorf, S. Tismer, M. Mittag, A. Cismak, M. Lorenz, M. Grundmann, Th. Höche: *Laser-Welded Fused Silica Substrates Using a Luminescent Fresnoite-Based Sealant*, Optics & Laser Technol. **80**, 176-185 (2016)

A. de Pablos-Martin, S. Tismer, G. Benndorf, M. Mittag, M. Lorenz, M. Grundmann, Th. Höche: *Laser soldering of sapphire substrates using a BaTiAl$_6$O$_{12}$ thin-film glass sealant*, Optics & Laser Technol. **81**, 153-161 (2016)

N. Petkov, J. Volk, R. Erdélyi, I. Endre Lukács, T. Nagata, C. Sturm, M. Grundmann: *Contacting ZnO individual crystal facets by direct write lithography*, ACS Appl. Mater. Interfaces **8**(36), 23891-23898 (2016)

A. Reinhardt, H. Frenzel, H. von Wenckstern, D. Spemann, M. Grundmann: *Electron transport mechanism in rf-sputtered amorphous zinc oxynitride thin films*, phys. stat. sol. (a) **213**(7), 1767-1773 (2016)

S. Richter, T. Michalsky, C. Sturm, B. Rosenow, M. Grundmann, R. Schmidt-Grund: *Exceptional points in anisotropic planar microcavities*, arxiv: 1609.07653 (2016)

W.T. Ruane, K.M. Johansen, K. Leedy, D.C. Look, H. von Wenckstern, M. Grundmann, L.J. Brillson: *Defect Segregation and Optical Emission in ZnO Nano– and Microwires*, Nanoscale **8**, 7631-7637 (2016)

A. Shkurmanov, C. Sturm, J. Lenzner, G. Feuillet, F. Tendille, P. De Mierry, M. Grundmann: *Selective growth of tilted ZnO nanoneedles and nanowires by PLD on patterned sapphire substrates*, AIP Adv. **6**, 095013 (5 pages) (2016)

A. Shkurmanov, C. Sturm, H. Hochmuth, M. Grundmann: *Growth kinetics of ultrathin ZnO Nanowires grown by Pulsed Laser Deposition*, Proc. Eng. **168**, 1156-1159 (2016)

M. Stiller, J. Barzola-Quiquia, P. Esquinazi, D. Spemann, J. Meijer, M. Lorenz, M. Grundmann: *Strong out-of-plane magnetic anisotropy in ion irradiated anatase TiO$_2$ thin films*, AIP Adv. **6**, 125009 (13 pages) (2016)

C.Sturm, M. Grundmann: *The Singular Optical Axes in Biaxial Crystals and Analysis of Their Spectral Dispersion Effects in β-Ga$_2$O$_3$*, Phys. Rev. A **93**, 053839 (8 pages) (2016)

C. Sturm, R. Schmidt-Grund, C. Kranert, J. Furthmüller, F. Bechstedt, M. Grundmann: *Dipole Analysis of the Dielectric Function of Colour Dispersive Materials: Application to Monoclinic Ga$_2$O$_3$*, arxiv: 1601.07892 (2016)

C. Sturm, R. Schmidt-Grund, C. Kranert, J. Furthmüller, F. Bechstedt, M. Grundmann: *Dipole analysis of the dielectric function of color dispersive materials: Application to monoclinic Ga$_2$O$_3$*, Phys. Rev. B **94**, 035148 (11 pages) (2016)

M. Thunert, A. Janot, H. Franke, C. Sturm, T. Michalsky, M.D. Martín, L. Viña, B. Rosenow, M. Grundmann, R. Schmidt-Grund: *Cavity Polariton Condensate in a Disordered Environment*, Phys. Rev. B **93**, 064203 (12 pages) (2016)

H. Wei, M. Grundmann, M. Lorenz: *Confinement-driven metal-insulator transition and polarity-controlled conductivity of epitaxial LaNiO$_3$/LaAlO$_3$ (111) superlattices*, Appl. Phys. Lett. **109**, 082108 (5 pages) (2016)

M. Wille, T. Michalsky, E. Krüger, M. Grundmann, R. Schmidt-Grund: *Absorptive lasing mode suppression in ZnO nano- and microcavities*, Appl. Phys. Lett. **109**, 061102 (4 pages) (2016)

M. Wille, C. Sturm, T. Michalsky, R. Röder, C. Ronning, R. Schmidt-Grund, M. Grundmann: *Carrier density driven material dynamics of lasing ZnO Nanowires*, arxiv: 1601.03866 (2016)

M. Wille, C. Sturm, T. Michalsky, R. Röder, C. Ronning, R. Schmidt-Grund, M. Grundmann: *Carrier density driven material dynamics of lasing ZnO Nanowires*, Nanotechnology **27**(22), 225702 (7 pages) (2016)

C. Yang, M. Kneiß, F.-L. Schein, M. Lorenz, M. Grundmann: *Room-temperature domain-epitaxy of copper iodide thin films for transparent CuI/ZnO heterojunctions with high rectification ratios larger than 109*, Sci. Rep. **6**, 21937 (8 pages) (2016)

C. Yang, M. Kneiß, M. Lorenz, M. Grundmann: *Room-temperature Synthesized Copper Iodide Thin Film as Degenerate p-Type Transparent Conducting Material with a Boosted Figure of Merit*, PNAS **113**(46), 12929-12933 (2016)

Z. Zhang, H. von Wenckstern, J. Lenzner, M. Lorenz, M. Grundmann: *Visible-blind and solar-blind ultraviolet photodiodes based on $(In_xGa_{1-x})_2O_3$*, Appl. Phys. Lett. **108**, 123503 (5 pages) (2016)

Z. Zhang, H. von Wenckstern, J. Lenzner, M. Grundmann: *Wavelength-selective ultraviolet (Mg,Zn)O photodiodes: Tuning of parallel composition gradients with oxygen pressure*, Appl. Phys. Lett. **108**, 243503 (5 pages) (2016)

J. Zúñiga-Pérez, L. Kappei, C. Deparis, F. Reveret, M. Grundmann, E. de Prado, O. Jamadi, J. Leymarie, S. Chenot, M. Leroux: *Homoepitaxial nonpolar (10-10) ZnO/ZnMgO heterostructures: from single layers to monolithic Bragg reflectors and optical microcavities*, Appl. Phys. Lett. **108**, 251904 (5 pages) (2016)

V. Zviagin, Y. Kumar, I. Lorite, P. Esquinazi, M. Grundmann, R. Schmidt-Grund: *Ellipsometric Investigation of $ZnFe_2O_4$ Thin Films in Relation to Magnetic Properties*, Appl. Phys. Lett. **108**, 131901 (4 pages) (2016)

V. Zviagin, P. Richter, T. Böntgen, M. Lorenz, M. Ziese, D.R.T. Zahn, G. Salvan, M. Grundmann, R. Schmidt-Grund: *Comparative Study of Optical and Magneto-Optical Properties of Normal, Disordered and Inverse Spinel Type Oxides*, phys. stat. sol. (b) **253**(3), 429-436 (2016)

Books

M. Grundmann: *The Physics of Semiconductors, An Introduction including Nanophysics and Applications*, 3rd edition, (Springer, Heidelberg, 2016), ISBN 978-3-319-23879-1

Patents

M. Grundmann, H. Frenzel, A. Lajn, H. von Wenckstern: *TRANSPARENT RECTIFYING METAL/METAL OXIDE/SEMICONDUCTOR CONTACT STRUCTURE AND METHOD FOR THE PRODUCTION THEREOF AND USE*, JP 5897621 B2 (Japan Patent Office, 2016)

Talks

S. Bitter, P. Schlupp, H. von Wenckstern, M. Grundmann: *Influence of cation stoichiometry on performance of unipolar and bipolar zinc-tin-oxide diodes*, DPG spring meeting, Regensburg, Germany, March 2016

S. Bitter, P. Schlupp, H. von Wenckstern, M. Grundmann: *Influence of cation stoichiometry on performance of bipolar zinc-tin-oxide diodes*, EMRS Fall Meeting 2016, Warsaw, Poland, September 2016

M. Grundmann: *Bipolar Oxide Diodes: Role of the Interface for Type-I, -II and -III Heterostructures*, 43rd Conference on the Physics and Chemistry of Surfcaes and Interfaces (PCSI-43), Palm Springs, CA, USA, January (invited)

M. Grundmann, C. Sturm, C. Kranert, R. Schmidt-Grund, J. Furthmüller, F. Bechstedt, Z. Zhang, H. von Wenckstern: *Tensor Properties of Gallium Oxide and Related Materials*, EMRS Spring Meeting, Lille, France, May 2016 (invited)

M. Grundmann: *Semiconducting oxide thin films: Novel rectifying contacts for electronic and photonic applications*, 18th International Conference on Solid Films and Surfaces (ICSFS 18), Chemnitz, August 2016 (invited)

O. Herrfurth, S. Richter, T. Michalsky, C. Sturm, H. Franke, M. Grundmann, R. Schmidt-Grund: *Pump-probe time-resolved spectroscopic ellipsometry with sub-picosecond resolution*, 7th International Conference on Spectroscopic Ellipsometry (ICSE-7), Berlin, Germany, June 2016

R. Karsthof: *Semi-transparent UV-active solar cells*, Annual Conference of the Graduate School BuildMoNa, Leipzig, Germany, March 2016

R. Karsthof, H. von Wenckstern, M. Grundmann: *Semi-transparent UV Solar Cells*, vistit of SUNY Binghamton, Leipzig, Germany, June 2016

R. Karsthof, H. von Wenckstern, M. Grundmann: *Analyse elektrischer Verlustmechanismen in transparenten UV-Solarzellen*, 6. Workshop Transparente Leitfähige Materialien, Erfurt, Germany, November 2016 (invited)

C. Kranert C. Sturm, R. Schmidt-Grund, M. Grundmann: *Raman Tensor Formalism for Anisotropic Crystals*, DPG spring meeting, Regensburg, Germany, March 2016

T. Michalsky, M. Wille, E. Krüger, H. Franke, M. Grundmann, R. Schmidt-Grund: *Tunable lasing from hexagonal ZnO micro wires at room temperature*, DPG spring meeting, Regensburg, Germany, March 2016

T. Michalsky, M. Wille, R. Buschlinger, H. Franke, U. Peschel, M. Grundmann, R. Schmidt-Grund: *Coexistance of strong and weak coupling in ZnO nanowire cavities*, 33th International Conference on the Physics of Semiconductors, ICPS2016, Beijing, China, August 2016

J. Rensberg, C. Wan, S. Richter, Y. Zhou, S. Zhang, R. Schmidt-Grund, S. Ramanathan, F. Capasso, M.A. Kats, C. Ronning: *Wavelength- and Temperature-Tunable Ultra-Thin Perfect Absorbers Using Ion Beam Irradiation*, MRS Fall Meeting 2016, Boston, USA, November 2016

S. Richter, T. Michalsky, C. Sturm, H. Franke, M. Grundmann, R. Schmidt-Grund: *Radiative modes in anisotropic planar microcavities*, DPG spring meeting, Regensburg, Germany, March 2016

S. Richter, C. Sturm, R. Schmidt-Grund, M. Grundmann: *Circularly polarized mode degeneracies in uniaxial planar microcavities*, Annual Conference of the Graduate School BuildMoNa, Leipzig, Germany, March 2016

P. Schlupp, H. von Wenckstern, M. Grundmann: *Schottky barrier diodes on amorhpous zinc tin oxide*, DPG spring meeting, Regensburg, Germany, March 2016

P. Schlupp, H. von Wenckstern, M. Grundmann: *Schottky barrier diodes on amorhpous zinc tin oxide*, EMRS Fallmeeting, Warsaw, Poland, September 2016

P. Schlupp, H. von Wenckstern, M. Grundmann: *Flexible elektronische Bauelemente auf Basis transparenter Oxide*, 6. EFDS Workshop "Transparente leitfähige Materialien (TCO/TCM)", Erfurt, Germany, November 2016 (invited)

R. Schmidt-Grund: *Lasing and Quantum Gases in ZnO Nanostructures*, CIMTEC 2016, Perugia, Italy, June 2016 (invited)

R. Schmidt-Grund: *Emerging materials - magnetic spinels and biaxial Ga2O3*, 1st ELIps User Workshop, Dolní Brezany & Brno, Czech Republic, October 2016 (invited)

A. Shkurmanov, C. Sturm, H. Hochmuth, M. Grundmann: *CMOS-compatible PLD-growth of ultrathin ZnO nanowires*, DPG spring meeting, Regensburg, Germany, March 2016

D. Splith, S. Müller, F. Schmidt, H. von Wenckstern, M. Grundmann: *Method of choice for the fabrication of Schottky contacts for unipolar devices on heteroepitaxial Ga_2O_3*, DPG spring meeting, Regensburg, Germany, March 2016

C. Sturm, C. Kranert, J. Furthmüller, F. Bechstedt, R. Schmidt-Grund, M. Grundmann: *Dielectric and Raman tensor of monoclinic Ga_2O_3*, DPG spring meeting, Regensburg, Germany, March 2016

C. Sturm, C. Kranert, J. Furthmüller, F. Bechstedt, R. Schmidt-Grund, M. Grundmann: *Dielectric function of optically anisotropic materials and its application to monoclinic beta-Ga_2O_3*, 7th International Conference on Spectroscopic Ellipsometry (ICSE-7), Berlin, Germany, June 2016

C. Sturm, A. Shkurmanov, J. Volk, I Lukács, N.Q. Khánh, M. Grundmann: *On chip integration of piezoelectric Nanowires*, Eurosensors XXX, Budapest, Hungary, September 2016 (Talk at the PiezoMat Open Session)

H. von Wenckstern: *Semiconducting oxides - From material design to basic devices*, Orlando, USA, January 2016 (invited)

H. von Wenckstern: *Defects in wide bandgap semiconducting oxides - Bulk material, epitaxial thin films and microresonators*, EMRS spring meeting Lille, Symposium BB: "Defect-induced effects in nanomaterials", Lille, France, May 2016 (invited)

H. von Wenckstern: *Semiconducting oxides - From material design to basic devices*, Aalto University School of Science, Antimatter and Nuclear Engineering Group, Espoo, Finland, May 2016 (invited)

H. von Wenckstern: *Deep-UV photo detectors based on group-III sesquioxides*, German-Japanese Gallium Oxide Technology Meeting 2016, Berlin, Germany, September 2016 (invited)

M. Wille, C. Sturm, T. Michalsky, R. Röder, C. Ronning, R. Schmidt-Grund, M. Grundmann: *Carrier density driven lasing dynamics in ZnO nanowires*, DPG spring meeting, Regensburg, Germany, March 2016

M. Wille, C. Sturm, T. Michalsky, R. Röder, C. Ronning, R. Schmidt-Grund, M. Grundmann: *Lasing dynamics in ZnO nanowires*, Annual Conference of the Graduate School BuildMoNa, Leipzig, Germany, March 2016

V. Zviagin, P. Richter, Y. Kumar, I. Lorite, M. Lorenz, D. Spemann, J. Meijer, D.R.T. Zahn, G. Salvan, P. Esquinazi, M. Grundmann, R. Schmidt-Grund: *Spectroscopic Ellipsometry and MOKE as a Probe for Structural Properties of Spinel Oxide Thin Films*, DPG spring meeting, Regensburg, Germany, March 2016

V. Zviagin, P. Richter, M. Bonholzer, Y. Kumar, I. Lorite, D. Spemann, J. Meijer, D.R.T. Zahn, G. Salvan, P. Esquinazi, M. Grundmann, R. Schmidt-Grund: *Spectroscopic Ellipsometry as a Probe for Structural Properties of Spinel Ferrite Thin Films*, 7th International Conference on Spectroscopic Ellipsometry (ICSE-7), Berlin, Germany, June 2016

Posters

K. Dorywalski, M. Piasecki, B. Andriyevsky, R. Schmidt-Grund, M. Grundmann, N. Lemee, T. Krzyzynski: *Optical properties of epitaxial $Na_xBi_{1-x}TiO_3$ lead-free piezoelectric thin films: ellipsometric and theoretical studies*, Poster at the 7th International Conference on Spectroscopic Ellipsometry (ICSE-7), Berlin, Germany, June 2016

O. Herrfurth, S. Richter, T. Michalsky, C. Sturm, H. Franke, M. Grundmann, R. Schmidt-Grund: *Towards time-resolved spectroscopic ellipsometry with femtosecond-resolution*, ELI summer school 2016, Dolní Brezany, Czech Republic, August 2016

C. Kranert, C. Sturm, R. Schmidt-Grund, M. Grundmann: *Determination of the Raman Tensor of Optically Anisotropic Crystals*, 7th International Conference on Spectroscopic Ellipsometry (ICSE-7), Berlin, Germany, June 2016

C. Kranert, C. Sturm, R. Schmidt-Grund, M. Grundmann: *Determination of the Raman Tensor of Optically Anisotropic Crsystals*, 33th International Conference on the Physics of Semiconductors, ICPS2016, Beijing, China, August 2016

T. Michalsky, H. Franke, O. Herrfurth, R. Buschlinger, U. Peschel, M. Grundmann, R. Schmidt-Grund: *Coexistence of strong and weak coupling in ZnO nanowire cavities*, DPG spring meeting, Regensburg, Germany, March 2016

T. Michalsky, M. Wille, R. Buschlinger, H. Franke, U. Peschel, M. Grundmann, R. Schmidt-Grund: *Coexistence of strong and weak coupling in ZnO nanowire cavities*, Conference on Physics of Light-Matter Coupling in Nanostructures (PLMCN 17), Nara, Japan, March 2016

S. Richter, T. Michalsky, M. Wille, C. Sturm, H. Franke, M. Grundmann, R. Schmidt-Grund: *Radiative modes in anisotropic planar microcavities*, Conference on Physics of Light-Matter Coupling in Nanostructures (PLMCN 17), Nara, Japan, March 2016

S. Richter, T. Michalsky, C. Sturm, B. Rosenow, M. Grundmann, R. Schmidt-Grund: *Cavity photon modes in anisotropic planar microcavities*, 33th International Conference on the Physics of Semiconductors, ICPS2016, Beijing, China, August 2016

S. Richter, T. Michalsky, C. Sturm, M. Grundmann, R. Schmidt-Grund: *1D photonic crystals with broken rotational symmetry*, BuildMoNa Module 2016-T4: From Molecules to Materials - Artificial molecules and solid state crystals, Leipzig, Germany, September 2016

S. Richter, T. Michalsky, C. Sturm, B. Rosenow, M. Grundmann, R. Schmidt-Grund: *Anisotropic planar microcavities and the occurrence of exceptional points*, BuildMoNa Module 2016-T6: Hybrid Systems - Metamaterials, Leipzig, Germany, September 2016 (Poster award)

A. Shkurmanov, C. Sturm, H. Hochmuth, G.Feuilett, F.Tendille, P. De Mierry, M. Grundmann: *Growth of tilted ZnO nanowires by PLD on pre-structured sapphire substrates*, DPG spring meeting, Regensburg, Germany, March 2016

A. Shkurmanov, C. Sturm, H. Hochmuth, G.Feuilett, F.Tendille, P. De Mierry, M. Grundmann: *Growth of ultrathin ZnO nanowires at CMOS compatible temperature by pulsed laser deposition*, E-MRS Spring Meeting 2016, Lille, May 2016

A. Shkurmanov, C. Sturm, H. Hochmuth, M. Grundmann: *Controlling of the geometrical shape of ZnO nanowires by pulsed laser deposition*, International Conference on Nanogenerators and Piezotronics 2016, Rome, June 2016

A. Shkurmanov, C. Sturm, H. Hochmuth, M. Grundmann: *Growth kinetics of ultrathin ZnO Nanowires grown by Pulsed Laser Deposition*, EUROSENSORS 2016, Budapest, September 2016

A. Shkurmanov, C. Sturm, H. Hochmuth, G.Feuilett, F.Tendille, P. De Mierry, M. Grundmann: *Tilted nanowires as building block for hyperbolic metamaterials*, BuildMoNa Module 2016-T6: Hybrid Systems - Metamaterials, Leipzig, Germany, September 2016

D. Splith, S. Müller, F. Schmidt, H. von Wenckstern, M. Grundmann: *Method of choice for the fabrication of Schottky contacts for unipolar devices on heteroepitaxial Ga_2O_3*, Annual Conference of BuildMoNa, Leipzig, Germany 2016

C. Sturm, R. Schmidt-Grund, M. Grundmann: *Singular Optical Axes in Biaxial Crystals*, 7th International Conference on Spectroscopic Ellipsometry (ICSE-7), Berlin, Germany, June 2016 (Best-Poster Award)

C. Sturm, R. Schmidt-Grund, C. Kranert, J. Furthmüller, F. Bechstedt, M. Grundmann: *Dielectric Function of Optically Anisotropic Materials: Application to Monoclinic Ga_2O_3*, 33th International Conference on the Physics of Semiconductors, ICPS2016, Beijing, China, August 2016

M. Thunert, S. Lange, H. Franke, C. Sturm, T. Michalsky, M. Grundmann, R. Schmidt-Grund: *Temporal coherence properties of a polariton condensate in a disordered environment*, DPG spring meeting, Regensburg, Germany, March 2016

M. Thunert, S. Lange, M. Wille, H. Franke, C. Sturm, T. Michalsky, M. Grundmann, R. Schmidt-Grund: *Temporal coherence properties of a polariton condensate in a disordered environment*, Conference on Physics of Light-Matter Coupling in Nanostructures (PLMCN 17), Nara, Japan, March 2016

M. Wille, T. Michalsky, R. Röder, C. Ronning, R. Schmidt-Grund, M. Grundmann: *Carrier density driven lasing dynamics in ZnO Nanowires*, Conference on Physics of Light-Matter Coupling in Nanostructures (PLMCN 17), Nara, Japan, March 2016

M. Wille, T. Michalsky, C. Sturm, E. Krüger, R. Röder, C. Ronning, R. Schmidt-Grund, M. Grundmann: *Electronic structure dynamics in highly excited nano- and microwire lasers*, 33th International Conference on the Physics of Semiconductors, ICPS2016, Beijing, China, August 2016

V. Zviagin, P. Richter, Y. Kumar, I. Lorite, M. Lorenz, D.R.T. Zahn, G. Salvan, P. Esquinazi, M. Grundmann, R. Schmidt-Grund: *Optical and Magneto-Optical Investigation of Normal and Disordered $ZnFe_2O_4$ in Relation to Magnetic Properties*, DPG spring meeting, Regensburg, Germany, March 2016

V. Zviagin, Y. Kumar, I. Lorite, D. Spemann, J. Meijer, P. Esquinazi, M. Grundmann, R. Schmidt-Grund: *Magnetic and Optical Properties of Normal, Disordered, and Inverse Spinel Oxides*, 33th International Conference on the Physics of Semiconductors, ICPS2016, Beijing, China, August 2016

V. Zviagin, P. Richter, M. Bonholzer, Y. Kumar, I. Lorite, D.R.T. Zahn, G. Salvan, P. Esquinazi, M. Grundmann, R. Schmidt-Grund: *Ellipsometric and Magneto-Optical Study of Ionic Structure of Spinel Oxide Thin Films with Respect to their Magnetic Properties*, 33th International Conference on the Physics of Semiconductors, ICPS2016, Beijing, China, August 2016

8.25 Graduations

Doctorate

- Michael Bonholzer
  Magnetic Tunnel Junctions based on spinel $Zn_xFe_{3-x}O_4$
  October 2016

- Abdurashid Mavolonov
  Doping Efficiency and Limits in Wurtzite (Mg,Zn)O Alloys
  November 2016

- Stefan Müller
  Schottky-Kontakte auf Zinkoxid- und β-Galliumoxid-Dünnfilmen: Barrierenformation, elektrische Eigenschaften und Temperaturstabilität
  February 2016

- Zhipeng Zhang
  Ultraviolet Photodiodes Based on (Mg,Zn)O and $(Ga,In)_2O_3$ Thin Films
  October 2016

Master

- Max Kneiß
  Transporteigenschaften und optische Charakterisierung von CuI-Kristallen und -Dünnfilmen
  April 2016

- Michael Scheibe
  Defekte in (Mg, Zn, O) Dünnfilmen: Einfluss der Pufferschicht und des Substratschnitts
  January 2016

Bachelor

- Tobias Abel
  Deposition and characterization of Zn-doped CuI Thin Films
  March 2016

- Selina Helmbold
  Schottky-Kontakte auf Zinkoxinitrid basierend auf Silber-Platin-Mischungen
  September 2016

- Florian Jung
  Growth and characterisation of MgO/TiN superlattices
  October 2016

- Evgeny Krüger
  Lasingprozesse in ZnO-Mikrodrähten bei Raumtemperatur
  January 2016

- Oliver Lahr
  Strukturelle und elektrische Charakterisierung epitaktischer SnO_2 Dünnfilme
  July 2016

- Julian Pohl
  Herstellung und elektrische Charakterisierung von Galliumoxid-Transistoren
  September 2016

- Benjamin Wehr
  Untersuchung des Wachstumsverhaltens von Kupfer-Gallium-Oxiden auf c-orientiertem Zinkoxid
  July 2016

8.26 Guests

- M.S. Ramachandra Rao
  Indian Institute of Technology (IIT) Madras, India
  June 2016

- Martin Allen
  University Christchurch, New Zealand
  December 2016

9

Superconductivity and Magnetism

9.1   Introduction

The main interests of the group at the division are phenomena related to superconductivity and magnetism in solids. In the last few years the research activities in superconductivity have been mainly concentrated in searching for its existence in graphite, especially at graphite interfaces between Bernal-like crystalline regions. This research issue started in our division in Leipzig in the year 2000 and became supporting experimental evidence quite recently, indicating the existence of superconductivity at temperatures above 100 K. Future work will be concentrated in the localization of the superconducting phases and the increase of the superconducting yield.

Our division was the first to show that atomic lattice defects can produce magnetic order in graphite without the need of magnetic ions. This phenomenon is known nowadays as Defect-Induced Magnetism and it is found in a broad spectrum of different materials. We are involved in a collaborative research project with the aim of triggering this phenomenon in nominally non-magnetic oxides, via vacancies and/or hydrogen doping. Further research topic is the study of the electrical and magnetic properties of oxide multilayers of thickness starting from a few unit cells. Main research issues are related to the magnetic coupling at the interfaces of oxide layers, i.e. exchange bias phenomena, with different magnetic properties as well as the possibility to develop a two-dimensional electron gas at the interfaces.

Pablo Esquinazi

9.2   Topological Hall effect in antiferromagnetically coupled SrRuO$_3$/La$_{0.7}$Sr$_{0.3}$MnO$_3$ epitaxial heterostructures

I. Vrejoiu[*], M. Ziese

[*]II. Physikalisches Institut, Universität zu Köln, D-50937 Köln, Germany

Interaction of conduction electrons with non-coplanar or non-collinear spin textures in magnetically ordered systems might result in a topological Hall effect. We studied the Hall effect in epitaxial heterostructures of the ferromagnetic oxides SrRuO$_3$ and

$La_{0.7}Sr_{0.3}MnO_3$. We identified a Hall effect contribution that we attributed to a topological effect that arises most likely from the non-coplanar ordering of the Ru and Mn magnetic moments in the individual ferromagnetic layers, which exhibit different magnetocrystalline anisotropies and a strong antiferromagnetic interlayer-coupling. Already the different field dependences of Hall resistivity and magnetization shown in Fig. 9.1 indicate that there is an additional Hall effect process beyond the anomalous Hall effect.
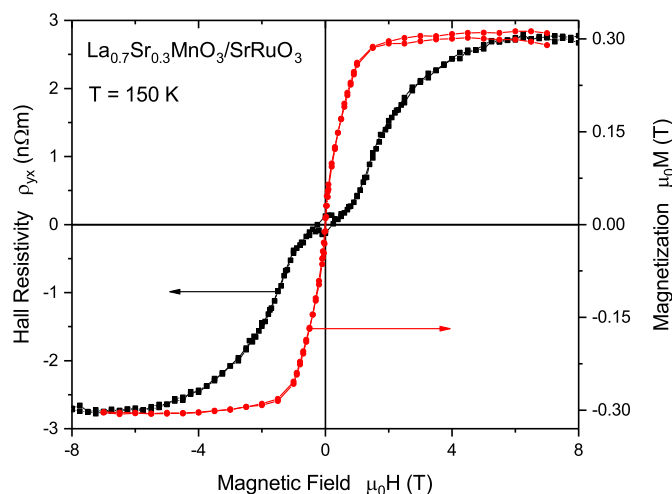
Figure 9.1: Hall resistivity (left axis) and corresponding magnetization (right axis) of a LSMO/SRO sample at 150 K.

9.3 Magnetic and magnetotransport properties of ultrathin $La_{0.7}Ba_{0.3}MnO_3$ epitaxial films embedded in $SrRuO_3$

F. Bern, M. Ziese, I. Vrejoiu[*], X. Li[†], P.A. van Aken[†]

[*]II. Physikalisches Institut, Universität zu Köln, D-50937 Köln, Germany
[†]Max-Planck-Institut für Festkörperforschung, Stuttgart Center for Electron Microscopy, Heisenbergstrasse 1, D-70569 Stuttgart, Germany

The structural, magnetic and magnetotransport properties of $La_{0.7}Ba_{0.3}MnO_3$ layers interfaced with $SrRuO_3$ layers were studied. In this embedded geometry $La_{0.7}Ba_{0.3}MnO_3$ layers are ferromagnetic even for a thickness of only one unit cell. This is illustrated in Fig. 9.2 showing the magnetic moment for 1 and 2 unit cell thick $La_{0.7}Ba_{0.3}MnO_3$ as well as the Curie temperature dependence on the $La_{0.7}Ba_{0.3}MnO_3$ layer thickness. This result is in contrast to $La_{0.7}Ba_{0.3}MnO_3$ films grown on $SrTiO_3$ that turn antiferromagnetic below a thickness of about 8 unit cells. The stabilization mechanism due to the adjacent $SrRuO_3$ layers is still under investigation.
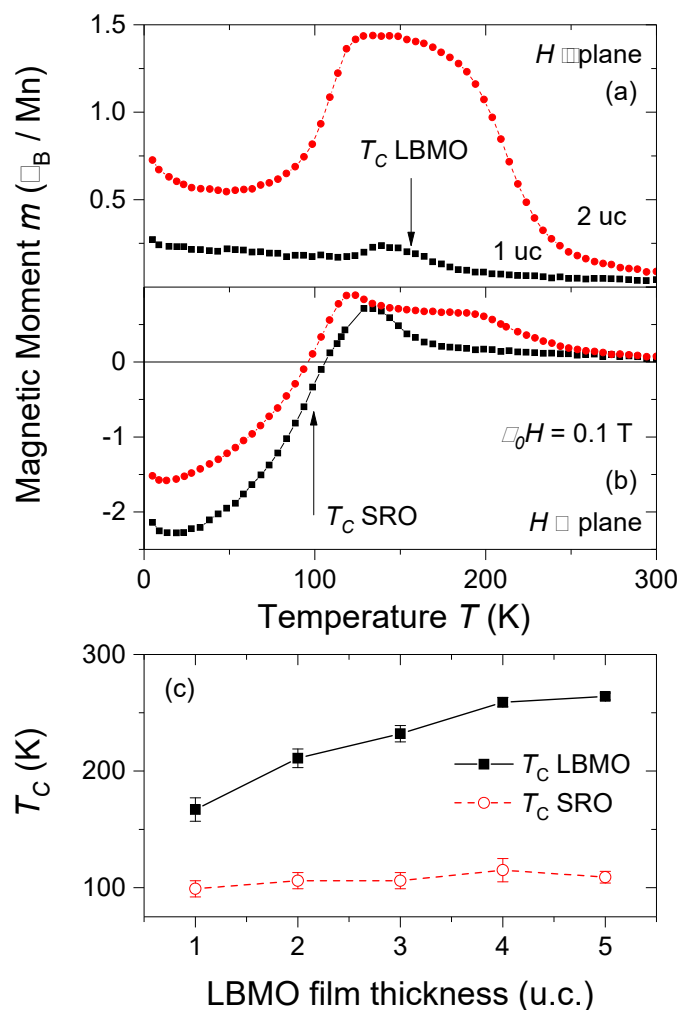
Figure 9.2: (a) and (b) Magnetic moment as a function of temperature for 1 and 2 unit cell thick La$_{0.7}$Ba$_{0.3}$MnO$_3$ layers embedded in SrRuO$_3$. The magnetic field of 0.1 T was applied (a) parallel and (b) perpendicular to the layers. (c) Curie temperature as a function of La$_{0.7}$Ba$_{0.3}$MnO$_3$ layer thickness.

9.4 Strong out-of-plane magnetic anisotropy in ion irradiated anatase TiO$_2$ thin films

M. Stiller, J. Barzola-Quiquia, P. Esquinazi, D. Spemann[*], J. Meijer[†], M. Lorenz[‡], M. Grundmann[‡]

[*]Physics Department, Leibniz Institute for Surface Modification, Permoserstr. 15,
D-04318 Leipzig, Germany
[†]Division of Nuclear Solid State Physics, Felix Bloch Institute for Solid State Physics,
University of Leipzig, D-04103 Leipzig, Germany
[‡]Semiconductor Physics Group, Felix Bloch Institute for Solid State Physics,
University of Leipzig, D-04103 Leipzig, Germany

The temperature and field dependence of the magnetization of epitaxial, undoped anatase TiO$_2$ thin films on SrTiO$_3$ substrates was investigated. Low-energy ion irradiation was used to modify the surface of the films within a few nanometers, yet with high enough energy to produce oxygen and titanium vacancies. The as-prepared thin

film shows ferromagnetism which increases after irradiation with low-energy ions. An optimal and clear magnetic anisotropy was observed after the first irradiation, opposite to the expected form anisotropy, see Fig. 9.3. Taking into account the experimental parameters, titanium vacancies as di-Frenkel pairs appear to be responsible for the enhanced ferromagnetism and the strong anisotropy observed in our films, see Fig. 9.4. The magnetic impurities concentrations was measured by particle-induced X-ray emission with ppm resolution. They are ruled out as a source of the observed ferromagnetism before and after irradiation.
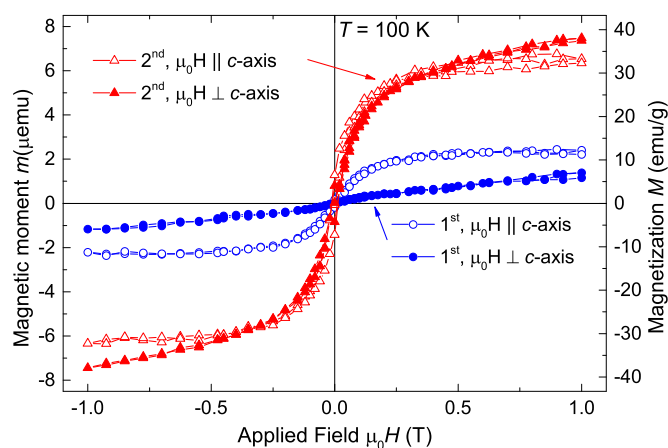
Figure 9.3: Anisotropy of the saturated magnetization after first and second argon ion irradiation at a temperature of $T = 100$ K. After first treatment, an easy axis perpendicular to the film surface can be observed.
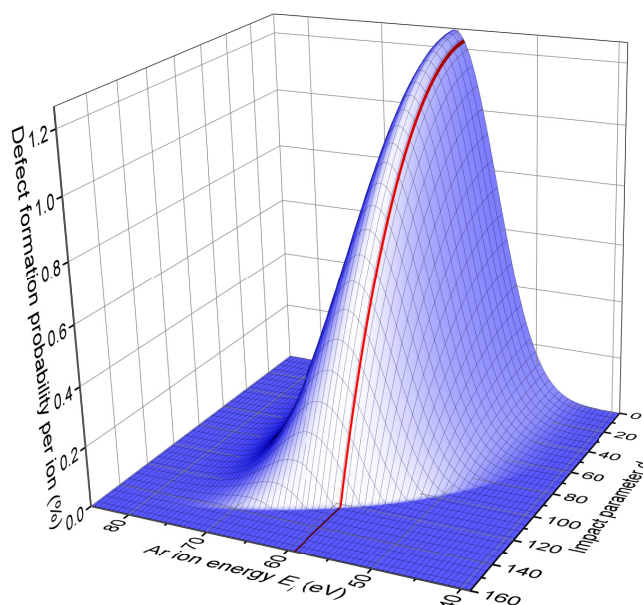
Figure 9.4: The Ti defect formation probability (DFP) as a function of incident ion energy and impact parameter d. The red line indicates the mean ion energy $E_i = 59.2$ eV. The fraction of ions having a probability to produce defects of less than 0 %, is not shown.

9.5 Identification of a possible superconducting transition above room temperature in natural graphite crystals

C. E. Precker, P. Esquinazi, A. Champi[*], J. Barzola-Quiquia, M. Zoraghi, S. Muiños-Landin, A. Setzer, W. Böhlmann, D. Spemann[†], J. Meijer[‡], T. Muenster[§], O. Baehre[§], G. Kloess[§], H. Beth[¶]

[*]Centro de Ciências Naturais e Humanas, Universidade Federal do ABC, 09210-170, Santo André, São Paulo, Brazil

[†]Physics Department, Leibniz Institute for Surface Modification, Permoserstr. 15, D-04318 Leipzig, Germany

[‡]Division of Nuclear Solid State Physics, Felix Bloch Institute for Solid State Physics, University of Leipzig, D-04103 Leipzig, Germany

[§]Institut für Mineralogie, Kristallographie und Materialwissenschaft, Fakultät für Chemie und Mineralogie, Universität Leipzig, Scharnhorststraße 20, D-04275 Leipzig, Germany

[¶]Golden Bowerbird Pty Ltd., 32 Alidenes Rd., 2482 Mullumbimby, Nsw Australia

We have measured with high precision the electrical resistance of highly ordered natural graphite samples from mines of Sri Lanka and Brazil. In both kind of graphite samples, we have identified a transition at $\approx$ 350 K with $\approx$ 40 K transition width. The step-like change in temperature of the resistance, its magnetic irreversibility and time dependence after a field change, consistent with trapped flux and flux creep, and the partial magnetic flux expulsion obtained by magnetization measurements, see Fig. 9.5, suggest the existence of granular superconductivity below 350 K. The zero-field virgin state can only be reached again after zero field cooling the sample from above the transition, see Fig. 9.6. The existence of well-ordered rhombohedral graphite phase in all measured samples has been proved by X-ray diffraction measurements, suggesting its interfaces with the Bernal phase as a possible origin for the high-temperature superconductivity, as theoretical studies predicted. The localization of the granular superconductivity at these two dimensional interfaces prevents the observation of a zero resistance state or of a full Meissner state.

9.6 Superconductivity in the amorphous phase of topological insulator BiSb alloys

J. Barzola-Quiquia, C. Lauinger[*] M. Zoraghi M. Stiller S. Sharma[†] P. Häussler[‡]

[*]LuK, GmbH & Co., D-77815 Bühl, Germany

[†]Department of Physics, Govt. Dungar College Bikaner, Rajasthan, India

[‡]Division of Thin Films Physics, Institute of Physics, Chemnitz University of Technology, 09107 Chemnitz, Germany

In this work we investigated the electrical properties of rapidly quenched amorphous BiSb alloys in the temperature range of 1.2 K to 345 K. The resistance reveals that for a
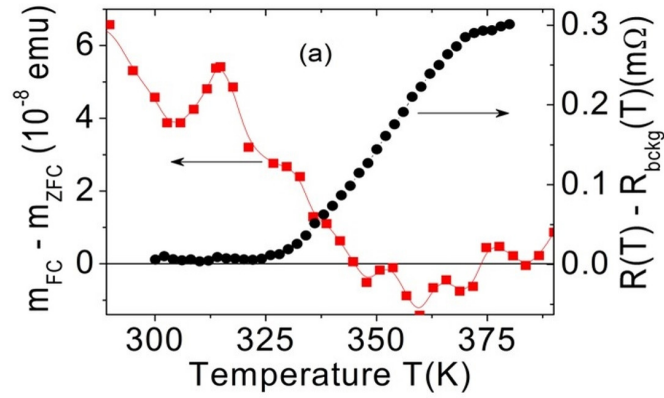
Figure 9.5: The difference (left y-axis, red points) between the measured field cooled magnetic moment m_{FC} and the zero field cooled m_{ZFC} vs. temperature at a field of 50 mT applied at 250 K for a natural graphite crystal from Brazil. Right y-axis: Difference between the measured resistance and a linear in temperature background vs. temperature for a sample from the same batch at zero field.
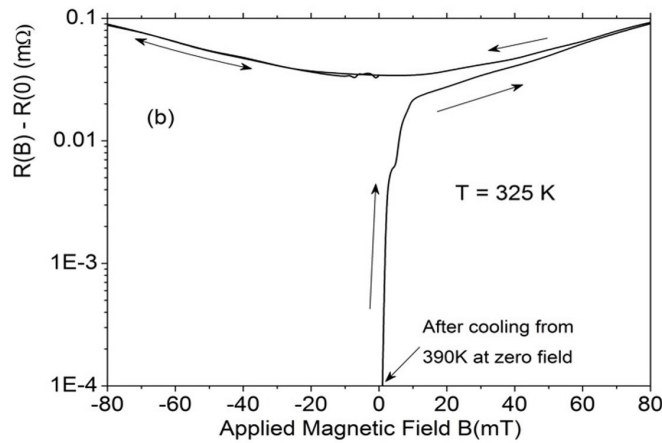
Figure 9.6: Change of the resistance with field at a temperature of 325 K after cooling it from 390 K at zero field. The field was applied normal to the interfaces.

broad range of different compositions, including that for the topological insulator (TI), a superconducting state in the amorphous phase is present. After crystallization and annealing at intermediate temperature, we found that in pure Bi and BiSb alloys with composition corresponding to the TI, the superconductivity persist, but the transition shifts to lower temperature, see Fig. 9.7. The highest superconducting transition temperature T_{C0} was found for pure Bi and those TI's, with a shift to low temperatures when the Sb content is increased, see Fig. 9.8. After a annealing at a maximum temperature of $T = 345$ K, the samples are non-superconducting within the experimental range and the behavior changes from semiconducting-like for pure Bi, to metallic-like for pure Sb. Transition temperature T_{C0} of the amorphous BiSb alloys have been calculated in the BCS-Eliashberg-McMillan framework, modified for binary alloys. The results can explain very well the experimental results and show that amorphous BiSb exhibits a strong to intermediate electron-phonon coupling.
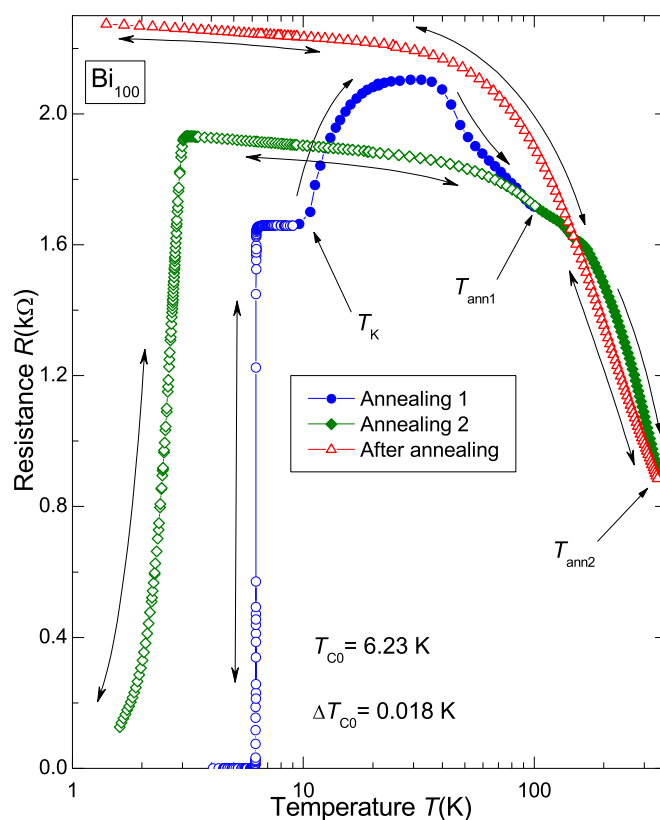
Figure 9.7: Resistance of the *in-situ* prepared Bi film, measured immediately after preparation and during annealing. Symbols: $\longrightarrow$ irreversible changes; $\longleftrightarrow$ reversible changes of the resistance. The experimental data plotted with open symbols are after annealing and refer to the reversible state.
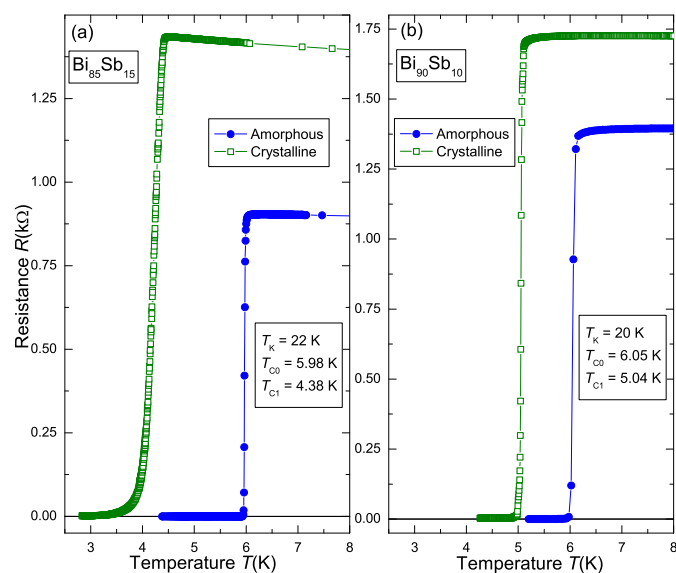
Figure 9.8: Resistance of (a) $Bi_{85}Sb_{15}$ and (b) $Bi_{90}Sb_{10}$ films. A Superconducting transition in the amorphous state and after crystallization is visible. The crystalline phase was obtained after annealing the sample up to $T = 60$ K.

9.7 Funding

Defect-induced Magnetism in Oxides
Prof. Dr. Pablo Esquinazi
DFG SFB 762/3, B1

Magnetic and electric properties of ultrathin oxide films
Prof. Dr. Pablo Esquinazi and Prof. Dr. Michael Ziese
DFG SFB 762/3, B5

Study of the reentrant metallic behavior of the interfaces in graphite at very high fields
Prof. Dr. Pablo Esquinazi
DAAD - PPP USA 2016/2017

9.8 Organizational Duties

P. Esquinazi
- Project Reviewer: Deutsche Forschungsgemeinschaft (DFG), National Science Foundation (USA), German-Israeli Foundation (GIF), Israel Science Foundation, Department of Energy (Washington), DAAD
- Referee: Phys. Rev. Lett, Phys. Rev. B., Appl. Phys. Lett., Chem. Phys. Lett., Nature Physics, Nature Materials, Physica C, Phys. Lett. A, phys. stat. sol., J. Low Temp. Phys., Carbon, J. Chem. Phys., Eur. J. Phys. B, J. Magn. Magn. Mater.

M. Ziese
- Head of the Basic Physics Laboratory
- Dean of Studies
- Referee: Phys. Rev. Lett., Phys. Rev. B., Adv. Mater., Appl. Phys. A, Current Nanoscience, Eur. Phys. J. B, IEEE Trans. Magn., J. Phys.: Condens. Matter, J. Phys. D: Appl. Phys., J. Alloys Comp., J. Appl. Phys., J. Am. Ceram. Soc., J. Magn. Magn. Mater., J. Mater. Research, J. Mater. Science, Materials Science and Engineering B, Nanotechnology, phys. stat. sol., Thin Solid Films

W. Böhlmann
- Referee: J. Physical Chemistry, J. of American Chemical Society, Microporous and Mesoporous Materials

9.9 External Cooperations

Academic

- State University of Campinas, Campinas, Brazil
  Prof. Dr. Yakov Kopelevich

- Universität zu Köln, Cologne, Germany
  Dr. Ionela Vrejoiu

- Max-Planck Institute of Microstructure Physics, Halle, Germany
  Dr. Arthur Ernst

- Martin-Luther Universität Halle-Wittenberg, Halle, Germany
  Prof. Ingrid Mertig

- Martin-Luther Universität Halle-Wittenberg, Halle, Germany
  Prof. Wolfram Hergert

- Martin-Luther Universität Halle-Wittenberg, Halle, Germany
  Dr. Angelika Chassé

- Martin-Luther Universität Halle-Wittenberg, Halle, Germany
  Dr. Manfred Dubiel

- Stanford Synchrotron Radiation Laboratory, USA
  Dr. Hendrik Ohldag

- Laboratorio de Física de Sistemas Pequeños y Nanotecnologíia, Consejo Superior de Investigaciones Científicas, Madrid, Spain
  Prof. N. García (Madrid)

- Forschungszentrum Dresden-Rossendorf e.V., Institut für Ionenstrahlphysik und Materialforschung, Germany
  Dr. W. Anwand

- Forschungszentrum Dresden-Rossendorf e.V., Institut für Ionenstrahlphysik und Materialforschung, Germany
  Dr. G. Brauer

- Tucuman University, Argentina
  Prof. S. P. de Heluani

- University of La Plata, Argentina
  Dr. C. E. Rodriguez Torres

- Universidad Autónoma de Madrid, Spain
  Prof. Dr. Miguel Angel Ramos

- Bar Ilan University, Israel
  Dr. G. D. Nessim

9.10 Publications

Journals

V. Zviagin, Y. Kumar, I. Lorite, P. Esquinazi, M. Grundmann, and R. Schmidt-Grund:
Ellipsometric investigation of $ZnFe_2O_4$ thin films in relation to magnetic properties
Appl. Phys. Lett. **108**, 131901 (2016)

F. Bern, M. Ziese, I. Vrejoiu, X. Li and P. van Aken:
Magnetic and magnetotransport properties of ultrathin $La_{0.7}Ba_{0.3}MnO_3$ epitaxial films embedded in $SrRuO_3$
New J. Phys. **18**, 053021 (2016)

B. Dolgin, I. Lorite, Y. Kumar, P. Esquinazi, G. Jung, B. Straube and S. Perez de Heluani:
Conductivity fluctuations in proton-implanted ZnO microwires
Nanotechnology **27**, 305702 (2016)

I. Lorite, Y. Kumar, P. Esquinazi, S. Friedländer, A. Pöppl, T. Michalsky, J. Meijer, M. Grundmann, T. Meyer, and I. Estrela-Lopis:
Photo-enhanced magnetization in Fe-doped ZnO nanowires
Appl. Phys. Lett. **109**, 012401 (2016)

C. E. Precker, P. D. Esquinazi, A. Champi, J. Barzola-Quiquia, M. Zoraghi, S. Muiños-Landin, A. Setzer, W. Böhlmann, D. Spemann, J. Meijer, T. Muenster, O. Baehre, G. Kloess and H. Beth:
Identification of a possible superconducting transition above room temperature in natural graphite crystals
New J. Phys. **18**, 113041 (2016)

M. Stiller, J. Barzola-Quiquia, P. Esquinazi, D. Spemann, J. Meijer, M. Lorenz, and M. Grundmann:
Strong out-of-plane magnetic anisotropy in ion irradiated anatase TiO_2 thin films
AIP Advances **6**, 125009 (2016)

S. Friedländer, J. Liu, M. Addicoat, P. Petkov, N. Vankova, R. Rüger, A. Kuc, W. Guo, W. Zhou, B. Lukose, Z. Wang, P. G. Weidler, A. Pöppl, M. Ziese, T. Heine, and C. Wöll:
Linear Chains of Magnetic Ions Stacked with Variable Distance: Ferromagnetic Ordering with a Curie Temperature above 20 K
Angew. Chem. Int. Ed. **55**, 12683 (2016)

in press

J. Barzola-Quiquia, C. Lauinger, M. Zoraghi, M. Stiller, S. Sharma and P. Häussler:
Superconductivity in the amorphous phase of topological insulator Bi_xSb_{100-x} alloys
Supercond. Sci. Technol. **30**, 015013 (2017)

I. Lindfors-Vrejoiu and M. Ziese:
Topological Hall effect in antiferromagnetically coupled $SrRuO_3$/$La_{0.7}Sr_{0.3}MnO_3$ epitaxial heterostructures
Phys. Status Solidi B, 1-8 (2016), DOI 10.1002/pssb.201600556

X. Li, I. Vrejoiu, M. Ziese, and P. van Aken:
Direct observation of interfacial coupling of oxygen octahedra and its impact on ferromagnetic order in $La_{0.7}Sr_{0.3}MnO_3$/$SrTiO_3$ epitaxial heterostructures
European Microscopy Congress 2016: Proceedings (2016), DOI: 10.1002/9783527808465.-EMC2016.6219

X. Li, I. Lindfors-Vrejoiu, M. Ziese, A. Gloter, and P. A. van Aken:
Impact of interfacial coupling of oxygen octahedra on ferromagnetic order in $La_{0.7}Sr_{0.3}$-MnO_3/$SrTiO_3$ heterostructures
Scientific Reports **7**, 40068 (2017)

Talks

Magnetic and Magnetotransport Properties of Superlattices with Ultrathin $SrRuO_3$ Layers
M. Ziese
Universität zu Köln

9.11 Graduations

Master

- B. Sc. Mahsa Zoraghi
  The Influence of Rhombohedral Stacking on the Electrical Transport Properties of Multilayer Graphene before and after Oxygen Plasma Treatment
  29.09.2016

Bachelor

- cand. B. Sc. Andrea Schwetzler
  Structural and magnetic properties of $ZnFe_2O_4$ and $NiFe_2O_4$ films on (100), (110), (111) oriented $MgAl_2O_4$ substrates
  29.09.2016

9.12 Guests

- Dr. Carlos Sabater Piqueres
  Leiden Universlty, lnstitute of Physics, Atomic and Nuclear Conductors, Leiden/Netherlands
  02/2016

- Dr. Barbara Pacáková
  lnstitute of Physics of the Czech Academy of Sciences, Dept. of Magnetic Nanosystems, Prague/Czech Republic
  04/2016

- Prof. Dr. Ana Melva Champi Farfán
  Universidade Federal do ABC, Santo André, São Paulo/Brazil
  05/2016 - 06/2016

- Henrique Ferreira dos Santos (PhD)
  Universidade Federal do ABC, Santo André, São Paulo/Brazil
  05/2016 - 06/2016

- Marco Hauke (PhD)
  Technische Universität München/Germany
  05/2016 - 06/2016

- Henning Beth
  Golden Bowebird Pty Ltd., Mullumbimby/Australia
  06/2016

- Gideon Oppong Adjei Mensah (PhD)
  Kwame Nkrumah University of Science and Technology, Knust/Ghana
  06/2016 - 08/2016

- Stefano de Avila Souza Spindola (PhD)
  Federal University of São Carlos/Brazil
  07/2016 - 09/2017

- Prof. Dr. Eugene Kogan
  Department of Physics, Faculty of Exact Sciences, Bar-Ilan University/Israel
  10/2016

III

Institute for Theoretical Physics

10

Computational Quantum Field Theory

10.1   Introduction

The Computational Physics Group performs basic research into classical and quantum statistical physics with special emphasis on phase transitions and critical phenomena. In the centre of interest are the physics of spin glasses, diluted magnets and other materials with quenched, random disorder, soft condensed matter physics with focus on fluctuating paths and interfaces, biologically motivated problems such as protein folding, aggregation and adsorption as well as related properties of homopolymers, and the intriguing physics of low-dimensional quantum spin systems.

The methodology is a combination of numerical and analytical techniques. The numerical tools are mainly Monte Carlo and Molecular Dynamics computer simulations as well as exact enumeration techniques. The computational approach to theoretical physics is expected to gain more and more importance with the future advances of computer technology, and is likely to become the third cornerstone of physics besides experiment and analytical theory as sketched in Fig. 10.1. Already now it often helps to bridge the gap between experiments and the often necessarily approximate calculations in analytic approaches. To achieve the desired high efficiency of the numerical studies we develop new algorithms and, to guarantee the flexibility required by basic research, all computer codes are implemented by ourselves. The technical tools are Fortran, C, C++, and Python programs running under Unix or Linux operating systems and computer algebra using Maple or Mathematica. The software is developed and tested at the Institute on a cluster of PCs and workstations, where also most of the numerical analyses are performed. Currently we are also exploring the possibilities of the rapidly developing graphics card computing, that is computer simulations on graphics processing units (GPUs) with many cores. Large-scale simulations requiring vast amounts of computer time are carried out at the Institute on quite powerful compute servers, at the parallel computers of the Saxon computing centre in Dresden, and, upon successful grant application, at the national supercomputing centres in Jülich, Stuttgart and München on parallel high-capability computers. This hierarchy of various platforms gives good training and qualification opportunities for the students, which offers promising job perspectives in many different fields for their future careers.

Our research activities are closely integrated into the Graduate School "Build-
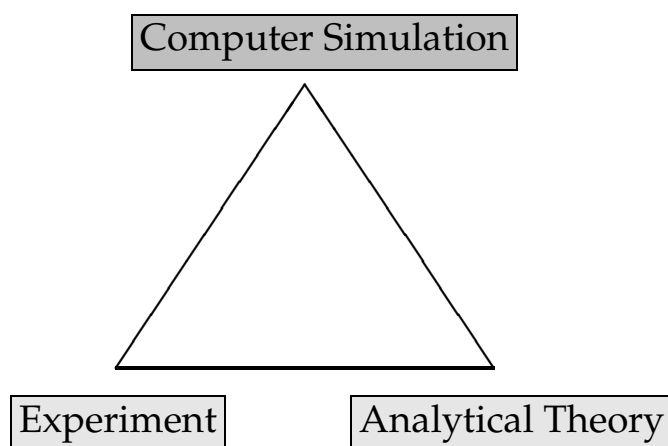
Figure 10.1: Sketch of the "triangular" relationship between experiment, analytical theory and computer simulation.

MoNa": Leipzig School of Natural Sciences – *Building with Molecules and Nano-objects*, the International Max Planck Research School (IMPRS) *Mathematics in the Sciences*, and the International Doctoral College *Statistical Physics of Complex Systems* with Université de Lorraine in Nancy, France, supported by the Deutsch-Französische Hochschule (DFH-UFA). In the second funding period 2011–2013, Coventry University in England has been integrated as an associated partner, and in the third funding period 2014–2016, also the National Academy of Sciences of Ukraine in Lviv has joined as another associated partner institution, offering our PhD students now several interesting options for secondments. For instance, in 2014, one PhD student started a "co-tutelle de thèse" jointly supervised with a colleague from Coventry University. Currently the DFH-UFA Doctoral College under the acronym "$\mathbb{L}^4$" is in its fourth funding period 2017–2020. The three Graduate Schools are all "Classes" of the Research Academy Leipzig (RALeipzig), providing the organizational frame for hosting visiting students and senior scientists, offering language courses, organizing childcare and for many other practical matters.

At a more post-graduate level our research projects are embedded into the Sonderforschungsbereich/Transregio SFB/TRR 102 *Polymers under Multiple Constraints: Restricted and Controlled Molecular Order and Mobility* together with Halle University. Our group also actively contributes to two of the top level research areas ("Profillinien") and the Centre for Theoretical Sciences (NTZ) of the University. Beside "BuildMoNa" the latter structures are particularly instrumental for our cooperations with research groups in experimental physics and biochemistry on the one hand and with mathematics and computer science on the other.

On an international scale, our research projects are carried out in a wide net of collaborations which are currently mainly funded by the Alexander von Humboldt Foundation through an Institute Partnership with the National Academy of Sciences in Lviv, Ukraine, on *Polymers in Porous Environments and on Disordered Substrates* and the EU IRSES Network DIONICOS: *Dynamics of and in Complex Systems*, a consortium of 6 European and 12 non-European partners, including sites in Austria, England, France and Germany as well as in Armenia, Russia, Ukraine, India, the United

States and Venezuela, which commenced work in 2014. Further close contacts and collaborations are established with research groups in Armenia, Austria, China, France, Great Britain, India, Israel, Italy, Japan, Poland, Russia, Spain, Sweden, Taiwan, Turkey, Ukraine, and the United States. These contacts are refreshed and furthered through topical Workshops, Advanced Training Modules and Tutorials, and our International Workshop series *CompPhys: New Developments in Computational Physics*, taking annually place at the end of November just before the first advent weekend.
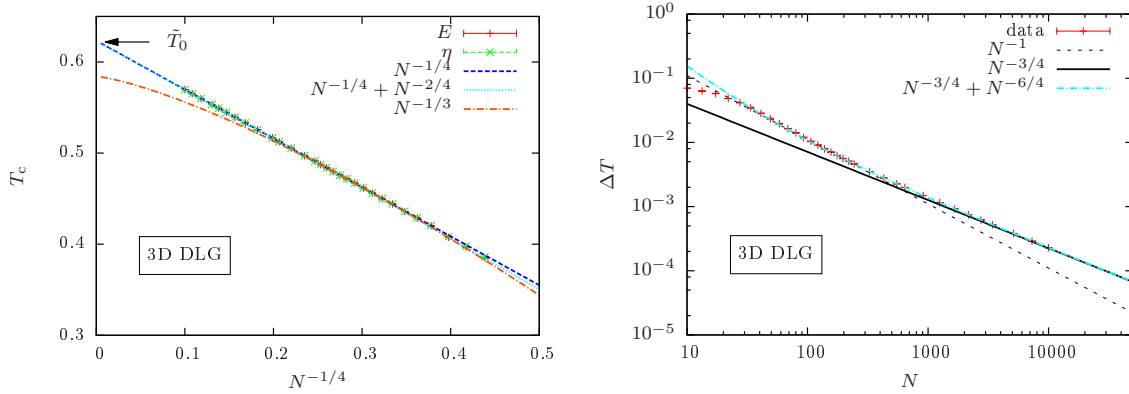
Wolfhard Janke

Figure 10.2: Finite-size scaling of (a) the transition temperature and (b) the transition rounding of a three-dimensional lattice gas at fixed density $\rho = 10^{-2}$.

10.2 Finite-size scaling predictions for the droplet condensation-evaporation transition

J. Zierenberg, A. Nußbaumer[*], E. Bittner[†], W. Janke

[*]Institut für Physik, Johannes Gutenberg Universität Mainz, Germany
[†]Institut für Theoretische Physik, Universität Heidelberg, Germany

We investigated the finite-size scaling behaviour of the droplet condensation-evaporation transition for the two- and three-dimensional Ising lattice gas as well as the three-dimensional Lennard-Jones gas [1, 2]. The lattice models allow to exploit the equivalence to the Ising model, comparing to exact results in two dimensions and low-temperature series expansions in three dimensions. The Lennard-Jones model ensured the generality of our results. Opposed to the consideration at fixed temperature [3], for which leading-order predictions exist [4], we considered here an orthogonal setup at fixed density. The relation of the two approaches was recently reviewed in Ref. [5].

Applying in the fixed density approach Taylor expansions around the infinite-system limit, we obtain the same leading-order scaling behaviour as in the fixed temperature case for the finite-size transition temperature $T_c(N)$ and rounding ΔT of a D-dimensional system with N particles:

$$T_c(N) - T_0 \quad \propto N^{-1/(D+1)}, \tag{10.1}$$
$$\Delta T \quad \propto N^{-D/(D+1)}. \tag{10.2}$$

This is not the standard $1/N$ finite-size scaling of a first-order phase transition, because droplet condensation-evaporation describes a transition between a homogenous gas phase and an inhomogeneous or mixed phase where a single droplet is in equilibrium with surrounding vapor. A comparison with our numerical results from parallel multicanonical simulations [6] is shown in Fig. 10.2 for the case of the three-dimensional lattice gas.

For intermediate system sizes, we observe a non-expected scaling regime where the system behaves as for homogeneous phase transitions, i.e., $T_c(N) - T_0 \propto N^{-1/D}$ and $\Delta T \propto N^{-1}$. For the three-dimensional lattice gas we can compare to low-temperature series expansion estimates of the transition temperature $\tilde{T}_0(\rho)$ and the agreement is very

good. With our approach, we were able to reach up to $N = 10\,000$ lattice particles and the finite-size scaling analysis suggests that we are in fact quite close to the asymptotic scaling regime.

[1] J. Zierenberg, W. Janke: Phys. Rev. E **92**, 012134 (2015)
[2] J. Zierenberg, W. Janke: in *Computer Simulation Studies in Condensed-Matter Physics XXIX*, eds. D.P. Landau, H.-B. Schüttler, S. Lewis, M. Bachmann, J. Phys.: Conf. Ser. **750**, 012017 (2016)
[3] J. Zierenberg et al.: J. Phys: Conf. Ser. **510**, 012017 (2014)
[4] M. Biskup et al.: Europhys. Lett. **60**, 21 (2002); Commun. Math. Phys. **242**, 137 (2003)
[5] A. Nußbaumer et al.: J. Phys.: Conf. Ser. **759**, 012009 (2016)
[6] J. Zierenberg et al.: Comput. Phys. Comm. **184**, 1155 (2013)

10.3 Free-energy barriers of particle and polymer condensation

J. Zierenberg, P. Schierz, W. Janke

A common approach to study nucleation rates is the estimation of free-energy barriers. This usually requires knowledge about the shape of the forming droplet, a task that becomes notoriously difficult in macromolecular setups starting with a proper definition of the cluster boundary or a proper ensemble choice. Here, we demonstrate that a shape-free determination of temperature-driven cluster formation is directly accessible in the canonical ensemble for particle as well as polymer systems. Combined with rigorous results on canonical equilibrium droplet formation, this allows for a well-defined finite-size scaling analysis of the effective interfacial free energy at fixed density as illustrated in Fig. 10.3. We first verified the theoretical predictions for the formation of a liquid droplet in a supersaturated particle gas by (parallelized) generalized-ensemble Monte Carlo simulations [1–3] of a Lennard-Jones system [4–6]. Going one step further, we then generalized this approach to the aggregation process in a dilute polymer solution [6], cf. Fig. 10.4. Our results suggest an analogy between particle condensation and polymer aggregation, when the macromolecules are interpreted as extended particles.

Because the standard approach in Monte Carlo simulations is to work in the conformational ensemble governed by potential energy only, we show that excluding the kinetic energy from the partition function leads to finite-size differences in the free energy compared to the full ensemble [7, 8] but retains intensive parameters in the thermodynamic limit [6]. Our study of nucleation rates at fixed density corresponds to a heating-cooling framework where simulation and experiment may meet at the nanometer scale.

[1] B.A. Berg, T. Neuhaus: Phys. Lett. B **267**, 249 (1991); Phys. Rev. Lett. **68**, 9 (1992)
[2] W. Janke: Int. J. Mod. Phys. C **03**, 1137 (1992); Physica A **254**, 164 (1998)
[3] J. Zierenberg et al.: Comput. Phys. Comm. **184**, 1155 (2013)
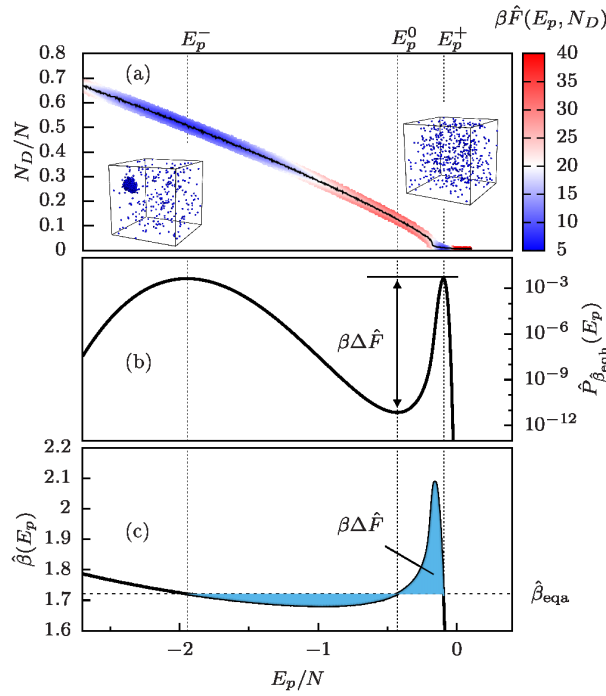[4] J. Zierenberg, W. Janke: Phys. Rev. E **92**, 012134 (2015)

Figure 10.3: (a) Illustration of the free-energy landscape $\beta\hat{F}(E_p, N_D)$ (color map) as a function of potential energy E_p and droplet size N_D for $N = 512$ Lennard-Jones particles. The minimal free-energy path (black solid line) connects a droplet ($E_p \approx E_p^-$) and a gaseous ($E_p \approx E_p^+$) phase, visualized by the snapshots at $E_p^\pm$. The projection onto the reaction-coordinate E_p yields the canonical potential-energy probability distribution $\hat{P}_\beta(E_p)$, where the free-energy barrier $\beta\Delta\hat{F}$ is encoded in the ratio between maximum and minimum at $\hat{\beta}_{\text{eqh}}$. (c) Equivalently, $\beta\Delta\hat{F}$ is the (equal) area size enclosed between the microcanonical inverse temperature $\hat{\beta}(E_p)$ and the accordingly defined transition temperature $\hat{\beta}_{\text{eqa}}$, where $\hat{\beta}_{\text{eqa}} = \hat{\beta}_{\text{eqh}} = 1.72099(3)$.

[5] J. Zierenberg, W. Janke: in *Computer Simulation Studies in Condensed-Matter Physics XXIX*, eds. D.P. Landau, H.-B. Schüttler, S. Lewis, M. Bachmann, J. Phys.: Conf. Ser. **750**, 012017 (2016)

[6] J. Zierenberg et al.: Nat. Commun. **8**, 14546 (2017)

[7] P. Schierz et al.: Phys. Rev. E **94**, 021301(R) (2016)

[8] W. Janke et al.: *Transition barrier at a first-order phase transition in the canonical and microcanonical ensemble*, Leipzig preprint (2017), to appear in *Computer Simulation Studies in Condensed-Matter Physics XXX*, eds. D.P. Landau, H.-B. Schüttler, S. Lewis, M. Bachmann, J. Phys.: Conf. Ser. (2017), in print

10.4 Binding transition of two grafted polymers

K. Tholen, J. Zierenberg, W. Janke

In this project we studied the binding of two flexible polymers grafted closeby to a steric surface. More specifically, we fixed one of their end points to a steric surface covering the $x - y$ plane at $z = 0$. No monomer was allowed to cross this geometric constraint,
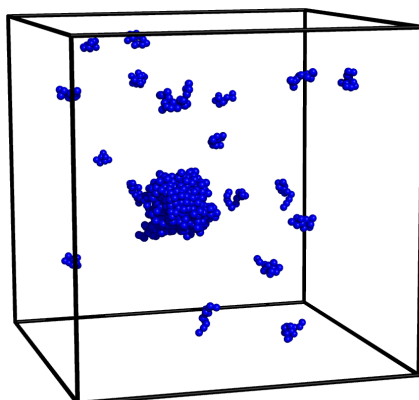
Figure 10.4: Illustration of an aggregate of polymers in a dilute solution ($N = 64$ bead-spring polymers with 13 monomers each; monomer density $\rho = 10^{-2}$). The snapshot stems from the droplet phase ($E_p \approx E_p^-$).

i.e., monomer coordinates with $z_i < 0$ were forbidden. No further interactions with the (inert) surface are assumed. The end points are grafted with distance $d = r_0$ (the equilibrium bond length of a FENE spring connecting the monomers) and are immobilized. If the polymers are not grafted, we enclose them in a cubic box of side length L with steric walls. For an illustration see Fig. 10.5.

As "binding" we refer to the process where two polymers attach to each other, in our case flexible polymers. If specific inter-polymer interactions are considered this may quickly lead to effects also characterized as zipping. Even more interesting is the equivalence between two-polymer binding of directed polymers and adsorption [1]. This should qualitatively remain valid also for flexible polymers, especially if one imagines the crossover scenario of a flexible polymer adsorbed to a nanowire, equivalent to the stiff limit of a polymer chain [2, 3], or a flexible polymer adsorbing to a flexible surface [4]. In fact, it was shown that grafting alters the first-order-like adsorption transition to a second-order-like transition [5].

From our Monte Carlo simulation data we conclude [6] that when grafting two polymers to a steric surface at a close distance an analogous scenario holds true, i.e., we observe a second-order-like binding transition, which is in contrast to the first-order-like finite-size binding transition for free polymers in a steric box. This is relevant for an experimental study of polymer binding, where in vitro polymers would be commonly grafted. In this case, one will neither observe a latent heat nor hysteresis effects associated with first-order-like transitions, which would be expected to occur in vivo. Still, grafted polymers may be studied with respect to aggregate properties and their dynamics which are expected to sufficiently coincide for observables which are not directly influenced by the geometric constraint. One exception is the average end-to-end distance and subsequently (no longer isotropic) geometric properties. Interesting effects may be anticipated for interacting surfaces, where the binding of polymers would
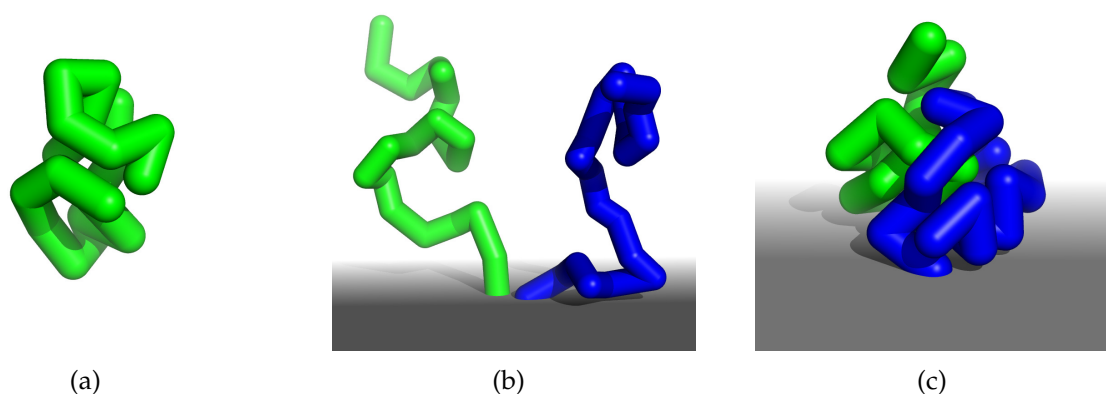
(a)   (b)   (c)

Figure 10.5: Snapshots of (a) a single polymer of length $N = 20$ in the globular phase below the collapse transition ($T = 0.7$) and two polymers of length $N = 20$ grafted to a steric surface (b) above ($T = 4$) and (c) below ($T = 0.7$) the binding transition.

compete with the surface attraction. Connecting to experimental setups, the surfaces may be considered both flat or curved, e.g., when grafting polymers to nanoparticles.

[1] J. Kierfeld, R. Lipowsky: Europhys. Lett. **62**, 285 (2003)
[2] T. Vogel et al.: J. Chem. Phys. **142**, 104901 (2015)
[3] J. Gross et al.: Phys. Chem. Chem. Phys. **17**, 30702 (2015)
[4] S. Karalus et al.: Phys. Rev. E **84**, 031803 (2011)
[5] M. Möddel et al.: Macromolecules **44**, 9013 (2011)
[6] J. Zierenberg et al.: Eur. Phys. J. Special Topics **226**, 683 (2017)

10.5   Polymer adsorption to a nano-sphere

H. Arkın[*], W. Janke

[*]Department of Physics Engineering, Faculty of Engineering, Ankara University, Tandogan, 06100 Ankara, Turkey

The interaction of macromolecules with differently shaped substrates is particularly important for interdisciplinary research and nano-technological applications including, e.g., the fabrication of biosensors and peptide adhesion to metals or semiconductors. The knowledge of structure formation for a variety of interfaces has therefore been a challenging subject of numerous experimental and computational studies.

Recently we have investigated the purely steric confinement effect of a spherical cage enclosing a simple flexible polymer chain to determine its influence on the location of the collapse and freezing transitions [1]. Another hybrid system under consideration was a polymer chain inside an attractive spherical cage for which we have constructed the finite-temperature phase diagram depending on the attraction strength of the sphere inner wall and the temperature [2, 3] and investigated the ground-state properties [4]. We have also compared the results with the attractive flat surface [5, 6]. These systems exhibit a rich phase behaviour ranging from highly ordered, compact to extended, random coil structures.
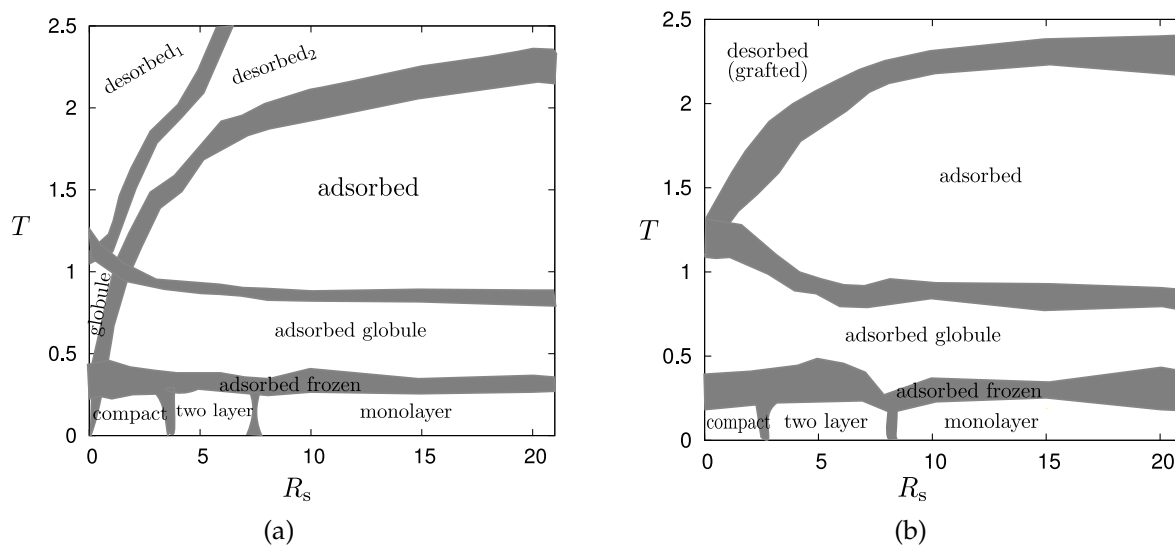
Figure 10.6: The phase diagram of a homopolymer interacting with an attractive spherical surface of radius R_s for (a) a non-grafted and (b) an end-grafted 20mer.

Here, we consider the opposite situation: A nano-sphere whose attractive outer spherical surface is the target for the adsorbing polymer. This problem could have practical implications for a broad variety of applications ranging from protein-ligand binding, designing smart sensors to molecular pattern recognition and for the discovery of new drugs that bind to specific receptors. Therefore it is interesting to study the adsorption of macromolecules on different types of substrates and identify the conformational changes that a polymer can experience at the interface.

In this project we investigate a simple coarse-grained polymer model interacting with a spherical surface of varying radius (and consequently curvature) by means of extensive generalized-ensemble Monte Carlo computer simulations [7]. The employed multicanonical method enables us to describe the different phases of the finite chain over a wide range of sphere radius and temperature. In a comparative study, we determined how the structural phase diagram changes with the sphere radius and temperature, both for non-grafted and end-grafted polymer chains. The band widths of the boundaries separating the individual conformational phases in Fig. 10.6 indicate the variation of the peak locations of temperature derivatives of different structural observables which we have analyzed simultaneously [7]. Typical conformation for the case of a non-grafted polymer are shown in Fig. 10.7.

[1] M. Marenz et al.: Condens. Matter Phys. **15**, 43008 (2012)

[2] H. Arkın, W. Janke: Phys. Rev. E **85**, 051802 (2012)

[3] H. Arkın, W. Janke: J. Chem. Phys. **138**, 054904 (2013)

[4] H. Arkın, W. Janke: J. Phys. Chem. B **116**, 10379 (2012)

[5] M. Möddel et al.: J. Phys. Chem. B **113**, 3314 (2009); Phys. Chem. Chem. Phys. **12**, 11548 (2010); Macromolecules **44**, 9013 (2011)

[6] H. Arkın, W. Janke: Eur. Phys. J. Special Topics **216**, 181 (2013)

[7] H. Arkın, W. Janke: *Polymer adsorption on curved surfaces*, Ankara/Leipzig preprint (2017), to appear in Phys. Rev. E, in print
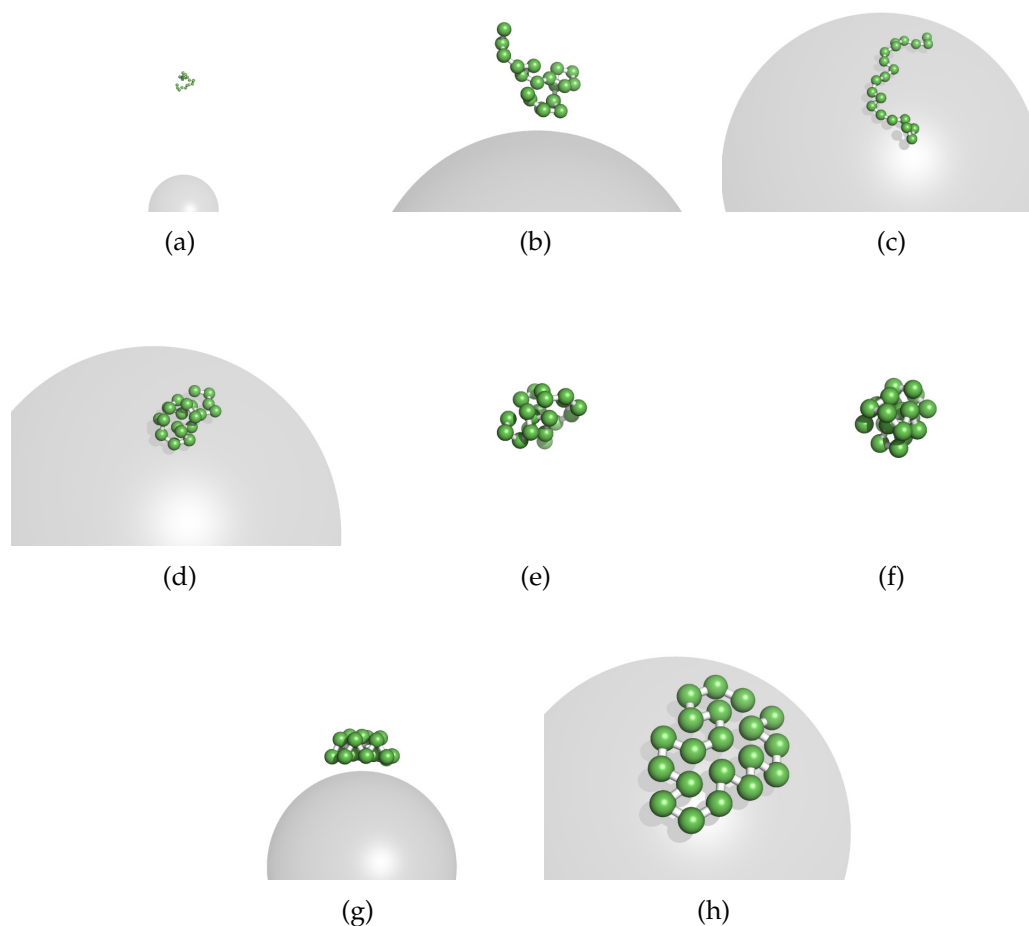
Figure 10.7: Typical conformations for the regions (a) desorbed$_1$, (b) desorbed$_2$, (c) adsorbed, (d) adsorbed globule, (e) globule, (f) compact, (g) two layer, and (h) monolayer in the phase diagram of a non-grafted polymer.

10.6 Polymer knots as a topological order parameter

M. Marenz, W. Janke

For the investigation of the generic behaviour of polymers and proteins with computer simulations, it is common to use minimalistic, coarse-grained models since this is the only possibility to investigate large time scales, length scales or parameter ranges. In this study we used a bead-stick model for a semiflexible polymer defined by the Hamiltonian

$$H = E_{\text{LJ}} + \kappa E_{\text{Bend}} = 4 \sum_{i=1}^{N-2} \sum_{j=i+2}^{N} \left(\frac{1}{r_{ij}^{12}} - \frac{1}{r_{ij}^{6}} \right) + \kappa \sum_{i} (1 - \cos \theta_i) , \qquad (10.3)$$

where r_{ij} is the distance between non-adjacent monomers, and θ_i is the angle of two adjacent bonds. The parameter κ allows to vary the bending stiffness of the polymer from flexible over semiflexible to stiff [1].

Figure 10.8: Sketch of the phase diagram for a semiflexible bead-stick model exhibiting several phases: E – elongated, R – rod-like, G – globular, F – frozen, K – knotted, B – bent. Next to the phase diagram two typical knots of types 5_1 and 8_{19} for a 28mer are shown.

To simulate the system in the complete (T, κ)-plane we used two advanced Monte Carlo algorithms. A parallel multicanonical algorithm [2] combined with a one-dim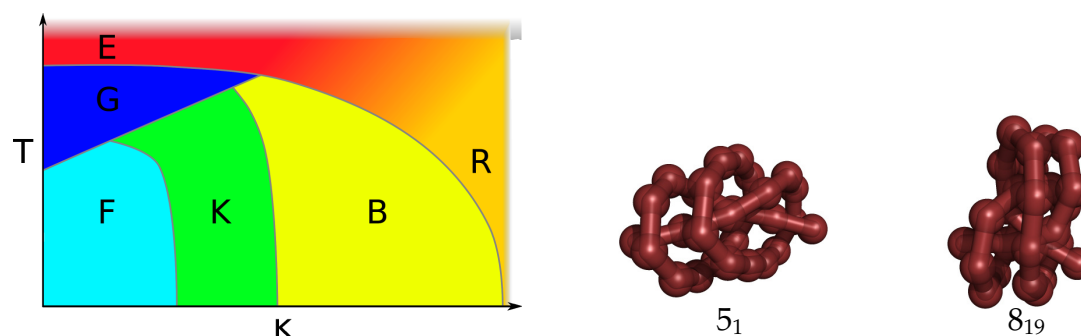ensional replica exchange in the κ direction and a two-dimensional replica-exchange method, which simulates the system in parallel in the T and κ direction. Employing both algorithms, we calculated surface plots of various observables (energy, end-to-end distance, radius of gyration, eigenvalues of gyration tensor) to construct the full pseudo-phase diagram for several polymer lengths ($N = 14, 28, 42$) [3, 4].

Despite the simplicity of the model, the phase diagram sketched in Fig. 10.8 is remarkably rich. Compared to former work simulating similar coarse-grained models [5], we observed a novel type of phases labeled by "K", which are characterized by thermodynamically stable knots [6], which may be considered as topological order parameters. The transitions into these knot phases exhibit some intriguing characteristics. Although we observed clear signals of a first-order transition between the knotted and unknotted phases, the transition apparently shows no latent heat [3, 4]. Instead the two sub-energies, the Lennard-Jones energy and the bending energy, are transformed into each other while the polymer knots itself, see Fig. 10.9.

[1] J. Zierenberg et al.: Polymers **8**, 333 (2016)
[2] J. Zierenberg et al.: Comput. Phys. Comm. **184**, 1155 (2013)
[3] M. Marenz, W. Janke: Phys. Rev. Lett. **116**, 128301 (2016)
[4] M. Marenz, W. Janke: In *Computer Simulation Studies in Condensed-Matter Physics XXIX*, eds. D.P. Landau, H.-B. Schüttler, S. Lewis, M. Bachmann, J. Phys.: Conf. Ser. **750**, 012006 (2016)
[5] D.T. Seaton et al.: Phys. Rev. Lett. **110**, 028103 (2013)
[6] L.H. Kauffman: *Knots and Physics*, 2nd ed. (World Scientific, Singapore, 1991)

10.7   Comparative simulations of poly(3-hexylthiophene) models
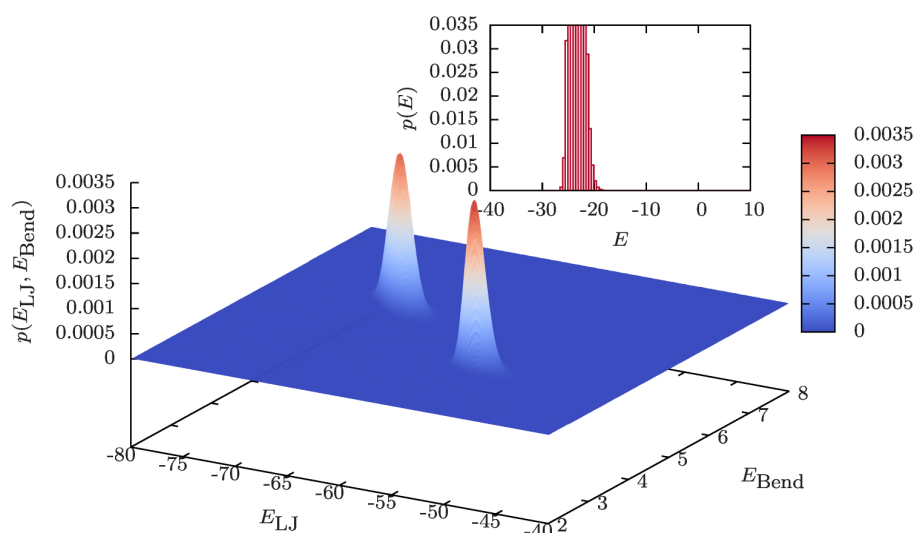
J. Gross, M. Ivanov, W. Janke

Figure 10.9: Two-dimensional energy histogram $p(E_{\mathrm{LJ}}, E_{\mathrm{Bend}})$ of a 28mer at the transition into the knot phase signaling clear phase coexistence. The inset shows the one-dimensional energy histogram $p(E)$ of the total energy $E = E_{\mathrm{LJ}} + \kappa E_{\mathrm{Bend}}$, which corresponds to a projection along the diagonal of the two-dimensional histogram. In this projection, the two peaks fall on top of each other, so only a single peak is visible in $p(E)$.

Regioregular Poly(3-hexylthiophene) (P3HT) is a very interesting conjugated polymer due to its electronic and optical properties [1]. One of its applications is the use as semi-conducting layer in organic photovoltaics [2–4]. Studies of P3HT on the microscopic level are of great importance for a fundamental understanding of the tuneability of electronic properties and their dependence on external constraints, e.g. the adsorption on electrode surfaces. Hence a number of experimental studies addressed for example the influence of structure formation by polymer self-assembly on ideal surfaces on the electronic properties of oligo- and polythiophenes [5]. Due to the complexity of these macromolecules many of the experimental findings have not been supported with simulations so far, which in contrast is well-established for studies of small organic molecules. Our pervious study [6] reported on an collaborative effort within the DFG SFB/TRR 102 project to combine the experimental observation of polymer chain conformations adsorbed on a metal surface with Monte Carlo simulations of a coarse-grained P3HT model developed by Huang *et al.* [7]. Based on our previous work on a three beads per monomer coarse-grained model, we expanded our studies in two directions. We focused our interest on the polymer itself and, firstly, investigated an even coarser model with one bead per monomer [8] using Monte Carlo simulations. Secondly, we simulated a fully atomistic representation of P3HT using molecular dynamics. We pursue these two routes to gauge the level of detail that is necessary to reproduce experimental findings more accurately. Another interest is the development of our own simplified model by systematically performing the coarse-grain procedure ourselves. For this we looked at the iterative Boltzmann inversion method [9]. The comparative analysis of all three models regarding structural observables, but also computational effort are discussed in Refs. [10, 11].
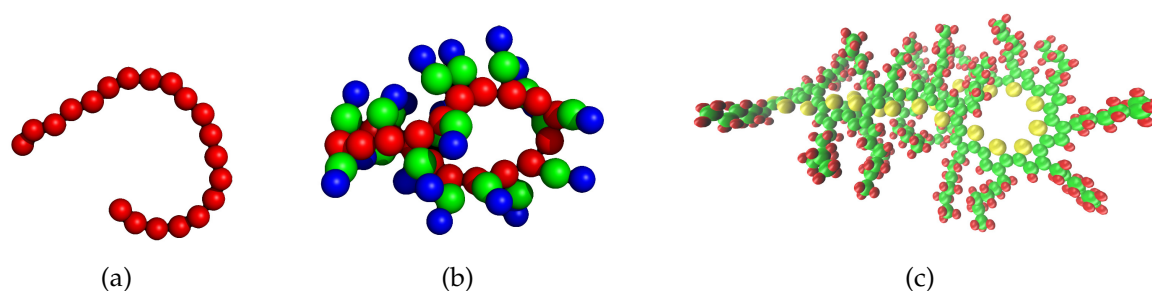
Figure 10.10: Hairpin conformations of Poly(3-hexylthiophene) for a degree of polymerization DP_n = 20 in three different models. (a) One-particle coarse-grained model (one bead per monomer), (b) three-particle coarse-grained model, and (c) fully atomistic model.

[1] X. Bai, S. Holdcroft: Macromolecules **26**, 4457 (1993); Z. Bao et al.: Appl. Phys. Lett. **69**, 4108 (1996); M.R. Andersson et al.: J. Mater. Chem. **9**, 1933 (1999); B.W. Boudouris et al.: Macromolecules **44**, 6653 (2011)
[2] J.M. Frost et al.: Nano Letters **6**, 1674 (2006)
[3] M. Campoy-Quiles et al.: Nat. Mater. **7**, 158 (2008)
[4] A.M. Ballantyne et al.: Adv. Funct. Mater. **18**, 2373 (2008)
[5] Z.Y. Yang et al.: ACS Nano **2**, 743 (2008); Y.F. Liu et al.: Nanoscale **5**, 7936 (2013)
[6] S. Förster et al.: J. Chem. Phys. **141**, 164701 (2014)
[7] D.M. Huang et al.: J. Chem. Theory Comput. **6**, 526 (2010)
[8] C.K. Lee et al.: Energy Environ. Sci. **4**, 4124 (2011)
[9] D. Reith et al.: J. Comput. Phys. **24**, 1624 (2003); Macromolecules **36**, 5406 (2003)
[10] J. Gross et al.: J. Phys.: Conf. Ser. **750**, 012009 (2016)
[11] J. Gross et al.: Eur. Phys. J. Special Topics **226**, 667 (2017)

10.8   Effect of temperature on the scaling laws governing the kinetics of collapse of a homopolymer

S. Majumder, J. Zierenberg, W. Janke

The collapse transition of a polymer upon transfer from a good solvent (high temperature) to a poor solvent (low temperature) bears significant connection to the folding process of proteins and other biomolecules. Thus understanding the kinetics of a homopolymer in that respect may provide useful primary information on the underlying mechanism of more realistic problems [1, 2]. On the other hand, if one considers the usual "pear-necklace" like picture of the collpase [3] as shown in Fig. 10.11 (a), it also resembles coarsening phenomena popular in spin and particle systems [4]. Over the last two years we have been exploiting this connection to understand the kinetics of collapse of a homopolymer [5, 6].

In this work, from the state of the art Monte Carlo simulations of an off-lattice polymer model, we understand the effect of the quench temperature (T_q) on the various scaling laws related to the collapse viz., scaling of the cluster growth and the dynamical
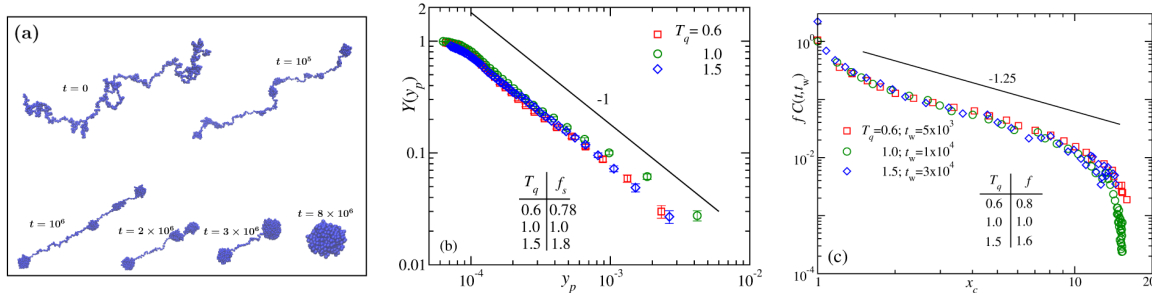
Figure 10.11: (a) Snapshots [1] showing the sequence of events occurring during the collapse of a polymer upon being quenched from an expanded state (at high temperature) into the globular phase (at low temperatures). (b) Universal finite-size scaling function $Y(y_p)$ with a non-universal metric factor (f_p) in the scaling variable y_p describing the scaling in the cluster growth during the collapse [2]. (c) Temperature-independent scaling plot for the aging and related dynamical scaling, probed by the behavior of a suitable density-density autocorrelation function $C(t, t_w)$ against $x_c = C_s(t)/C_s(t_w)$, the ratio of cluster sizes $C_s(t)$ at the observation time (t) and the waiting time (t_w) [2].

scaling related to the aging. Our results in conjunction with a nonequilibrium finite-size scaling analysis [7] show that the cluster growth is rather universal in nature and can be described by a universal finite-size scaling function with a non-universal metric factor that depends on the amplitudes of the growth, see Fig. 10.11 (b) [2]. Furthermore, the scaling related to the aging (which is probed by a suitable two-time density-density autocorrelation function) is also found to be independent of the quench temperature T_q, shown in Fig. 10.11 (c).

[1] S. Majumder, W. Janke: J. Phys.: Conf. Ser. **750**, 012020 (2016)
[2] S. Majumder et al.: Soft Matter **13**, 1276 (2017)
[3] A. Halperin, P. Goldbart: Phys. Rev. E **61**, 565 (2000)
[4] A.J. Bray: Adv. Phys. **51**, 481 (2002)
[5] S. Majumder, W. Janke: Europhys. Lett. **110**, 58001 (2015)
[6] S. Majumder, W. Janke: Phys. Rev. E **93**, 032506 (2016)
[7] S. Majumder, S.K. Das: Phys. Rev. E **81**, 050102(R) (2010); Phys. Rev. E **84**, 021110 (2011)

10.9 Kinetics of the collapse transition in lattice polymers

H. Christiansen, S. Majumder, W. Janke

The nonequilibrium properties of homopolymer collapse were investigated using Monte Carlo simulations of the interacting self-avoiding walk on a simple cubic lattice with short nearest neighbor [1] and longer range next-nearest neighbor interactions. We were able to reproduce the phenomenological picture of pearl necklace polymer collapse [2] (see Fig. 10.12), in which a polymer, when transferred from a good solvent to a bad solvent, undergoes a collapse transition from an expanded coil by forming clusters at locally higher densities which then subsequently coalesce with each other until only a single globular cluster is left. Recently, the scaling behavior of the average cluster size
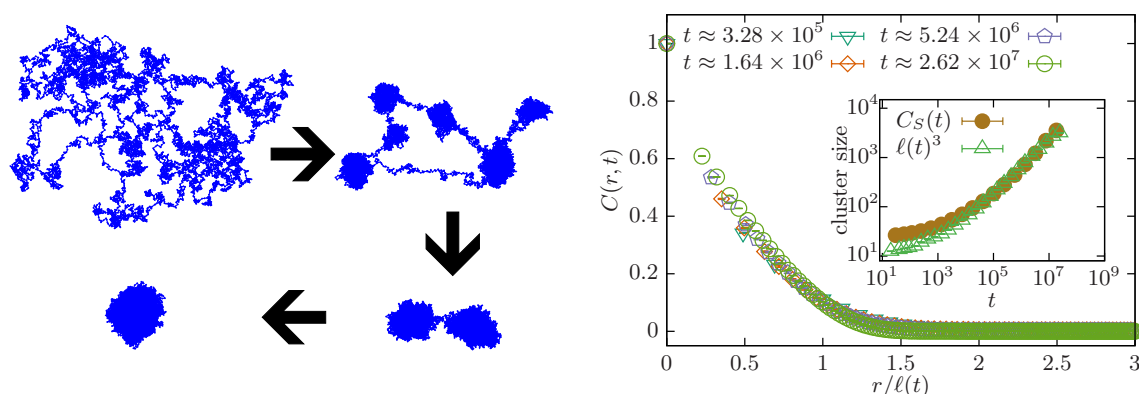
Figure 10.12: (a) Collapse of a polymer with length N = 8192 showing the formation and subsequent coarsening of clusters. (b) Scaling of the two point equal-time correlation function $C(r,t)$ at different times as a function of $r/\ell(t)$. The inset shows the comparison of $\ell(t)^3$ extracted from the correlation function and the cluster size $C_s(t)$ determined using the same method as in off-lattice simulations.

as well as aging was investigated using an off-lattice polymer model [3–5] by applying methods from domain coarsening investigations used in spin and particle systems to polymers. We extend this work to an investigation of lattice polymer collapse in order to be able to simulate one order of magnitude longer polymer chains (when compared to the off-lattice investigations) and define properties that are dependent on the underlying structure, like the equal-time two-point correlation function (see Fig. 10.12). The power-law growth exponent of the clusters of monomers was observed to be similar for both interaction ranges, however significantly smaller than in the off-lattice case ($\alpha \approx 0.6$ vs. $\alpha = 1$). In addition we investigated aging during the coarsening and found the same dynamic aging exponent with respect to the growing characteristic length of clusters as in the off-lattice model for both interaction ranges ($\lambda_c = 1.25$).

[1] H. Christiansen et al.: *Coarsening and aging of lattice polymers: Influence of bond fluctuations*, Leipzig preprint (2017), to appear in J. Chem. Phys., in print
[2] A. Halperin, P.M. Goldbart: Phys. Rev. E **61**, 565 (2000)
[3] S. Majumder, W. Janke: Phys. Rev. E **93**, 032506 (2016)
[4] S. Majumder, W. Janke: Europhys. Lett. **110**, 58001 (2015)
[5] S. Majumder et al.: Soft Matter **13**, 1276 (2017)

10.10 Periodically driven DNA: A comparative study of Langevin and Brownian dynamics

R. Kumar, S. Kumar[*], W. Janke

[*]Department of Physics, Banaras Hindu University, Varanasi 221 005, India

DNA replication is one of the most important biological processes in living organisms. Under the influence of special enzymes, two strands of the DNA double helix can separate themselves like a zip. The first step in the process of DNA replication is to
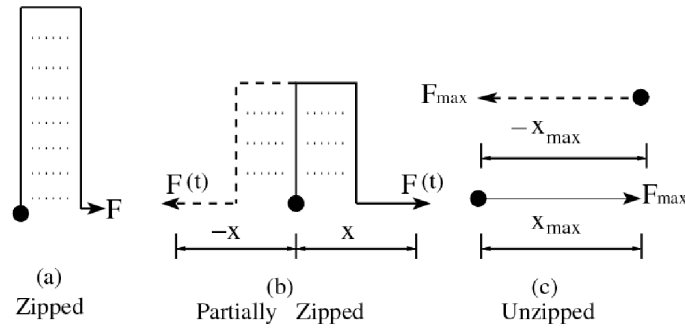
Figure 10.13: Schematic representations of DNA: (a) zipped, (b) partially zipped, and (c) unzipped state. One end is kept fixed (indicated by solid circles), while the other end may move.
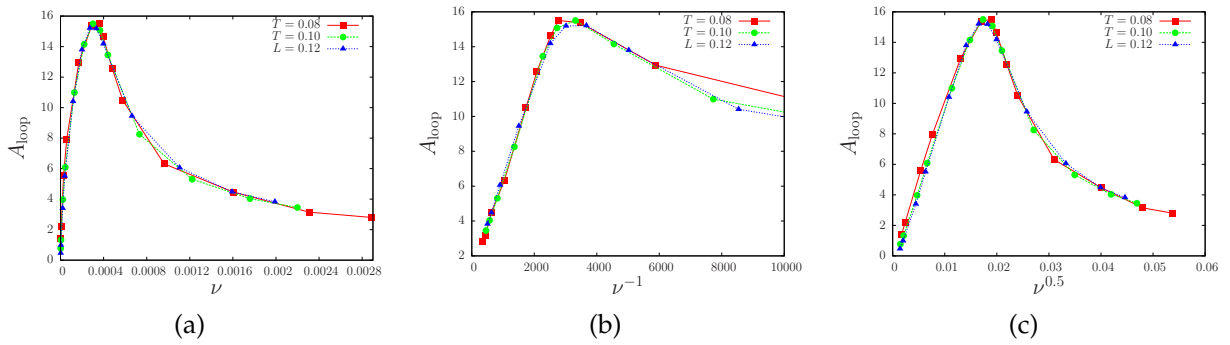

Figure 10.14: Effect of temperature on the area of the hysteresis loop for the model with parameters $L = 32$, $F = 1.0$, and $\gamma = 0.4$ for (a) A_{loop} vs. ν, (b) area vs. ν^{-1} in the higher frequency regime, and (c) area vs. $\nu^{0.5}$ in the lower frequency regime. Here the x-axis is rescaled in order to show the data collapse for all temperatures.

unzip the double-helix structure of the DNA molecule. Therefore, it is very important to study the unzipping of DNA. There has been some experimental studies at a constant force or loading rate used in SMFS experiments to unzip the DNA *in vitro*. In these experiments one end of the DNA was fixed and a constant force was applied on its other end. However, such processes are driven by different types of molecular motors *in vivo* [1].

A constant force or loading rate used in SMFS experiments provides a limited picture of these processes *in vitro*. Hence, the picture provided by constant force unzipping is not complete. This has been highlighted in recent studies, where it was suggested that by varying the frequency and amplitude of the applied force new aspects of a force-driven transition can be introduced [2–5], which otherwise would not be possible in the case of a steady force.

This model was further simplified in [6, 7] by reducing the degrees of freedom and studying the overdamped limit using Brownian dynamics. This simplified model was investigated only at zero temperature. Therefore, it became crucial to further investigate how the temperature effects the dynamics of such system using the detailed model described in [3]. Emphasis was placed on the effect of different temperatures on the scaling properties. Moreover, we compared results of the Langevin dynamics for the detailed model and Brownian dynamics for the simplified model. We observed that

the temperature and over-damped limit does not effect the scaling exponents. Hence, the model proposed by us is good enough to study the scaling properties and provides a possibility of analytic studies within certain limits. Moreover, currently we are trying to understand the effect of the over-damped limit in the detailed model proposed in [3].

[1] B. Alberts et al.: *Molecular Biology of the Cell* (Garland Publishing, New York, 1994)
[2] S. Kumar, M. S. Li: Phys. Rep. **486**, 1 (2010)
[3] S. Kumar, G. Mishra: Phys. Rev. Lett. **110**, 258102 (2013)
[4] G. Mishra et al.: Phys. Rev. E **87**, 022718 (2013)
[5] R.K. Mishra et al.: J. Chem. Phys. **138**, 244905 (2013)
[6] S. Kumar et al.: Phys. Rev. E **93**, 010402(R) (2016)
[7] R. Kumar et al.: *Comparative study of Brownian and Langevin dynamics for periodically driven DNA*, Leipzig/Varanasi preprint (2017), to be published

10.11 Computer simulations of semiflexible polymers in disordered environments

J. Bock, W. Janke

(a) Weighting histogram

(b) Semiflexible polymer in 3D disorder
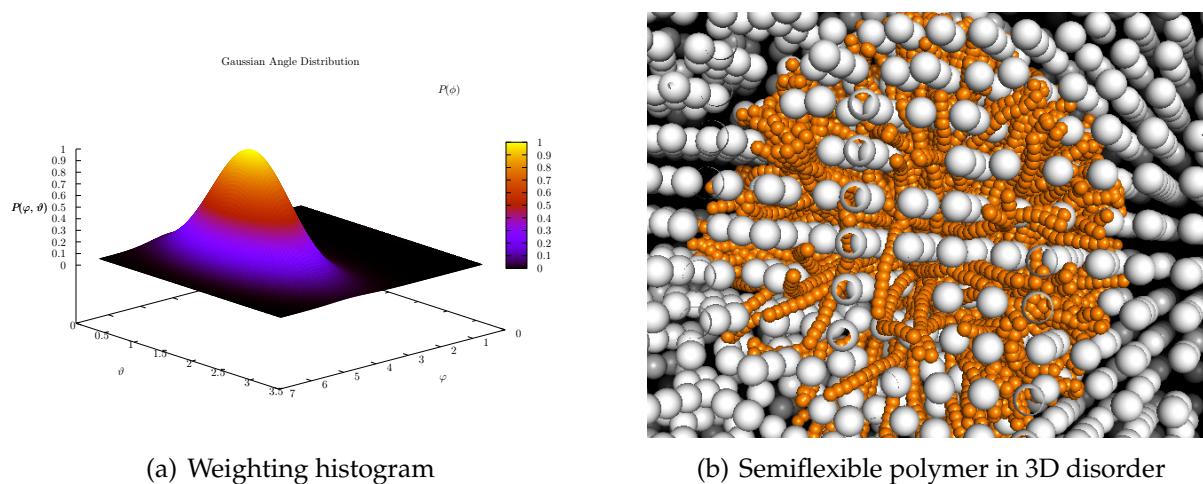
Figure 10.15: (a) Histogram used for the guiding field in 3D and (b) an examplary configuration of a polymer with $N = 30$ and $\xi = 1$.

Single-molecule experiments have established the wormlike chain (WLC) as a standard model for semiflexible polymers [1]. Exploiting the analogy of the WLC with a one-dimensional Heisenberg ferromagnet, it can be shown that the equilibrium tangent-tangent correlation function decays exponentially. The decay rate defines the thermal persistence length l_p. When the same polymer is embedded in a quenched, disordered environment in three dimensions, this property may change quantitatively or even qualitatively. We addressed this problem by performing extensive numerical simulations of

(a) Free polymers   (b) Polymers in disorder

Figure 10.16: End-to-end distance distributions for (a) free polymers and (b) polymers in gaseous disorder, both in 3D.

semiflexible polymers in a simple lattice disorder and in a gaseous disorder constructed by microcanonical Lennard-Jones gas simulation which represents the disordered environment. Further plans are to simulate the polymers in algebraically correlated disorder. Only the space between the spheres is accessible to the polymer. The extreme strength and density of the environmental constraints are a great challenge to conventional Monte Carlo simulati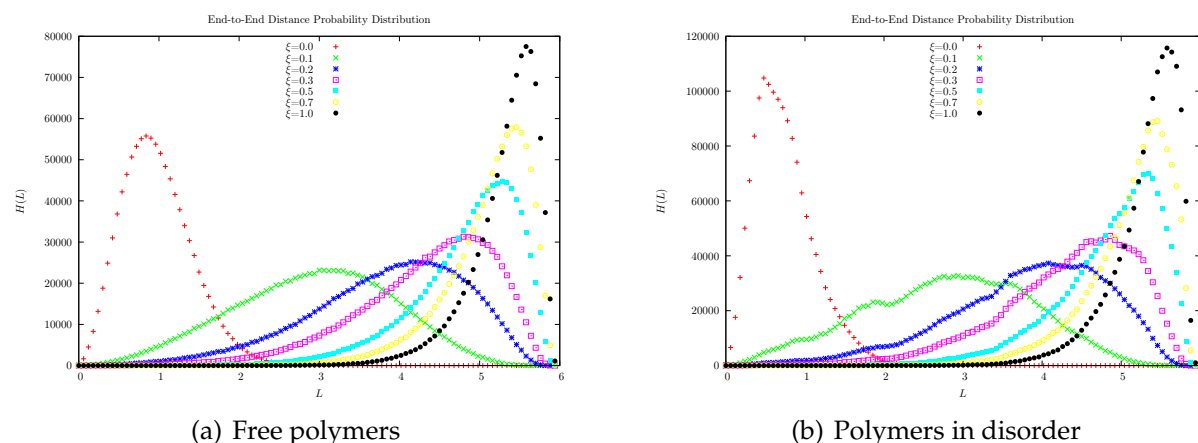on schemes, which we found hard to overcome even with a sophisticated multicanonical histogram reweighting procedure [2]. We have therefore adopted a breadth-first chain-growth algorithm [3] that resolves this difficulty by circumventing energy barriers instead of trying to cross them [2, 4], see examples in Fig. 10.15. Therefore the already existing procedures were expanded to the third dimension to investigate the behaviour of the tangent-tangent correlation length, the mean square end-to-end distance and the end-to-end probability distribution function, see Fig. 10.16. A difference in behaviour is clear and the task now is to check wether the differences scale similarly as in two dimensions, where the disorder renormalization is stated to be [5]:

$$\frac{1}{l_p^*} = \frac{1}{l_p} + \frac{1}{l_p^D},$$

with l_p^* the renormalized persistence length, l_p the persistence length given as simulation parameter and l_p^D the measured disorder persistence length.

[1] O. Otto et al.: Nat. Commun. **4**, 1780 (2013)
[2] S. Schöbl et al.: Phys. Rev. E **84**, 051805 (2011)
[3] T. Garel, H. Orland: J. Phys. A: Math. Gen. **23**, L621 (1999)
[4] S. Schöbl et al.: J. Phys. A: Math. Theor. **45**, 475002 (2012)
[5] S. Schöbl et al.: Phys. Rev. Lett. **113**, 238302 (2014)

10.12 Self-avoiding walks on critical percolation clusters in 2 – 7 dimensions
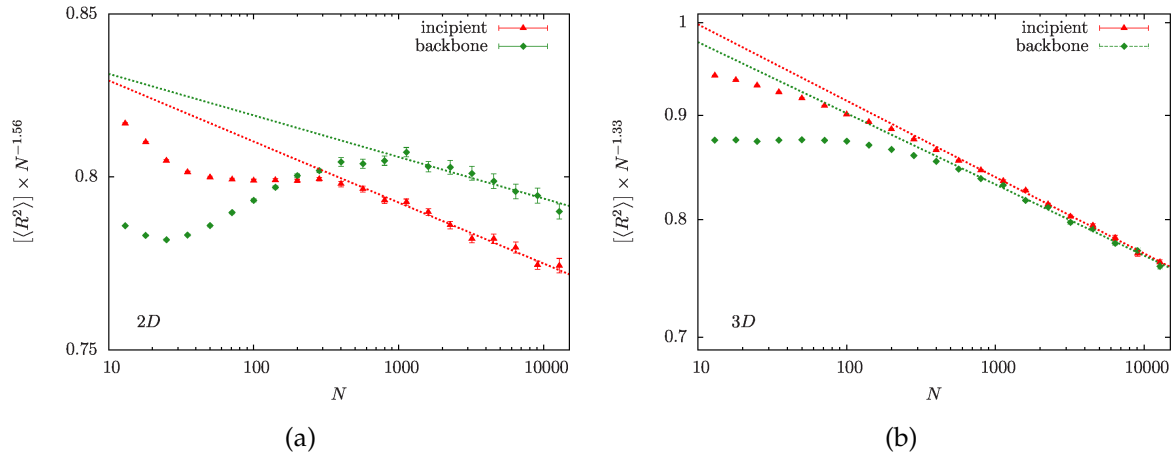
N. Fricke, W. Janke

(a) (b)

Figure 10.17: Scaled disorder averages of the mean squared end-to-end distance as a function of the number of SAW steps on critical clusters and cluster backbones in (a) 2D and (b) 3D on a double-logarithmic scale. The values have been divided by $\approx N^{2\nu_{p_c}}$ for better visibility. Straight lines show least-squares power-law fits to the data in the range $N = 800 - 12\,800$ for 2D and 3D incipient clusters and $N = 1131 - 12\,800$ for 3D backbones.

Self-avoiding walks (SAWs) on critical percolation clusters are a simple model for polymers in highly disordered environments such as porous rocks or a biological cell [1, 2]. The system is also appealing from a theoretical perspective as it combines two of the most ubiquitous models from statistical physics. It has therefore been studied intensely in the past both analytically and numerically. However, despite its conceptual simplicity, the problem proved extremely challenging. Few reliable predictions exist for the SAWs' scaling exponents, and our qualitative understanding of the model is also still limited. In particular, it is unclear how the disorder and the medium's fractal structure, characterized by its various fractal dimensions, impacts the SAWs' asymptotic scaling behavior. This understanding is crucial when we want to generalize from the results and make predictions for real-world systems.

The main difficulty for numerical investigation of the problem can be overcome by making use of the self-similar geometry of critical percolation clusters to factorize the problem, in an approach that we called scale-free enumeration (SFE) [3, 4]. In two preceding studies, we had used this method to investigate SAWs on critical percolation clusters in 2D [5] and 3D [6]. Recently we have expanded this perspective and looked at systems in up to 7D [7], above the supposed upper critical dimension of $D_{uc} = 6$.

We mainly focused on the scaling of the increase of the mean squared end-to-end distance with the number of steps,

$$[\langle R^2 \rangle] \sim N^{2\nu} \qquad (10.4)$$

where ν is a universal scaling exponent. The reduced time complexity of our recently introduced SFE method allows us to exactly enumerate SAWs of over $N = 10^4$ steps, easily amounting to 10^{2000} conformations. Previously, only up to $N = 45$ steps on 2D clusters and 40 steps on 3D clusters could be handled by the standard "brute-force" enumeration method.

In 2D and 3D we studied walk lengths increasing in multiplicative steps of $\sqrt{2}$ from $N = 13$ up to $N = 12\,800$ ($= 100 \times 2^7$). For each length we took independent samples of at least 5×10^4 randomly generated percolating clusters and backbones. The results for the mean squared end-to-end distance as a function of N and least-squares fits of Eq. (10.4) to the data are shown in Fig. 10.17 on a double-logarithmic scale. The y-axes have been rescaled by $\approx N^{-2\nu_{p_c}}$, so that the slopes are close to zero and more details are visible. Note that while the conformational averages are evaluated exactly, we still have statistical fluctuations of the disorder averages reflected by the error bars.

Repeating this procedure in 4D – 7D, we finally arrive at Fig. 10.18, where we have also included a comparison with analytical predictions from various sources.
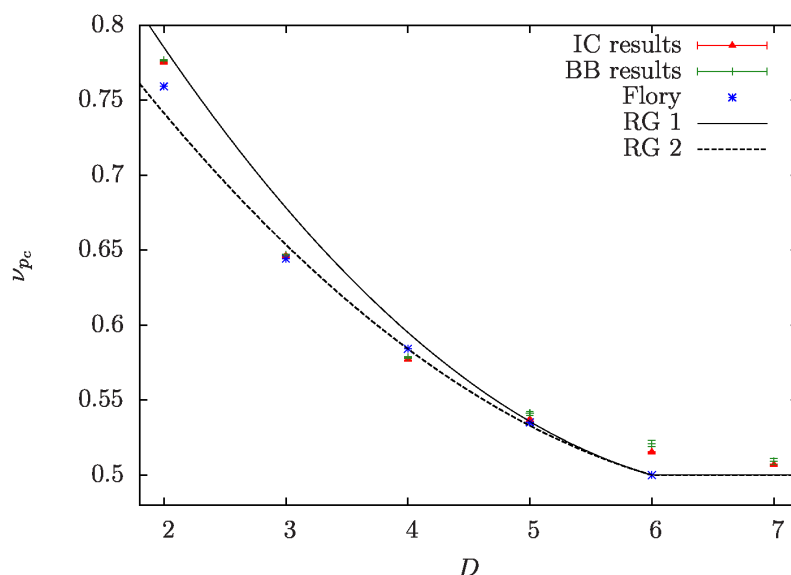
Figure 10.18: Results for ν_{p_c} on incipient clusters (IC, red) and backbones (BB, green) as a function of dimension compared to various analytical predictions. The blue asterisks correspond to Flory estimates [7]. The lines represent the field-theory estimates from [8] (RG1, solid) and [9] (RG2, dashed).

[1] D. Ben-Avraham, S. Havlin: *Diffusion and Reactions in Fractals and Disordered Systems* (Cambridge University Press, Cambridge, 2000)

[2] B.K. Chakrabarti (ed.): *Statistics of Linear Polymers in Disordered Media* (Elsevier, Amsterdam, 2005)

[3] N. Fricke, W. Janke: Eur. Phys. J. Special Topics **216**, 175 (2013)

[4] N. Fricke, W. Janke: *How to enumerate 10^{1000} self-avoiding walk conformations on a critical percolation cluster*, Leipzig preprint (2017), to be published

[5] N. Fricke, W. Janke: Europhys. Lett. **99**, 56005 (2012)

[6] N. Fricke, W. Janke: Phys. Rev. Lett. **113**, 255701 (2014); Phys. Rev. Lett. **115**, 149902 (Erratum)
[7] N. Fricke, W. Janke: J. Phys. A: Math. Theor. **50**, 264002 (2017)
[8] C. von Ferber et al.: Phys. Rev. E **70**, 035104 (2004)
[9] H.K. Janssen, O. Stenull: Phys. Rev. E **75**, 020801 (2007); Phys. Rev. E **85**, 051126 (2012)

10.13   Dynamical greedy algorithm for the Edwards-Anderson model

S. Schnabel, W. Janke

One of the most intuitive and natural approaches to optimization problems is realized by so-called greedy algorithms. These methods create trajectories in the space of possible solution by always choosing the next step such that the energy is maximally reduced (or a fitness function maximally increased). Naturally, this will usually not find the global optimum, just as starting at a random spot and always walking uphill will usually not lead a wanderer to the summit of Mt. Everest. Therefore, in practice many attempts with randomly created starting points are made and if the problem is not too difficult the global optimum may be found this way.

On the other hand, there is practically no chance of success if the energy landscape is as complicated and possesses as many local minima as in the case of the Edwards-Anderson spin-glass model [1], whose Hamiltonian is given by

$$\mathcal{H} = \sum_{\langle ij \rangle} J_{ij} S_i S_j,$$

where the spins can take two values $S_i \in \{-1, 1\}$ and adjacent spins interact via normally distributed random couplings J_{ij}. If such a model on a three-dimensional cubic lattice of 1000 spins is considered, about 10^{30} attempts would be necessary in order to find the ground state this way.

However, the greedy algorithm can still be a very helpful tool, since it is a comparatively simple and reliable method to reach states of low energy. We devised a method to efficiently update the greedy algorithm, i.e., to reuse the data created during a minimization from a configuration $\mathbf{S}$ to the configuration $\mathbf{S}_{\min}$ to obtain the result $\mathbf{S}'_{\min}$ of the minimization from a configuration $\mathbf{S}'$ which differs from $\mathbf{S}$ only in the values of one or very few spins [2]. If furthermore, both, the terminal configuration, delivered by the greedy algorithm, and its energy are understood as attributes of the starting configuration, it is possible to use the energy of the minimized configurations $\mathbf{S}_{\min,t}$ to steer a path in the space of starting configurations $\mathbf{S}_t$.

A simple application is to apply the greedy algorithm again: It is tested which alteration (e.g., which single spin flip) of the starting configuration will reduce the energy of the *minimized* configuration by the largest amount and this locally optimal step is performed. Repeating this simple procedure as long as viable as a "second order greedy algorithm" will lead to much lower energies albeit not the ground state.

Alternatively, the energy of the minimized configuration can be used as argument for the occupation probability for a generalized ensemble [3]:

$$P(\mathbf{S}) = P(\mathbf{S}_{\min}),$$

which can then be sampled using Monte Carlo techniques. All states in the same "valley" in the energy landscape, i.e., all configuration which minimize to the same local energy minimum, now occur with the same probability and the barriers of high energy which greatly hamper standard Monte Carlo simulations simply vanish. In consequence, the configuration space is sampled much more easily and the performance of ground-state search is greatly improved.

[1] S.F. Edwards, P.W. Anderson: J. Phys. F **5**, 965 (1975)
[2] S. Schnabel, W. Janke: *Dynamic greedy algorithms for the Edwards-Anderson model*, Leipzig preprint (2017), to appear in Comput. Phys. Comm. (2017), in print
[3] D.J. Wales: J. Phys. Chem. A **101**, 5111 (1997)

10.14   Distribution of local minima for the Edwards-Anderson model

S. Schnabel, W. Janke

In statistical physics the term "complex behaviour" is usually used to characterize systems that posses a rough free-energy landscape with many metastable states. This can be the result of competing interactions on different scales like in the case of protein folding or it may arise from quenched disorder as for spin glasses. A conceptually simple model for such a system is the Edwards-Anderson model [1], whose Hamiltonian is given by

$$\mathcal{H} = \sum_{\langle ij \rangle} J_{ij} S_i S_j,$$

where the spins sit on the sites of a cubic lattice, can take two values $S_i \in \{-1, 1\}$, and adjacent spins interact via normally distributed random couplings J_{ij}. Since these interactions can be both ferromagnetic and antiferromagnetic, there is no clear order established at low temperatures. Instead, many very different pure states might coexist, each one of them corresponding to a minimum in free energy.

Albeit not identical, minima of the energy, i.e., spin configurations that are stable against single spin flips are closely related to these states. It is thought that minima in energy form the end points of hierarchical tree-like structures with the branches corresponding to different states. Understanding the properties of these minima might, therefore, improve our understanding of the behaviour of the system. However, they have proven to be a very demanding subject of inquery.

We have developed an advanced Monte Carlo method that allows to sample the local energy minima with uniform distribution, i.e., each minimum configuration is occupied with equal probability. This is achieved by establishing within the simulation the combination of a spin configuration together with a random minimization thereof.

I.e., the repeated flipping of spins with positive energy until a local minimum is reached. If one now alters the spin configuration and the parameters of the minimization in a suitable way it is possible to ensure that all local minima are equally likely found this way.

A basic application of this method is the measurement of the distribution of the energy minima. Since existing algorithms are unable to perform such a task, there is no numerical data for comparison. However, we can use our results to test analytical predictions [2] that are based on the expansion of mean-field solutions.

[1] S.F. Edwards, P.W. Anderson: J. Phys. F **5**, 965 (1975)
[2] A.J. Bray, M.A. Moore: J. Phys. C **14**, 1313 (1981)

10.15   Spin glasses with variable frustration

R. Kumar, M. Weigel[*], W. Janke

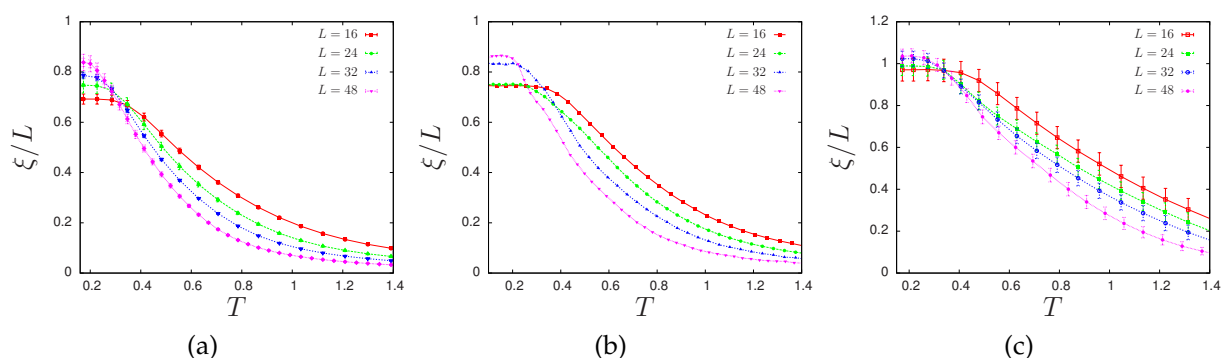[*]Applied Mathematics Research Centre, Coventry University, England, UK

Figure 10.19: Correlation length as a function of temperature for (a) stochastically frustrated system, (b) a system with 46% frustration, and (c) a system with 20% frustration.

Together with randomness, frustration is believed to be a crucial prerequisite for the occurrence of glassy behaviour in spin systems. The degree of frustration is normally the result of a chosen distribution of exchange couplings in combination with the structure of the lattice under consideration. Here, however, we discuss a process for tuning the frustration content of the Edwards-Anderson model on arbitrary lattices. With the help of extensive parallel-tempering Monte Carlo simulations we study such systems on the square lattice and compare the outcomes to the predictions of a recent study employing the Migdal-Kadanoff real-space renormalization procedure [1]. We use a cluster algorithm proposed in [2] in order to reduce the equilibration time. The phase transition studies are done by looking at the divergence of the correlation length, see Fig. 10.19. The results are benchmarked by comparing to the stochastic case described in [3]. We also study the freezing temperature of such a system and observe a different behaviour compared to the stochastically frustrated case. Studies on larger system sizes are very crucial to confirm these differences.

We find that the divergence of the correlation length occurs at non-zero finite temperature for the 2D Ising spin glass. This gives hints of a phase transition, but such transitions have to be studied carefully in order to fully understand the phases [4].

[1] E. Ilker, A.N. Berker: Phys. Rev. E **89**, 042139 (2014)
[2] J. Houdayer: Eur. Phys. J. B **22**, 479 (2001)
[3] H.G. Katzgraber, L.W. Lee: Phys. Rev. B **71**, 134404 (2005)
[4] A. Hartmann: Phys. Rev. B **67**, 214404 (2003)

10.16 Ground-state and low-energy excitations of the random field q-state Potts model

R. Kumar[*], M. Kumar[†‡], M. Weigel[§], V. Banerjee[‡], S. Puri[†], W. Janke

[*]Doctoral College for the Statistical Physics of Complex Systems, Leipzig-Lorraine-Lviv-Coventry ($\mathbb{L}^4$)
[†]School of Physical Sciences, Jawaharlal Nehru University, New Delhi – 110067, India
[‡]Department of Physics, Indian Institute of Technology, Hauz Khas, New Delhi – 110016, India
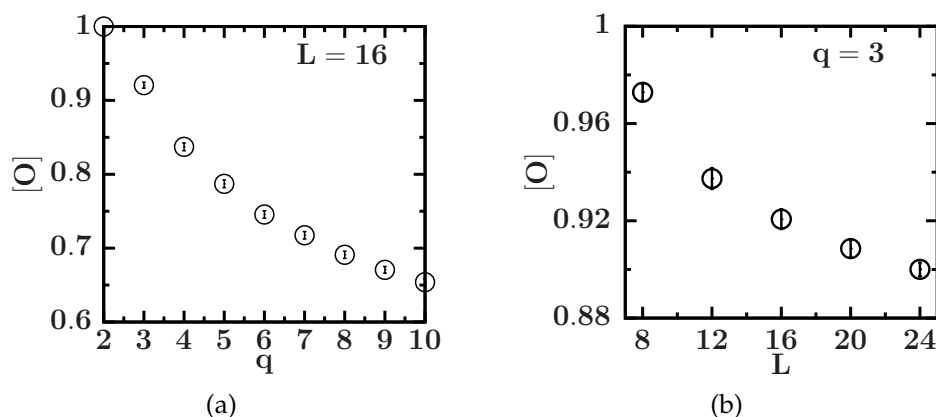[§]Applied Mathematics Research Centre, Coventry University, England, UK

Figure 10.20: Overlap between the lowest states found by graph-cut methods (GCM) and the putative ground state (a) as a function of the number of Potts states q and (b) as a function of system size L.

While the ground-state (GS) problem for the random-field Ising model is polynomial, and can be solved using a number of well-known algorithms for maximum flow [1–4], the analogue random-field q-state Potts model with $q \geq 3$ corresponds to a multi-terminal flow problem that is known to be NP hard. Hence an efficient exact algorithm is extremely unlikely to exist [5]. Still, it is possible to employ an embedding of binary degrees of freedom into the Potts spins to use graph-cut methods (GCMs) to solve the corresponding ground-state problem approximately with polynomial methods. It is shown here that this works relatively well. We compare results produced by

this heuristic algorithm to energy minima found by an appropriately tuned parallel tempering method that is configured to find ground states for the considered system sizes with high probability. The method based on graph cuts finds the same states in a fraction of the time. The new method is used for a first exploratory study of the random-field Potts model in $d = 2, 3$.

We observe that the probability of finding a ground state decreases exponentially with q for GCM, but for parallel tempering this decay is linear. Hence, GCM is more suitable for lower q studies. We also find that the lower energies found by GCM are very close to the ground state and the excess energy is very small. The probability of finding the ground state falls exponentially with the system size, whereas for GCM it falls linearly. Therefore, GCM is better suited for studying larger system sizes. This is one very good feature of GCM as for the smaller system sizes we have larger finite-size effects. The overlap between the states found by GCM and the ground state is observed to be very large (see Fig. 10.20). Hence, we conclude that GCM produces the approximate GS which can be treated as an exact GS for sufficiently small q ($q = 3, 4$) for studying the critical behaviour and ground-state morphologies.

[1] G.P. Shrivastav et al.: Europhys. Lett. **96**, 36003 (2011)
[2] G.P. Shrivastav et al.: Phys. Rev. E **90**, 032140 (2014)
[3] G.P. Shrivastav et al.: Eur. Phys. J. E **37**, 98 (2014)
[4] V. Banerjee et al.: Ind. J. Phys. **88**, 1005 (2014)
[5] J.C. Angles d'Auriac et al.: J. Physique Lett. **46**, L173 (1985)

10.17 Boundary drive induced phase transitions in stochastic transport condensation models

H. Nagel, H. Christiansen, W. Janke

Stochastic mass transport processes such as the asymmetric simple exclusion process (ASEP) or the zero-range process (ZRP) are simple transport models for particle hopping aiming to improve the understanding of basic phenomena in the dynamics of particles in driven diffusive systems. An important class of such phenomena that can be studied and understood on an abstract level is the emergence of generic condensates. In this project we considered such a transport processes under driven particle exchange through open boundaries and systematically studied the emerging phase diagrams. While boundary drive induced phase transitions are known since long for the ASEP, the research for the ZRP with condensation dynamics is more recent [1].

More precisely we investigated transport processes with tunable weights [2] as well as various types of interactions at the boundaries to study these effects on a much broader scale. The tunable model allowed us to effectively interpolate between ZRP-type as well as strong short-range interactions. At the boundaries we considered the existence of fixed versus loose couplings as well as different approaches to particle injection and removal rates. For the generated cases we produced the phase diagrams under differing strengths of the driven particle exchange at the boundaries for symmetric and totally asymmetric dynamics [3–5]. The main phases, as shown in Fig. 10.21, are:
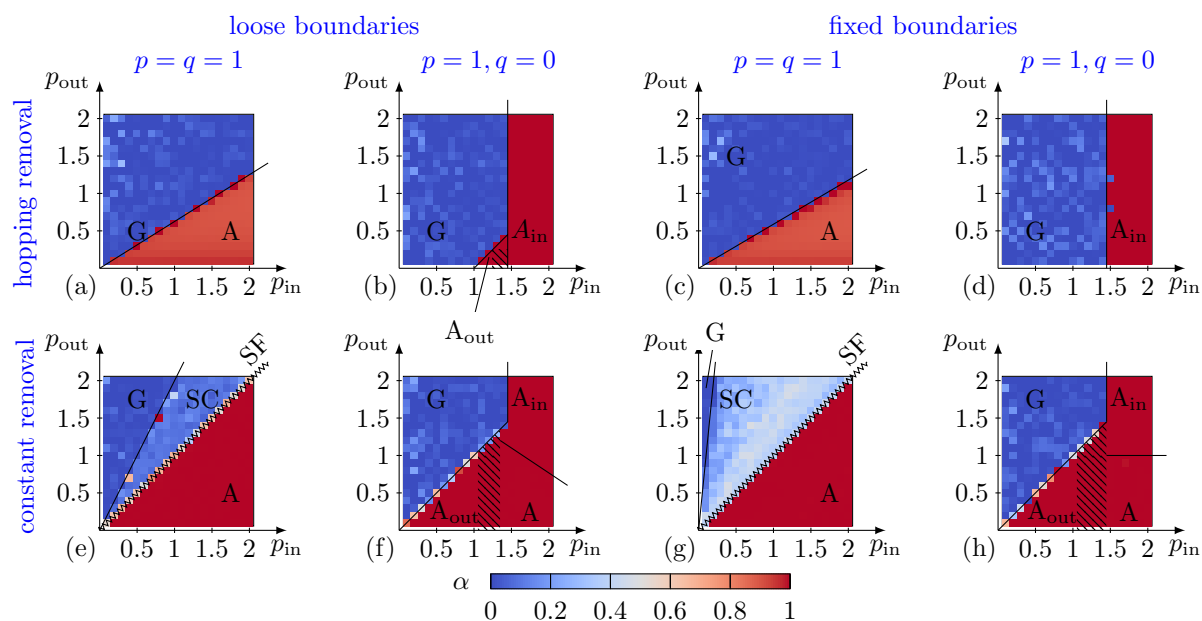
Figure 10.21: Phases induced by driven particle exchange through open boundary conditions of the system [5]. With respect to the specific implementation of the interaction at the boundary, different phase diagrams are observed.

a thin particle gas (G), formation of aggregate condensates (A) and the spanning bulk condensate (SC). While the phase diagrams with vanishing as well as stronger short-range interactions are very similar except for the SC phase, we observed a qualitatively different mechanism for aggregate condensate formation with short-range interactions.

[1] E. Levine et al.: J. Stat. Phys. **120**, 759 (2005)

[2] B. Wacław et al.: Phys. Rev. Lett. **103,** 080602 (2009)

[3] H. Nagel et al.: in *Computer Simulation Studies in Condensed-Matter Physics XXVII*, eds. H.-B. Schüttler, S. Lewis, M. Bachmann, D.P. Landau, Physics Procedia **57**, 77 (2014)

[4] H. Nagel et al.: Europhys. Lett. **111**, 30001 (2015)

[5] H. Nagel, W. Janke: J. Stat. Mech.: Theor. Exp., 013207 (2016)

10.18   Gate Opening, Diffusion, and Adsorption of CO_2 and N_2 Mixtures in ZIF-8

T. Chokbunpiam[*], S. Fritzsche, C. Chmelik[†], J. Caro[‡], W. Janke, S. Hannongbua[§]

[*]Department of Chemistry, Faculty of Science, Ramkhamhaeng University, Bangkok 10240, Thailand

[†]Institute for Experimental Physics I

[‡]Institute of Physical Chemistry and Electrochemistry, Leibniz University Hannover, Germany

[§]Computational Chemistry Unit Cell (CCUC), Department of Chemistry, Faculty of Science, Chulalongkorn University, Bangkok 10330, Thailand
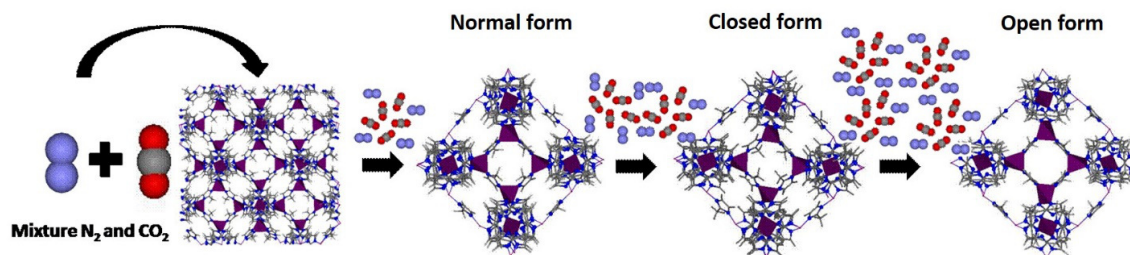
Figure 10.22: The change of the window sizes, i.e., 4-membered (normal lines, foreground) and 6-membered rings (strong lines) of ZIF-8 from normal to closed and to open forms.

Porous materials play an increasingly important role in research and industry. Particularly, during the past decade metal-organic frameworks (MOFs) [1] came into the focus of interest because of their great diversity, the big pores, and the possibility of custom-made design. Some of them have the highest internal surface areas per gram of all porous materials known to date. They consist of metal ions or metal oxide clusters that are connected by organic linkers forming porous frameworks. Replacing the organic linkers, new structures can be created and also exchange of the metal ions or metal ion clusters can change the properties of MOFs thus giving the possibility of tailoring the MOFs to specific applications. Zeolitic Imidazolate Frameworks (ZIFs) belong to the most promisings among the recently developed MOFs because of their extraordinary thermal and chemical stability and the huge variety of structures that can be designed [2]. In some of them, structural changes under increased loadings with guest molecules have been observed, e.g., the separation of an ethane/ethylene mixture could be drastically enhanced in ZIF-7 since only for ethane a gate opening effect took place. This gate opening leads to wider apertures (windows) between adjacent cavities that allow larger molecules to pass these bottlenecks or to enhance their diffusion inside the MOF framework.

In this project we investigate the possibility of gate opening for CO_2 and CO_2/N_2 mixtures in ZIF-8 by Molecular Dynamics (MD) simulations with a flexible lattice and Gibbs ensemble Monte Carlo (GEMC) simulations with a rigid lattice. We define "gate opening" as the transition of a closed to an open window by conformational changes of the linker molecules, cf. Fig. 10.22. Gate-opening effects could be observed for both single-component gas adsorption [3] and in a CO_2/N_2 mixture [4]. In the mixture, the start of gate opening of ZIF-8 is more sensitive to N_2 because of its higher fugacity compared to CO_2. Evaluation of the self-diffusion coefficient and diffusion selectivity from MD and adsorption selectivity from GEMC made it possible to calculate membrane selectivities that agree satisfactorily with experiments.

[1] K.K. Gangu et al.: Inorg. Chim. Acta **446,** 61 (2016)
[2] K.S. Park et al.: Proc. Natl. Acad. Sci. USA **103,** 10186 (2006)
[3] T. Chokbunpiam et al.: Chem. Phys. Lett. **648,** 178 (2016)
[4] T. Chokbunpiam et al.: J. Phys. Chem. C **120,** 23458 (2016)

10.19   Boundary conditions and non-local constraints in plaquette models

M. Müller, W. Janke, D.A. Johnston*

*Department of Mathematics and the Maxwell Institute for Mathematical Sciences, Heriot-Watt University, Edinburgh, UK
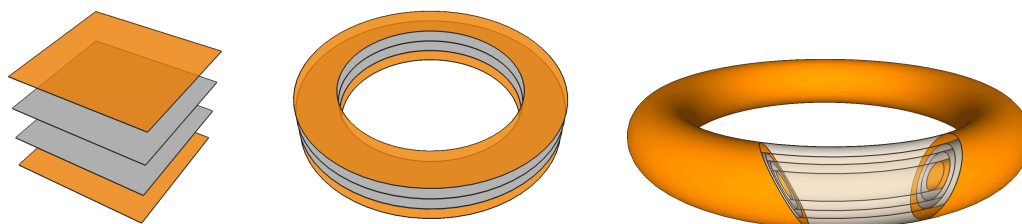

Figure 10.23: Fuki-Nuke models with free boundary conditions in one direction permit different topology of the lattice. We sketch the layers of independent layers of spins: (a) free boundary conditions in *all* directions, (b) periodic boundary conditions are set in one, and only one direction, and (c) periodic boundary conditions are set in both other directions.

An anisotropic limit of the $3d$ plaquette Ising model, in which the plaquette couplings in one direction were set to zero, was solved for free boundary conditions by Suzuki [1], who later dubbed it the fuki-nuke, or "no-ceiling", model. Defining new spin variables as the product of nearest-neighbour spins transforms the Hamiltonian into that of a stack of (standard) $2d$ Ising models and reveals the planar nature of the magnetic order, which is also present in the fully isotropic $3d$ plaquette model [2]. More recently, the solution of the fuki-nuke model was discussed for periodic boundary conditions applied to the spin lattice, which require a slightly different approach to defining the product spin transformation, by Castelnovo et al. [3].

We find that the essential features of the differences between free and periodic boundary conditions when using a product spin transformation are already present in the $1d$ Ising model [4], which thus provides an illuminating test case for its use in solving plaquette spin models and an alternative method for solving the $1d$ Ising model with periodic boundary conditions.

We clarify the exact relation between partition functions expressed in terms of the original and product spin variables for the $1d$ Ising model, $2d$ plaquette and $3d$ fuki-nuke models with free and periodic boundary conditions. Representing graphically the combinatorial factors that contribute to the partition function, we are able to solve the $2d$ plaquette model with free, periodic and helical boundary conditions and various combination of these in x- and y-directions, see Fig. 10.23. The various exactly solved examples illustrate how correlations can be induced in finite systems as a consequence of the choice of boundary conditions.

For the three-dimensional fuki-nuke model the exact finite-size partition function may be written as a product of $2d$ Ising partition functions in the case of free boundary conditions using the product variable transformation. A similar decoupling is not manifest with periodic boundary conditions, where all n-point $2d$ Ising spin-spin correlations also contribute to the expression for the $3d$ fuki-nuke partition function. As illustrated

in Fig. 10.24, this can be most easily understood in a pictorial way by employing the high-temperature expansion/dimer approach. It is perhaps worth remarking that the discussion of the fuki-nuke model in [3] conflates the discussion of free and periodic boundary conditions, although the overall picture of a 2d Ising-like transition in the thermodynamic limit of the 3d fuki-nuke model remains, of course, correct in both cases.
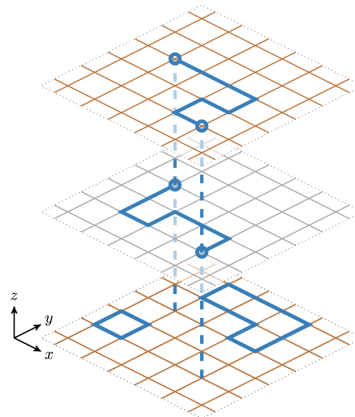

Figure 10.24: A dimer configuration of the Fuki-Nuke model with $L_z = 3$ that can contribute to the partition function, although the mid and top layer have dangling ends (symbolised by open circles). These are connected through the constraints (dashed vertical lines) and contribute to the two-point function in each of the two upper layers. Notice that additional, standard 2d Ising loops may appear, as those shown in the bottom layer, which are the standard contributions to the partition function of each layer.

A further consequence of the planar flip symmetry is found in a Hamiltonian related to the quantum dual of the plaquette model. This fits into the general framework developed in [5, 6] in which novel fracton topological phases are constructed by gauging symmetries acting on subsystems of dimension $2 \le d_s < d$. Since the spin-flip symmetry in the 3d plaquette model acts on 2d planes it has precisely this property. The procedure for constructing the fracton Hamiltonian follows closely that of the Kitaev toric code, giving commuting electric and magnetic operators. We outline the role played by the spin-flip symmetry in enabling the appearance of fracton topological defects in a Hamiltonian related to the dual of the quantum version of the model [7].

[1] M. Suzuki: Phys. Rev. Lett. **28**, 507 (1972)

[2] M. Mueller et al.: Nucl. Phys. B **894**, 1 (2015); D.A. Johnston et al.: Mod. Phys. Lett. **B29**, 1550109 (2015)

[3] C. Castelnovo et al.: Phys. Rev. B **81**, 184303 (2010)

[4] M. Mueller et al.: Nucl. Phys. B **914**, 388 (2017)

[5] S. Vijay et al.: Phys. Rev. B **94**, 235157 (2016)

[6] D.J. Williamson: Phys. Rev. B **94**, 155128 (2016)

[7] D.A. Johnston et al.: Eur. Phys. J. Special Topics **226**, 749 (2017)

10.20   The two-dimensional Blume-Capel model: Scaling and universality

J. Zierenberg, N.G. Fytas[*], M. Weigel[*], W. Janke, A. Malakis[†]

[*]Applied Mathematics Research Centre, Coventry University, England, UK
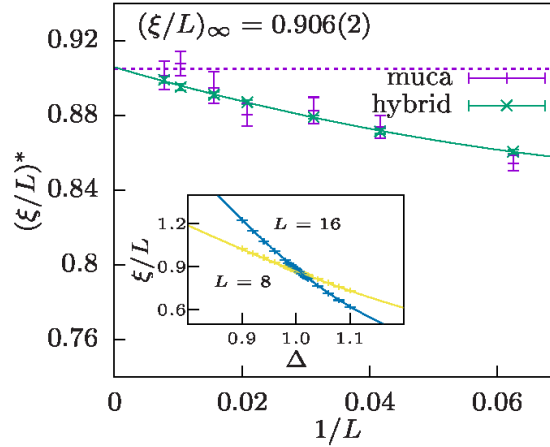[†]Department of Physics, University of Athens, Greece

Figure 10.25: Finite-size scaling at $T = 1.398$ of the correlation length crossings $(\xi/L)^*$. The dashed horizontal shows the asymptotic value for the square-lattice Ising model with periodic boundaries. Compared are data from the multicanonical ("muca") and hybrid methods. The line shows a quadratic fit in $1/L$ to the data from the hybrid method. The inset demonstrates the crossing point of $L = 8$ and $L = 16$ obtained from both the muca (lines) and hybrid (data points) method.

The Blume-Capel model [1, 2] is a perfect test model for studies of phase transitions. We consider this spin-one Ising model in a crystal field on a square lattice in two dimension (2D), described by the Hamiltonian

$$\mathcal{H} = -J \sum_{\langle ij \rangle} \sigma_i \sigma_j + \Delta \sum_i \sigma_i^2 = E_J + \Delta E_\Delta \,. \tag{10.5}$$

We investigate the behaviour in the vicinity of the first-order and second-order regimes of the ferromagnet-paramagnet phase boundary, respectively [3]. To achieve high-precision results, we utilize a combination of (i) a parallel version of the multicanonical algorithm and (ii) a hybrid updating scheme combining Metropolis and generalized Wolff cluster moves. These techniques are combined to study for the first time the correlation length ξ of the model, using its scaling with system size L in the regime of second-order transitions to illustrate universality through the observed identity of the limiting value of ξ/L with the exactly known result for the Ising universality class, see Fig. 10.25.

In contrast to most previous work, we focused on crossing the phase boundary at constant temperature by varying the crystal field Δ [4]. Employing a multicanonical scheme in Δ allowed us to get results as continuous functions of Δ and to overcome

the free-energy barrier in the first-order regime of the transitions. A finite-size scaling analysis based on a specific-heat-like quantity and the magnetic susceptibility provided us with precise estimates for the transition points in both regimes of the phase diagram that compare very well to the most accurate estimates of the current literature. In the first-order regime, we found a somewhat surprising $1/L$ correction in the scaling of the conventionally defined magnetic susceptibility χ. As it turns out, this is due to the explicit symmetry breaking by using the absolute value of the magnetisation (i.e., $|M|$ instead of M) in the definition of χ. For a modified symmetry breaking prescription that leaves the disordered peak invariant, this correction disappears. It would be interesting to see whether similar corrections are found in other systems with first-order transitions, such as the Potts model.

[1] M. Blume: Phys. Rev. **141**, 517 (1966)
[2] H.W. Capel: Physica (Utr.) **32**, 966 (1966)
[3] J. Zierenberg et al.: Eur. Phys. J. Special Topics **226**, 789 (2017)
[4] J. Zierenberg et al.: Phys. Rev. E **91**, 032126 (2015)

10.21 Finite-size scaling properties of the real microcanonical ensemble

P. Schierz, J. Zierenberg, W. Janke

The definition of the microcanonical ensemble can be found in any standard textbook on statistical physics. Usually this ensemble is quickly dismissed in favor of the canonical ensemble since it is quite unrealistic for most physical systems in a laboratory. In the literature on phase transitions, however, this ensemble gained some interest also due to the development of the generalized ensemble methods MUCA [1, 2] and Wang-Landau [3]. Here, however, one refers to the microcanonical ensemble at constant *potential* energy while the "real" microcanonical ensemble was originally defined at constant *total* energy.

We previously investigated the behaviour of molecular dynamics and Monte Carlo simulations within this ensemble and made the interesting observation that a Monte Carlo simulation in this ensemble sampled the first-order aggregation transition in a very efficient way [4]. We found that this behaviour was previously described by Martin-Mayor [5] for the temperature-driven first-order phase transition in the Potts lattice model. We further investigated this simulation technique in the real microcanonical ensemble for a continuous Lennard-Jones system and found the same sampling advantage. We reached the same amount of particles with these simulations as with the sophisticated MUCA simulation technique.

In Ref. [6] we were able to develop a framework based on the generalization of the equal-area rule which allowed us to explain the obtained simulation behaviour of the real microcanonical ensemble. For comparisons we introduced the transition barrier of an ensemble as

$$B = \ln\left[P^{\mathrm{eqh}}\left(E_p^{\pm}\right)/P^{\mathrm{eqh}}\left(E_p^0\right)\right], \tag{10.6}$$
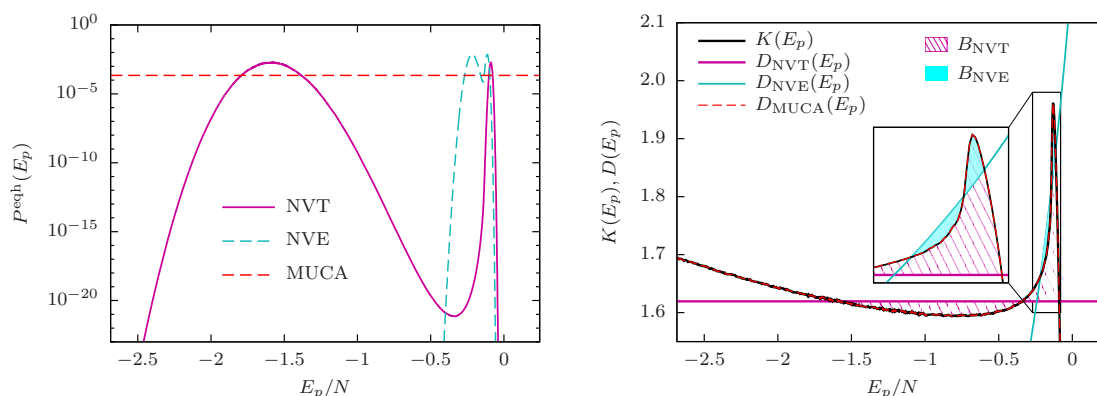
Figure 10.26: (a) The potential-energy histogram at equal height for three different ensembles for the $N = 2048$ Lennard-Jones system [6]. (b) The system dependent quantity $K(E_p)$ and the ensemble dependent $D(E_p)$ for the considered ensembles as defined in [6].

where $P^{\text{eqh}}\left(E_p^{\pm}/E_p^0\right)$ denotes the equal-height histogram emerging due to phase coexistence, $E_p^{\pm}$ the positions of the two maxima and E_p^0 the position of the minimum in between. This quantity hence allows one to evaluate how "hard" the first-order transition between two phases is within an ensemble. This framework leads to the conclusion that the barrier in the canonical ensemble is always larger than in the microcanonical ensemble, $B_{\text{NVT}} > B_{\text{NVE}}$. In the microcanonical ensemble the transition barrier can even vanish as it was observed in [4, 7] for polymer aggregation and by reproducing the data from Ref. [5]. For the example of the Lennard-Jones system with $N = 2048$ particles we discovered that the sampling with the microcanonical ensemble is of the order of $\exp\left(B_{\text{NVT}} - B_{\text{NVE}}\right) \approx 10^{16}$ more efficient than simulations in the canonical ensemble due to the difference of the barriers.

[1] B.A. Berg, T. Neuhaus: Phys. Lett. B **267**, 249 (1991); Phys. Rev. Lett. **68**, 9 (1992)
[2] W. Janke: Int. J. Mod. Phys. C **03**, 1137 (1992); Physica A **254**, 164 (1998)
[3] F. Wang, D.P. Landau: Phys. Rev. Lett. **86**, 2050 (2001); Phys. Rev. E **64**, 056101 (2001)
[4] P. Schierz et al.: J. Chem. Phys. **143**, 134114 (2015)
[5] V. Martin-Mayor: Phys. Rev. Lett. **98**, 137207 (2007)
[6] P. Schierz et al.: Phys. Rev. E **94**, 021301(R) (2016)
[7] W. Janke et al.: *Transition barrier at a first-order phase transition in the canonical and microcanonical ensemble*, Leipzig preprint (2017), to appear in *Computer Simulation Studies in Condensed-Matter Physics XXX*, eds. D.P. Landau, H.-B. Schüttler, S. Lewis, M. Bachmann, J. Phys.: Conf. Ser. (2017), in print

10.22 Convergence of Stochastic Approximation Monte Carlo and modified Wang-Landau algorithms: Tests for the Ising model

S. Schneider, M. Müller, W. Janke

The Wang-Landau algorithm [1] has proven to be a very efficient tool for determining the density of states (DOS) of statistical systems near phase transitions where traditional

local importance sampling algorithms like the Metropolis algorithm are likely to run into critical slowing down or become trapped in local free-energy minima [2]. It has, however, been pointed out that the error of the estimator for the DOS obtained by the Wang-Landau algorithm cannot be made arbitrarily small just by using longer simulations [3], the (systematic) error saturates at some (small) value. To overcome this, it has been suggested to change the behaviour of the refinement parameter in the $1/t$ modification ($1/t$-WL) of the Wang-Landau algorithm in order to circumvent the error saturation [4, 5].

Another approach is the Stochastic Approximation Monte Carlo (SAMC) algorithm first introduced in Ref. [6] and refined in Ref. [7], which works similar to the modified Wang-Landau algorithm regarding the choice of refinement scheme. While the algorithm proposed by Belardinelli and Pereyra has been tested for the Ising model, for the calculation of multidimensional integrals and was applied to lattice polymer models, the SAMC algorithm has only been tested for an artificial, non-physical model with a very small number of states [7] compared to models currently studied in statistical physics and for an off-lattice polymer model [8]. The standard test case, the Ising model, however, was still missing and we closed this gap [9].

The $1/t$-method inherits the problem of needing to know the range of admissible energies for the considered model from the Wang-Landau algorithm. In SAMC, this needs not to be known beforehand, since histogram checking is not necessary in principle. The SAMC algorithm, on the other hand, sometimes failed to converge in our examined run times. This is caused by the simulation failing to explore the low-energy states. Therefore no flat histogram can be produced, see Fig. 10.27. Since both variants of the Wang-Landau algorithm regularly check the histogram for adequate flatness, it is ensured that all energies are visited at least once. While the SAMC algorithm should converge to the desired distribution if all conditions are met, it is necessary to check if the histogram measured during the simulation was really flat at the end. This dampens the advantage of a predictable run time, since it is possible that a complete run of the algorithm turns out to be unusable due to an inappropriate choice of t_0. Monitoring the flatness of the histogram during the run is no help, because this would introduce a stochastic quantity into the algorithm, making the run time unpredictable and require the same *a-priori* knowledge of the admissible energy range as the Wang-Landau algorithm and its modifications. The rule of thumb for the choice of t_0 given by Liang et al. [7] is violated even by the 128×128 Ising model, showing that finding an appropriate t_0 can be a quite cumbersome task. The $1/t$-WL algorithm suffers from a similar restriction in this regard: While we could not find anything comparable in the Ising model, other studies suggest that the overall convergence behaviour can also be sensitive to the details of the $1/t$-refining scheme for more complicated models [5, 10]. Regarding the common features of the SAMC and $1/t$-WL algorithms, it seems reasonable to assume that the proof of convergence for SAMC also extends to the $1/t$-WL algorithm as well, since their long-time behaviour is the same. Therefore the choice of algorithm to apply to a certain problem is a practical one. With the modifications proposed in Refs. [10, 11], allowing it to adapt to *a-priori* unknown energy ranges, and in Refs. [5, 10], allowing it to find the right time for the onset of the $1/t$-refinement, the $1/t$-WL algorithm might be able to overcome its drawback for complicated systems with unknown ground states. SAMC still has the advantage of allowing to generate weights not only according to the density of states, but also according to other distributions [6, 7], which can improve

estimators [12] and might prove useful for complex systems like spin glasses or polymers, because sampling with distributions other than the inverse density of states can speed up round trip times significantly [13].
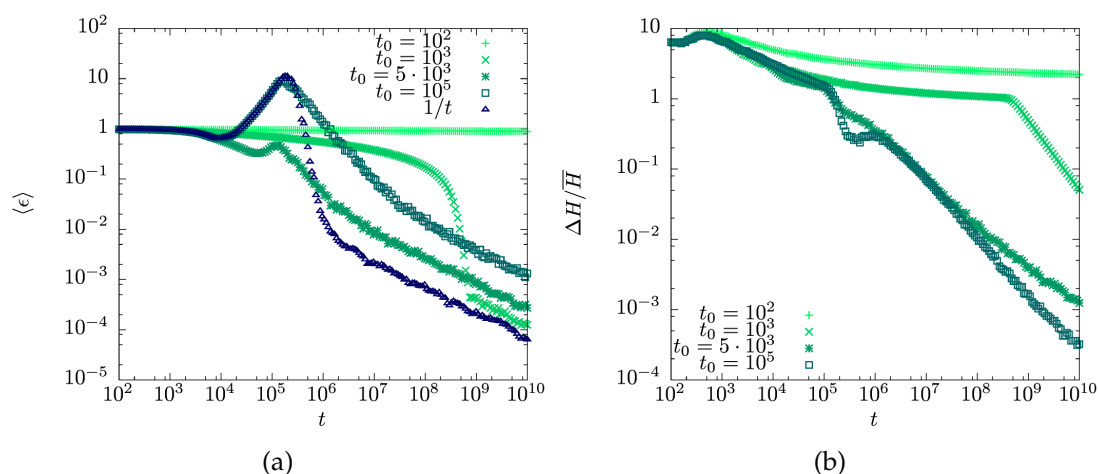

(a)   (b)

Figure 10.27: (a) The behaviour of the average deviation from the exact solution $\langle \epsilon(t) \rangle_E$ over MC time t for SAMC for different t_0 and $1/t$-WL simulations of the 16×16 Ising model. Obviously, tweaking the free parameter t_0 is essential for practical convergence. (b) The flatness of the histogram over MC time t for different choices of t_0. All data was obtained by averaging over 40 independent runs of the algorithm to reduce statistical noise.

[1] F. Wang, D.P. Landau: Phys. Rev. Lett. **86**, 2050 (2001); Phys. Rev. E **64**, 056101 (2001)

[2] W. Janke, W. Paul: Soft Matter **12**, 642 (2016)

[3] Q. Yan, J.J. de Pablo: Phys. Rev. Lett. **90**, 035701 (2003)

[4] R.E. Belardinelli, V.D. Pereyra: J. Chem. Phys. **127**, 184105 (2007); Phys. Rev. E **75**, 046701 (2007)

[5] C. Zhou, J. Su: Phys. Rev. E **78**, 046705 (2008)

[6] F. Liang: J. Stat. Phys. **122**, 511 (2006)

[7] F. Liang et al.: J. Amer. Statist. Assoc. **102**, 305 (2007)

[8] B. Werlich et al.: Comput. Phys. Comm. **186**, 65 (2015)

[9] S. Schneider et al.: Comput. Phys. Comm. **216**, 1 (2017)

[10] A.D. Swetnam, M.P. Allen: J. Comput. Chem. **32**, 816 (2011)

[11] T. Wüst, D.P. Landau: Phys. Rev. Lett. **102**, 178101 (2009)

[12] B. Hesselbo, R.B. Stinchcombe: Phys. Rev. Lett. **74**, 2151 (1995)

[13] S. Trebst et al.: Phys. Rev. E **70**, 046701 (2004)

10.23 Population annealing: Massively parallel simulations in statistical physics

M. Weigel[*], L.Yu. Barash[†‡], M. Borovský[§], L.N. Shchur[†‡¶], W. Janke

[*]Applied Mathematics Research Centre, Coventry University, England, UK

[†]Landau Institute for Theoretical Physics, 142432 Chernogolovka, Russia

[‡]Science Center in Chernogolovka, 142432 Chernogolovka, Russia
[§]P.J. Šafárik University, Park Angelinum 9, 040 01 Košice, Slovak Republic
[¶]National Research University Higher School of Economics, 101000 Moscow, Russia

The canonical technique for Monte Carlo simulations in statistical physics is importance sampling via a suitably constructed Markov chain [1]. While such approaches are quite successful, they are not particularly well suited for parallelization as the chain dynamics is sequential, and if replicated chains are used to increase statistics each of them relaxes into equilibrium with an intrinsic time constant that cannot be reduced by parallel work. Population annealing is a sequential Monte Carlo method that simulates an ensemble of system replica under a cooling protocol. This method was first suggested in 2001 by Iba [2] and later on discussed in more detail by Hukushima and Iba [3] as a method to tackle potentially difficult sampling problems, but with no particular view to a parallel implementation. More recently, Machta [4] used a variant that avoids the recording of weight functions through population control in every step. This is the variant we adapted in our own implementation.

The population element makes this method naturally well suited for massively parallel simulations, and bias can be systematically reduced by increasing the population size. To demonstrate this, we developed an implementation of population annealing on graphics processing units (GPUs) [5] and benchmarked its behaviour for different systems undergoing continuous and first-order phase transitions [6, 7].

[1] D.P. Landau, K. Binder: *A Guide to Monte Carlo Simulations in Statistical Physics*, 4th ed. (Cambridge University Press, Cambridge, 2015)
[2] Y. Iba: Trans. Jpn. Soc. Artif. Intell. **16**, 279 (2001)
[3] K. Hukushima, Y. Iba: AIP Conf. Proc. **690**, 200 (2003)
[4] J. Machta: Phys. Rev. E **82**, 026704 (2010)
[5] L.Yu. Barash et al.: *GPU accelerated population annealing algorithm*, Moscow/Coventry/Košice/Leipzig preprint (2017), arXiv:1703.03676 [physics.comp-ph], to appear in Comput. Phys. Comm., in print
[6] L.Yu. Barash et al.: Eur. Phys. J. – Special Topics **226**, 595 (2017)
[7] M. Weigel et al.: *Population annealing: Massively parallel simulations in statistical physics*, to appear in: *Computer Simulation Studies in Condensed-Matter Physics XXX*, Coventry/Moscow/Košice/Leipzig preprint (2017), eds. D.P. Landau, H.-B. Schüttler, S. Lewis, M. Bachmann, J. Phys.: Conf. Ser. (2017), in print

10.24 Framework for programming Monte Carlo simulations (βMC)

M. Marenz, J. Zierenberg, W. Janke

Monte Carlo (MC) computer simulations are a very powerful tool for investigating and understanding the thermodynamic behaviour of a wide variety of physical systems. These systems range from such simple ones like the Ising spin model to complex ones like the adsorption properties of proteins on surfaces [1]. In contrast to Molecular

Dynamics (MD) simulations, the other important class of algorithm to simulate microscopic systems, MC simulations are not suitable to investigate dynamical properties. On the other hand, the ability of modern MC methods to explore effectively the phase space of physical systems, especially those with a phase transition, makes them a very powerful and indispensable tool.

Another difference to MD simulations is the lack of a widely used program package for generic MC simulations. One reason for this lack is the versatility of modern MC algorithms – there are various different algorithm and many different possibilities to adjust a MC simulation to a specific problem. This was the starting point for the development of our framework for advanced MC algorithms. The aim of the framework is to enable the programmer to implement specific simulations in an easy and efficient way, without the need to implement all the tricky details for every new problem. The framework is implemented in the C++ programming language and is designed such that it separates basics parts of a MC algorithm in separate building blocks. These building blocks can be used by the programmer to implement a specific simulation.

There are 5 basic building blocks as illustrated in Fig. 10.28: The first one is the "system", which defines the Hamiltonian and the structure of the physical system. This means that the "system" building block encapsulates the energy calculation and the structure of the considered physical problem. For off-lattice system this block contains a smaller subpart, the "atom" block, which encodes the geometry of the system (e.g., boundary conditions). As systems we have implemented so far different kinds of coarse-grained homopolymers, the Lennard-Jones gas, the TIP4P water model, lattice polymers and the Potts model in different dimensions. On top of the "system" are the last two other building blocks, the "move" and the "MC technique". A "move" defines a single update proposal, propagating the system from the current state to the next one. Additionally a "constraint" can be added to every "move" in order to simulate efficiently systems with geometrical confinements. The "MC technique" implements the Monte Carlo algorithm itself. At the moment we have implemented various algorithms such as Metropolis MC, parallel tempering, multicanonical MC, multimagnetic MC and the Wang-Landau MC algorithm. One of the most advanced MC algorithms we have implemented is a parallel version of the multicanonical algorithm [2], see Fig. 10.29.

The boundaries between these blocks are well defined, so that one can easily exchange one of them. For example one can use two different algorithm to simulate a specific system without implementing a completely new program. The framework is already in practical use for different studies, for example the investigation of the influence of bending stiffness on a coarse-grained homopolymer, the influence of spherical confinement on pseudo-phase transitions of homopolymers, and the study of polymer aggregation of several polymers for a large set of parameters (e.g., temperature, bending stiffness). Thus, the framework is very useful and has led already to several publications [2–10].

[1] M. Bachmann et al.: Angew. Chem. Int. Ed. **49**, 9530 (2010) [Angew. Chem. **122**, 9721 (2010), in German]

[2] J. Zierenberg et al.: Comput. Phys. Comm. **184**, 1155 (2013)

[3] M. Marenz et al.: Condens. Matter Phys. **15**, 43008 (2012)

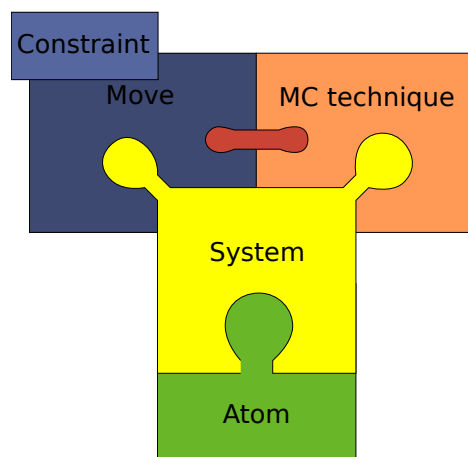[4] J. Zierenberg et al.: J. Phys.: Conf. Ser. **510**, 012017 (2014)

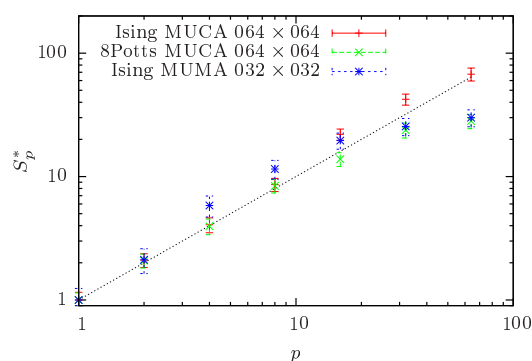**Figure 10.28:** The 5 basic building blocks.

Figure 10.29: Scaling properties of the parallel multicanonical algorithm as a function of the number of processors p.

[5] J. Zierenberg et al.: J. Chem. Phys. **141**, 114908 (2014)

[6] J. Zierenberg, W. Janke: Europhys. Lett. **109**, 28002 (2015)

[7] M. Mueller et al.: in *Computer Simulation Studies in Condensed-Matter Physics XXVIII*, eds. D.P. Landau, H.-B. Schüttler, S. Lewis, M. Bachmann, Physics Procedia **68**, 95 (2015)

[8] M. Marenz, W. Janke: Phys. Rev. Lett. **116**, 128301 (2016)

[9] J. Zierenberg et al: Polymers **8**, 333 (2016)

[10] J. Zierenberg et al.: Nat. Commun. **8**, 14546 (2017)

10.25   Funding

10.26   Organizational Duties

Wolfhard Janke
- Director, Institute for Theoretical Physics (ITP), Universität Leipzig
- Director, Naturwissenschaftlich-Theoretisches Zentrum (NTZ), Universität Leipzig
- Member of Department Council ("Fakultätsrat"), Faculty for Physics and Earth Sciences, Universität Leipzig
- Member of the Steering Committee ("Direktorium") of the Graduate Centre *Mathematics/Computer Science and Natural Sciences*, Research Academy Leipzig
- Principal Investigator of the Graduate School "BuildMoNa"
- Scientific Member of the International Max Planck Research School (IMPRS) *Mathematics in the Sciences*
- Principal Investigator of the DFG Sonderforschungsbereich/Transregio SFB/TRR 102 *Polymers under Multiple Constraints: Restricted and Controlled Molecular Order and Mobility*
- Principal Investigator of "Profillinie" *Complex Matter*, Universität Leipzig
- Principal Investigator of "Profillinie" *Mathematical and Computational Sciences*, Universität Leipzig

- Spokesperson of the German-French Graduate College *Statistical Physics of Complex Systems* with Nancy (France), and associated partners in Coventry (England, UK) and Lviv (Ukraine), of the Deutsch-Französische Hochschule (DFH-UFA)
- Spokesperson of the German-Ukrainian Institute Partnership Leipzig-Lviv of the Alexander von Humboldt Foundation (AvH)
- External Member of the Jagiellonian University Graduate School *International Ph.D. Studies in Physics of Complex Systems*, Krakow, Poland
- *International Visiting Professor* of Coventry University, England, UK
- *Adjunct Professor* of The University of Georgia, Athens, Georgia, USA
- Permanent Member of the International Advisory Board for the Annual *Conference of the Middle European Cooperation in Statistical Physics (MECO)*
- Organizer (with J. Gross, P. Schierz) of the Contribution *3D-Visualisierung von Polymeren – oder: Wie verkleben Spaghetti* to the "Lange Nacht der Wissenschaften", Universität Leipzig, 24. June 2016
- Organizer of the Workshop *CompPhys16* – 17th International NTZ Workshop on *New Developments in Computational Physics*, ITP, Universität Leipzig, 24.–26. November 2016
- Organizer of the Workshop *CompPhys17* – 18th International NTZ Workshop on *New Developments in Computational Physics*, ITP, Universität Leipzig, 30. November – 01. December 2017
- Editor "Computational Physics", Central European Journal of Physics, Krakow, Poland
- Member of Editorial Board, Condens. Matter Phys., Lviv, Ukraine
- External Reviewer for Deutsche Forschungsgemeinschaft (DFG), Humboldt-Stiftung (AvH), Studienstiftung des deutschen Volkes, Fond zur Förderung der wissenschaftlichen Forschung (FWF), Österreich, The Royal Society, UK, The Engineering and Physical Sciences Research Council (EPSRC), UK, Israel Science Foundation, Israel, National Science Foundation (NSF), USA, Natural Sciences and Engineering Research Council of Canada (NSERC), Canada, The Jeffress Memorial Trust, Bank of America, Virginia, USA, Universität Mainz, Germany, The University of Warwick, England, UK, Coventry University, England, UK, CECAM, Lyon, France
- Referee for Physical Review Letters, Physical Review B, Physical Review E, Journal of Chemical Physics, Europhysics Letters, Physics Letters A, Physics Letters B, The European Physical Journal B, Physica A, Proceedings of the Royal Physical Society, Journal of Physics A, Computer Physics Communications, JSTAT, Condens. Matter Phys., PLOS ONE, New Journal of Physics, International Journal of Modern Physics C

10.27 External Cooperations

Academic

- Institute of Physics, Jagiellonian University, Kraków, Poland
  Prof. Dr. Piotr Białas, Dr. Leszek Bogacz, Prof. Dr. Zdzisław Burda

- CEA/Saclay, Service de Physique Théorique, France
  Dr. Alain Billoire

- Institut für Physik, Universität Mainz, Germany
  Prof. Dr. Kurt Binder, Andreas Nußbaumer, Prof. Dr. Friderike Schmid

- Institut für Theoretische Physik, Universität Heidelberg, Germany
  Dr. Elmar Bittner

- Laboratoire de Physique des Matériaux (UMR CNRS No 7556), Université de Lorraine, Nancy, France
  Prof. Dr. Bertrand Berche, Dr. Christophe Chatelain, Dr. Olivier Collet, Prof. Dr. Malte Henkel, Prof. Dr. Dragi Karevski

- Groupe de Physique des Matériaux (UMR CNRS No 6634), Université de Rouen, France
  Dr. Pierre-Emmanuel Berche

- SUPA, School of Physics and Astronomy, University of Edinburgh, Scotland, UK
  Dr. Richard A. Blythe, Prof. Dr. Martin R. Evans, Dr. Bartłomiej Wacław

- Istituto Nazionale di Fisica Nucleare, Sezione di Milano-Bicocca, Milano, Italy
  Prof. Dr. Pablo Butera

- Applied Mathematics Research Centre, Coventry University, England, UK
  PD Dr. Christian von Ferber, Dr. Nikolaos G. Fytas, Prof. Dr. Ralph Kenna, Dr. Thierry Platini, Dr. Martin Weigel

- Jülich Supercomputing Centre (JSC), Forschungszentrum Jülich, Germany
  Prof. Dr. Peter Grassberger, PD Dr. Thomas Neuhaus

- IAC-1, Universität Stuttgart, Germany
  Prof. Dr. Rudolf Hilfer, Prof. Dr. Christian Holm

- Max Planck Institute for Polymer Research, Mainz, Germany
  Dr. Hsiao-Ping Hsu, Prof. Dr. Kurt Kremer

- Complex Systems Division, Department of Theoretical Physics, Lunds Universitet, Lund, Sweden
  Prof. Dr. Anders Irbäck

- Department of Mathematics and the Maxwell Institute for Mathematical Sciences, Heriot-Watt University, Edinburgh, Scotland, UK
  Prof. Dr. Desmond A. Johnston

- Inst. für Theoretische Physik, FU Berlin, Germany
  Prof. Dr. Hagen Kleinert

- Department of Physics, University of Athens, Greece
  Prof. Dr. Anastasios Malakis

- Atominstitut, TU Wien, Austria
  Prof. Dr. Harald Markum

- Jacobs Universität Bremen, Germany
  Prof. Dr. Hildegard Meyer-Ortmanns, Darka Labavić

- Applied Mathematics, Universitat Pompeu Fabra, Barcelona, Spain
  Prof. Dr. Ramon Villanova

- CERN (PH-SFT), Geneva, Switzerland
  Dr. Sandro Wenzel

- Department of Engineering of Physics, Ankara University, Ankara, Turkey
  Prof. Dr. Handan Arkın (Olgar), Mustafa Bilsel, Buket Taşdizen

- Dept. of Physics, Hacettepe University, Ankara, Turkey
  Prof. Dr. Tarik Çelik, Gökhan Gökoğlu

- Dept. of Physics Engineering, Hacettepe University, Ankara, Turkey
  Prof. Dr. Fatih Yaşar

- Institute for Condensed Matter Physics, National Academy of Sciences, Lviv, Ukraine
  Dr. Viktoria Blavatska, Prof. Dr. Yurij Holovatch

- Yerevan Physics Institute, Yerevan, Armenia
  Prof. Dr. David B. Saakian

- Alikhanyan National Science Laboratory, Yerevan, Armenia
  Prof. Dr. Nerses Ananikyan, Dr. Nikolay Izmailyan

- Landau Institute for Theoretical Physics, Chernogolovka, Russia
  Dr. Lev Yu. Barash, Prof. Dr. Lev N. Shchur

- Center for Simulational Physics, The University of Georgia, Athens, USA
  Prof. Dr. Michael Bachmann, Prof. Dr. David P. Landau

- Dept. of Physics, Florida State University, Tallahassee, USA
  Prof. Dr. Bernd A. Berg

- Dept. of Chemistry and Biochemistry, University of Oklahoma, Norman, USA
  Prof. Dr. Ulrich H.E. Hansmann

- Los Alamos National Laboratory, Los Alamos, USA
  Dr. Christoph Junghans

- Dept. of Physics and Astronomy, Texas A&M, College Station, USA
  Prof. Dr. Helmut G. Katzgraber

- Dept. of Physics, Virginia Tech, Blacksburg, USA
  Prof. Dr. Michel Pleimling, Prof. Dr. Royce K.P. Zia

- Physics Department, Carnegie Mellon University, Pittsburgh, USA
  Prof. Dr. Robert H. Swendsen

- Stetson University, DeLand, USA
  Dr. Thomas Vogel

- Jawaharlal Nehru Centre for Advanced Scientific Research (JNCASR), Jakkur, India
  Prof. Dr. Subir K. Das

- Computational Chemistry Unit Cell (CCUC), Department of Chemistry, Chulalongkorn University, Bangkok, Thailand
  Prof. Dr. Supot Hannongbua, Dr. Oraphan Saengsawang

- Ramkhamhaeng University, Department of Chemistry, Faculty of Science, Bangkok, Thailand
  Dr. Tatiya Chokbunpiam

- Laboratory of Statistical and Computational Physics, Institute of Physics, Academia Sinica, Nankang, Taipei, Taiwan
  Prof. Dr. Chin-Kun Hu

- The University of Tokyo, Tokyo, Japan
  Prof. Dr. Nobuyasu Ito

- Banaras Hindu University, Varanasi, India
  Prof. Dr. Sanjay Kumar

- Nagoya University, Nagoya, Japan
  Dr. Tetsuro Nagai, Prof. Dr. Yuko Okamoto

- Zhejiang Institute of Modern Physics, Zhejiang University, Hangzhou, P.R. China
  Prof. Dr. He-Ping Ying, Prof. Dr. Bo Zheng

10.28   Publications

Journals

S. Basu, S. Majumder, S. Sutradhar, S.K. Das, R. Paul: *Phase Segregation in a Binary Fluid Confined Inside a Nanopore*, Europhys. Lett. **116**, 56003-1–7 (2016)

T. Chokbunpiam, S. Fritzsche, C. Chmelik, J. Caro, W. Janke, S. Hannongbua: *Gate Opening Effect for Carbon Dioxide in ZIF-8 by Molecular Dynamics – Confirmed, but at High CO_2 Pressure*, Chem. Phys. Lett. **648**, 178–181 (2016)

T. Chokbunpiam, S. Fritzsche, C. Chmelik, J. Caro, W. Janke, S. Hannongbua: *Gate Opening, Diffusion, and Adsorption of CO_2 and N_2 Mixtures in ZIF-8*, J. Phys. Chem. C **120**, 23458–23468 (2016)

J. Gross, M. Ivanov, W. Janke: *Comparing Atomistic and Coarse-Grained Simulations of P3HT*, in *Computer Simulation Studies in Condensed-Matter Physics XXIX*, eds. D.P. Landau, H.-B. Schüttler, S. Lewis, M. Bachmann, J. Phys.: Conf. Ser. **750**, 012009-1–5 (2016)

W. Janke, M. Marenz: *Stable Knots in the Phase Diagram of Semiflexible Polymers: A Topological Order Parameter?*, in *Computer Simulation Studies in Condensed-Matter Physics XXIX*, eds. D.P. Landau, H.-B. Schüttler, S. Lewis, M. Bachmann, J. Phys.: Conf. Ser. **750**, 012006-1–5 (2016)

W. Janke, W. Paul: *Thermodynamics and Structure of Macromolecules from Flat-Histogram Monte Carlo Simulations* (invited review), Soft Matter **12**, 642–657 (2016)

S. Kumar, R. Kumar, W. Janke: *Periodically Driven DNA: Theory and Simulation*, Phys. Rev. E **93**, 010402(R)-1–5 (2016)

S. Majumder, W. Janke: *Evidence of Aging and Dynamic Scaling in Collapse of a Polymer*, Phys. Rev. E **93**, 032506-1–6 (2016)

S. Majumder, W. Janke: *Aging and Related Scaling During the Collapse of a Polymer*, in *Computer Simulation Studies in Condensed-Matter Physics XXIX*, eds. D.P. Landau, H.-B. Schüttler, S. Lewis, M. Bachmann, J. Phys.: Conf. Ser. **750**, 012020-1–5 (2016)

M. Marenz, W. Janke: *Knots as a Topological Order Parameter for Semiflexible Polymers*, Phys. Rev. Lett. **116**, 128301-1–6 (2016)

H. Nagel, W. Janke: *Emergence of Dynamic Phases in the Presence of Different Kinds of Open Boundaries in Stochastic Transport with Short-Range Interactions*, J. Stat. Mech.: Theor. Exp., 013207-1–19 (2016)

H. Nagel, W. Janke: *Dynamics of Condensate Formation in Stochastic Transport with Pair-Factorized Steady States: Nucleation and Coarsening Time Scales*, Phys. Rev. E **93**, 052112-1–12 (2016)

A. Nußbaumer, J. Zierenberg, E. Bittner, W. Janke: *Numerical Test of Finite-Size Scaling Predictions for the Droplet Condensation-Evaporation Transition* (invited talk), in Conference Proceedings *CCP2015*, IIT Guwahati, India, J. Phys.: Conf. Ser. **759**, 012009-1–8 (2016)

P. Schierz, J. Zierenberg, W. Janke: *First-Order Phase Transitions in the Real Microcanonical Ensemble* (Editors' Suggestion), Phys. Rev. E **94**, 021301(R)-1–5 (2016)

J. Zierenberg, W. Janke: *Finite-Size Scaling of Lennard-Jones Droplet Formation at Fixed Density*, in *Computer Simulation Studies in Condensed-Matter Physics XXIX*, eds. D.P. Landau, H.-B. Schüttler, S. Lewis, M. Bachmann, J. Phys.: Conf. Ser. **750**, 012017-1–5 (2016)

J. Zierenberg, M. Marenz, W. Janke: *Dilute Semiflexible Polymers with Attraction: Collapse, Folding and Aggregation* (invited review), Polymers **8**, 333-1–19 (2016)

in press

K. Austin, J. Zierenberg, W. Janke: *Interplay of Adsorption and Semiflexibility: Structural Behavior of Grafted Polymers under Poor Solvent Conditions*, Macromolecules **50**, 4054–4063 (2017)

L. Yu. Barash, M. Weigel, L.N. Shchur, W. Janke: *Exploring First-Order Phase Transitions with Population Annealing*, Eur. Phys. J. Special Topics **226**, 595–604 (2017)

T. Chokbunpiam, S. Fritzsche, J. Caro, C. Chmelik, W. Janke, S. Hannongbua: *Importance of ZIF-90 Lattice Flexibility on Diffusion, Permeation, and Lattice Structure for an adsorbed H_2/CH_4 Gas Mixture: A Re-Examination by Gibbs Ensemble Monte Carlo and Molecular Dynamics Simulations*, J. Phys. Chem. C **121**, 10455–10462 (2017)

N. Fricke, W. Janke: *Exact Enumeration of Self-Avoiding Walks on Critical Percolation Clusters in 2–7 Dimensions*, J. Phys. A **50**, 264002-1–17 (2017)

N. Fricke, J. Zierenberg, M. Marenz, F. P. Spitzner, V. Blavatska, W. Janke: *Scaling Laws for Random Walks in Long-Range Correlated Disordered Media*, Condens. Matter Phys. **20**, 13004-1–11 (2017)

J. Gross, M. Ivanov, W. Janke: *Single-Chain Behavior of Poly(3-hexyl-thiophene)*, Eur. Phys. J. Special Topics **226**, 667–681 (2017)

D.A. Johnston, M. Mueller, W. Janke: *Plaquette Ising Models, Degeneracy and Scaling*, Eur. Phys. J. Special Topics **226**, 749–764 (2017)

S. Majumder, J. Zierenberg, W. Janke: *Kinetics of Polymer Collapse: Effect of Temperature on Cluster Growth and Aging*, Soft Matter **13**, 1276–1290 (2017)

M. Mueller, D.A. Johnston, W. Janke: *Exact Solutions to Plaquette Ising Models with Free and Periodic Boundaries*, Nucl. Phys. B **914**, 388–404 (2017)

S. Schneider, M. Mueller, W. Janke: *Convergence of Stochastic Approximation Monte Carlo and Modified Wang-Landau Algorithms: Tests for the Ising Model*, Comput. Phys. Comm. **216**, 1–7 (2017)

J. Zierenberg, N.G. Fytas, M. Weigel, W. Janke, A. Malakis: *Scaling and Universality in the Phase Diagram of the 2D Blume-Capel Model*, Eur. Phys. J. Special Topics **226**, 789–804 (2017)

J. Zierenberg, P. Schierz, W. Janke: *Canonical Free-Energy Barrier of Particle and Polymer Cluster Formation*, Nat. Commun. **8**, 14546-1–7 (2017)

J. Zierenberg, K. Tholen, W. Janke: *Effect of Grafting on the Binding Transition of Two Flexible Polymers*, Eur. Phys. J. Special Topics **226**, 683–692 (2017)

L.Yu. Barash, M. Weigel, M. Borovský, W. Janke, L.N. Shchur: *GPU Accelerated Population Annealing Algorithm*, arXiv:1703.03676, to appear in Comput. Phys. Comm. (2017), in print

W. Janke, M. Marenz, J. Zierenberg: *Generalized Ensemble Computer Simulations for Structure Formation of Semiflexible Polymers*, to appear in Proceedings of the International Conference *Supercomputer Simulations in Science and Engineering (SSSE2016)*, Moscow, Russia, Lobachevskii J. Math., in print

W. Janke, P. Schierz, J. Zierenberg: *Transition Barrier at a First-Order Phase Transition in the Canonical and Microcanonical Ensemble*, to appear in *Computer Simulation Studies in Condensed-Matter Physics XXX*, eds. D.P. Landau, H.-B. Schüttler, S. Lewis, M. Bachmann, J. Phys.: Conf. Ser. (2017), in print

S. Schnabel, W. Janke: *Dynamic Greedy Algorithms for the Edwards-Anderson Model*, to appear in Comput. Phys. Comm. (2017), in print

M. Weigel, L.Yu. Barash, M. Borovský, W. Janke, and L.N. Shchur: *Population Annealing: Massively Parallel Simulations in Statistical Physics*, to appear in *Computer Simulation Studies in Condensed-Matter Physics XXX*, eds. D.P. Landau, H.B. Schüttler, S. Lewis, M. Bachmann, J. Phys.: Conf. Ser. (2017), in print

Talks

J. Bock: *Computer Simulations of Semiflexible Polymers in Disordered Media*, Institute for Condensed Matter Physics of the National Academy of Sciences of Ukraine, Lviv, Ukraine, 11. November 2016

J. Gross, M. Ivanov, W. Janke: *Comparing Atomistic and Coarse-Grained Simulations of P3HT*, 29th Annual CSP Workshop *Recent Developments in Computer Simulation Studies in Condensed Matter Physics*, The University of Georgia, Athens, Georgia, USA, 22.-26. February 2016

J. Gross, M. Ivanov, W. Janke: *Comparing Atomistic and Coarse-Grained Simulations of P3HT*, Spring Meeting of the German Physical Society, Regensburg, Germany, 07.–11. March 2016

J. Gross, J, Zierenberg, M. Weigel, W. Janke: *Massively Parallel Multicanonical Simulations on GPUs*, 17th International NTZ-Workshop on *New Developments in Computational Physics – CompPhys16*, Universität Leipzig, Germany, 25. November 2016

W. Janke, J. Zierenberg, P. Schierz: *Finite-Size Scaling of Free-Energy Barrier in Droplet Formation and Nucleation-Like Processes*, Conference of the Middle European Cooperation in Statistical Physics – MECO41, Vienna, Austria, 15. February 2016

W. Janke, M. Marenz: *Knots as a Topological Order Parameter for Semiflexible Polymers*, 29th CSP Workshop on *Recent Developments in Computer Simulation Studies in Condensed Matter Physics*, The University of Georgia, Athens, Georgia, USA, 22.–26. February 2016

W. Janke, M. Mueller, D.A. Johnston: *Planar Order in the 3D Plaquette Gonihedric Ising Model*, DPG Frühjahrstagung 2016, Regensburg, Germany, 07.–11. March 2016

W. Janke: *Introduction to Monte Carlo Simulations*, SFB/TRR 102 Advanced Training Module *Introduction to Monte Carlo and Molecular Dynamics Simulation*, Leipzig/Halle, 27./28. April 2016

W. Janke: *Generalized Ensemble Computer Simulations of Macromolecules*, invited *Ising Lectures 2016*, Institute for Condensed Matter Physics of the National Academy of Sciences of Ukraine, Lviv, Ukraine, 17.–19. May 2016

W. Janke, M. Marenz: *Knots as Stable Order Parameter for Semiflexible Polymers*, invited talk, Workshop *From Computational Biophysics to Systems Biology* (CBSB16), Hacettepe University Ankara, Turkey, 23.–25. May 2016

W. Janke: *Generalized Ensemble Computer Simulations for Structure Formation of Semiflexible Polymers*, invited plenary talk, International Conference *Supercomputer Simulations in Science and Engineering (SSSE)*, Higher School of Economics, Moscow, Russia, 6.–10. September 2016

S. Majumder, W. Janke: *Evidence of Aging and Dynamical Scaling During Collapse of a Polymer* 29th Annual CSP Workshop *Recent Developments in Computer Simulation Studies in Condensed Matter Physics*, The University of Georgia, Athens, Georgia, USA, 25. February 2016

S. Majumder, W. Janke: *Aging and Dynamical Scaling During Collapse of a Polymer*, Soft-Matter Day, Universität Leipzig, Germany, 10. June 2016

S. Majumder, H. Christiansen, W. Janke: *Scaling Laws in Polymer Collapse: Lattice vs Off-Lattice*, 17th International NTZ-Workshop on *New Developments in Computational Physics – CompPhys16*, Universität Leipzig, Germany, 24. November 2016

M. Mueller, D.A. Johnston, W. Janke: *Exact Solutions to Plaquette Ising Models with Free and Periodic Boundaries*, 17th International NTZ-Workshop on *New Developments in Computational Physics – CompPhys16*, Universität Leipzig, Germany, 24. November 2016

P. Schierz, J. Zierenberg, W. Janke: *The Microcanonical Barrier and the Ensemble Tailoring Framework*, 17th International NTZ-Workshop on *New Developments in Computational Physics – CompPhys16*, Universität Leipzig, Germany, 25. November 2016

S. Schnabel, W. Janke: *Local Energy Minima of the 3d Edwards-Anderson Model*, 17th International NTZ-Workshop on *New Developments in Computational Physics – CompPhys16*, Universität Leipzig, Germany, 25. November 2016

J. Zierenberg, W. Janke: *Exploring Different Regimes in Finite-Size Scaling of the Droplet Condensation-Evaporation Transition*, 29th Annual CSP Workshop *Recent Developments in Computer Simulation Studies in Condensed Matter Physics*, The University of Georgia, Athens, Georgia, USA, 24. February 2016

J. Zierenberg, P. Schierz, W. Janke: *Finite-Size Scaling of Free-Energy Barrier in Droplet Formation and Nucleation-Like Processes*, DPG Frühjahrstagung, Regensburg, Germany, 09. March 2016

J. Zierenberg, P. Schierz, W. Janke: *Canonical Free-Energy Barrier of Particle and Polymer Cluster Formation*, 17th International NTZ-Workshop on *New Developments in Computational Physics – CompPhys16*, Universität Leipzig, Germany, 24. November 2016

Posters

H. Christiansen, S. Majumder, W. Janke: *Coarsening and Aging of Lattice Polymers*, 17th International NTZ-Workshop on *New Developments in Computational Physics – CompPhys16*, Universität Leipzig, Germany, 25. November 2016

N. Fricke, W. Janke: *Asymptotic Scaling Behavior of Self-Avoiding Walks on Critical Percolation Clusters*, 17th International NTZ-Workshop on *New Developments in Computational Physics – CompPhys16*, Universität Leipzig, Germany, 25. November 2016

J. Gross, J. Zierenberg, M. Weigel, W. Janke: *Parallel Multicanonical Simulations on GPUs*, Conference on *Phase Transitions and Critical Phenomena*, Coventry University, United Kingdom, 6.–8. April 2016

W. Janke, N. Fricke: *Asymptotic Scaling Behavior of Self-Avoiding Walks on Critical Percolation Clusters*, 26th IUPAP International Conference on *Statistical Physics – StatPhys26*, Lyon, France, 22.–28. July 2016

R. Kumar: *Approximate Ground States of the Random-Field Potts Model from a Graph-Cut Method and Parallel Tempering*, 17th International NTZ-Workshop on *New Developments in Computational Physics – CompPhys16*, Universität Leipzig, Germany, 25. November 2016

S. Majumder, W. Janke: *Evidence of Aging and Dynamical Scaling During Collapse of a Polymer*, Conference of the Middle European Cooperation in Statistical Physics – MECO41, Vienna, Austria, 15.-17. February 2016

M. Mueller, D.A. Johnston, W. Janke: *Planar ("Fuki-Nuke") Ordering and Finite-Size Effects for a Model with Four-Spin Interactions*, 26th IUPAP International Conference on *Statistical Physics – StatPhys26*, Lyon, France, 22.–28. July 2016

P. Schierz, J. Gross, W. Janke: *3D-Visualisierung von Polymeren – oder: Wie verkleben Spaghetti*, Lange Nacht der Wissenschaften, Universität Leipzig, Germany, 24. June 2016

J. Zierenberg, W. Janke: *From Amorphous Aggregates to Polymer Bundles: The Role of Stiffness on Structural Phases in Polymer Aggregation*, NIC Symposium, Forschungszentrum Jülich, Germany, 11.-12. February 2016

10.29 Graduations

Doctorate

- Niklas Fricke
  Polymers in Fractal Disorder
  28. April 2016

Master

- Benjamin Schott
  Aggregation of Lattice Polymers
  28. January 2016

- Jan Meischner
  Knotted Polymers
  17. March 2016

- Marius Bause
  Fisher-Zeros of Semiflexible Interacting Self-Avoiding Walk
  30. June 2016

- Henrik Christiansen
  Kinetics of the Collapse Transition in Lattice Polymers
  20. September 2016

Bachelor

- Katharina Tholen
  Metropolis-Simulationen von Polymeren bei externer Kraft
  04. May 2016

- Robert Wiesen
  Step-Size Dependence of Update Moves in Monte Carlo Simulations
  27. June 2016

- Lisa Fiedler
  (1+1)D Ising Ladder under Constraints
  05. July 2016

- Shane Carlson
  Persistence, Domain Growth, and Fractality in Quenched 2D Ising and Potts Spin Lattices
  15. October 2016

- Jan Philipp Hess
  Monte Carlo Simulation of the Surface Tension in the 2D Ising Model
  20. November 2016

10.30   Guests

- Dr. Peter Virnau
  Institut für Physik, Johannes Gutenberg-Universität Mainz, Germany
  Physik-Kolloquium (19. January 2016)
  Knots in Polymers, Proteins and DNA – A Tangled Challenge
  19.–20. January 2016

- Prof. Dr. Nerses Ananikyan
  Alikhanyan National Science Laboratory, Yerevan, Armenia
  NTZ/DFH-UFA and EU IRSES Network DIONICOS Colloquium (12. May 2016)
  Magnetization Plateau and Partition Function Zeros on a Diamond Chain: Spin-1/2 & 1 Ising-Heisenberg models
  17. April – 16. June 2016

- Prof. Dr. Ulrich H.E. Hansmann
  University of Oklahoma, Norman, USA
  Physik-Kolloquium (10. June 2016)
  Modeling Protein Aggregation
  09.–11. May 2016

- Prof. Dr. Subir K. Das
  Jawaharlal Nehru Centre for Advanced Scientific Research, Bangalore, India
  NTZ/DFH-UFA and EU IRSES Network DIONICOS Colloquium (06. July 2016)
  Continuously Varying Growth Exponent in Kinetics of Vapor-Solid Phase Transitions
  01.–07. July 2016

- Dr. Martin Weigel
  Applied Mathematics Research Centre, Coventry University, England, UK
  Physik-Kolloquium (25. October 2016)
  Fragmentation of Fractal Random Structures
  Joint NTZ-SFB/TRR 102 Colloquium (24. November 2016)
  Population Annealing: Massively Parallel Simulations in Statistical Physics
  01. August – 31. December 2016

- Dr. Lev Yu. Barash
  Landau Institute, Chernogolovka, Russia
  NTZ/DFH-UFA and EU IRSES Network DIONICOS Colloquium (27. October 2016)

Monte Carlo Calculations with the Population Annealing Algorithm and its Massively Parallel Realization
10.–30. October 2016

- Dr. Nikolay Izmailyan
  Yerevan Physics Institute, Armenia
  NTZ/DFH-UFA and EU IRSES Network DIONICOS Colloquium (17. November 2016)
  Ising Model on Plane: Numerical Solution
  15. October – 15. December 2016

- Liliia Ziganurova
  Landau Institute, Chernogolovka, and Higher School of Economics, Moscow, Russia
  17. October – 13. November 2016

- Prof. Dr. George Savvidy
  Demokritos Nat. Res. Center, Athens, Greece
  NTZ/DFH-UFA Colloquium (03. November 2016)
  The Gonihedric Ising Model
  01. November 2016 – 31. January 2017

- Dr. Nikolaos G. Fytas
  Coventry University, England, UK
  Phase Transitions in Disordered Systems: The Example of the Random-Field Ising Model in Four Dimensions
  22.–26. November 2016

- Prof. Dr. Hans Werner Diehl
  Univ. Duisburg-Essen, Germany
  Fluctuation-Induced Forces in Confined He and Bose Gases
  23.–25. November 2016

- Hamid Khoshbakht
  Applied Mathematics Research Centre, Coventry University, England, UK
  On the Uniform Sampling of Ground States in the 2D ±J Ising Spin-Glass Model
  23.–25. November 2016

- Dr. Francesco Parisen Toldin
  Universität Würzburg, Germany
  Critical Behavior in the Presence of an Order-Parameter Pinning Field
  23.–25. November 2016

- Dr. Hsiao-Ping Hsu
  MPI für Polymerforschung, Mainz, Germany
  Detailed Analysis of Rouse Mode and Dynamic Scattering Function of Highly Entangled Polymer Melts in Equilibrium
  23.–26. November 2016

- Prof. Dr. Nobuyasu Ito
  Univ. of Tokyo, Japan
  Joint NTZ-DFH/UFA Colloquium (25. November 2016)
  Social Simulation with Exascale Computer
  23.–26. November 2016

- Dr. Sebastian Kapfer
  FAU Erlangen, Germany
  Melting in 2D and a Fresh Perspective on Monte Carlo
  23.–26. November 2016

- Dr. Arnab Barua
  IIT Bombay, India
  23.–27. November 2016

- Pascal Fieth
  Universität Oldenburg, Germany
  Improving Causal Gaussian Bayesian Network Inference using Parallel Tempering
  23.–27. November 2016

- Prof. Dr. Ferenc Igloi
  Wigner Research Centre, Budapest, Hungary
  Random Quantum Systems with Long-Range Interactions
  23.–27. November 2016

- Dr. Benjamin Jäger
  ETH Zürich, Switzerland
  Towards the QCD Phase Diagram using Complex Langevin
  23.–27. November 2016

- Hendrik Schawe
  Universität Oldenburg, Germany
  Convex Hulls of Self-Avoiding Random Walks: A Large-Deviation Study
  23.–27. November 2016

- Dr. Arnulf Möbius
  IFW Dresden, Germany
  24.–25. November 2016

- Prof. Dr. Walter Selke
  RWTH Aachen, Germany
  24.–25. November 2016

- Dr. Elmar Bittner
  Universität Heidelberg, Germany
  24.–26. November 2016

11

Quantum Field Theory and Gravity

11.1 Introduction

The focus of investigation in the group of Quantum Field Theory and Gravity consists of three main strands: (1) Quantum field theory in curved spacetimes (Prof. Dr. R. Verch, Dr. T. P. Hack), (2) mathematical structure of gauge field theories and their quantization (Prof. Dr. G. Rudolph (retired), Dr. M. Schmidt) and (3) quantum fields under the influence of external conditions (PD Dr. M. Bordag).

In quantum field theory in curved spacetimes, several research fields are pursued, such as mathematical and conceptual foundations of local covariant quantum field theory and of the early epoch of cosmology, characterization of locally thermal states and their application to the Unruh effect, and in cosmology; and furthermore some aspects of quantum field theory on spacetimes that contain closed timelike curves. A sideline of this research is quantum field theory on non-commutative geometries. One of the aims is to gain a better understanding of essential ingredients for a potential theory of quantum gravity. In the research on gauge theories, one focus is on the topological structure of gauge orbit spaces. A complementary line of research is devoted to a better understanding of gauge field theories on lattices. In quantum field theory under the influence of external conditions, a central research field is the influence of boundaries, as in the Casimir effect, and singular potentials and their role in quantization. Some of the effects studied in this line of research have concrete applications in experiments.

Prof. Dr. Rainer Verch

11.2 Causal pathologies in quantum field theory

R. Verch, J. Tolksdorf[*]

[*]Max Planck Institute for Mathematics in the Sciences

Analogue models for states in the presence of closed timelike curves which are popular in quantum information theory are studied within quantum field theory together with J. Tolksdorf (Max Planck Institute for Mathematics in the Sciences).

[1] J. Tolksdorf and R. Verch: arXiv:1609.01496 [math-ph]

11.3 Thermal and non-equilibrium steady states in quantum field theory

R. Verch, D. Buchholz[*], C. J. Fewster[†], M. Gransee[‡], T.-P. Hack, N. Pinamonti[§]

[*]Universität Göttingen
[†]University of York
[‡]Max Planck Institute for Mathematics in the Sciences
[§]University of Genoa

A new description of local thermal equilibrium is being investigated together with M. Gransee and N. Pinamonti (University of Genova).

Fundamental aspects of the Unruh effect are studied together with D. Buchholz (Universität Göttingen) and C. J. Fewster (University of York).

Non-equilibrium steady states of the interacting scalar field in four spacetime dimensions are constructed and investigated.

[1] M. Gransee, N. Pinamonti and R. Verch: J. Geom. Phys. **117** (2017) 15, doi:10.1016/j.geomphys.2017.02.014
[2] D. Buchholz and R. Verch: Gen. Rel. Grav. **48** (2016) no.3, 32, doi:10.1007/s10714-016-2029-2

11.4 Quantum field theory and cosmology

R. Verch, R. Brunetti[*], K. Fredenhagen[†], M. B. Fröb[‡], T.-P. Hack, M. Hänsel, A. Higuchi[‡], N. Pinamonti[§], K. Rejzner[‡]

[*]University of Trento
[†]Universität Hamburg
[‡]University of York
[§]University of Genoa

Fundamental aspects of stability in cosmology (pertaining to solutions to the semiclassical Friedmann equations) are under investigation together with M. Hänsel.

An all-order perturbative description of the quantum theory of inflationary perturbations is developed together with R. Brunetti (University of Trento), K. Fredenhagen (Universität Hamburg), N. Pinamonti (University of Genova) and K. Rejzner (University of York) [1].

The localisation and infrared properties of observables in theory of inflationary perturbations are investigated together with M. Fröb (University of York) and A. Higuchi (University of York) [2].

[1] R. Brunetti, K. Fredenhagen, T.-P. Hack, N. Pinamonti and K. Rejzner: JHEP **1608** (2016) 032, doi:10.1007/JHEP08(2016)032
[2] M. B. Fröb, T.-P. Hack and A. Higuchi, arXiv:1703.01158 [gr-qc].

11.5 Structure of the gauge orbit space and study of gauge theoretical models

G. Rudolph, Sz. Charzynski[*], E. Fuchs, H. Grundling[†], J. Huebschmann[‡], P. Jarvis[§], J. Kijowski[*], M. Schmidt

[*]U Warsaw
[†]U Sydney
[‡]U Lille
[§]U Hobart

The investigation of gauge theories in the Hamiltonian approach on finite lattices with emphasis on the role of nongeneric strata was continued.

As a further step towards a generalization of the results of [1] on stratified Kähler quantization to larger lattices, the defining relations for lattice gauge models with gauge group SU(2) have been derived [2]. E. Fuchs worked on the formulation of stratified Kähler quantization in terms of coherent states.

Based on [3] and [4], in collaboration with H. Grundling, the investigation of the structure of the algebra of observables and its representations for specific models of quantum lattice gauge theory in terms of gauge invariant quantities was continued.

As a new project, investigation of the deformation quantization of classical lattice gauge theory was started in collaoration with Markus Pflaum (U Boulder).

[1] J. Huebschmann, G. Rudolph, M. Schmidt: Commun. Math. Phys. **286**, Nr. 2 (2009) 459–494

[2] F. Fürstenberg, G. Rudolph, M. Schmidt: Defining relations for the orbit type strata of SU(2)-lattice gauge models (submitted to J. Geom. Phys.).

[3] J. Kijowski, G. Rudolph: J. Math. Phys. **43** (2002) 1796–1808;
J. Kijowski, G. Rudolph: J. Math. Phys. **46** (2005) 032303; Rep. Math. Phys. **55** (2005) 199
P. Jarvis, J. Kijowski, G. Rudolph: J. Phys. A **38** (2005) 5359

[4] H. Grundling, G. Rudolph, Commun. Math. Phys. **318** (2013) 717–766 ; Commun. Math. Phys. **349** (2016) pp 1163–1202

11.6 Vacuum interaction between topological objects

M. Bordag

Boundary conditions play an important role in quantum field theory. On the one hand side they are generalizations of interactions which are concentrated on a region of higher co-dimensions. On the other hand, boundary conditions appear naturally when considering topological objects, for example boundary conditions can be found in some treatments of quantum field in black hole backgrounds, in the quantum Hall effect, in the physics of graphene etc. An interesting question appears about the vacuum quantum interaction of topological objects. As a first example in a larger project on this topic the vacuum interaction energy of two kinks was calculated. The results were

extended to the vacuum interaction of two cosmic strings. Here the problem appears, that the background changes the topology of the space-time, thus providing a long range interaction. As a consequence it is not clear a'priori whether the subtraction of the empty space contribution will be sufficient to remove the ultraviolet divergences. This question was investigated in detail by two methods, the heat kernel expansion and a mode sum calculation. Both confirm, after nontrivial compensation, the validity of the subtraction procedure.

11.7   Funding

Symplektische Reduktion im Unendlichdimensionalen mit Anwendung auf das Cauchy-Problem der Yang-Mills Gleichung
T. Diez
IMPRS fellowship, MPI-MIS

Local thermal equilibrium in quantum field theory
M. Gransee
IMPRS fellowship, MPI-MIS

Stability in cosmology
M. Hänsel
Universität Leipzig

Stability of black holes
F. Kurpicz
IMPRS fellowship, MPI-MIS

11.8   Organizational Duties

Prof. Dr. Rainer Verch
- Ansprechpartner, Forschungsprofilbereich "Mathematical and Computational Sciences", Universität Leipzig
- Berufungsbeauftragter des Rektorats
- Book Series Editor, Fundamental Theories of Physics (Springer)
- IMPRS Board Member
- Referee for the German Research Council (DFG) and the Alexander von Humboldt Foundation
- Referee: Ann. H. Poincaré, Commun. Math. Phys., Found. Phys., Class. Quantum Grav., J. Geom. Phys.

Prof. em. G. Rudolph
- Referee: Class. Quant. Grav., J. Math. Phys., J. Geom. Phys., J. Phys. A, Rep. Math. Phys., Commun. Math. Phys.
- Referee for the German Research Council (DFG) and the Alexander von Humboldt Foundation

Priv.-Doz. Dr. Michael Bordag

- Member of the Steering Committee of the ESF Research Networking Program *New Trends and Applications of the Casimir Effect (CASIMIR)*
- Referee: J. Phys. A, Phys. Rev. D, J. Math. Phys.

Dr. Matthias Schmidt

- Referee: J. Phys. A and Int. J. Mod. Phys. A

Dr. T.-P. Hack

- Referee for Alexander von Humboldt Foundation
- Referee: Ann. H. Poincaré, Class. Quantum Grav., Phys. Lett. B, Gen. Rel. Grav., Math. Rev. (AMS)

11.9   External Cooperations

Academic

- Mathematisches Institut, Universität Göttingen
  Prof. Dr. D. Bahns

- Dipartimento di Matematica, Universitá di Trento, Italy
  Prof. Dr. Romeo Brunetti

- Institut f. Theoretische Physik, Universität Göttingen
  Prof. Dr. D. Buchholz

- Department of Mathematics, University of York, England
  Prof. Dr. C. J. Fewster

- II. Institut f. Theoretische Physik, Universität Hamburg
  Prof. Dr. K. Fredenhagen

- Department of Mathematics, University of York, England
  Dr. M. B. Fröb

- Department of Mathematics, University of York, England
  Dr. A. Higuchi

- Department of Mathematics, University of York, England
  Dr. K. Rejzner

- Dipartimento di Matematica, Universitá di Genova, Italy
  Prof. Dr. N. Pinamonti

- Department of Mathematics, University of York, England
  Dr. K. Rejzner

- Max Planck Institute for Mathematics in the Sciences, Leipzig
  Dr. J. Tolkstorf

- University of Paderborn, Institute for Mathematics
  Prof. Dr. C. Fleischhack

- Polish Academy of Sciences, Center for Theoretical Physics, Warsaw
  Prof. Dr. J. Kijowski, Dr. Sz. Charzynski

- University of Boulder
  Prof. Dr. Markus Pflaum

- University of Tasmania, Hobart
  Prof. Dr. P. Jarvis

- Université des Sciences et Technologies de Lille
  Prof. Dr. J. Huebschmann

- University of New South Wales, Sydney
  Prof. H. Grundling

- National University, Dnepropetrovsk
  Prof. V. Skalozub

- Central Astronomical Observatory at Pulkovo of the Russian Academy of Science,
  Prof. V.M.Mostepanenko

- Baylor University, Texas
  Prof. K. Kirsten

- VIK Dubna
  Dr. V. Nesterenko, Dr. I. Pirozhenko

11.10   Publications

Journals

M. Bordag and I. G. Pirozhenko: *QED and surface plasmons on graphene*, Int. J. Mod. Phys. A **31** (2016) no.02n03, 1641027 doi:10.1142/S0217751X1641027X

M. Bordag, I. Fialkovskiy and D. Vassilevich: *Enhanced Casimir effect for doped graphene*, Phys. Rev. B **93** (2016) no.7, 075414, Erratum: [Phys. Rev. B **95** (2017) no.11, 119905] doi:10.1103/PhysRevB.93.075414, doi:10.1103/PhysRevB.95.119905

D. Buchholz and R. Verch: *Unruh versus Tolman: On the heat of acceleration*, Gen. Rel. Grav. **48** (2016) no.3, 32, doi:10.1007/s10714-016-2029-2

R. Brunetti, K. Fredenhagen, T.-P. Hack, N. Pinamonti and K. Rejzner: *Cosmological perturbation theory and quantum gravity*, JHEP **1608** (2016) 032, doi:10.1007/JHEP08(2016)032

A. Géré, T. P. Hack and N. Pinamonti: *An analytic regularisation scheme on curved space-times with applications to cosmological space-times*, Class. Quant. Grav. **33** (2016) no.9, 095009, doi:10.1088/0264-9381/33/9/095009

H. Grundling, G. Rudolph: *Dynamics for QCD on an Infinite Lattice*, Commun. Math. Phys. **349** (2016) 1163–1202

T.-P. Hack, F. Hanisch and A. Schenkel: *Supergeometry in locally covariant quantum field theory*, Commun. Math. Phys. **342** (2016) no.2, 615 doi:10.1007/s00220-015-2516-4

Verch, R.: *Wave equation with non-commutative space and time*, in: Finster, F. et al. (eds), 'Quantum Mathematical Physics', Birkhäuser, Basel, 2016

in press

N. Drago, T. P. Hack and N. Pinamonti: *The generalised principle of perturbative agreement and the thermal mass,* Annales Henri Poincare **18** (2017) no.3, 807, doi:10.1007/s00023-016-0521-6

M. Gransee, N. Pinamonti and R. Verch: *KMS-like Properties of Local Equilibrium States in Quantum Field Theory,* J. Geom. Phys. **117** (2017) 15, doi:10.1016/j.geomphys.2017.02.014

G. Rudolph, M. Schmidt: *Differential Geometry and Mathematical Physics. Part II. Fibre Bundles, Topology and Gauge Fields,* Springer Series in Theoretical and Mathematical Physics, 2017, p840

preprints

J. Tolksdorf and R. Verch: *Quantum physics, fields and closed timelike curves: The D-CTC condition in quantum field theory,* arXiv:1609.01496 [math-ph]

Talks

Prof. Dr. R. Verch: *Semiclassical Einstein Equation,* invited main talk, DPG-meeting Hamburg (29.02.2016)

Prof. Dr. R. Verch: *Unruh Effect and Tolman Temperature,* invited main talk, DPG-meeting Hamburg (01.03.2016)

Prof. Dr. R. Verch: *Unruh Effect and Tolman Temperature,* invited colloquium talk in the honor of K.-E. Hellwig, TU Berlin (29.04.2016)

Prof. Dr. R. Verch: *Unruh Effect and Tolman Temperature,* invited seminar talk, Dep. of Mathematics, University of York (06.10.2016)

Prof. Dr. R. Verch: invited research visit, Workshop "Recent Mathematical Developments in Quantum Field Theory", Mathematisches Forschungsinstitut Oberwolfach (24.-30.07.2016)

Prof. Dr. R. Verch: invited research visit, Dep. of Mathematics, University of York (02.10-07.10.2016)

Dr. T.-P. Hack: *Cosmological perturbation theory and perturbative quantum gravity,* invited talk, Workshop "Recent Mathematical Developments in Quantum Field Theory", Mathematisches Forschungsinstitut Oberwolfach (29 July 2016)

Dr. T.-P. Hack: *Cosmological perturbation theory and quantum gravity,* invited talk, GRK 1692 Colloquium, Universität Regensburg (14 July 2016)

Dr. T.-P. Hack: *Cosmological perturbation theory and quantum gravity,* Seminar on QFT, Gravity and Theoretical Particle Physics, Universität Leipzig (13 June 2016)

Dr. T.-P. Hack: *An analytic regularisation scheme on curved spacetimes,* Seminar on QFT, Gravity and Theoretical Particle Physics, Universität Leipzig (11 January 2016)

T. Diez: *Momentum maps for diffeomorphism and gauge groups*, Workshop Geometry and PDEs, Timisoara, (11.06.2016)

T. Diez: *Singular symplectic reduction in infinite dimensions using the Nash-Moser theorem*, (4 talks, invited by Tudor Ratiu), Jiao Tong University Shanghai, (10.2016)

T. Diez: *Singular symplectic reduction in infinite dimensions using the Nash-Moser theorem*, (invited by Bas Janssens and Marius Crainic), Seminar Geometry and Algebra + Geometry and Analysis, Utrecht University, (06.12.2016)

11.11   Graduations

Master

- Sophia Helmrich
  The non-relativistic limit of the quantized Klein-Gordon field
  09.02.2016

Bachelor

- Moritz Thurmair
  Gravitative Zeitdilatation in der Umgebung statischer, ungeladener schwarzer Löscher
  20.04.2016

- Alexander Schulze-Makuch
  No-Cloning Theorem in the presence of closed timelike curves
  27.09.2017

11.12   Guests

- Prof. Dr. Markus Pflaum
  U Boulder
  November 21–25, 2016

12

Statistical Physics

12.1 Introduction

The focus of research in the STP group is on low-dimensional and mesoscopic inter-acting systems. These systems are fascinating because on the one hand they allow to study fundamental questions of quantum statistical mechanics, and on the other hand they have a great potential for technological applications. The interplay of a reduced dimensionality with enchanced interaction effects, non-equilibrium physics, and possibly disorder allows the observation of many interesting phenomena, which pose a stimulating challenge for theoretical analysis. The mathematical language used for the description of these systems is quantum field theory, including techniques like functional integrals, renormalization group, instanton calculus, the Keldysh technique for non-equilibrium situations, and the replica method for disordered systems. These analytical tools are suplemented by the use of computer algebra (Mathematica) and numerical calculations (Matlab, Perl, C++). We try to combine the analysis of theoret-ically interesting problems with relevance to experiments on nanostructures.

Fractional quantum hall (QH) systems display perhaps the richest and most beautiful physics of all condensed matter systems. They are a prime example for the idea that the whole is more than the sum of its parts, as low lying excitations of a fractional QH fluid carry only a faction of the electron charge and are thus qualitatively different from the system constituents. Recently, interest in fractional QH physics has been reinvigorated by the prospect that quasiparticles (QPs) of the fractional QH state at filling fraction 5/2 may be non-abelian anyons, i.e. their braiding may not only give rise to a multiplication of the wave function with a complex phase, but in addition corresponds to a unitary transformation of the highly degenerate ground state. Due to the topological nature of braiding, these unitary transformations are robust against local perturbations and guarantee a high degree of stability of the quantum weave of braids, lending it to the construction of topological quantum bits. Future research in this field will concentrate on both the analysis of qualitative properties of topologically ordered systems and the description of experimentally relevant consequences in nanostructured systems.

Similarly to the edge states of QH systems, in single channel nanowires interactions strongly modify the dynamics of electrons. In the presence of strong spin-orbit coupling and in proximity to a superconductor, nanowires can support a topologically ordered state suitable for the formation of topological quantum bits. In multimode nanowires, a quantum phase transition between superconductor and diffusive metal can occur,

which is tuned by an external magnetic field and is experimentally realized in niobium and molybdenum-germanium systems. Comparatively small changes in the external magnetic field can give rise to a large change in conductivity. Quantum mechanical fluctuations of the superconducting phase can restore part of the density of states, which is reduced due to scattering of electrons off the superconducting order parameter.

B. Rosenow

12.2   Current Correlations from a Mesoscopic Anyon Collider

B. Rosenow, I.P. Levkivskyi[*], B.I. Halperin[†]

[*]Theoretische Physik, ETH Zurich, CH-8093 Zurich, Switzerland

[†]Physics Department, Harvard University, Cambridge, Massachusetts 02138, USA

One of the important differences between fermions and bosons is the difference in the probability of two identical particles being close to each other, which is associated with their exchange statistics. These differences are manifest in various ways, including Hanbury Brown-Twiss interference experiments. It is tempting to see whether any of these distinctions can be carried over to particles with fractional statistics such as appear in the fractional quantum Hall (FQH) effect

A possible realization of an anyonic two-particle interferometer was suggested by Campagnano et al. There, it was found that correlations exhibit partial bunching similar to bosons, but there also exist qualitative differences between the anyonic signal and the corresponding bosonic or fermionic signals. Here, we are proposing and analyzing a somewhat simpler experiment which does not depend on interference loops or phase coherence. We consider specifically the anyons which occur at the clean chiral edge of a quantized Hall state. We discuss explicitly only the single edge mode case but discuss the generalization to multi-mode cases qualitatively. In the setup Fig. 12.1, two dilute beams of anyons are produced on the upper and lower edge, which are eventually connected by a quantum point contact (QPC). We are considering current correlations on the two edges downstream from the QPC, and study cross-correlations at low frequencies, low temperatures and low voltages, such that the details of interactions at short distances are not important for the final results. For non-interacting fermions as occurring on the edge of the IQH effect, we find that cross-correlations are absent at zero net bias between the two edges, whereas for anyons we find finite cross-correlations. One may attempt to characterize these results as a measure of exclusion statistics. The results for the cross-correlations are related to the power laws governing the long time decay of the correlation functions on the edge, which due to conformal invariance are related to the spactial dependence which reflects the braiding statistics of anyons in the bulk.

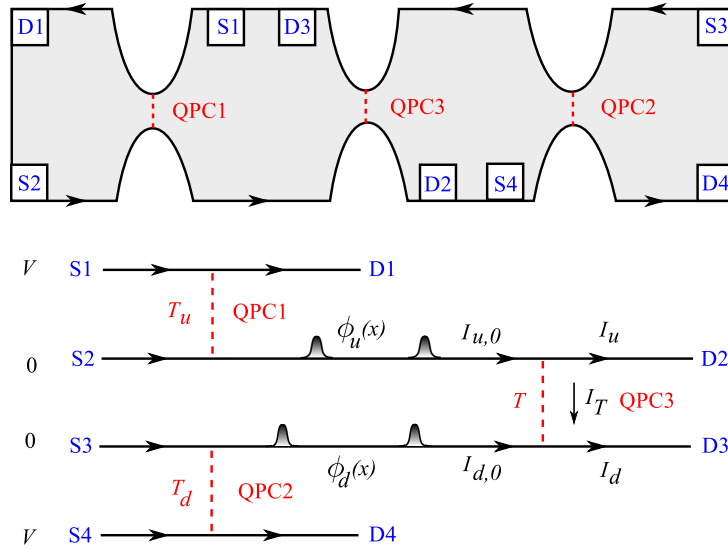[1] Bernd Rosenow, Ivan P. Levkivskyi, and Bertrand I. Halperin, Phys. Rev. Lett. **116**, 156802 (2016).

Figure 12.1: Sketch of the anyon collider, with Hall bar geometry in the upper panel and idealized geometry in the lower panel. Dilute quasi-particle beams are generate at QPC1 and QPC2, propagate along upper (u) and lower (d) edge, and collide at QPC3. Sources S1 and S4 are at voltage V, sources S2 and S3 are grounded

12.3   Non-local polarization feedback in a fractional quantum Hall ferromagnet

S. Hennel[*], B.A. Braem[*], S. Baer[*], L. Tiemann[*], P. Sohi[*], D. Wehrli[*], A. Hofmann[*], C. Reichl[*], W. Wegscheider[*], C. Rössler[*], T. Ihn[*], K. Ensslin[*], M.S. Rudner[†], B. Rosenow

[*]Solid State Physics Laboratory, ETH Zürich, 8093 Zürich, Switzerland
[†]Niels Bohr International Academy and Center for Quantum Devices, Niels Bohr Institute, University of Copenhagen, 2100 Copenhagen, Denmark

In a wide variety of low-dimensional electronic systems, the electron spin degrees of freedom are coupled to a bath of nuclear spins residing in the atomic cores of the host lattice. If the electronic system is driven out of equilibrium, this coupling may cause the nuclear spins to become *dynamically polarized,* in turn feeding back to locally affect the electronic state. In the simplest case, the result is decoherence or depolarization of the electronic spin state. More interestingly, complex dynamical phenomena arising from local feedback effects have also been reported Here we report an electronic–nuclear feedback mechanism that is *non-local* in nature: the spatial regions where polarization is created and those where the polarization rates are controlled are spatially separated, with feedback between these processes mediated through nuclear spin diffusion. In our experiments, we use a quantum point contact to locally control and probe the domain structure of different spin configurations emerging at the spin phase transition. Feedback between nuclear and electronic degrees of freedom gives rise to memristive behavior, where electronic transport through the quantum point contact depends on the history of current flow. We propose a model for this effect which suggests a novel route to studying edge states in fractional quantum Hall systems and may account for so-far unexplained oscillatory electronic-transport features observed

in previous studies. The model we propose relates the propagation direction of spin modes to spatial regions where spin is accumulated, suggesting novel possibilities for the study of edge reconstruction in FQH states that can undergo a spin-phase transition. More importantly perhaps, our work constitutes a first step towards a description of dynamic nuclear polarization (DNP) at the microscopic scale and may have important implications for resistively detected NMR, a method which is poorly understood and yet widely used in the study of coupled electron-nuclear spin systems.
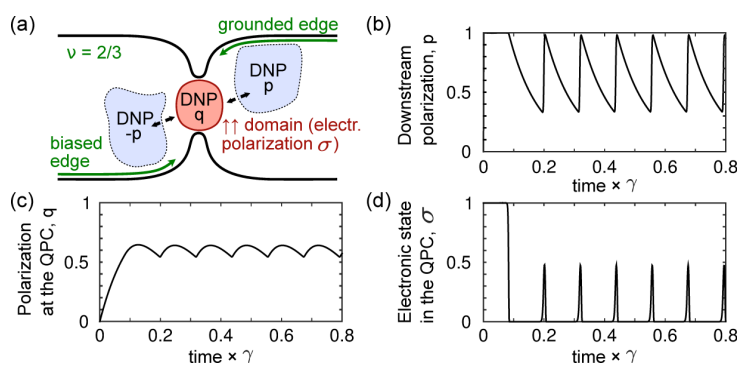
Figure 12.2: Model for self-oscillations driven by DNP. **(a)** A spin-polarized electron domain resides in the constriction, with degree of polarization σ, resulting in different transmissions for quasiparticles with up and down spins. Spin filtering leads to spin accumulation outside the constriction region, which is transferred to nuclei with polarization p and $-p$. Through nuclear spin diffusion, DNP (q) builds up in the constriction, destabilizing the polarized domain. When the domain shrinks the spin filtering effect stops; after the DNP diffuses away the domain reforms and oscillations result. **(b) to (d)** Time-dependent oscillations produced by the model system.

[1] Szymon Hennel, Beat A. Braem, Stephan Baer, Lars Tiemann, Pirouz Sohi, Dominik Wehrli, Andrea Hofmann, Christian Reichl, Werner Wegscheider, Clemens Rössler, Thomas Ihn, Klaus Ensslin, Mark S. Rudner, and Bernd Rosenow, Phys. Rev. Lett. **116**, 136804 (2016).

12.4   Cavity polariton condensate in a disordered environment

M. Thunert[*], A. Janot, H. Franke[*], C. Sturm[*], T. Michalsky[*], M.D. Martín[†], L. Viña[†], B. Rosenow, M. Grundmann[*], R. Schmidt-Grund[*]

[*]Institut für Experimentelle Physik II, Universität Leipzig, 04103 Leipzig, Germany
[†]Departamento de Física de Materiales, Universidad Autónoma de Madrid, Madrid 28049, Spain

The observation of a macroscopically coherent quantum state of exciton-polaritons, a so-called polariton Bose-Einstein condensate (BEC),has opened an active and challenging research field. Exciton-polaritons (for brevity polaritons) are mixed light-matter excitations in a microcavity (MC).At finite quasi-particle density, several fascinating

phenomena like superfluidity and the formation of quantum vortices, were discovered. This allows for numerous novel applications which are usually restricted to low temperatures. However, polariton BECs even at room-temperature were observed in MCs based on wide band gap materials like GaN and ZnOor organic materials, paving the way for technological applications. At the moment, experiments in these materials are significantly affected by disorder, and a thorough understanding of the impact disorder has on experimental observables in a polariton BEC is called for. In contrast to conventional BECs, occurring for example in cold atom systems, polaritons have a finite lifetime, which gives rise to unique properties of the condensate. Nonetheless, there remain similarities, for instance, in the absence of disorder quasi-long range order of a two-dimensional polariton condensate and superfluidity is theoretically expected and experimentally observed. However, recent theoretical studies have revealed exciting differences between equilibrium and non-equilibrium condensates [1]For example, it is predicted that correlation functions for the condensate wave function decay exponentially and that superfluidity vanishes in the presence of disorder. [1] We report on the influence of disorder on an exciton-polariton condensate in a ZnO based bulk planar microcavity and compare experimental results with a theoretical model for a non-equilibrium condensate. Experimentally, we detect intensity fluctuations within the far-field emission pattern even at high condensate densities which indicates a significant impact of disorder. We show that these effects rely on the driven dissipative nature of the condensate and argue that they can be accounted for by spatial phase inhomogeneities induced by disorder, which occur even for increasing condensate densities realized in the regime of high excitation power. Thus, non-equilibrium effects strongly suppress the stabilization of the condensate against disorder, contrarily to what is expected for equilibrium condensates in the high density limit. Numerical simulations based on our theoretical model reproduce the experimental data.

[1] A. Janot, T. Hyart, P. R. Eastham, and B. Rosenow, Phys. Rev. Lett. **111**, 230403 (2013).
[2] M. Thunert, A. Janot, H. Franke, C. Sturm, T. Michalsky, M. Martin, L. Vina, B. Rosenow, M. Grundmann, R. Schmidt-Grund, Phys. Rev. B **93**, 064203 (2016).

12.5 Topological Polaritons in a Quantum Spin Hall Cavity

A. Janot, B. Rosenow, G. Refael[*]

[*]Institute of Quantum Information and Matter, Department of Physics, California Institute of Technology, Pasadena, CA 91125, USA

Recently, topologically nontrivial states of matter with protected edge or surface states have attracted much attention While the first realizations were found in electronic systems, topologically nontrivial phases of periodically driven systems and photons have been discovered within the last years. A time reversal (TR) invariant topological phase can exist when a band inversion occurs, as a function of momentum, between orbital states with different parity, and when these orbital states are coupled by spin-orbit interaction.
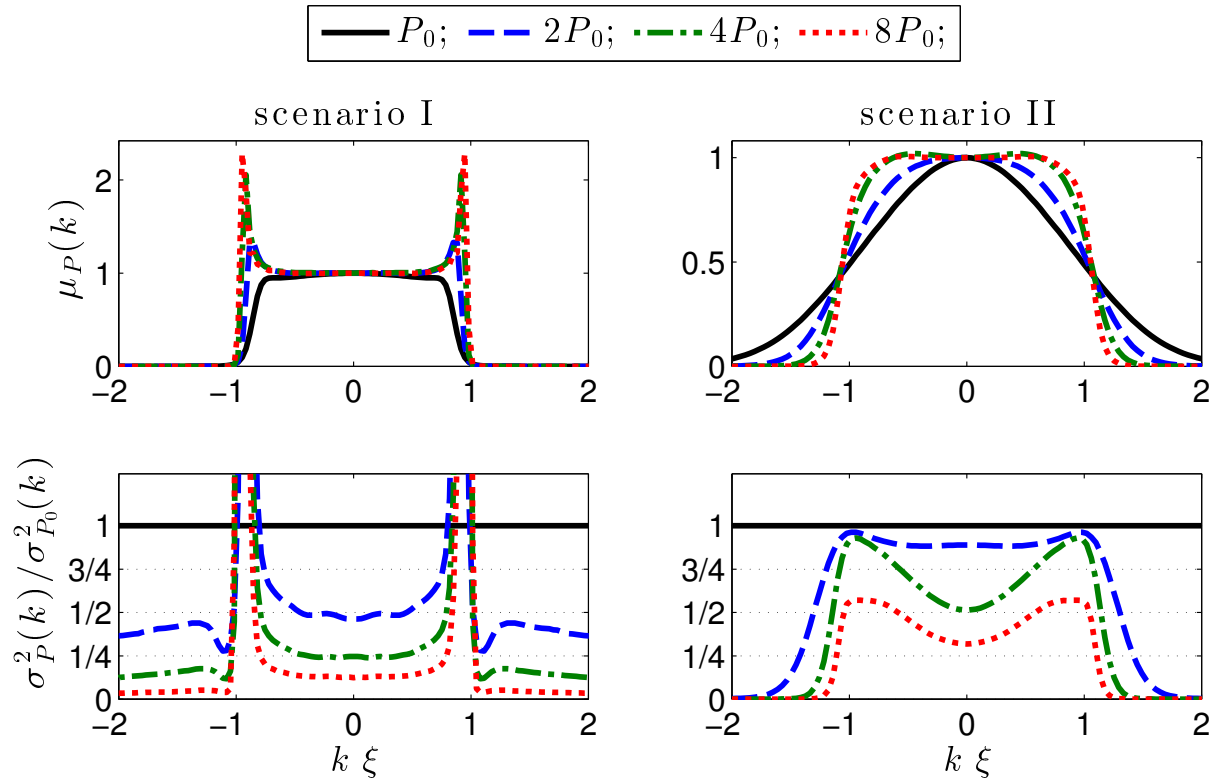
Figure 12.3: Expectation value μ_P (upper row) and variance σ_P^2 (lower row) of the (normalized) intensity distribution $I_P(k)$. In order to compare the fluctuations for increasing excitation powers we present the ratio $\sigma_P^2(k)/\sigma_{P_0}^2(k)$ with $P_0 = 4P_{th}$ with P_{th} the threshold power for condensation. The left and right column depict a quasi-equilibrium (scenario I) and a driven dissipative (scenario II) condensate, respectively. For wavevectors $|k\xi| \lesssim 1$, scenario I shows a linear reduction of fluctuations with inverse excitation power, $\sigma_P^2(k) \propto 1/P$, while scenario II exhibits a suppressed stabilization with increasing excitation power. We averaged 1560 disorder realizations.

In electronic systems, the time reversal operator squares to minus one, $T^2 = -1$, implying the existence of degenerate Kramers pairs, such that the crossing of topological edge states is protected. In contrast, for bosonic systems with $T^2 = +1$, in general there is no TR invariant topologically nontrivial phase. The photonic topological insulators either break TR or have a built-in degeneracy, which protects edge states in a way similar to the Kramer's degeneracy in fermionic systems.

We consider strongly coupled light-matter systems in two-dimensions, so-called polaritons, in which the bosonic polariton can inherit its topological properties from the electronic part. Building on such an example, realized by quantum spin Hall (QSH) electrons coupled to cavity photons, we develop a framework which allows to characterize topological states of polaritons. In contrast to recent proposals of topological polaritons Here, we go considerably beyond previous works and i) define a topological invariant for TR symmetric bosonic systems, ii) explain that contrary to a topologically non-trivial phase is possible due to a vortex-like singularity in the exciton-photon coupling, and iii) describe how TR-invariant topological polaritons can be detected experimentally by looking for dark excitonic states and edge states, and by studying the polarization in the presence of an external Zeeman field.
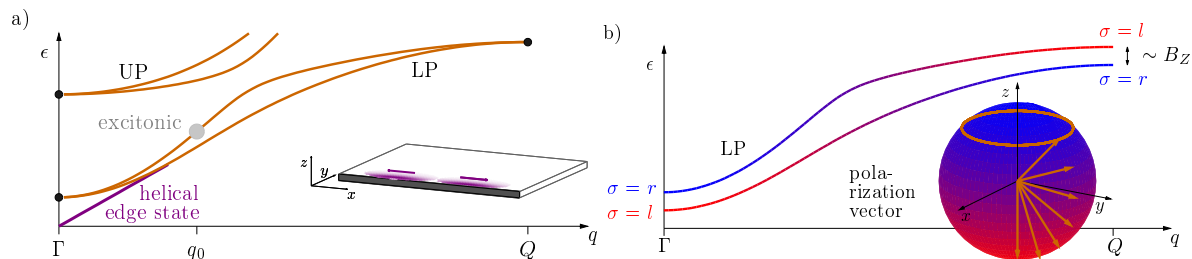
Figure 12.4: Defining properties of a topologically nontrivial polariton: a) the lower (LP) and upper polariton (UP) branches (orange lines) are split by spin-orbit coupling, except at TR invariant momenta (Γ, Q) (thick black dots). For topological polaritons purely excitonic states (gray dot) emerge along a line $\vec{q} = \vec{q}_0$, and helical edge states (thick purple line) are present below the LP. b) with a TR breaking Zeeman field $B_Z \neq 0$, the polarization vector $\vec{n}$ of each LP-dispersion branch can be tracked over the whole Brillouin zone. The polariton is topologically nontrivial if $\vec{n}$ covers the entire Bloch sphere (inset). Here, the north (south) pole (blue (red) color) stands for right (left) circular polarization, while the x-y plane represents linearly polarized light.

[1] A. Janot, B. Rosenow, G. Refael, Phys. Rev. B **93**, 161111(R) (2016).

12.6 Thermodynamic properties of a quantum hall anti-dot interferometer

S.L. Schreier[*], A. Stern[*], B. Rosenow, B.I. Halperin[†]

[*]Department of Condensed Matter Physics, Weizmann Institute of Science, Rehovot, Israel 76100

[†]Department of Physics, Harvard University, Cambridge, Massachusetts 02138, USA

Early after the discovery of the fractional quantum Hall states it was realized that the charged excitations that characterize these states carry fractional charge and satisfy fractional statistics, abelian or non-abelian. Abelian fractional statistics is manifested in the phase accumulated by one quasi-particle going around another. The natural arena for an experimental observation of such a phase is that of interferometry. Consequently, large experimental and theoretical effort has been devoted to the study of quantum Hall interferometers of various types, such as the Fabry-Perot and the Mach-Zehnder interferometers. In these interferometers, current is introduced from a source and is distributed between two drains. The relative distribution between the drains involves interference between trajectories that go around an interference loop. Here, we study quantum Hall interferometers in which the interference loop encircles a quantum anti-dot. We base our study on thermodynamic considerations, which we believe reflect the essential aspects of interference transport phenomena. We find that similar to the more conventional Fabry-Perot quantum Hall interferometers, in which the interference loop forms a quantum dot, the anti-dot interferometer is affected by the electro-static Coulomb interaction between the edge modes defining the loop. We show that in the Aharonov-Bohm regime, in which effects of fractional statistics should be visible, is easier to access in interferometers based on anti-dots than in those based

on dots. We discuss the relevance of our results to recent measurements on anti-dots interferometers.
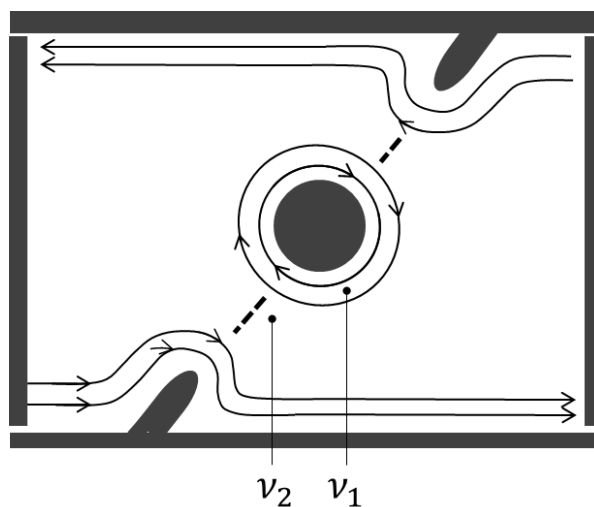
Figure 12.5: Schematic layouts of the edge states through anti-dot based devices. The partially transmitted edge channel separates two quantized Hall states corresponding to rational filling factors ν_1 and ν_2, with ν_1 being closer to the island. The weak back scattering limit where the filling factor is given by ν_2 is shown.

[1] Sarah Levy Schreier, Ady Stern, Bernd Rosenow, and Bertrand I. Halperin, Physica E **76**, 82 (2016).

12.7   Backscattering in helical edge states from a magnetic impurity and Rashba disorder

L. Kimme, B. Rosenow, A. Brataas[*]

[*]Department of Physics, Norwegian University of Science and Technology, NO-7491 Trondheim, Norway

Soon after the theoretical prediction, the quantum spin Hall effect (QSHE) was realized in HgTe/CdTe quantum wells, and the quantized conductance as well as the demonstration of nonlocal transport were crucial signatures for this first-time experimental observation. However, already in this first as well as in subsequent experiments, deviations from the quantized conductance with a weak temperature dependence were found for edges longer than approximately $1\,\mu$m. Moreover, in short samples, where the conductance is essentially quantized, small conductance fluctuations are observed as the back-gate voltage is tuned. After the prediction of the QSHE in InAs/GaSb/AlSb quantum wells, the same qualitative behavior of the conductance as in HgTe/CdTe was observed also in these devices

A multitude of other mechanisms beyond elastic single particle backscattering have been proposed as possible explanations for the relatively short mean free pathAlthough

these mechanisms are very diverse, many of them have in common a pronounced temperature dependence, usually some power law T^α with positive exponent α for the resistance. However, only a weak temperature dependence has been observed experimentally, with the exception of a recent study using very low excitation currents.. In fact, in some experiments, a slight increase of the resistance is observed when the temperature is decreased. In this work, we consider scattering of helical edge electrons from a magnetic impurity with spin $S \geq 1/2$ in combination with a spatially fluctuating Rashba spin-orbit coupling. The latter originates from a fluctuating electric field in the out-of-plane direction due to disorder in the doping layers From a T-matrix calculation accounting for the combined scattering events off these perturbations, we derive an effective additional coupling to the impurity. This coupling provides a backscattering mechanism which is enhanced by an increased polarization of the impurity with spin $S > 1/2$. The polarization of the impurity spin is determined from the steady state solution to a semiclassical scattering rate equation. We consider the linear and the nonlinear regime. Upon entering the nonlinear regime with the source drain voltage larger than temperature, the impurity gets polarized and the Rashba disorder induced effective coupling leads to an increased resistance, thus providing a possible explanation for the experimental results. We assume that the relevant Kondo temperature is exponentially suppressed and well below the temperature regime studied in our analysis. Since the dominant contribution to backscattering is elastic in our model, quantum interference between different scatterers is possible, and can give rise to conductance fluctuations.
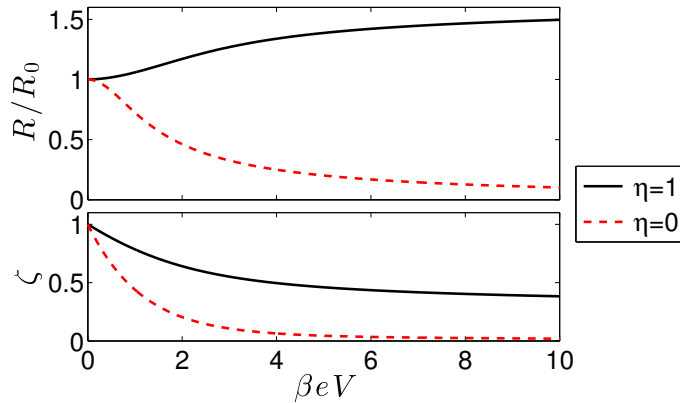
Figure 12.6: Normalized impurity induced backscattering probability R/R_0 and impurity polarization ζ as function of the ratio of transport voltage and temperature $\beta e V$. R_0 is enhanced by two orders of magnitude as the dimensionless strength of Rashba disorder η is increased from 0 to 1.

[1] Lukas Kimme, Bernd Rosenow, Arne Brataas, Phys. Rev. B **93**, 081301(R) (2016).

12.8 Existence of zero-energy impurity states in different classes of topological insulators and superconductors and their relation to topological phase transitions

L. Kimme, T. Hyart[*]

[*]Department of Physics and Nanoscience Center, P.O. Box 35 (YFL), FI-40014 University of Jyväskylä, Finland

Ever since the concept of topological order in condensed matter systems picked up momentum during the last decade, there has been the question as to which kind of perturbations can cause topological phase transitions. We study inhomogeneous perturbations which are often naturally present in candidate materials. We start by identifying the general conditions under which the eigenenergies of an arbitrary Hamiltonian H belonging to one of the Altland-Zirnbauer symmetry classes undergo a robust zero energy crossing as a function of an external parameter which can be, for example, the impurity strength. We define a generalized root of $\det H$, and use it to predict or rule out robust zero-energy crossings in all symmetry classes. We complement this result with an analysis based on almost degenerate perturbation theory, which allows a derivation of the asymptotic low-energy behavior of the ensemble averaged density of states $\rho \sim E^\alpha$ for all symmetry classes, and makes it transparent that the exponent α does not depend on the choice of the random matrix ensemble. Finally, we show that a lattice of impurities can drive a topologically trivial system into a nontrivial phase, and in particular we demonstrate that impurity bands carrying extremely large Chern numbers can appear in different symmetry classes of two-dimensional topological insulators and superconductors. We use the generalized root of $\det H(\vec{k})$ to reveal a spiderweblike momentum space structure of the energy gap closings that separate the topologically distinct phases in $p_x + ip_y$ superconductors in the presence of an impurity lattice.
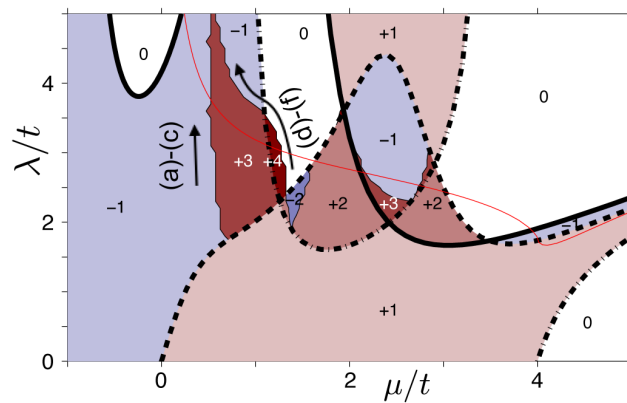
Figure 12.7: Phase diagram of the $p_x + ip_y$ superconductor in the presence of an impurity lattice as a function of impurity strength λ and chemical potential μ for $\Delta = 0.5\,t$ and $a = 3$. Thick lines are gap closings at the high symmetry points [solid: $(0,0)$, dashed: $(0,\pi)$ and $(\pi,0)$, dash-dot: (π,π)]. At thin lines, the gap closes away from the high-symmetry points. Numbers denote the sum of Chern numbers of occupied bands in the respective phase. The thin red line is λ_c^∞. The gap closes in the momentum space at the lines (a)-(c) and (d)-(f).

[1] Lukas Kimme, Timo Hyart, Phys. Rev. B **93**, 035134 (2016)

12.9 Topological superconductivity in Quantum Hall–superconductor hybrid systems

B. Zocher, B. Rosenow

Non-abelian anyons are zero-energy quasiparticles whose ground-state wave function is rotated in the space of degenerate ground states under particle exchange. Searching for non-abelian anyons, is motivated both by possible applications to fault-tolerant quantum computation, and by the pursuit of exotic fundamental physics. Recently, there has been much interest in Majorana fermions (MFs), which are a prime example for non-abelian anyons. MFs are their own antiparticles, and a pair of MFs can encode a fermionic two-level system in a nonlocal way.

The first system which was proposed to realize MFs is the fractional quantum Hall (QH) state at filling fraction $\nu = 5/2$. Recently, the superconducting proximity effect has been suggested as a way to effectively induce p-wave pairing in semiconductors with strong spin-orbit coupling, and a series of experimental works presented first evidence for MFs in such heterostructures. However, despite the effort which has been invested, unambiguous experimental signatures of the unconventional nature of MFs are still missing.

Here, we develop an alternative scenario to engineer a topological superconductor (SC) whose zero-energy quasiparticles are MFs. In contrast to previous proposals, we consider the strong magnetic field limit where a $\nu = 1$ integer QH system is proximity coupled to an s-wave SC via a spin sensitive barrier. Due to the spin sensitivity of the barrier, an effective p-wave pairing potential is induced in the spin-polarized lowest Landau level (LLL). In the presence of an external magnetic field necessary to reach the QH regime, the superconducting pairing potential has a triangular Abrikosov vortex lattice imprinted, with a flux of $h/2e$ per vortex. In the LLL, there is one electronic state per flux quantum h/e threading the system, such that there are two superconducting vortices per electronic state. This lattice system can be described by a pair of commuting generalized translation operators $\mathcal{T}_x$ and $\mathcal{T}_y$ which define a Bloch problem with generalized momenta $\mathbf{k} = (k_x, k_y)$, despite the absence of translational invariance of the Hamiltonian for electrons in a magnetic field

The superconducting pairing couples momenta $\mathbf{k}$ and $-\mathbf{k}$ with an amplitude $\Delta_\mathbf{k}$, similar to the situation without magnetic field. Interestingly, there are ten unpaired momenta in the Brillouin zone, since $\Delta_\mathbf{k}$ is represented as $\Delta_\mathbf{k} \sim \partial_x \Delta(\mathbf{r} = l_B^2 \mathbf{k} \times \hat{z})$, with $\Delta(\mathbf{r})$ denoting an s-wave superconducting pair potential with an imprinted Abrikosov vortex lattice (see Fig. 12.8(a)). The unpaired momenta arise due to the four maxima and six saddle points of $|\Delta(\mathbf{r})|$. The zeroes of $\Delta(\mathbf{r})$ all have a finite slope since superconducting vortices correspond to simple zeroes, and hence do not give rise to unpaired momenta. As illustrated in Fig. 12.8(b), the first Brillouin zone can be decomposed into two hexagons, each associated with one vortex of the unit cell. Drawing an analogy between one such hexagon and the Brillouin zone of the honeycomb lattice in graphene, the three unpaired momenta originating from the saddle points correspond to the M points, and

the remaining two correspond to the K and K' points. Due to the vortex lattice in the presence of a strong magnetic field, the hybrid system is characterized by ten unpaired generalized momenta, which have degeneracies such that always an even number of them crosses the Fermi level, implying that the hybrid system always stays in a trivial phase. Adding a periodic potential with Fourier components connecting some of the unpaired momenta, one can lift the degeneracies in such a way that the system is driven into a topologically nontrivial superconducting phase.
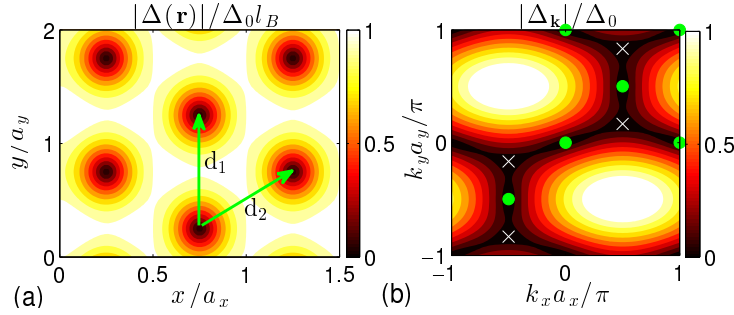
Figure 12.8: (a) Real space structure of the s-wave pairing potential $\Delta(\mathbf{r})$ with triangular vortex lattice in the LLL approximation. The arrows denote the lattice vectors $\mathbf{d}_1 = a_y \mathbf{e}_y$ and $\mathbf{d}_2 = (a_x \mathbf{e}_x + a_y \mathbf{e}_y)/2$. (b) Brillouin zone of the rectangular unit cell comprising two vortices, and induced p-wave pairing potential $\Delta_\mathbf{k} \sim \partial_x \Delta(\mathbf{r} = l_B^2 \mathbf{k} \times \hat{z})$. Markers denote the unpaired momenta, which correspond to the M points (dots) and the K, K' points (crosses) of the hexagonal Brillouin zone of the vortex lattice. By pairwise coupling the M points, the system can by driven into a topologically nontrivial phase.

[1] Björn Zocher and Bernd Rosenow, Topological superconductivity in Quantum Hall-superconductor hybrid systems, Phys. Rev. B **93**, 214504 (2016).

12.10 Enhancing triplet superconductivity by the proximity to a singlet superconductor in oxide heterostructures

M. Horsdal[*], G. Khaliullin[†], T. Hyart[‡], B. Rosenow

[*]Department of Physics, University of Oslo, P. O. Box 1048 Blindern, N-0316 Oslo, Norway
[†]Max Planck Institute for Solid State Research, Heisenbergstrasse 1, D-70569 Stuttgart, Germany
[‡]Department of Physics and Nanoscience Center, University of Jyväskylä, P.O. Box 35 (YFL), FI-40014 University of Jyväskylä, Finland

The prospect of realizing Majorana bound states that can be used for quantum information processing has led to a large interest in odd parity superconductivity. Native triplet superconductivity, believed to be realized in, e.g., Sr_2RuO_4, is fragile and only present at very low temperatures. It is known that a singlet superconductor (SC) can induce triplet pairing correlations in systems with Rashba spin-orbit coupling

and/or ferromagnetism due to the proximity effect, and it has been suggested to induce triplet superconductivity in hybrid structures with such properties. Rashba spin-orbit coupling and ferromagnetism can also give rise to a Josephson coupling between s and p-wave SCs.

Here we suggest an alternative way to improve the robustness of an odd parity SC by tunnel coupling it to an even parity singlet SC in all-oxide-based heterostructures. This mechanism is neither due to Rashba coupling nor ferromagnetism, but by virtue of a strong *intraionic* spin-orbit coupling inherent to late transition metal compounds such as iridium oxide Sr_2IrO_4. To have a coherent coupling between two SCs of opposite parity, the tunneling has to "rotate" the Cooper pairs, since the wavefunctions of the odd and even parity superconducting condensates are orthogonal to each other. We consider a heterostructure consisting of three quasi two-dimensional layers: The even parity spin-singlet "cuprate" SC (B-layer) is separated from the odd parity spin-triplet "ruthenate" SC (A-layer) by an insulating layer, the "iridate convertor", see the inset of Fig. 12.9. The superconductivity takes place in the $d_{x^2-y^2}$ band of the B-layer, and in the Ru-orbitals of t_{2g} symmetry in the A-layer. The tunnel coupling between the two SCs is provided via the spin-orbit entangled Ir t_{2g}-orbitals in the middle layer. This strong intraionic spin-orbit coupling in the middle layer gives rise to an effective tunneling matrix between the two SCs, where the diagonal and off-diagonal elements have opposite parity. The time reversal and mirror symmetric tunneling matrix results in a coherent coupling between the two SCs and leads to an enhancement of the odd parity order parameter, see Fig. 12.9.
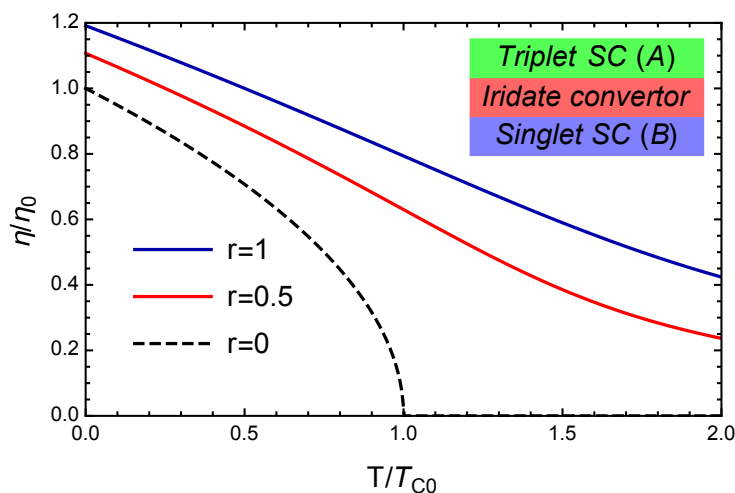
Figure 12.9: (Color online) The p-wave order parameter η as a function of temperature for different values of the enhancement parameter r of the odd parity order parameter. (η_0 and T_{C0} are bare values of the order parameter and critical temperature). The inset shows the three-layer hybrid structure: a singlet SC (B), the "iridate convertor", and the triplet SC (A).

[1] M. Horsdal, G. Khaliullin, T. Hyart, and B. Rosenow, Phys. Rev. B **93**, 220502(R) (2016).

12.11   Impact of Iron-site defects on Superconductivity in LiFeAs

S. Chi,[*], R. Aluru,[†], U.R. Singh,[‡], R. Liang,[*], W.N. Hardy,[*], D.A. Bonn,[*], A. Kreisel, Brian M. Andersen[§], R. Nelson,[¶], T. Berlijn,[‖], W. Ku,[**], P.J. Hirschfeld,[††], P. Wahl[†]

[*]Department of Physics and Astronomy, University of British Columbia, Vancouver BC, Canada V6T 1Z1

[†]SUPA, School of Physics and Astronomy, University of St. Andrews, North Haugh, St. Andrews, Fife, KY16 9SS, United Kingdom

[‡]Max-Planck-Institut für Festkörperforschung, Heisenbergstr. 1, 70569 Stuttgart, Germany

[§]Niels Bohr Institute, University of Copenhagen, Universitetsparken 5, 2100 Copenhagen, Denmark

[¶]Institute of Inorganic Chemistry, RWTH Aachen University, Landoltweg 1, 52056 Aachen, Germany

[‖]Center for Nanophase Materials Sciences, Oak Ridge National Laboratory, Oak Ridge, Tennessee 37831, USA

[**]Department of Physics and Astronomy, Shanghai Jiao Tong University, Shanghai 200240, China

[††]Dept. of Physics, U. Florida, Gainesville, FL 32611 USA

While there is strong evidence for $s_\pm$ superconductivity in many of the iron-based superconductors, this may not be universal, and in some of them there are claims that other order parameters prevail, LiFeAs is a stoichiometric superconductor ($T_c = 17$ K), making it particularly amenable to a comparison with theory. Further, it exhibits an atomically flat non-polar surface that does not undergo reconstruction – making it suitable for spectroscopic studies of the order parameter by ARPES and STM. Crude aspects of the gap structure of LiFeAs have now been fairly well established by these methods.The overall agreement of multiple experimental groups and methods led to several theoretical attempts[2]to calculate the detailed gap function, all of which led to the identification of sign-changing s-wave gaps, but different on the sets of Fermi surface pockets that manifested the same sign. Disputes over these details illustrate the current capabilities of materials-specific calculations of superconducting properties. One way to distinguish among these various proposals is to test their predictive power for impurity states, sensitive probes of gap symmetry and structure. In conventional s-wave superconductors, only magnetic impurities exhibit impurity bound states, whereas for an $s_\pm$ order parameter they can occur for both magnetic and non-magnetic impurities. Impurity bound states in superconductors can thus provide important insight into the order parameter. Here, we present a combined experimental and theoretical study of native and engineered iron-site defects in LiFeAs. Detailed comparison of tunneling spectra measured on impurities with spin fluctuation theory reveals a continuous evolution from negligible impurity bound state features for weaker scattering potential to clearly detectable states for somewhat stronger scattering potentials. All bound states for these intermediate strength potentials are pinned at or close to the gap edge of the smaller gap, a phenomenon that we explain and ascribe to multi-orbital physics. Semiquantitative agreement of theory with spectra can be obtained, but only by assuming some renormalization of first principles impurity potentials and local Fe-Wannier functions[3]. The high level of agreement between theory and experiment supports an $s\pm$ pairing scenario for the pnictide superconductors.
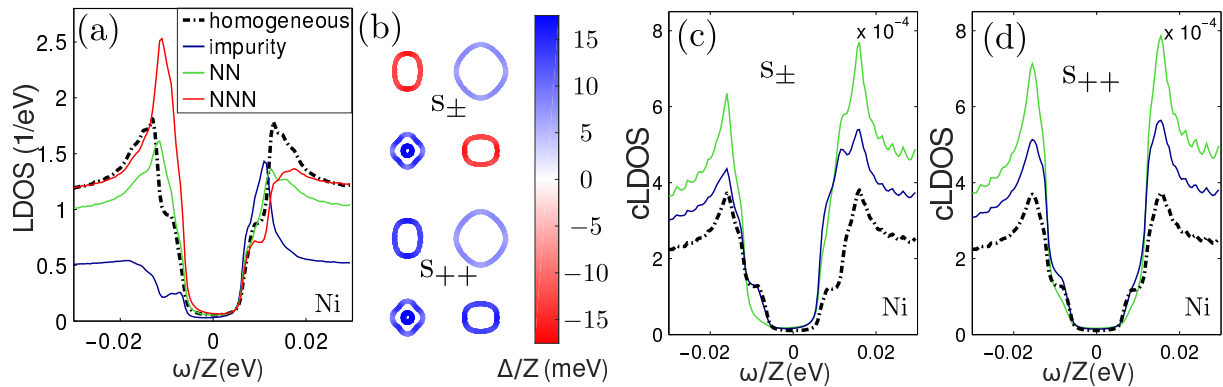
Figure 12.10: (a) Lattice local density of states (LDOS) for an $s_\pm$ order parameter and a Ni impurity. Note the strong enhancement at negative bias at the NN and NNN positions relative to the impurity. (b) Superconducting order parameter on the Fermi surface for the two scenarios: Sign-changing $s_\pm$ order parameter as obtained from spin-fluctuation pairing calculations (top) and s_{++} order parameter with identical gap magnitudes, but everywhere the same sign, yielding an identical density of states in the homogeneous case. (c) Continuum LDOS in $[eV\mathrm{bohr}^3]^{-1}$, taking into account the coupling of the electronic states to the tip ("NN" refers here to the cLDOS at the dimer maximum. The largest change in the density of states due to the defect is now seen at positive bias. (d) The continuum LDOS obtained assuming the same gap magnitude but with equal signs of the order parameter on all Fermi surfaces (s_{++}). The change in the LDOS on the impurity is almost symmetric with respect to zero bias.

[1] Shun Chi, Ramakrishna Aluru, Udai Raj Singh, Ruixing Liang, Walter N. Hardy, D. A. Bonn, A. Kreisel, Brian M. Andersen, R. Nelson, T. Berlijn, W. Ku, P. J. Hirschfeld, Peter Wahl, Phys. Rev. B **94**, 134515 (2016)

[2] Y. Wang, A. Kreisel, V. B. Zabolotnyy, S. V. Borisenko, B. Büchner, T. A. Maier, P. J. Hirschfeld, and D. J. Scalapino, Phys. Rev. B **88**, 174516 (2013).

[3] P. Choubey, T. Berlijn, A. Kreisel, C. Cao, and P. J. Hirschfeld, Phys. Rev. B **90**, 134520 (2014)

12.12   Towards a quantitative description of tunneling conductance of superconductors: application to LiFeAs

A. Kreisel, R. Nelson[*], T. Berlijn[†], W. Ku[‡], R. Aluru[§], S. Chi[¶], H. Zhou[‖], U.R. Singh[§], P. Wahl[§], R. Liang[¶], W.N. Hardy[¶], D.A. Bonn[¶], P.J. Hirschfeld[**], M.B. Andersen[††]

[*]Institute of Inorganic Chemistry, RWTH Aachen University, Landoltweg 1, 52056 Aachen, Germany

[†]Center for Nanophase Materials Sciences, Oak Ridge National Laboratory, Oak Ridge, Tennessee 37831, USA

[‡]T. D. Lee Institute, Shanghai Jiao Tong University, Minhang, Shanghai 200240, China

[§]Max-Planck-Institut für Festkörperforschung, Heisenbergstr. 1, D-70569 Stuttgart, Germany

[¶]Department of Physics and Astronomy, University of British Columbia, Vancouver BC, Canada V6T 1Z1

[||]SUPA, School of Physics and Astronomy, University of St. Andrews, North Haugh, St. Andrews, Fife, KY16 9SS, United Kingdom

[**]Dept. of Physics, U. Florida, Gainesville, FL 32611 USA

[††]Niels Bohr Institute, University of Copenhagen, Universitetsparken 5, DK-2100 Copenhagen

Scanning Tunneling Microscopy (STM) has become a widely used experimental technique to study superconductivity, yet new approaches are unraveling so far unknown properties. A number theories have been used to explain the qualitative origin of superconducting pairing in Fe-based superconductors (FeSC), but quantitative, material-specific comparisons to experimental results have been made in few cases only. Here, a novel approach to theoretical simulation of STM is used which combines first-principles calculations to obtain material-specific Wannier functions and lattice Green functions from BdG or T-matrix calculations[2, 3]. The method takes into account crystal symmetries such that it improves the traditional lattice calculations from two perspectives: Effects of the tunneling layers are contained qualitatively and the spatial resolution is not limited to the lattice spacing, thus comparable to the resolution of experimentally available data. By calculating the local density of states relevant for the tunneling process, it is possible to simulate images of impurities on the surface of superconductors. Here we present a comparison between theory and experiment on the Fe-based superconductor LiFeAs. LiFeAs, with T_c of 18 K, has lent itself particularly well to spectroscopic characterization by angular resolved photoemission spectroscopy (ARPES) and scanning tunneling microscopy (STM) due to the non-polar surface and the high quality of the samples. This enables a detailed comparison between spectroscopy and predictions by theory, and assessment of the status of the theoretical understanding of superconductivity in LiFeAs and iron-based superconductors in general. In this work, results for the homogeneous surface as well as impurity states are presented as a benchmark test of theoretical predictions for the order parameter the properties of the pairing mechanism. For the homogeneous system, we argue that the maxima of topographic image intensity may be located at positions above either the As or Li atoms, depending on tip height and the setpoint current of the measurement. We further report the experimental observation of transitions between As and Li-registered lattices as functions of both tip height and setpoint bias, in agreement with this prediction. Next, we give a detailed comparison between the simulated scanning tunneling microscopy images of transition-metal defects with experiment.

[1] A. Kreisel, R. Nelson, T. Berlijn, W. Ku, Ramakrishna Aluru, Shun Chi, Haibiao Zhou, Udai Raj Singh, Peter Wahl, Ruixing Liang, Walter N. Hardy, D. A. Bonn, P. J. Hirschfeld, Brian M. Andersen, Phys. Rev. B **94**, 224518 (2016)

[2] P. Choubey, T. Berlijn, A. Kreisel, C. Cao, and P. J. Hirschfeld, Phys. Rev. B **90**, 134520 (2014).

[3] A. Kreisel, P. Choubey, T. Berlijn, W. Ku, B. M. Andersen, and P. J. Hirschfeld, Phys. Rev. Lett. **114**, 217002 (2015)
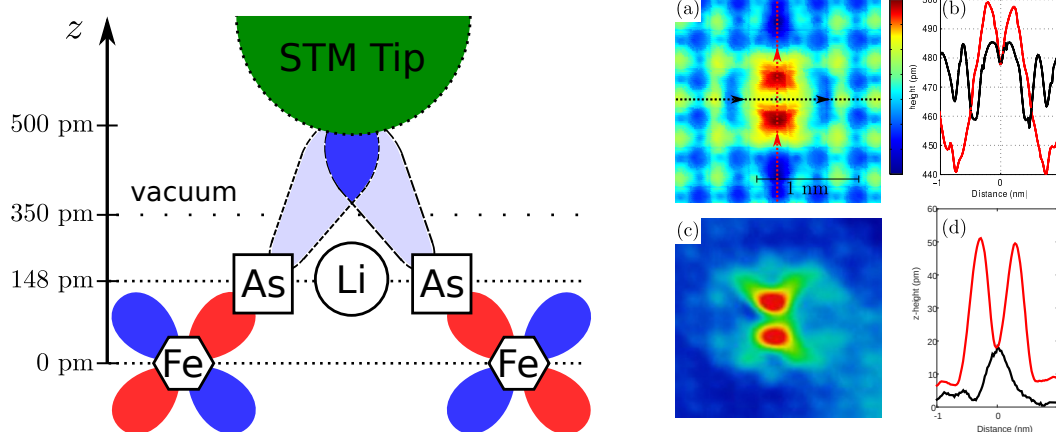
Figure 12.11: (left) Schematic illustration of the tunneling process indicating how tunneling into As states can lead to an intensity maximum above the Li positions: Interference between electrons in Wannier states of neighboring Fe atoms (phase of wave function symbolized by red/blue color) can give rise to maximal tunneling when the STM tip is located above the Li atom. A tip closer to the surface will shift the maximal tunneling positions towards the As atoms. (right) Simulated topograph (a) for a Ni impurity at a bias of 30 mV calculated using a shifted Wannier function at the impurity position to approximate the distortion close to the impurity and corresponding cut along the dashed lines in vertical and horizontal direction (b). (c) Experimental STM topograph of a single Ni impurity at $V_s = 10\,$mV, $I = 500\,$pA. (d) Line cuts along and normal to the Ni impurity shown in (c).

12.13 Funding

12.14 Organizational Duties

B. Rosenow
- Member of the Qualitätssicherungskommission of the Faculty of Physics and Earth Sciences
- Referee for Science, Phys. Rev. Lett., Phys. Rev. B, Europhys. Lett. Adv. Con. Matter, JSTAT, Physica A, NSF, Studienstiftung des Deutschen Volkes
- Vertrauensdozent (Studienstiftung des Deutschen Volkes)

A. Kreisel

- Referee for Phys. Rev. Lett., Phys. Rev. B, Nano Letters, Nature Physics, Nature Communications, Physica Status Solidi B

12.15 External Cooperations

Academic

- University of Vermont, USA
  Adrien Del Maestro

- Universität Heidelberg, Germany
  Dr. Michael M. Scherer

- Max-Planck-Institut für Festkörperforschung, Stuttgart, Germany
  G. Khaliullin

- RWTH Aachen, Germany
  Prof. Dr. Carsten Honerkamp

- Universiteit Leiden, Netherlands
  Dr. Timo Hyart

- School of Physics and CRANN, Trinity College, Ireland
  Prof. Paul Eastham

- Weizmann Institute for Science, Israel
  Prof. Yuval Gefen, Prof. Ady Stern, Prof. Yuval Oreg

- Harvard University, USA
  Prof. Bert Halperin

- McGill University, Canada
  Pierre/Francois Duc, Michel Savard, Matei Petrescu, Guillaume Gervais

- University of California, Los Angeles, USA
  So Takei

- Universität zu Köln, Germany
  Prof. Dr. Alexander Altland

- Princeton University, USA
  Curt von Keyserlingk

- University of Oxford, United Kingdom
  Steve Simon

- Niels Bohr Institute, Denmark
  Brian M. Andersen

- University of Florida, USA
  Peter J. Hirschfeld

- Cornell University, USA
  J.C. Séamus Davis

- Unversity of St. Andrews, Scotland
  Peter Wahl

- Oak Ridge National Labatory, USA
  Tom Berlijn

12.16 Publications

Journals

Bernd Rosenow, Ivan P. Levkivskyi, and Bertrand I. Halperin, Current Correlations from a Mesoscopic Anyon Collider, Phys. Rev. Lett. **116**, 156802 (2016).

Szymon Hennel, Beat A. Braem, Stephan Baer, Lars Tiemann, Pirouz Sohi, Dominik Wehrli, Andrea Hofmann, Christian Reichl, Werner Wegscheider, Clemens Rössler, Thomas Ihn, Klaus Ensslin, Mark S. Rudner, and Bernd Rosenow, Nonlocal Polarization Feedback in a Fractional Quantum Hall Ferromagnet, Phys. Rev. Lett. **116**, 136804 (2016).

A. Janot, B. Rosenow, G. Refael, Topological Polaritons in a Quantum Spin Hall Cavity,Phys. Rev. B **93**, 161111(R) (2016).

M. Horsdal, G. Khaliullin, T. Hyart, and B. Rosenow, Enhancing Triplet Superconductivity by the Proximity to a Singlet Superconductor in Oxide Heterostructures, Phys. Rev. B **93**, 220502(R) (2016).

Björn Zocher and Bernd Rosenow, Topological superconductivity in Quantum Hall-superconductor hybrid systems, Phys. Rev. B **93**, 214504 (2016).

M. Thunert, A. Janot, H. Franke, C. Sturm, T. Michalsky, M. Martin, L. Vina, B. Rosenow, M. Grundmann, R. Schmidt-Grund, Cavity Polariton Condensate in a Disordered Environment, Phys. Rev. B **93**, 064203 (2016).

Sarah Levy Schreier, Ady Stern, Bernd Rosenow, and Bertrand I. Halperin, Thermodynamic properties of a quantum Hall anti-dot interferometer, Physica E **76**, 82 (2016).

Lukas Kimme, Bernd Rosenow, Arne Brataas, Backscattering in helical edge states from a magnetic impurity and Rashba disorder, Phys. Rev. B **93**, 081301(R) (2016).

Lukas Kimme, Timo Hyart, Existence of zero-energy impurity states in different classes of topological insulators and superconductors and their relation to topological phase transitions, Phys. Rev. B **93**, 035134 (2016)

Shun Chi, Ramakrishna Aluru, Udai Raj Singh, Ruixing Liang, Walter N. Hardy, D. A. Bonn, A. Kreisel, Brian M. Andersen, R. Nelson, T. Berlijn, W. Ku, P. J. Hirschfeld, Peter Wahl, Impact of Iron-site defects on Superconductivity in LiFeAs, Phys. Rev. B **94**, 134515 (2016)

A. Kreisel, R. Nelson, T. Berlijn, W. Ku, Ramakrishna Aluru, Shun Chi, Haibiao Zhou, Udai Raj Singh, Peter Wahl, Ruixing Liang, Walter N. Hardy, D. A. Bonn, P. J. Hirschfeld, Brian M. Andersen, Towards a quantitative description of tunneling conductance of superconductors: application to LiFeAs, Phys. Rev. B **94**, 224518 (2016)

in press

Alexander Schneider, Mirco Milletari, Bernd Rosenow, Transient Features in Charge Fractionalization, Local Equilibration and Non-equilibrium Bosonization

Benedikt Friess, Yang Peng, Bernd Rosenow, Felix von Oppen, Vladimir Umansky, Klaus von Klitzing, Jurgen H. Smet, Negative permittivity attests to local attractive interactions in bubble and stripe phases

Peter O. Sprau, Andrey Kostin, Andreas Kreisel, Anna E. Böhmer, Valentin Taufour, Paul C. Canfield, Shantanu Mukherjee, Peter J. Hirschfeld, Brian M. Andersen, J.C. Séamus Davis, Discovery of Orbital-Selective Cooper Pairing in FeSe

A. Kreisel, Brian M. Andersen, Peter O. Sprau, Andrey Kostin, J.C. Séamus Davis, P. J. Hirschfeld, Orbital selective pairing and gap structures of iron-based superconductors

Talks

B. Rosenow, Quantum Hall interferometry with Majorana anyons, Workshop Majorana 2016, Schloss Waldthausen, February 2016.

B. Rosenow, Dissipative superfluidity and mesoscale confinement, Workshop Light-matter Interaction and Quantum Control in Many-body Systems, Aspen Center for Physics, Juni 2016.

A. Kreisel, Towards a realistic simulation of disorder in unconventional superconductors, ITF-Seminar, Leibnitz Institut für Festkörper- und Werkstoffforschung, Dresden, August 2016

A. Kreisel, Realistic simulation of tunneling in STM for cuprates, Department of Physics, University of Florida, Gainesville, FL, December 2016

Posters

B. Rosenow und B. Zocher, Topological superconductivity in Quantum Hall-superconductor hybrid systems, Bernd Rosenow und Bjoern Zocher, Workshop, "Topological Quantum Matter: Progress and Applications", Aspen Center for Physics, January 2016

C. Drukier, P. Lange, P. Kopietz, Non-analytic corrections to quasiparticle properties of two-dimensional Fermi liquids, Tsinghua Xin Center 2nd International Winter School - Physics at the Edge: from Topological surfaces to Oxide Interfaces, Tel Aviv, January 2016

Giovanni Andrea Frigeri, Daniel Scherer, Bernd Rosenow Subperiods and pairing in quantum Hall interferometers with Coulomb coupling of edge channels, QDev/NBIA 2016 Summer school "Quantum information in condensed matter physics", July 2016

Giovanni Andrea Frigeri, Daniel Scherer, Bernd Rosenow, Subperiods and pairing in quantum Hall interferometers with Coulomb coupling of edge channel, Bad Honnef Physics school "Frontiers of quantum matter", September 2016

12.17 Graduations

Doctorate

- Lukas Kimme
  Bound states and resistive edge transport in two-dimensional topological phases
  13.10.2016

- Alexander Janot
  Quantum condensates and topological Bosons in coupled light-matter excitations
  29.02.2016

Master

- Niels John
  Multiple Edge Reconstruction ad Edge State Velocity in the $\nu = 1$ Quantum Hall State
  14.12.2016

- Florian Knoop
  Functional Renormalization Group study of a multi-orbital Hubbard model for the LAO/STO interface
  29.11.2016

- Encrio Lohmann
  Dephasing of fractional Fabry-Pérot interferometers due to edge reconstruction
  28.09.2016

Bachelor

- Matthias Thamm
  Energy of Vortices in Superfluids from the Gross-Pitaevskii Equation
  08.08.2016

- Pit Strub
  Kennlinien von Typ II und Typ III Heteroübergängen
  23.08.2016

12.18 Guests

- Dr. Jinhong Park
  Department of Condensed Matter Physics, Weizmann Institute of Science, Israel
  09.03. - 15.03.

- Dr. Alexander Zyuzin
  Department of Physics University of Basel
  10.03. - 11.03.

- Dr. Andreas Kreisel
  Niels Bohr Institute, Copenhagen
  22.03.-23.03.

- Dr. Ivan Levkivski
  ETH Zürich, Switzerland
  18.05. - 20.05.

- Prof. Dr. Adrian Del Maestro
  University of Vermont, USA
  08.08. - 21.08.

- Prof. Dr. Yuval Gefen
  Department of Condensed Matter Physics, Weizmann Institute of Science, Israel
  16.10. - 19.10.

13

Theory of Condensed Matter

13.1 Introduction

Major research topics of our groups include nonequilibrium phenomena and pattern formation in systems of various nature, e.g. in soft condensed matter and in biological systems. Modern analytic methods of statistical physics and computer simulations complement and stimulate each other. Cooperations with mathematicians, theoretical and experimental physicists, biologists and medical researchers in Germany, Europe and around the world are well established.

Stochastics and pattern formation (Behn). Noise induced phenomena like nonequilibrium phase transitions are studied with analytical and computational methods in stochastically driven nonlinear systems with many degrees of freedom. Methods of nonlinear dynamics and statistical physics are used to formulate and investigate mathematical models of the adaptive immune system. We describe the randomly driven evolution of idiotypic networks of the B-lymphocyte subsystem and its role in self tolerance and autoimmunity.

The lineage commitment and plasticity of $CD4^+$ T cells is modeled using a minimal Boolean network to describe the intracellular signal transduction.

Non-equilibrium dynamics in soft-condensed-matter systems (Kroy). The group's activities can be subsumed under the name of "Soft Mesoscopics", the study of emerging properties in soft and biological matter. Studied phenomena range from structure formation by wind-blown sand resulting in ripples and dunes, through nonequilibrium dynamics of hot nanoparticles, proteins and polymers, the viscoelastic and inelastic mechanics of the cytoskeleton, to the tension propagation in single DNA molecules under strong external fields. (Related experimental work is currently in progress at EXP1: MON, MOP, PWM.) A common theme is the presence of strong fluctuations and stochastic dynamics on the microscale. The emergence of the mesoscopic structure and transport is to be understood. The applied methods comprise a broad statistical mechanics toolbox including stochastic (integro-)differential equations, liquid-state theories, effective hydrodynamic equations, various systematic coarse-graining techniques, and massively parallel numerical simulations on GPUs.

Ulrich Behn, Klaus Kroy

13.2 Phase Transitions and Critical Phenomena in Stochastic Systems with Many Degrees of Freedom

U. Behn, R. Kürsten

Arrays of coupled nonlinear dynamical systems driven by multiplicative or additive noise show close analogies to phase transitions in equilibrium [1].

Methods, originally developed to characterize the critical manifold in continuous non-equilibrium phase transitions [2], are applied and extended to models with competing interaction terms which exhibit discontinuous phase transitions, for example, tight bounds for the tricritical point are analytically derived. In the coexistence region of the parameter space, the scaling of the central and the side peaks of the probability with increasing system size is numerically investigated using the newly developed patchwork simulation technique [3].

The patchwork sampling allows by a suitable decomposition of the state space an efficient computer simulation of nonlinear stochastic differential equations to sample probability densities also in sparsely visited regions of the support [4]. The computational costs can be reduced by several orders of magnitude. The method is based on the concept of truncated Markov chains for reversible processes and can be extended to the non-reversible case [5].

[1] F. Sagués, J. García-Ojalvo, J.M. Sancho: Rev. Mod. Phys. **79**, 829 (2007)
[2] R. Kürsten, S. Gütter, U. Behn: Phys. Rev. E **88**, 022114 (2013)
[3] R. Kürsten, U. Behn: Phys. Rev. E **94**, 062135 (2016)
[4] R. Kürsten, U. Behn: Phys. Rev. E **93**, 033307 (2016)
[5] R. Kürsten: *Critical Phenomena in Non-Markovian and Nonlinear Diffusion Processes*, Dissertation, Universität Leipzig, 2017

13.3 The Elephant Random Walk and Percolation on Random Recursive Trees

R. Kürsten

Elephant random walks have infinite memory and can exhibit anomalous diffusive behaviour [1].

A connection between these walks and bond percolation on random recursive trees is exploited to translate results from elephant random walks to the percolation process and vice versa. Among other quantities, exact expressions for the first and the second moment of the root cluster size and of the number of nodes in child clusters of the first generation are derived. Superdiffusion is related to the occurence of a giant connected root cluster in the percolation problem. Subdiffusion is explained with the existence of an effective internal time [2]. An extension to a skew random walk, and to arbitrary dimensions is proposed. For the latter extension, the diffusive behaviour can be completely classified [3].

[1] G.M. Schütz, S. Trimper: Phys. Rev. E **70**, 045101 (2004)

[2] R. Kürsten: Phys. Rev. E **93**, 032111 (2016)
[3] R. Kürsten: *Critical Phenomena in Non-Markovian and Nonlinear Diffusion Processes*, Dissertation, Universität Leipzig, 2017

13.4 Randomly Driven Evolution of Idiotypic Networks

U. Behn, S. Landmann, J. Müller

We have investigated the problem of self tolerance and its failure -autoimmunity- in the frame of a minimal model of the idiotypic network [1], developed in our group [2–5]. For recent reviews of the idiotypic network paradigm, see Refs. [6, 7]. In our model a node represents a clone of B lymphocytes with certain idiotype, and a link indicates possible idiotypic interactions between clones of complementary idiotype. The model network evolves, driven by the random influx of new idiotypes and subject to deterministic selection rules, towards a highly organized modular architecture where groups of nodes which share statistical characteristics can be identified. Self is modeled by permanently occupied nodes. We found in simulations corroborated by an analytical modular mean field theory, that in the presence of self the architecture organizes in a way that the neighbors of self are only weakly occupied, such that self is tolerated [5].

We have studied perturbations of different kind which can induce an autoreactive state, like infections with antigen, alterations of the influx of new idiotypes, or reductions of the idiotypic repertoire by a phlebotomy, and devised, in the frame of the model, therapeutic protocols which reconstitute self-tolerance [8, 9].

In a more abstract setting, the response of an established architecture to perturbations of various kinds and the relative stability of different architectures is studied using numerical simulations and analytical methods. We measure the Hamming distance of two close realizations driven by different or identical influx. The simulation results are in good agreement with those from mean field theory. For the 12-group pattern we can identify two regimes: for weaker influx the Hamming distance reaches a stationary nonzero value, whereas for an influx above a certain threshold the distance become zero, the two realizations become synchronized. We further found selection rules for the mesostates in transitions between different architectures [10, 11]

[1] N.K. Jerne: Ann. Inst. Pasteur Immunol. **125C**, 373 (1974)
[2] M. Brede, U. Behn: Phys. Rev. E **67**, 031920 (2003)
[3] H. Schmidtchen, M. Thüne, U. Behn: Phys. Rev. E **86**, 011930 (2012)
[4] H. Schmidtchen, U. Behn: Phys. Rev. E **86**, 011931 (2012)
[5] R. Schulz, B. Werner, U. Behn: Frontiers in Immunology **5**, 00086 (2014), doi: 10.3389/fimmu.2014.00086
[6] U. Behn: Immunol. Rev. **216** 142 (2007)
[7] U. Behn: *Idiotype Network*, in: Encyclopedia of Life Sciences, John Wiley & Sons, Ltd, Chichester, doi:10.1002/9780470015902.a0000954.pub2 (2011)
[8] S. Landmann, N. Preuss, U. Behn: *Self tolerance and autoimmunity in a minimal model of the idiotypic network*, arXiv:1609.05735 (2016), submitted for publication
[9] S. Landmann, *Self-tolerance and Autoimmunity in a Minimal Model of the Idiotypic Network*, Master Thesis, Universität Leipzig, 2016

[10] J. Müller, *Stabilitätsuntersuchungen an einem minimalistischen Modell des idiotypischen Netzwerkes*, Master Thesis, Universität Leipzig, 2016

[11] J. Müller, U. Behn: *Randomly evolving networks: Stability properties*, in preparation.

13.5 Boolean Cellular Network Model for the Differentiation Process of Naive Helper and Regulatory T-Cells

U. Behn, C. Schöller

T helper cells play a significant role in the adaptive immune system. There are several subtypes which differ in their cytokine profiles. One can distinguish four major lineages: Th1, Th2, Th17 and regulatory T cells (Treg). A skewed balance between these lineages in foavour of Th2 cells is responsible for allergic reactions, they activate the production of IgE antibodies which provoke the well-known allergic symptoms. For a mathematical model of T-helper balance and the hyposensitization therapy see [1].

There are other diseases where the Th-subtype Th17 is suspected to play a decisive role. They include allergic asthma, Crohn's disease and ulcerative colitis, rheumatoid arthritis, and many others. Th17 cells have a much higher plasticity compared to Th1 and Th2 cells.

To describe the lineage commitment and the plasticity of CD4+ T cells we have developed a minimalistic model of the network of intracellular signal transduction [2] based on Boolean cellular automata. Already in its simplest version the Boolean network has attractors which describe Th1, Th2, Treg, and Th17 phenotypes and hybrids such as Th1/Th17, Th2/Th17, and Treg/Th17 and reproduces, for example, the high plasticity of Th17 cells [3].

We continued the research with a critical analysis of previous results and studying properties of the model in variant architectures of the network including probabilistic components and embedded a collective of cells into a common cytokine background. The temporal evolution of the cells phenotype in the model invites for a new interpretation of the biological term 'lineage commitment' [4].

[1] F. Groß, G. Metzner, U. Behn: J. Theor. Biol. **269**, 70-78 (2011)

[2] J. Zhu, W.E. Paul: Immunol. Rev. **238**, 247-262 (2010)

[3] D. Kröber: Master thesis, Universität Leipzig, 2011

[4] C. Schöller: *Boolean Cellular Network Model for the Differentiation Process of Naive Helper and Regulatory T-Cells*, Master Thesis, Universität Leipzig, 2016

13.6 Grain-scale modeling and splash parametrization for aeolian sand transport

M. Lämmel, K. Dzikowski, L. Oger, A. Valance, K. Kroy

The collision of a spherical grain with a granular bed is commonly parametrized by the splash function, which provides the velocity of the rebounding grain and the velocity distribution and number of ejected grains [1]. In Ref. [3], we derived a rebound parametrization for the collision of a spherical grain with a granular bed, starting from elementary geometric considerations and physical principles, like momentum conservation and energy dissipation in inelastic pair collisions. Combined with a recently proposed energy-splitting model [2] that predicts how the impact energy is distributed among the bed grains, this yields a coarse-grained but complete characterization of the splash as a function of the impact velocity and the impactor–bed grain-size ratio. The predicted mean values of the rebound angle, total and vertical restitution, ejection speed, and number of ejected grains are in excellent agreement with experimental literature data and with our own discrete-element computer simulations. We extract a set of analytical asymptotic relations for shallow impact geometries, which can readily be used in coarse-grained analytical modeling or computer simulations of geophysical particle-laden flows.
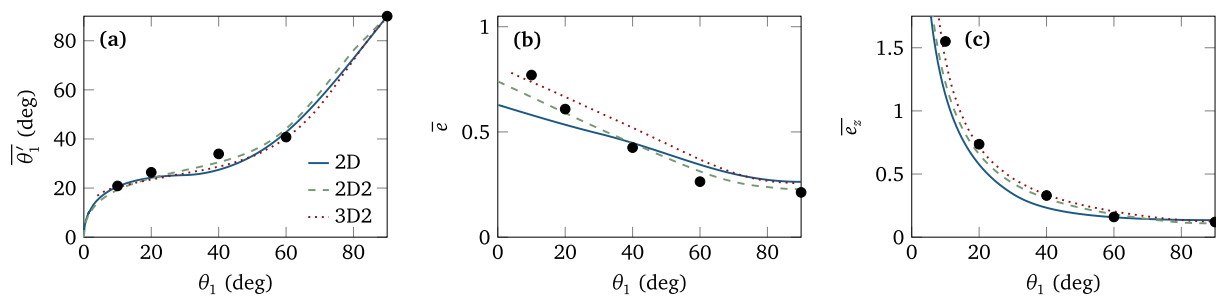
Figure 13.1: Splash model compared with literature data (taken from Ref. [3]). The dependence of the mean rebound angle (a), the total restitution (b), and the vertical restitution (c) on the impact angle as predicted by the two-dimensional model version with (2D2) and without (2D) a second bed collision and the full three-dimensional version (3D2) is fitted to experimental data obtained for plastic PVC beads [4] (dots). Two microscopic restitution coefficients served as global fit parameters.

[1] J. E. Ungar, P. K. Haff: Sedimentology **34**, 289 (1987)
[2] T. D. Ho, P. Dupont, A. Ould El Moctar, A. Valance: Phys. Rev. E **85**, 052301 (2012)
[3] M. Lämmel, K. Dzikowski, K. Kroy, L. Oger, A. Valance: Phys. Rev. E **95**, 022902 (2017)
[4] D. Beladjine, M. Ammi, L. Oger, A. Valance: Phys. Rev. E **75**, 061305 (2007)

13.7 Analytical mesoscale modeling of aeolian sand transport

M. Lämmel, A. Meiwald, K. Kroy

The mesoscale structure of aeolian sand transport plays a crucial role for the understanding and control of a variety of natural phenomena in planetary and Earth science. We analyze it beyond the mean-field level, combing insights we gained from a previously proposed two-species transport model [1] with a recently developed parametrization scheme of the collision process between hopping grains and the sand bed [2]. Analytical predictions for the height-resolved sand flux and other important mesoscale characteristics of the aeolian transport layer are derived. Their remarkable agreement with numerical simulations of the transport model and with a comprehensive compilation of field and wind tunnel data suggests that the essential mesoscale physics is robustly captured by the coarse-grained analytical model. It also reveals that certain widely accepted experimental procedures are prone to systematic measurement errors and suggests new ways to avoid them.

[1] M. Lämmel, D. Rings, K. Kroy: New J. Phys. **14**, 093037 (2012)
[2] M. Lämmel, K. Dzikowski, K. Kroy, L. Oger, A. Valance: Phys. Rev. E **95**, 022902 (2017)

13.8 Aeolian sand sorting and megaripple formation

M. Lämmel, A. Meiwald, Y. Hezi, H. Tsoar, I. Katra, K. Kroy

Sand is blown across beaches and deserts by turbulent winds. The seemingly chaotic process creates monumental dunes [1, 3] and delicate ripple patterns [2], but hardly anything in between. By the very same process, grains are constantly sorted, as smaller ones advance faster, heavier ones trail behind. In this work, we argue that sand sorting and structure formation under prevalent erosive wind conditions can conspire to create distinct bedforms in the "forbidden wavelength gap" between aeolian ripples and dunes [4]. These so-called megaripples are shown to co-evolve with an unusual, predominantly bimodal grain-size distribution [5]. Combining theory and field measurements, we generate a mechanistic understanding of their shape and migration speed, as well as their cyclic aging, renewal, and sedimentary memory, in terms of the intermittent wind statistics.

[1] K. Kroy, G. Sauermann, H. J. Herrmann: Phys. Rev. Lett. **88**, 054301 (2002)
[2] O. Durán, P. Claudin, B. Andreotti, Bruno: Proc. Natl. Acad. Sci. U.S.A. **111**, 15665 (2014)
[3] B. Andreotti, P. Claudin, S. Douady: Eur. Phys. J. B **28**, 341 (2002)
[4] J. M. Ellwood, P. D. Evans, I. G. Wilson: J. Sediment. Res. **45**, 554 (1975)
[5] H. Yizhaq, I. Katra and O. Isenberg, H. Tsoar: Aeolian Research **6**, 1 (2012)

13.9 Interacting Brownian dynamics in a nonequilibrium particle bath

S. Steffenoni, G. Falasco, K. Kroy

The notion of Brownian motion refers to the thermal fluctuations of some mesoscopic particles in contact with a bath of smaller particles, e.g. described by so-called Langevin equations. The scale separation between the Brownian and bath degrees of freedom allows for a systematic coarse-graining of an otherwise intractable many-body system. At equilibrium, the derivation of the mesoscopic equation is thereby greatly simplified, as it permits the application of thermodynamics concepts to the bath degrees of freedom. If some of the mesoscopic degrees of freedom are externally driven out of equilibrium, the theory remains valid, as long as local detailed balance persists. Less known and more interesting is the case in which the bath itself is driven out of equilibrium. Indeed, not only is the detailed balance of the Brownian degrees of freedom then lost, but also stochastic forces are no longer of gradient-type, and the action-reaction principle is macroscopically violated.

We set up a mesoscopic theory for interacting Brownian particles embedded in a nonequilibrium environment, starting from the microscopic interacting many-body theory [1]. Using nonequilibrium linear-response theory, we characterize the effective dynamical interactions on the mesoscopic scale and the statistics of the nonequilibrium environmental noise, arising upon integrating out the fast degrees of freedom. As hallmarks of nonequilibrium, the breakdown of the fluctuation-dissipation and action-reaction relations for Brownian degrees of freedom is exemplified with two prototypical models for the environment, namely active Brownian particles and stirred colloids. In the former we suppose linear coupling between the Brownian particles and the active particle of the environment. Such an analytically solvable model allows to quantify the violation of the fluctuation-dissipation relation. In the latter we consider a one-dimensional system consisting of two probes under harmonic confinement embedded in a fluid of particles moving freely in a periodic domain. The fluid is driven out of equilibrium by an external constant force that induces a net particle current and, consequently, the breaking of action-reaction relations.

[1] S. Steffenoni, K. Kroy, and G. Falasco. Phys Rev. E **94**, 062139 (2016)
[2] S. Steffenoni, G. Falasco, and K. Kroy. arXiv:1612.08404 (2016)

13.10 Boundary layer thickness of Janus particles

S. Auschra, R. Pfaller, G. Falasco, D. Chakraborty, K. Kroy

In this project, we study the propulsion mechanism of a Janus sphere – an artificial, micron-sized swimmer particle made of two hemispheres with unequal thermal and solvation properties which is constantly illuminated by laser light. Usually, they are manufactured by coating approximately half of a polystyrene bead with a thin gold layer. The persistent heating of the Janus sphere's gold cap keeps the immersed particle far from equilibrium, generating an asymmetric temperature distribution in

the surrounding fluid which induces the formation of a complex dissipative solvent flow [1]. We calculate it for realistic temperature fields, resolving the finite thickness of the boundary layer, under the assumption of an exponential decay of the driving force from the fluid-solid boundary. Comparison with atomistic computer simulations of active and passive Janus particles in a Lennard-Jones fluid yields a boundary layer thickness of approximately one Lennard-Jones atom diameter.

[1] T. Bickel, A. Majee, A. Würger: Phys Rev. E **88**, 012301 (2013)

13.11   Effective nonequilibrium temperatures of Janus spheres

S. Auschra, R. Pfaller, G. Falasco, D. Chakraborty, K. Kroy

Heated Janus spheres exhibit self-thermophoretic active swimming and passive hot Brownian motion. The latter randomizes the swimming path of the particle. As with thermophoresis in an externally imposed temperature gradient, which drives the solute particles either to the hot or to the cold, self-generated temperature gradients induce a persistent random walk of the Janus bead with persistence controlled by the competition between self-thermophoresis and rotational hot Brownian motion. We calculate the effective nonequilibrium temperatures [1, 2] for rotational and translational motion of a Janus particle, which characterize the effectively diffusive motion of the Janus bead in the Markovian limit and verify our theoretical predictions by MD simulations.

[1] G. Falasco, K. Kroy: Phys Rev. E **93**, 032150 (2016)
[2] G. Falasco, M. V. Gnann, D. Rings, K. Kroy: Phys Rev. E **90**, 032131 (2014)

13.12   Inealstic Biomechanics

C. Huster, K. Kroy

Inelastic biomechanics is modelling approach combing two important concepts in biomechanics. First, the bottom-up approach to biomechanics that traces back the mechanical response of living matter to its macromolecular constituents. And secondly, the idea that the mechanics of biological systems transcends the viscoelastic dynamics of semiflexible polymers (at least) by one very essential ingredient, namely the slow (un-)binding dynamics of weak reversible crosslinkers.

In the project a general framework for inelastic biomechnics is developed which can be used for comparing, interpreting and analysing existing inelastic models as well as for the construction of new models. A simple consistent description of the universal rheological properties of biomaterials is aspired.

In particular, the inelastic frame work is used for the description of non-linear deformations. The developed models are compared to experimental data.

13.13   Analytic modelling of catch-slip bonds

J. T. Bullerjahn, K. Kroy

Some biological bonds exhibit a so-called catch-slip behavior that plays an important role for the adhesion of cells, bacteria and platelets [1]. Unlike "normal" slip bonds, these bonds initially strengthen with increasing load. We build on our recent advances in slip-bond kinetics [2] to develop an analytically tractable, microscopic catch-slip bond model [3]. To facilitate the analysis of force-spectroscopy data, we calculate the bond's mean lifetime and the rupture-force distribution for static loading and linear force ramps. Our results are applicable for arbitrary forces and loading rates, covering the whole range of conditions found in experiments and all-atom simulations. A generalization to account for force transducers of finite stiffness is also provided.

[1] W. E. Thomas: Annu. Rev. Biomed. Eng. **10**, 39-57 (2008).
[2] J. T. Bullerjahn, S. Sturm & K. Kroy: Nat. Commun. **5**, 4463 (2014).
[3] J. T. Bullerjahn & K. Kroy: Phys. Rev. E **93**, 012404 (2016).

13.14   Microstructure of sheared entangled solutions of semiflexible polymers

M. Lämmel, E. Jaschinski, R. Merkel, K. Kroy

We study the influence of finite shear deformations on the microstructure and rheology of solutions of entangled semiflexible polymers theoretically and by numerical simulations and experiments with filamentous actin [1]. Based on the tube model of semiflexible polymers [2], we predict that large finite shear deformations strongly affect the average tube width and curvature, thereby exciting considerable restoring stresses. In contrast, the associated shear alignment is moderate, with little impact on the average tube parameters, and thus expected to be long-lived and detectable after cessation of shear. Similarly, topologically preserved hairpin configurations are predicted to leave a long-lived fingerprint in the shape of the distributions of tube widths and curvatures [3]. It was shown in Ref. [1] that our numerical and experimental data support the theory.

[1] M. Lämmel, E. Jaschinski, R. Merkel, K. Kroy: Polymers **8**, 353 (2016)
[2] D. C. Morse: Phys. Rev. E **58**, R1237 (1998)
[3] P. Fernandez, S. Grosser, K. Kroy: Soft Matter **5**, 10, 2047 (2009)

13.15   Viscoelastic response of stiff polymer solutions

M. Lämmel, K. Kroy

A central task in biomechanics is to establish a physical understanding of the unique mechanical properties of living cells and tissues in terms of the material properties

of their polymeric constituents. We propose an analytical model for the linear and nonlinear viscoelastic shear response of solutions of stiff polymers. It integrates locally non-affine bending deformations as captured by an effective-medium theory based on the tube model of semiflexible polymers [1] with transient non-affine polymer stretching [2] and elucidates the crucial role of the contour length for the macroscopic mechanical response.

[1] H. Isambert, A.C. Maggs: Macromolecules **29**, 1036 (1996)
[2] F. Gittes, F. MacKintosh: Phys. Rev. E **58**, R1241 (1998)

13.16   Funding

13.17   Organizational Duties

Ulrich Behn
- Speaker of the Condensed Matter Theory Group (until 31 March 2016)
- Vertrauensdozent für die Nobelpreisträgertagungen in Lindau (until 31 March 2016)
- Bibliotheksbeauftragter of the Faculty (until 31 March 2016)
- Member of the Library Commission of the University (until 31 March 2016)
- Member of Research Profile Area "Mathematical and Computational Sciences"
- Scientific Member of the International Max Planck Research School "Mathematics in the Sciences"
- Referee: Discrete and Continuous Dynamical Systems B
- Reviewer: 22th Contest of Academia Europaea Russian Prizes, Lindau Nobel laureate meeting

K. Kroy
- Member of the graduation grants committee of the University
- Study counselor for physics
- Scientific Member of the International Max Planck Research School "mathematics in the Sciences"
- Referee for Nature Commun., Proc. Natl. Acad. Sci. (USA), Phys. Rev. Lett., Phys. Rev. E, J. Chem. Phys., Biophysical Journal, Soft Matter, Physica A, J. Phys. Cond. Mat., and various funding organizations (e.g. DFG)

13.18 External Cooperations

Academic

- Joint Institute for Nuclear Research, Dubna, Russia
  Prof. Dr. N. M. Plakida

- Universität Heidelberg
  Prof. Frauke Gräter

- University of Padova
  Dr. F. Baldovin, Prof. Dr. M. Baiesi

- Forschungszentrum Jülich
  Prof. Dr. R. Merkel, Dipl. E. Jaschinski

- Indian Institute of Science Education and Research, Mohali
  Prof. Dr. D. Chakraborty

- University of Minnesota, USA
  Prof. Dr. David C. Morse

- Ben-Gurion University of the Negev, Israel
  H. Yizhaq, I. Katra, H. Tsoar

- Université de Rennes, France
  A. Valance

13.19 Publications

Journals

R. Kürsten: *Random Recursive Trees and the Elephant Random Walk*, Phys. Rev. E **93**, 03211 (2016), 11 pp.

R. Kürsten, U. Behn: *Patchwork Sampling of Stochastic Differential Equations*, Phys. Rev. E **93**, 033307 (2016), 14 pp.

R. Kürsten, U. Behn: *Discontinuous transitions in globally coupled potential systems with additive noise*, Phys. Rev. E. **94**, 062135 (2016), 14 pp.

A.A. Vladimirov, D. Ihle, N.M. Plakida: *Magnetic Order and Spin Excitations in the Kitaev-Heisenberg Model on the Honeycomb Lattice*, JETP **122**, 1060-1069 (2016)

S. Steffenoni, K. Kroy, G. Falasco "Interacting Brownian dynamics in a nonequilibrium particle bath", Phys. Rev. E **94** (6), 062139, 2016

K. Kroy, D. Chakraborty, F. Cichos, "Hot microswimmers", Eur. Phys. J. Special Topics **225**, 2207-2225, 2016

G. Falasco *et al.*, "Exact symmetries in the velocity fluctuations of a hot Brownian swimmer", Phys. Rev. E **94** (3), 030602, 2016

G. Falasco, F. Baldovin, K. Kroy, M. Baiesi, "Mesoscopic virial equation for nonequilibrium statistical mechanics", New J. Phys. **18**, 093043, 2016

G. Falasco, K. Kroy, "Nonisothermal fluctuating hydrodynamics and Brownian motion", Phys. Rev. E **93** (3), 032150, 2016

M. Baiesi, S. Ciliberto, G. Falasco, C. Yolcu, "Thermal response of nonequilibrium RC-circuits", Phys. Rev. E **94**, 022144, 2016

G. Falasco, M. Baiesi, "Nonequilibrium temperature response for stochastic overdamped systems", New J. Phys. **18** 043039, 2016

G. Falasco, M. Baiesi, "Temperature response in nonequilibrium stochastic systems", EPL, **113** 20005, 2016

M. Lämmel, E. Jaschinski, R. Merkel, K. Kroy, "Microstructure of Sheared Entangled Solutions of Semiflexible Polymers", Polymers **8** (10), 353, 2016

K. Kroy, "The Inelastic Hierarchy: Multiscale Biomechanics of Weak Bonds", Biophys. J. **111**, 898-899, 2016

J. T. Bullerjahn, K. Kroy, "Analytical catch-slip bond model for arbitrary forces and loading rates", Phys. Rev. E **93** (1), 012404, 2016

Preprints

S. Landmann, N. Preuss, U. Behn: *Self-tolerance and autoimmunity in a minimal model of the idiotypic network*, arXiv:1609.05735

S. Steffenoni, G. Falasco, K. Kroy, "Microscopic derivation of the hydrodynamics of active-Brownian-particle suspensions", arXiv:1612.08404, 2016

Talks

K. Kroy: *Analytical mesoscale modelling of aeolian sand transport I & II*, Geoflow Workshop, Dresden, March 20, 2016

K. Kroy: *Exact symmetries in the velocity fluctuations of a hot Brownian swimmer*, Theory seminar at the German Aerospace Center, Cologne, May 18, 2016

K. Kroy *Exact symmetries in the velocity fluctuations of a hot Brownian swimmer*, Annual meeting, DFG priority programme SPP 1726 – Microswimmers, Bonn, May 19, 2016

K. Kroy: *Exact symmetries in the velocity fluctuations of a hot Brownian swimmer*, International conference, DFG priority programme SPP 1726 – Microswimmers, Bonn, October 6, 2016

K. Kroy: *Microstructure of sheared entangled solutions of semiflexible polymers*, CECAM Workshop, Toulouse, October 10, 2016

K. Kroy: *Exact symmetries in the velocity fluctuations of a hot Brownian swimmer*, Colloquium, KU Leuven, November 10, 2016

Posters

S. Auschra *et al.*: *Hot Microswimmers: Experiments and Atomistic Simulations*, Annual meeting, DFG priority programme SPP 1726 – Microswimmers, Bonn, May 19, 2016

S. Auschra *et al.*: *Hot Janus Swimmers: Theory, Experiments and Simulations*, International conference, DFG priority programme SPP 1726 – Microswimmers, Bonn, October 6, 2016

13.20   Graduations

Doctorate

- S. Sturm
  Kinetics and dynamics of single biomolecules
  November 8, 2016

- Rüdiger Kürsten
  Critical Phenomena in Non-Markovian and Nonlinear Diffusion Processes
  29 March 2016

Master

- Stefan Landmann
  Self-tolerance and Autoimmunity in a Minimal Model of the Idiotypic Network
  September 15, 2016

- Johann Müller
  Stabilitätsuntersuchungen an einem minimalistischen Modell des idiotypischen Netzwerkes
  October 26, 2016

- Claudio Schöller
  Boolean Cellular Network Model for the Differentiation Process of Naive Helper and Regulatory T-Cells
  Oktober 27, 2016

- D. Rose
  Self-consistent Determination of Temporal Correlations in Non-linear Systems: Application to a Bistable System
  May 12, 2016

- C. Huster
  A Framework for Inelastic Biomechanics
  August 30, 2016

- M. Guthardt
  Stability of Barchan Dunes
  September 13, 2016

13.21   Guests

- E. Werner
  University of Gothenburg
  January 14, 2016

- E. Ferrero
  Grenoble Alpes University
  April 20, 2016

- M. Baiesi
  University of Padova
  June 15, 2016

- T. Kranz
  German Aerospace Center
  July 6, 2016

- T. Göppel
  TU Munich
  July 18, 2016

- E. Parteli
  University of Cologne
  September 28, 2016

- S. Pigolotti
  Polytechnic University of Catalonia, Barcelona
  November 2, 2016

- K. Gottschalk
  Ulm University
  November 23, 2016

Author Index

UNIVERSITÄT LEIPZIG

THE PHYSICS INSTITUTES

2016

UNIVERSITÄT LEIPZIG

TC2017

Transparent Conductive Oxides – Fundamentals and Applications

18-22 September 2017

Transparent materials are used for ohmic applications such as transparent contacts in displays and solar cells or electro-magnetic shielding. Also semiconducting transparent oxides for diodes and transistors have gained tremendous interest due to applications in transparent and flexible active electronics.

The TCO2017 meeting will focus on:

· theory of oxide electronic materials
· growth of bulk semiconducting oxides
· epitaxial oxide heterostructures
· metal-like n-type TCOs
· novel oxide semiconductors
· point defects in oxides
· oxide devices and applications
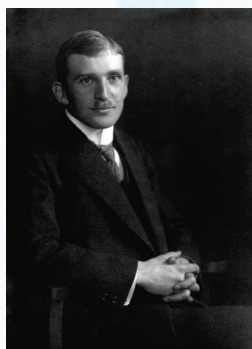
140 years ago Karl W. Bädeker, grandson of the founder of the Baedeker tour guides, was born in Leipzig. He reported 110 years ago in 1907 at Universität Leipzig the first transparent, conductive thin films, namely from cadmium oxide (n-type) and copper iodide (p-type). He also achieved the first doping of semiconductors via the variation of the iodine concentration in CuI.

Invited speakers

Oliver Bierwagen, PDI, Berlin
Armin Dadgar, OvG-Univ. Magdeburg
Peter Deák, Universität Bremen
Judith Driscoll, Cambridge University
Klaus Ellmer, HZB, Berlin
Geoffroy Hautier, Univ. Cath. de Louvain
Kevin D. Leedy, WP-AFB, Dayton, OH
Chris McConville, RMIT Univ., Melbourne
Marjorie Olmstead, U Washington, Seattle
Takahisa Omata, Tohoku University
Chris Sturm, Universität Leipzig
Joel B. Varley, Lawrence Livermore
Garcia Villora, NIMS, Tsukuba
Lasse Vines, University of Oslo
Jesús Zúñiga-Pérez, CRHEA, Valbonne

Program Committee

Martin Albrecht, Leibniz-IKZ, Berlin
Duncan Allsopp, University of Bath
Keith T. Butler, University of Bath
Jean-Michel Chauveau, CRHEA, Valbonne
Marius Grundmann, Universität Leipzig
Axel Hoffmann, TU Berlin
Holger von Wenckstern, Univ. Leipzig

supported by

Bundesministerium für Bildung und Forschung

BuildMoNa

PANalytical

DFG Deutsche Forschungsgemeinschaft

FAHL Fächerübergreifende Arbeitsgemeinschaft Halbleiterforschung Leipzig

Please register and submit your oral or poster contribution via www.buildmona.de/TCO2017

Venue: Lecture Hall for Theoretical Physics, Linnéstraße 5, Leipzig